DEVELOPMENT OF NOVEL HIGH-PERFORMANCE SIX-AXIS MAGNETICALLY LEVITATED INSTRUMENTS FOR NANOSCALE APPLICATIONS

A Dissertation

by

SHOBHIT VERMA

Submitted to the Office of Graduate Studies of
Texas A&M University
in partial fulfillment of the requirements for the degree of

DOCTOR OF PHILOSOPHY

August 2005

Major Subject: Mechanical Engineering

DEVELOPMENT OF NOVEL HIGH-PERFORMANCE SIX-AXIS MAGNETICALLY LEVITATED INSTRUMENTS FOR NANOSCALE APPLICATIONS

A Dissertation

by

SHOBHIT VERMA

Submitted to the Office of Graduate Studies of
Texas A&M University
in partial fulfillment of the requirements for the degree of

DOCTOR OF PHILOSOPHY

Approved by:

Chair of Committee,	Won-jong Kim
Committee Members,	Suhada Jayasuriya
	Alexander Parlos
	Shankar P. Bhattacharyya
Head of Department,	Dennis O’Neal

August 2005

Major Subject: Mechanical Engineering

ABSTRACT

Development of Novel High-Performance Six-Axis Magnetically Levitated Instruments for Nanoscale Applications.

(August 2005)

Shobhit Verma,
B. Tech., Indian Institute of Technology, Bombay;
M. Tech., Indian Institute of Technology, Bombay,
Chair of Advisory Committee: Dr. Won-jong Kim

This dissertation presents two novel 6-axis magnetic-levitation (maglev) stages that are capable of nanoscale positioning. These stages have very simple and compact structure that is advantageous to meet requirements in the next-generation nanomanufacturing. The 6-axis motion generation is accomplished by the minimum number of actuators and sensors.

The first-generation maglev stage is capable of generating translation of 300 μm in *x*, *y* and *z*, and rotation of 3 mrad about the three orthogonal axes. The stage demonstrates position resolution better than 5 nm rms and position noise less than 2 nm rms. It has a light moving-part mass of 0.2126 kg. The total power consumption by all the actuators is only around a watt. Experimental results show that the stage can carry, orient, and precisely position an additional payload as heavy as 0.3 kg.

The second-generation maglev stage is capable of positioning at the resolution of a few nanometers over a planar travel range of several millimeters. A novel actuation scheme was developed for the compact design of this stage that enables 6-axis force generation with just 3 permanent-magnet pieces. Electromagnetic forces were calculated and experimentally verified. The complete design and construction of the second-generation maglev stage was performed. All the mechanical part and assembly fixtures were designed and fabricated at the mechanical engineering machine shop. The single moving part is modeled as a pure mass due to the negligible effect of the magnetic spring and damping. Classical as well as advanced controllers were designed and implemented for closed-loop feedback control. A nonlinear model of the force was developed and applied to cancel the nonlinearity of the actuators over the large travel range. Various experiments were conducted to test positioning, loading, and vibration-isolation capabilities. This maglev stage has a moving-part mass of 0.267 kg. Its position resolution is 4 nm over a travel range of 5 × 5 mm in the *x*-*y* plane. Its actuators are designed to carry and precisely position an additional payload of 2 kg. Its potential applications include semiconductor manufacturing, micro-fabrication and assembly, nanoscale profiling, and nano-indentation.

To my parents

and

little nieces Nidhi and Samriddhi

ACKNOWLEDGMENTS

I would like to express deep gratitude to my dissertation advisor Dr. Won-jong Kim for his consistent encouragement, motivation and moral as well as financial support throughout my study at Texas A&M University. I appreciate his giving me excellent opportunities to publish and present my work several times and get recognition for it. I truly admire his knowledge of electromechanical systems that amazed me frequently in form of instant suggestions for troubleshooting the systems that typically took me long time to debug. My interaction with him over the past 3 years was a great learning experience in all aspects of research.

I wish to thank Drs. Jayasuriya, Parlos and Bhattacharyya for serving as my committee members. I sincerely appreciate the time, advice and support they provided me during my doctoral study. I learned a lot from the courses I took under Drs. Jayasuriya and Bhattacharyya. The significant contributions of the committee members brought this dissertation to success.

I would like to thank Jie Gu, a former student of Dr. Kim, for design of the first stage. Then I would like to give my special thanks to Huzefa Shakir and Yusuke Kawato. Huzefa always helped me a lot whenever I needed help with control system design and Yusuke's ideas in practical applications like mechanical design and troubleshooting were really appreciable. I wish to express my thanks to Mahesh Jalan for his help in learning Solidworks®. I would also like to thank Mike Walker of the mechanical engineering machine shop who occasionally criticized but helped me a lot while fabricating the parts. I appreciate all my labmates for the friendly and enjoyable atmosphere that they provided me in the lab.

My special appreciation goes to our research sponsor. This material is based upon work supported by National Science Foundation under Grant No. CMS-0116642 through Dr. Won-jong Kim.

Finally, I can never thank enough my parents Mrs. Laxmi Verma and Mr. Om Prakash Verma for their unconditional love and prayers, without which I could never have come so far.

TABLE OF CONTENTS

Page

CHAPTER

LIST OF FIGURES

FIGURE Page

FIGURE Page

CHAPTER I

INTRODUCTION

1.1 Role of Precision Positioning Stages in Industry Applications

In the modern era of nanosystems, the precise manufacture of nanoparts is a very crucial task [1]–[2]. Precision positioning and vibration isolation play a crucial role while manufacturing, manipulating, or scanning on micro/nano level. The nanopositioning stages need to meet the challenging positioning requirements of the current and future nanotechnology. These positioning stages along with cutting-edge manufacturing technologies will lead to the development of micro-assemblies and nanostructures. The applications of these stages include micro-stereolithography (μSTL), dip pen nanolithography (DPN), nanoscale profiling, and nano-indentation. The key role of a nanopositioning stage is to load, position, and orient such an object and keep it stable without much vibration or noise. The stage must be able to travel in all directions and place the object at the desired position with minimum error. This requires high accuracy, large travel range, and simultaneous generation of multi-DOF (degree-of-freedom) motions and high control bandwidth [3]. However, there are many theoretical and practical challenges in this early nanopositioning and nanomanipulation research stage. Important technical issues include the development of high-precision manipulation methodologies and the tools for specific applications [4].

This dissertation follows format of *IEEE Transactions on Automatic Control*.

1.2 Current Trends for High-Precision Positioning and Nanomanipulation

1.2.1 Scanning Probe Microscopy

Scanning probe microscopy (SPM) covers several technologies for imaging and measuring surfaces on a fine scale, down to the level of molecules and groups of atoms. A scan may cover a distance of over 100 μm in the *x* and *y* directions and 4 μm in z direction. By following a raster pattern, the sensor data forms an image of the probe-surface interaction [5]. SPM technologies share the concept of scanning an extremely sharp tip (3–50 nm radius of curvature) across the object surface. The tip is mounted on a flexible cantilever, allowing the tip to follow the surface profile. When tip moves in the proximity to the investigated object, interaction forces between the tip and the surface influence the movement of the cantilever. These movements are detected by selective sensors. Three commonest scanning probe techniques are: Atomic Force Microscopy (AFM), Scanning Tunneling Microscopy (STM) and Near-Field Scanning Optical Microscopy (NSOM). Currently most of the atomic-level positioning and profiling is accomplished by AFMs and STMs [6–9]. Although their primary application was topographical imaging, these instruments have become the prime tools for nanomanipulation.

The basic components of AFM and their functions have been shown in Fig. 1-1 [10]. The operation of AFM is based on measurement of attractive or repulsive forces between a tip and sample [11]. There is physical contact between the sample and the AFM tip while working in “contact” mode [12]. The tip mounted at the end of a leaf-spring-type cantilever touches the sample very lightly. While scanning through the area of sample the tip deflects up and down, the sensor system consisting of laser diode and position sensitive photo detector senses the deflection of the cantilever indicating the height of the sample at that point. Therefore the AFM measures the repulsive force between the AFM tip and the sample. While working in noncontact mode the AFM tip does not touch the sample but gets the topographic image of sample from attractive force [13]. The AFM have resolution up to 10 pm. The basic working principle of AFM is very much like a record player. However, it has several improvements that allow it to sense at atomic level e.g. sharp tips, force feedback, sensitive detection, flexible cantilevers, high-resolution tip-sample positioning, etc. The Dimension 3100 Scanning Probe Microscopy (SPM) shown in Fig. 1-2 by Veeco Instruments utilizes automated AFM and STM techniques to measure surface characteristics for semiconductor wafer, lithography masks, magnetic media, biomaterials, etc [14].

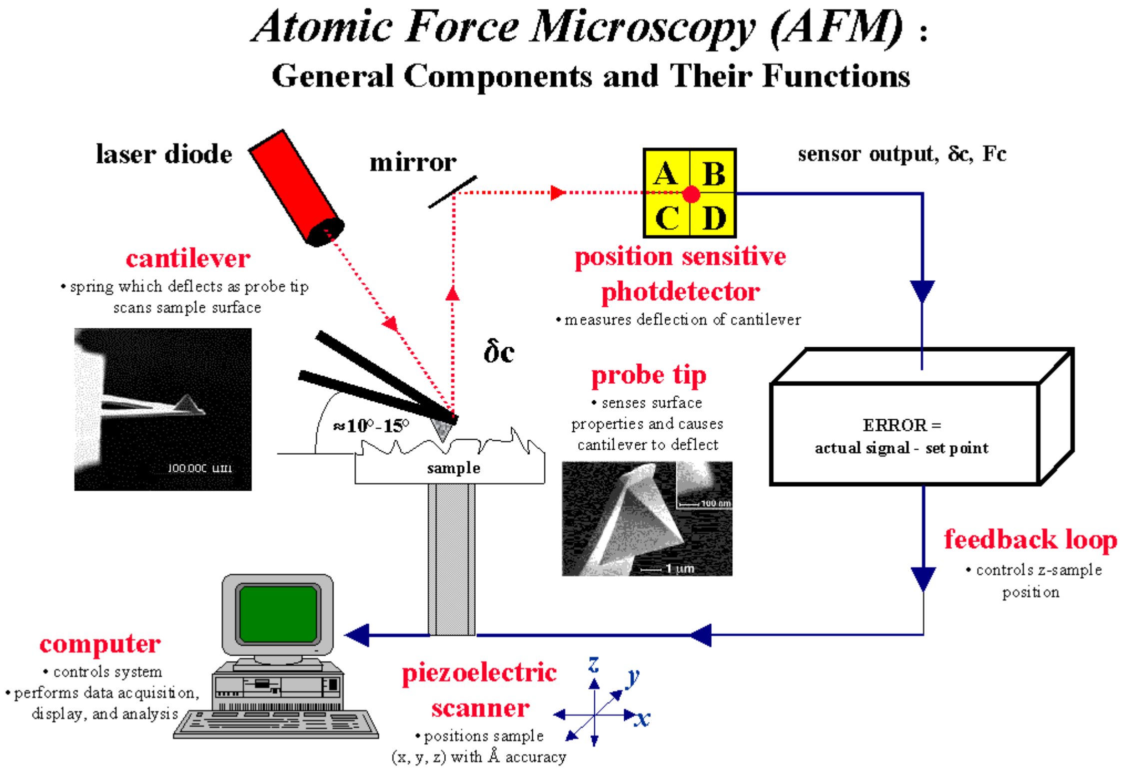

Fig. 1-1. Atomic force microscope and their function [10].

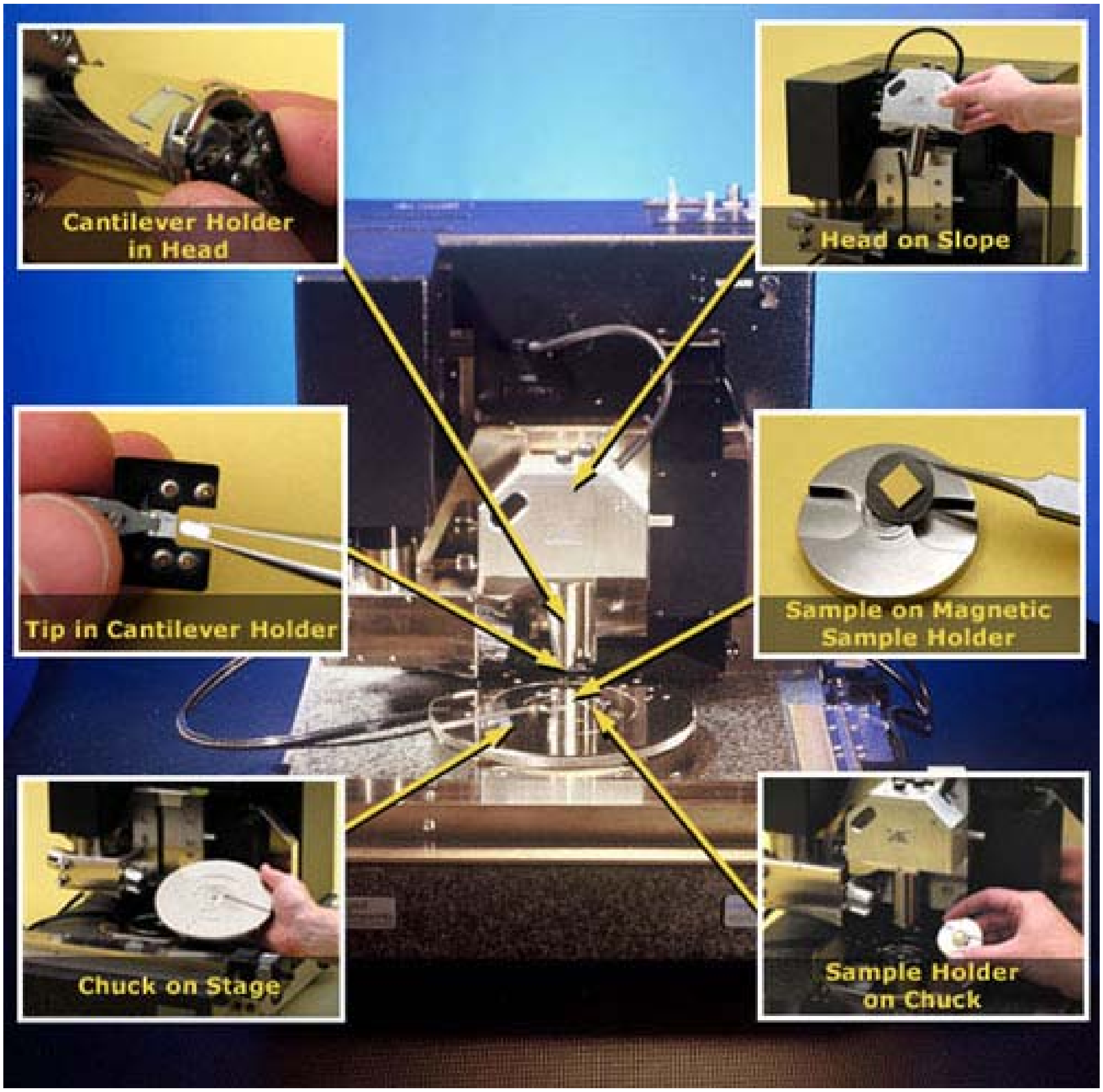

Fig. 1-2. Dimension 3100 AFM by Veeco Instruments [14].

The use of AFM as a nanomanipulator has already been shown [15–16]. The piezo scanner of the AFM has a bow effect due deflection of piezo tube. Therefore AFM space is different from Cartesian space. Various different 3-D nanomanipulation tasks such as nanolithography, trajectory tracking, pushing and cutting using AFM were demonstrated by Li et al. [15]. Shedd et al. showed the STM as a tool for nanofabrication and to study surfaces with sub-nanometer resolution in three spatial dimensions [17]. The possible modifications at the tip-sample interface (energy flux, potential barrier change, and forces) and parameters that can be changed directly (bias, tunnel gap width) are required for application of AFM in nanofabrication.

There are several challenges while performing micro/nanomanipulations using AFMs [18]. Notable shortcomings of such instruments are limited number of DOFs and small travel ranges; they are capable of limited manipulation in the *x*-*y* plane with a travel range of 100 μm and very small translation (a few micrometers) in the vertical direction with little rotational capability.

1.2.2 Piezoelectric Actuators

Most of the actuation units in micro/nanopositioning devices are based on piezoelectric materials. Piezoelectric actuators have become a standard solution in positioning applications where the displacement must be small. Zhang and Zhu developed a high-stiffness linear piezoelectric motor with a resolution of 5 nm. This motor is capable of generating force of 15 N over the travel range of 5 mm with the maximum step size of 3 μm [19]. This linear motor consisted of three piezoelectric actuators and one monolithic flexure frame. A platform for micropositioning was developed that is actuated by piezo-legs [20]. The legs have no joints and motion is performed by slow bending and quick stretching of the legs. During the quick stretching phase the leg tips slip over the ground surface and the platform moves for a small increment. Repetition of this procedure results in a continuous motion. This simple design achieves various motion speeds with precise positioning up to 0.1 μm.

Tan et al. applied a learning nonlinear PID (proportional-integral-derivative) controller for micropositioning of a linear piezoelectric motor [21]. Dong et al. presented a 10-DOF nanorobotic manipulator actuated by PZT (lead zirconium titanate) with a linear resolution of 30 nm and rotary resolution of 2 mrad [22]. An automated microrobot-based desktop station was applied for micro-assembly and handling of micro-objects [23]. These microrobots were capable of manipulation with 10-nm accuracy and several-mm/s speed.

However, there are several limitations with piezoelectric actuators. They are sensitive to environmental changes such as temperature. Moreover, severe nonlinearities are present in their dynamic behavior of PZT [24]. Well-known phenomena of hysteresis and creep, along with nonlinear voltage dependence affect negatively the dynamic response, sometimes precluding closed-loop operation [25–26]. Furthermore, the voltage required to operate piezoelectric actuators can be as high as several hundred volts.

1.2.3 Magnetic-levitation Stages

A novel positioning technology is required to overcome the limitations of prevailing techniques and to fulfill the performance specifications for nanomanipulation and nanofabrication processes. Previous research has shown that magnetic-levitation is a promising technology for such applications [27–35]. Jung and Baek presented a 6-DOF positioner that uses air-core magnetic actuators [27]. It also eliminated stiction, backlash, and hysteresis that limit the precision in position control. Kim et al. developed and demonstrated a high-precision planar maglev stage with large planar motion capability which had 10-nm resolution and 100-Hz control bandwidth [28–29]. Hollis et al. developed a 6-DOF wrist using a maglev technique that was capable of fine motions [30]. Hajjaji and Ouladsine built a nonlinear control model for long-range movement of a maglev system and tested it by real-time control implementation [31]. A maglev scanning stage that is capable of a 0.6-nm three-sigma horizontal position noise was fabricated and demonstrated by Holmes [32]. The development and motion control of a large-travel ultra-precision magnetic suspension stage was presented by Menq et al. [33–34]. Khamesee et al. demonstrated the application of magnetic-levitation in a micro-robotic system used for transportation and assembly of miniature parts in hazardous environment [35]. This microrobot can be remotely operated in 3 DOFs in an enclosed environment by transferring magnetic energy and optical signals from outside.

1.2.4 Other Techniques

There are other techniques that were applied successfully for micromanipulation. Sun et al. fabricated and experimented on a dual-axis electrostatic micro-actuation system [36]. This actuation system has a 0.01-µm resolution over a planar motion of 5 µm in the *x*- and *y*-axes. A high-bandwidth linear actuator consisting of an air-bearing and voice-coil motor was fabricated and tested by Mori et al. This actuator is capable of 1-nm steps without overshoots or undershoots [37]. Egashira et al. developed a precision stage using a non-resonant-type ultrasonic motor with a resolution of 0.69 nm [38]. Culpepper and Anderson came up with an idea of a low-cost nanomanipulator, which uses a six-axis compliant mechanism driven by electromagnetic actuators. The stage mechanism is monolithic and its errors are less than 0.2% of the full scale for a cubical volume travel of 100 µm [39].

Self-assembly was proposed as a possible solution for nanomanipulation. It is basically the same way that life has developed. Self-assembly is a bottom-up approach which is different from the conventional up-bottom approach used in photolithography and micromachining. Self-assembly will be important for some of the building blocks, but it seems unlikely that practically interesting structures, such as bearings can be constructed from self assembly [40]. A nanomanipulator developed by Zyvex Corporation is shown in Fig. 1-3 [41] that actuates using coarse and fine actuators with 12 mm in *x*, *y*, and *z* and provides resolution better than 5 nm.

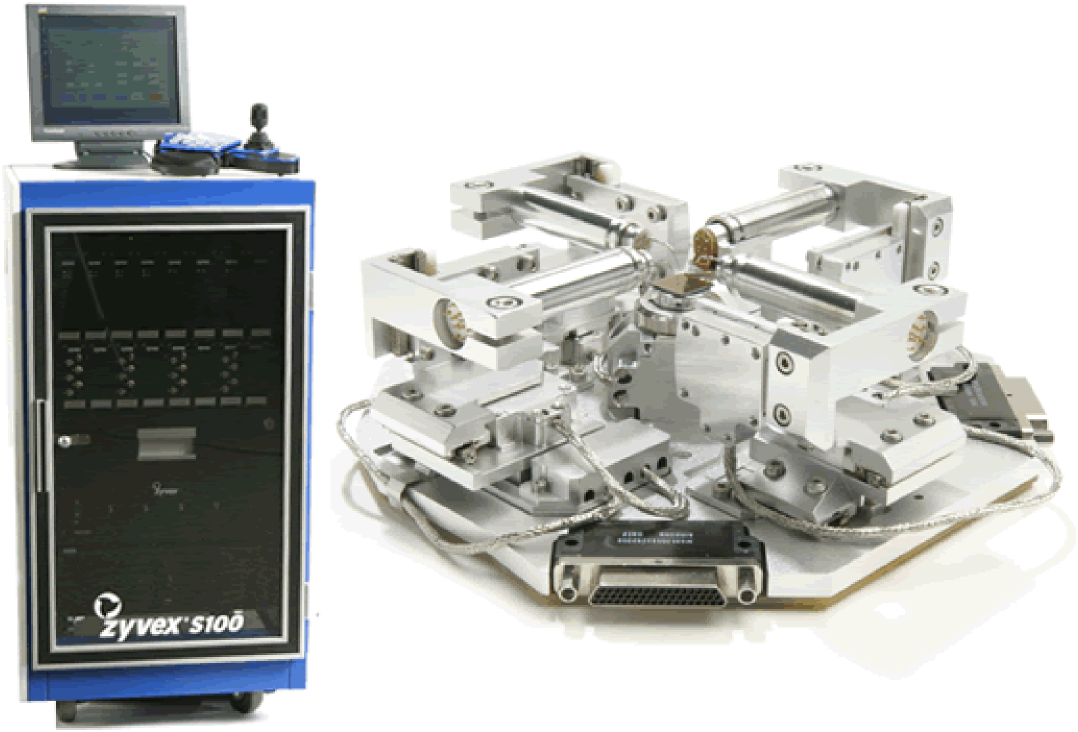

Fig. 1-3. Zyvex F100 nanomanipulator system with focus ion beam (FIB) [41].

1.3 Magnetic Suspension and Levitation in Physical World

Magnetic levitation has also been successfully implemented in various applications, such as high-speed train suspension, vibration isolation, magnetic bearings, electromagnetic launchers, superconducting gyroscope rotor suspension, and precision positioning [42]. Takahara [43] showed the applicability of a maglev concept in a precision antenna pointing system. Gupta, et al. [44] developed a steering mirror. In maglev stages there is no mechanical contact between the moving and stationary parts, so there is no mechanical friction that is one of the most severe factors limiting resolution [27].

Magnetic levitation has also been successfully applied for contactless bearing applications. The bearing assemblies composed of electromagnets and sensors in a same module enable easy maintenance and reduce the machining error [45–46]. A dual-axis repulsive maglev guiding system was developed using permanent magnets [47]. This system uses a modified voice-coil motor, a passive carrier, and an active track. Han et al. built a high-precision linear motion table with novel rare-earth permanent-magnet-biased magnetic-bearing suspension [48]. The permanent magnet provides bias flux and the electromagnet can increase or reduce flux of the permanent magnet. The flux path of the electromagnet does not pass through the permanent magnet so permanent magnet is not demagnetized. The 100-mm stroke of the stage is driven by linear brushless DC (BLDC) motors. Molenaar et al. designed and demonstrated the application of magnetic bearings for contactless precision positioning [49–50]. Three sets of E-shaped stator with primary coils and an I-shaped rotor with secondary coils divided in three parts were used. Experimental results showed 10-mm range in x and y with 80-mrad rotation in ϕ with suspension stiffness of 4×10^6 N/m and 0.2-µm of positioning accuracy.

1.4 Developed Magnetic-levitation Stages

1.4.1 First-generation Maglev Stage

Fig. 1-4 shows a photograph of the first maglev stage developed. This maglev stage used 6 single-axis actuators that were designed by Maheshwari [51]. The compact maglev stage uses the minimum number of actuators required for 6-DOF motion generation. Each vertical actuator consists of a magnet and a coil, and each horizontal actuator consists of two magnets and a coil.

Prevailing precision positioning devices like STMs and AFMs are able to position in the travel range of 100 μm in 3 DOFs. However, our maglev device is capable of motion control in all 6 DOFs with the travel ranges of 300 μm in the x-, y-, and z-translations and 3.5 mrad in the θ-, ϕ-, and ψ-rotations. The position resolution is better than 5 nm with position noise less than 2 nm rms (root-mean-square).

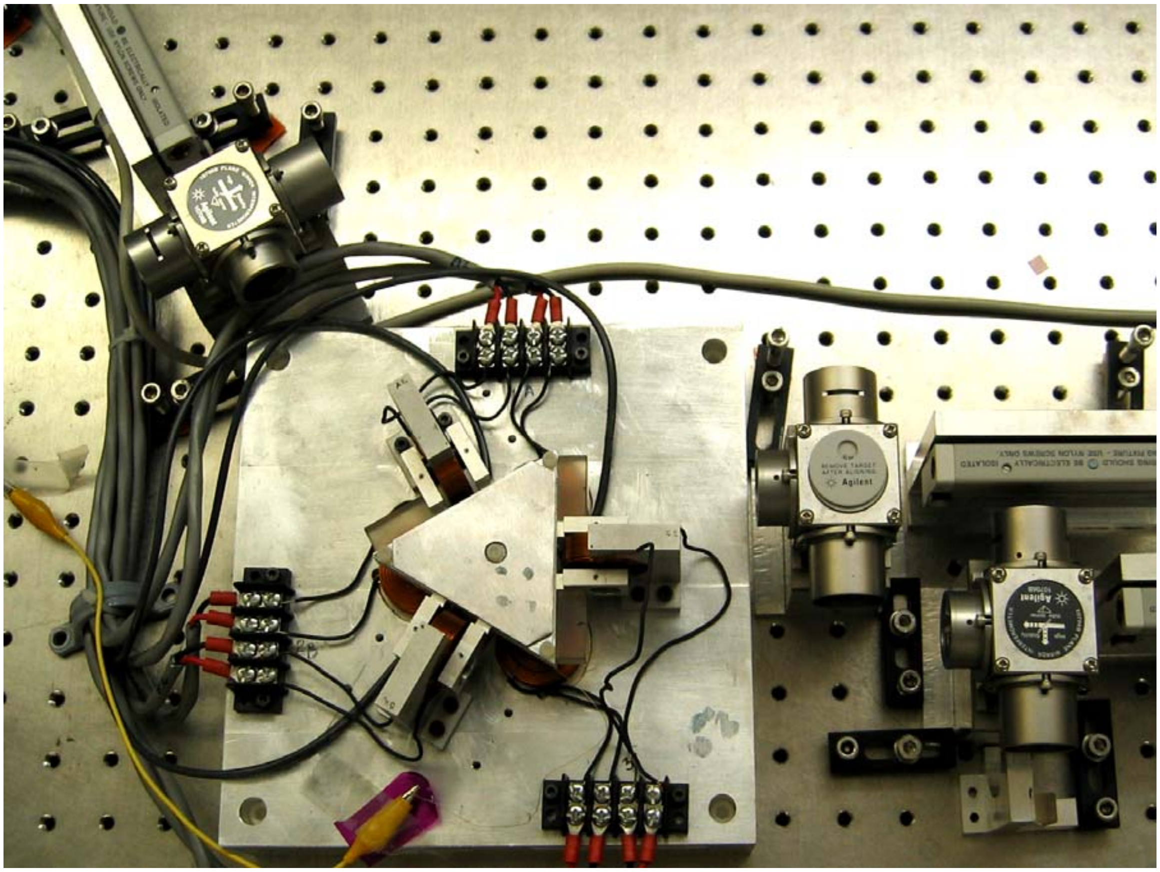

Fig. 1-4. Photograph of first-generation maglev stage.

1.4.2 Second-generation Maglev Stage

The second stage presented here is capable of nanoscale resolution over a large travel range of up to 7 mm. This stage, shown in Fig. 1-5, is based on a novel actuation mechanism in which forces in two perpendicular directions are applied on a single magnet that reduces the number of magnets by half and the mass of the moving part. There is only one moving part, namely the platen, of 0.267 kg. The translational travel range is 5 × 5 mm in the *x*-*y* plane. Due to sensor specifications this stage is currently limited to move 500 µm in the z-axis and 0.1° in

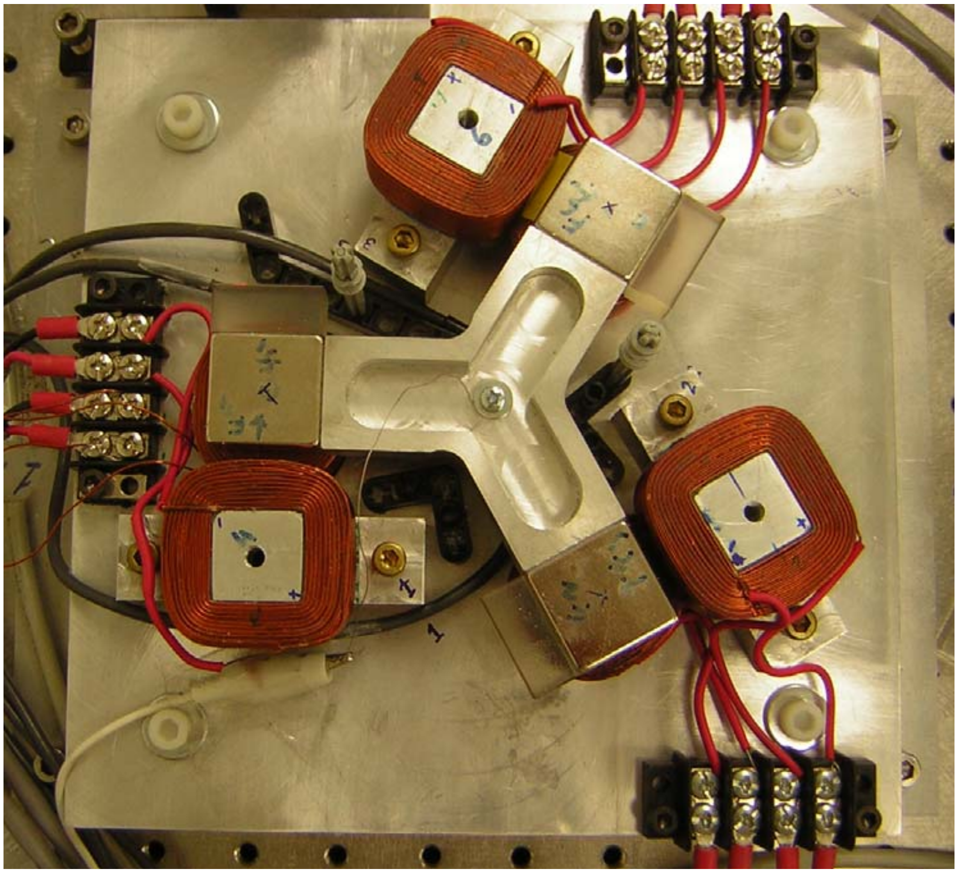

Fig. 1-5. Photograph of second-generation maglev stage.

rotation. However, the mechanical design of the stage makes it capable to rotate more than 5° and translate more than 7 mm in *z*. This stage is capable of up to 2.5-*g* acceleration in horizontal and 8-*g* acceleration in vertical directions. The payload capacity limited by actuator sizing is 2 kg.

The first-generation six-axis maglev stage is capable of 2 nm resolution over the travel range of 300 μm in the *x*-, *y*- and *z*-axes with a payload capacity of 0.3 kg. The second-generation stage has the travel range around 15 times as wide as that of the first one and the payload capacity of 2 kg as compared to previous 0.3 kg. The nominal power consumption per unit actuator is just 135 mW, less than half of the power consumption of the first stage, 320 mW. Moreover, the second stage has several additional unique advantages such as smaller number of parts and no mechanical restriction. There are less than two dozen parts in the whole stage with the minimum number (six) of coils. There are only three magnet pieces, and two coils share the horizontal and vertical magnetic fields of each magnet piece. Due to the absence of any mechanical restriction, the platen can be removed from the machine frame easily without disturbing any stationary parts. This facilitates easy loading and unloading of objects on the platen for various applications. Thus our second-generation maglev stage possesses competitive advantages in terms of travel range, payload capacity, simplicity in mechanical design, and power consumption. The resolution is currently a bit lower than the previous stage due to nonlinearities in the longer travel range.

1.5 Dissertation Overview

This dissertation contains nine chapters. Chapter I describes the importance of precision positioning stages for the development of technology. It presents a literature review of existing options of micro/nanopositioning with a brief description of their benefits and limitations. The SPM scanner, being a comparable performer, is described in detail along with various other techniques using piezoelectric actuators. The application of magnetic levitation for precision positioning and other successful uses like vibration isolation and magnetic bearings are discussed.

Chapter II presents the instrumentation structure of the maglev stages. The capacitance sensors and laser interferometers are described with their locations and specifications. The VME (Versa Module Eurocard) bus with data-acquisition cards, a digital-signal-processor (DSP) board and a VME PC (personal computer) are explained with their specific usage in our maglev stages.

Chapter III discusses the electromechanical and mechanical design of the first-generation maglev stage. The linear actuator units that levitate and propel the stage are explained. Fabrication of all the parts and their precision assembly is discussed. The working principle of the maglev stage is also explained in this chapter.

Chapter IV shows the dynamic modeling of the first maglev stage with modal force and displacement transformations. Control system design to run the maglev stage in closed loop is described. An extensive set of performance tests is carried out to test the precision motion control and loading performance of the stage.

Chapter V onwards the second-generation maglev stage is discussed. In this chapter the novel scheme to apply forces in two perpendicular directions on a single moving magnet is explained. The calculation procedure of magnetic force on the magnet due to current-carrying coils is discussed followed by actuator design. Calculated forces and their experimental verifications are shown.

Chapter VI explains the mechanical design issues of the second maglev stage. Various mechanical parts and their importance, assembly structure, and sensor mounting are described.

Finite element analyses of the platen and the base plate are carried out for natural-frequency and thermal expansion estimation.

Chapter VII discusses dynamic modeling of the second stage. The mass and inertia tensors are defined and, modal force and displacement transforms are calculated. A decoupled lead-lag controller is designed and applied. The step responses demonstrating the performance of the controller on the stage are shown.

Chapter VIII demonstrates the application of advanced control algorithms on the maglev stage. A MIMO linear quadratic regulator, feedforward decoupling compensation, and feedback linearization are applied and tested for their performance.

Chapter IX concludes this dissertation summarizing the achievements in this work and suggestions for possible future work. Appendices include engineering drawings of mechanical parts and programming codes used to run the maglev stages.

1.6 Dissertation Contributions

The main contribution of this dissertation is the design and realization of two high-resolution 6-axis maglev stages with very compact mechanical structures and their extensive testing. Various parts were designed and fabricated in the mechanical engineering machine shop. The precision assembly was performed using the fixtures that I designed and fabricated. Extensive precision-motion-control tests and load tests were performed using the real-time codes I developed.

The maglev stages have the minimum number of actuators using permanent magnets and current-carrying coils. The moving parts carry only permanent magnets without iron core, which makes it light-weight. There is no I^2R loss in the moving platen, which prevents thermal distortion. Each moving part is physically isolated from the stationary parts. That is, there are no umbilical cables connected to the moving part that might transmit nanoscale vibrations from environment. The actuator is of air-core type, and its design is very simple and easy to implement without the difficulty of complicated assembly and alignment. The novel actuation scheme designed for the second-generation stage applies forces in two directions on a single magnet using two coils. This reduces the mass of the moving part significantly, which leads to low power consumption (around 135 mW) and less heating and thermal distortion. The innovative symmetrical design of the platen results products of inertia zero and prevents dynamic coupling of rotations in different axes.

As compared to traditional positioning stages these maglev stages provide very high resolution. They have positioning noise of 2 nm rms in translation and 300 nrad in rotation. These maglev stages are superior to current trends in nanopositioning (AFM and STM) in terms of travel range as well. The second-generation maglev stage provides 5 × 5 mm of travel range in the *x*-*y* plane, 50 times greater than the travel range of AFM (around 100 µm). Also in *z* it is cable of 500 µm as compared to around 5 µm in AFMs. The second maglev stage can provide an acceleration of 8 *g* in the vertical and 2.5 *g* in the horizontal directions. It can position and orient an additional payload of 2 kg.

The enhanced positioning capabilities of these maglev stages make them more versatile for various applications from nanomanipulation and scanning to manufacturing of nanoparts using photolithography and microstereolithography. The larger travel range enables its application for nanopositioning lager objects. The longer *z* translation eliminates the requirement of additional vertical translation stage in probing tools. The rotational capabilities provide fine alignment capabilities in rotation. In summary, these maglev stages are excellent candidates for nanopositioning and nanomanipulation in the future nanotechnology.

CHAPTER II

INSTRUMENTATION

This chapter describes the instrumentation structure common to both the maglev stages. All the various units in the instrumentation structure are explained in detail with their specifications in the maglev systems.

2.1 Instrumentation Structure

We use a VME chassis as a communication backbone among various electronics boards. This VME chassis has a VME PC (VMIC 7751), a DSP board (Pentek 4284), a 16-bit data-acquisition board (Pentek 6102), and 3 laser-axis boards (Agilent 10897B). The overall instrumentation structure and information flow is shown in Fig. 2-1.

The horizontal displacement and velocity data are sensed by laser interferometers. The data from the laser receiver go to the laser axis boards mounted on the VME chassis and connected to the VME bus. The displacement and velocity values determined by the laser-axis boards are acquired by the DSP via the global bus. The capacitance probes sense the vertical positions of the platen at three different points and this information reaches to the DSP via the signal conditioning board, the anti-aliasing filters and the analog-to-digital converters (ADCs). The DSP takes real-time commands and desired positions from the VME PC, and calculates the outputs to the actuators. Then DSP computes the desired force by each actuator and transfers the

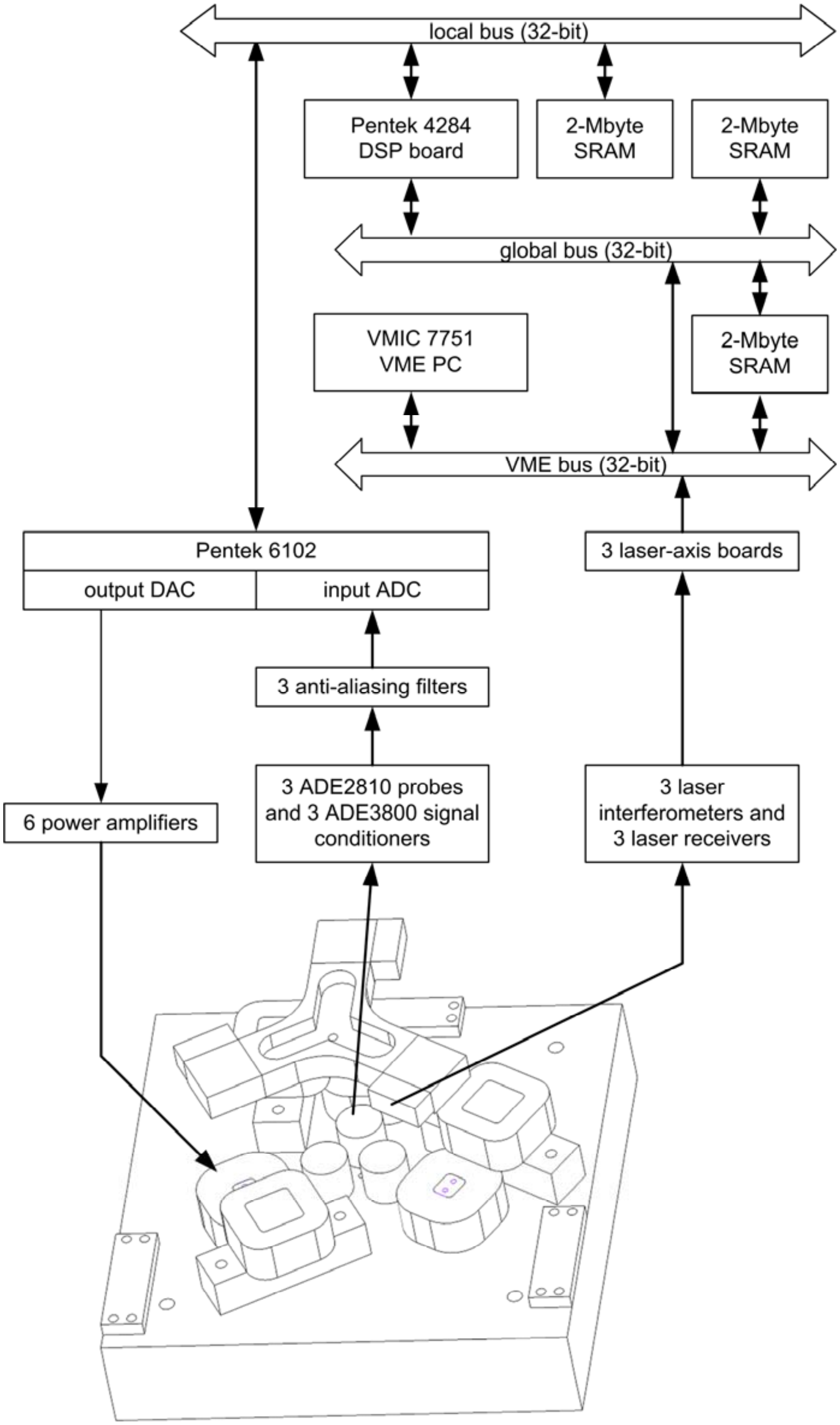

Fig. 2-1. Instrumentation structure.

corresponding voltage information to digital-to-analog converters (DACs). These voltage output signals are fed to the power amplifiers connected to the actuators. The power amplifiers flow the desired current into the actuator coils and the actuators generate the electromagnetic force on the platen.

2.2 Sensors

The actual displacement and velocity measurements of the platen are essential for real-time control. The 3-axis displacement and velocity in the horizontal plane (*x*-, *y*-translation, and ϕ-rotation) is sensed by laser interferometers. We use 3 capacitance gauges (ADE 2810) for vertical displacement sensing.

2.2.1 Laser Interferometry

We use an orthogonally polarized laser of wavelength 632 nm for interferometry. The source of the laser is a He-Ne laser head (5517D by Agilent). The laser is distributed into 3 equal parts using beam-splitters and directed by beam benders as shown in Fig. 2-2. One polarization of the laser beam gets internally reflected from the interferometer and falls on the laser receiver. The other polarization of the beam falls perpendicularly on to the plane mirror mounted on the platen after a pass though the interferometer. After two reflections from the plane mirror the beam falls on the laser receiver (10780C by Agilent). Due to the movement of the plane mirror, the path length traveled by the second half of the beam changes by 4 times of the displacement of the plane mirror. This causes a phase shift corresponding to the extra path traveled among the two beams and interference takes place. The receiver senses both the laser

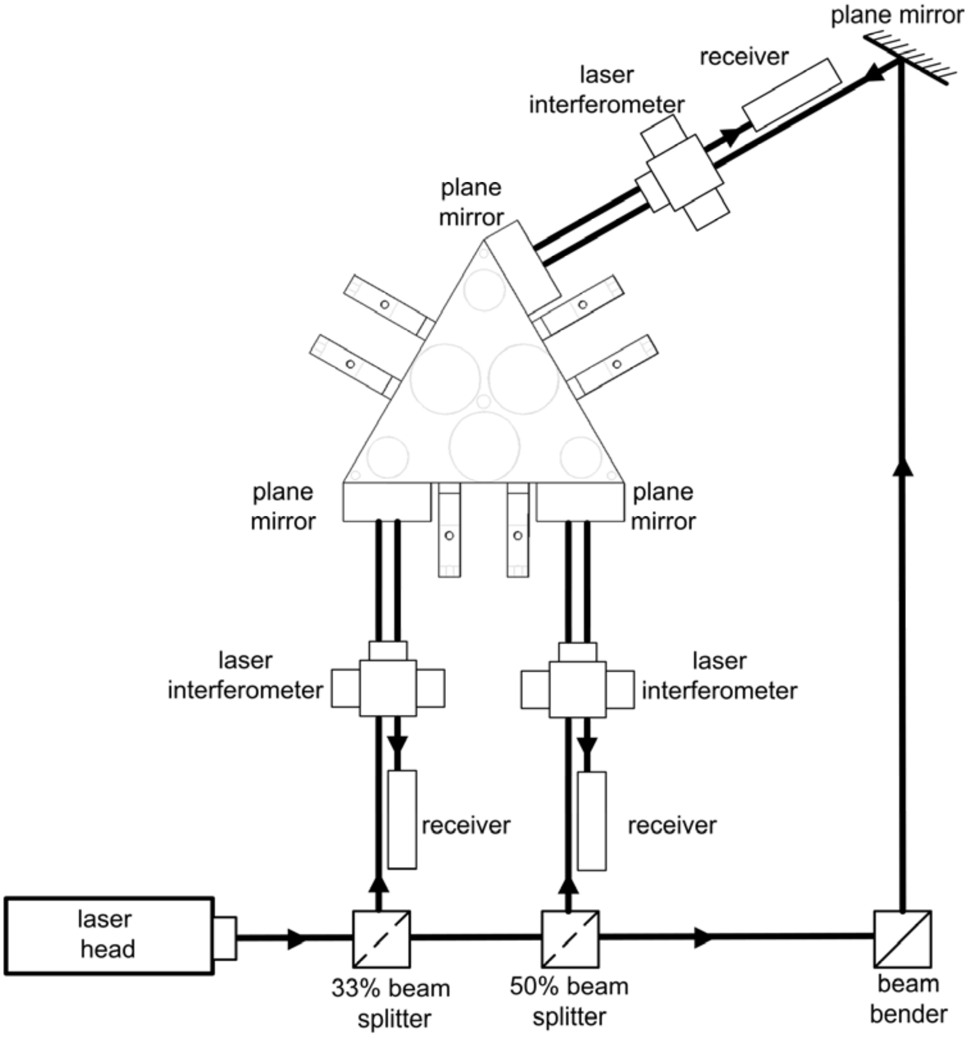

Fig. 2-2. Laser interferometry.

beams and sends the data corresponding to the phase difference to the laser-axis board (10897B by Agilent). This laser axis board processes the data from the laser receiver and the laser head. The laser-axis boards output at 10 MHz 35-bit displacement and 24-bit velocity data that are received by the DSP via the VME bus.

The interferometers used for this stage are high stability plane-mirror interferometers (10706B by Agilent). This interferometer uses the dual-pass method and provides 0.6-nm resolution over a travel range of 10 m. This new technique reduces the thermal measurement drift to 1/12 of the value typically achieved by conventional plane mirror interferometers. The maximum velocity that this interferometer can sense is 0.5 m/sec with the 5517D laser head.

The laser beam is reflected from the plane mirror two times and gets deflected if the mirror rotates. Since the receiving lens of the laser receiver has the diameter of around 6 mm, the reflected laser beam from the plane mirror goes out of the range for larger rotation of the plane mirror. The typical working range of the interferometer system is limited to around 3.5 mrad for 150 mm gap between plane mirror and interferometer. If the laser beam goes out of the receiver, the data transmitted by receiver are erroneous, which makes the system unstable. Therefore the rotational travel range of the system is limited to 3.5 mrad due to limited sensing range of the plane mirror laser interferometers.

2.2.2 Capacitance Probes

For the measurement of vertical motions of platen capacitance probes (ADE 2810) are used. These probes are cylindrical in shape with a 10-mm-diameter sensing area. These sensors measure the capacitance between the smooth bottom surface of the platen and the circular sensing area on the sensing probe. The linear sensing range of this sensor is 500 μm between the gap of 250 μm to 750 μm among the probe and the platen. These probes face the bottom surface of the platen to sense its height at 3 different locations as shown in Fig. 2-3. With a triangulation method we calculate the z-translation and ψ- and θ-rotations. The outputs of these probes are fed to their signal conditioning boards (ADE 3800). These ADE 3800 boards have been placed in a cage in the VME chassis. The ADE 3800 boards give the analog signals corresponding to the platen displacement in the vertical axes with output range of ±5.0 V. These boards have jumper settings and can change the output voltage swing. There are 3 LED (light-emitting-diodes) lights to indicate if the sensor reading is linear, below or above the sensing range.

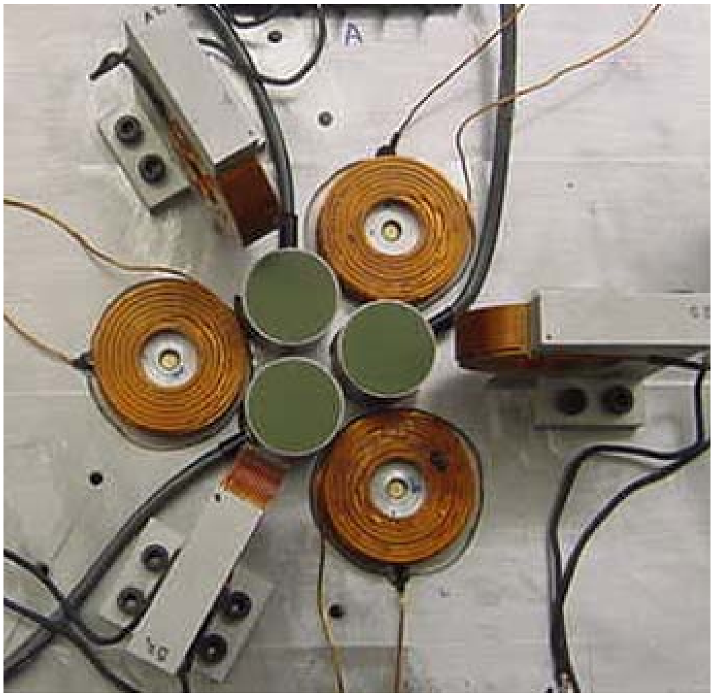

Fig. 2-3. View of all stationary parts showing capacitance probes.

To avoid aliasing of the sensor signals by higher frequency noise contents we use a set of first-order *RC* anti-aliasing filters with a cut-off frequency at approximately 1 kHz right before the ADCs. We used a 10 kΩ resistor and a 0.015 μF capacitor for this purpose. The schematic of the anti-aliasing filter has been show in Fig. 2-4.

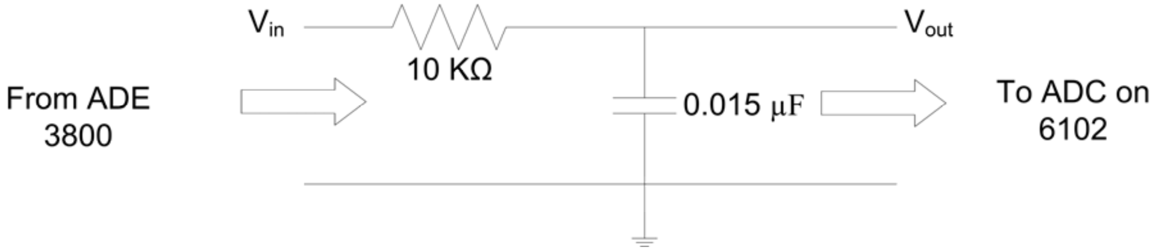

Fig. 2-4. Anti-aliasing filter.

2.3 VME Chassis

All of the electronic components of the system are mounted on a 19-inch instrumentation rack. This rack contains a VME chassis, a generic cage to mount ADE 3800 boards and some platforms to mount the power supplies and place the monitor, keyboard and mouse of the VME PC. A photograph of the instrumentation rack indicating important components is shown in Fig. 2-5.

2.3.1 VME Bus

The VME bus is standard computer bus architecture for industrial control applications. It can run the electronic cards that can produce the address widths up to 40 bits and data width up to 32 bits. There are three main types of device that may be connected to the bus as shown in Fig. 2-6. The Controller that supervises bus activity, the Master reads/writes data to a Slave board, and the Slave interface allows data to be accessed via a read/write from a Master.

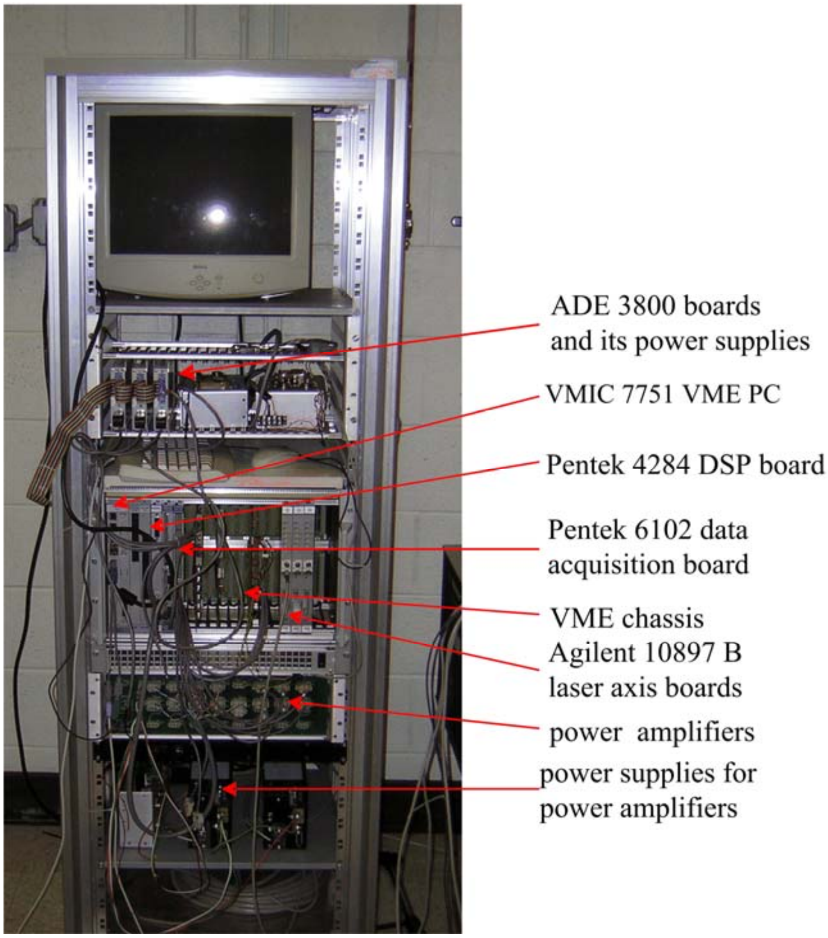

Fig. 2-5. The instrumentation rack.

Controller

There is only one bus Controller on a VME bus. Controller on the VME bus controls the access of other cards on the bus. When it receives a “Bus Request” signal from a bus Master, the Controller will “Bus Grant” the Master the access to the bus. Interrupts on the bus are also handled by the Controller. Upon receiving an interrupt on one of the IRQ (Interrupt ReQuest) lines the Controller processes it by accessing the interrupting card and acknowledges the interrupt [52]. In the system used here the VMIC 7751 VME PC acts as the bus controller.

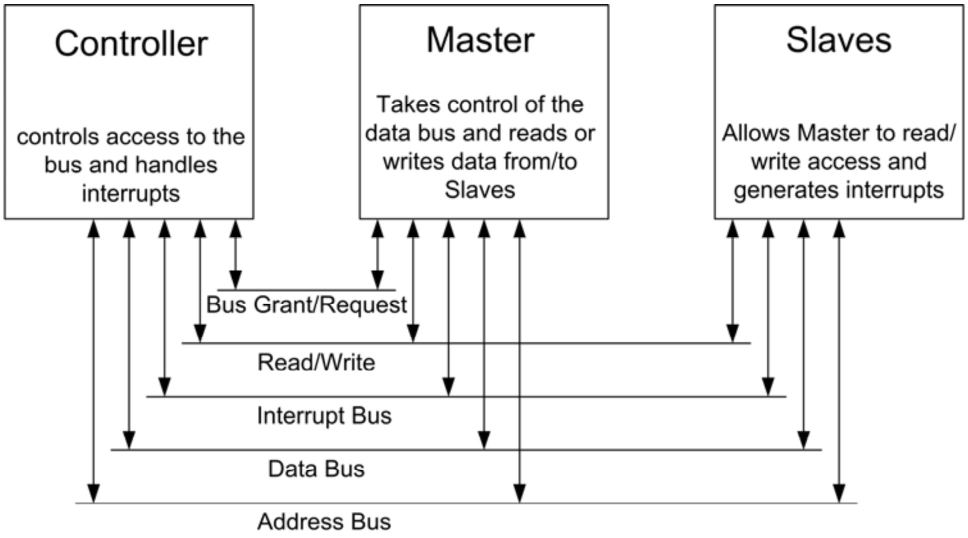

Fig. 2-6. Architecture of VME bus [52].

Master

The job of the Master on a VME bus is to Read and Write data to or from the Slave boards. The Master “Bus Requests” access to the VME bus from the Controller. Once the bus Controller gives the “Bus Grants” the Master, the Master drives the address and data bus to perform a data transfer to a Slave board. Any number of bus Masters may reside on the VME bus, but only one may have the control of the bus at any one time. In our system the Pentek 4284 DSP boards works as the Master.

Slave

A VME bus Slave interface monitors the address and data bus for Reads or Writes sent to it. Once an address is received the Slave will either receive information for a Write, or output information onto the Data bus in the case of a Read. The bus Master continues to control the Data bus during either interface. A Slave may also generate Interrupts over any of the 7 IRQ lines. The interrupts are acknowledged by the bus Controller. Any number of Slave boards may reside on the VME bus. We have several slave boards on the VME bus e.g. laser-axis boards (Agilent 10897 B) and data-acquisition board (Pentek 6102).

2.3.2 Digital-Signal-Processor Board (Pentek 4284)

We employ a Pentek 4284 DSP board that is made to work on a VME bus. The TMS320C40 DSP by Texas Instruments acts as a controller and performs high speed processing [53]. It takes care of all the foreground computing tasks in real-time control. It gathers the displacement and velocity data from the laser-axis boards and the data-acquisition board, takes real-time user commands or predefined positions and trajectories, applies the control law, calculates the control outputs, and generates the output commands via DACs available on Pentek 6102. All the above tasks are accomplished in an interrupt service routine (ISR) initiated by hardware interrupt at every 200 μs.

On VME bus Pentek 4284 can perform the roles of the Master as well as the Slave. As a bus Master it can Read or Write the whole 32-bit address space of the VME bus, thus communicating with any slave device on the bus. It can configure MIX bus subsystem that enhances its capability to support high-speed control and data transfers to any of the Pentek's MIX bus modules. Mapped directly into the local bus, this 32-bit channel includes full interrupt handling and generation support to ensure optimum real-time performance. We use this feature for communication between the DSP board the data acquisition board. This reduces the data traffic on the VME bus significantly. Also there is a 2-MB dual-port shared RAM (random access memory) on the DSP that acts as the communication medium between the VME PC and the DSP over the VME bus. The exchange of program and real-time commands take places via this dual-port RAM.

2.3.3 VME PC and Softwares

The VME PC is used to compile the C codes and download the executable files to the DSP and to transfer the commands in realtime via user interface. We use a VMIC 7751 VME PC that has a Pentium III 733-MHz processor and 256 MB of RAM on it. This PC has Swiftnet, Code Composer, Visual Studio, and other custom-made programs to run the maglev stage. The Swiftnet is the software by Pentek that acts as a controller panel communication and data exchange between the VME PC and the DSP board. This is a mandatory program to run the PC for continuous communication for real-time commands while the stage is in operation. The Code Composer by Texas Instruments is to compile the projects written in C language and link them to make a code executable on the DSP. Its development environment is similar to Visual C++. Once the code is compiled it can be downloaded to the DSP via Swiftnet. Along with the programs mentioned above we need a program that can provide a user friendly graphical user interface (GUI) for real-time commands and control. A program that fulfills the requirement was developed by Jie Gu using Visual C++.net. I modified the program to run the maglev stage as shown in Fig. 2-7. This GUI communicates with DSP to give real-time commands using the dual-port shared memory on the DSP board.

2.3.4 Data Acquisition Board (Pentek 6102)

The DSP inputs and outputs digital data. However the vertical displacement data by ADE 3800 boards and the outputs to the power amplifiers are analog. Thus we use a Pentek 6102 board that samples the analog signals and convert them to digital data using ADCs and makes it available to the DSP via the MIX bus. It also takes digital outputs for the 6 coils from the DSP and converts them to analog signals using DACs and outputs them to the power amplifiers.

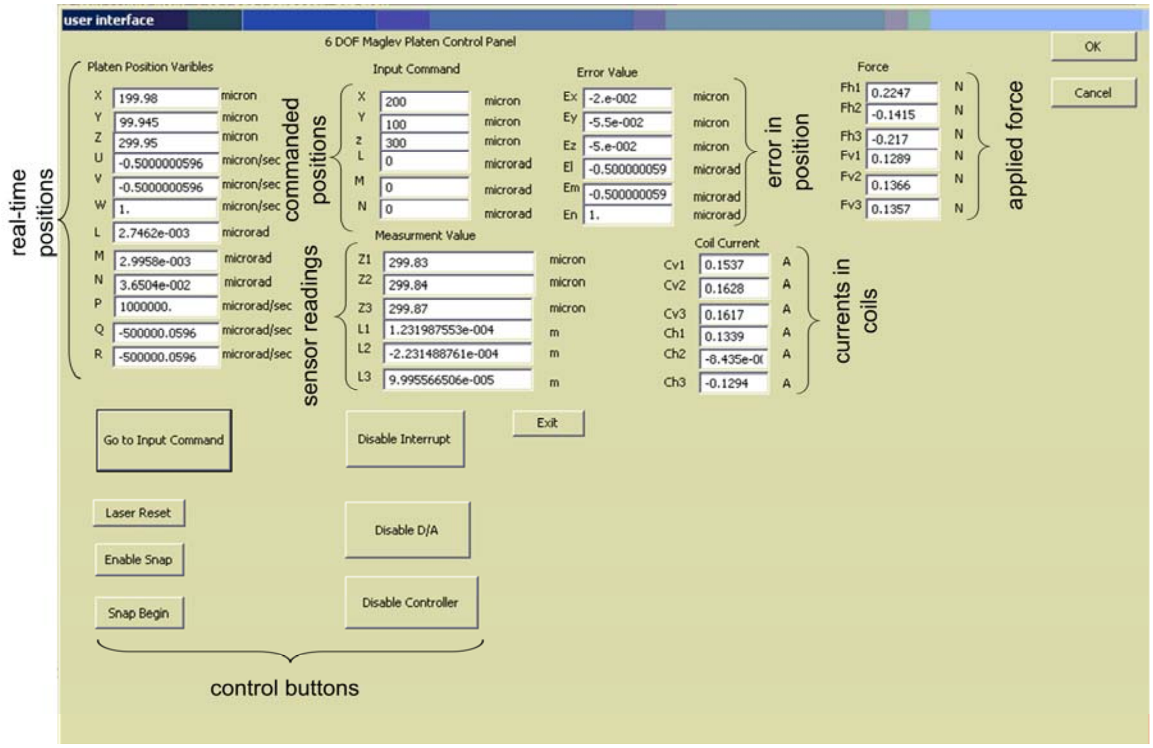

Platen Position Varibles

X 199.98 micron
Y 99.945 micron
Z 299.95 micron
U -0.5000000596 micron/sec
V -0.5000000596 micron/sec
W 1. micron/sec
L 2.7462e-003 microrad
M 2.9958e-003 microrad
N 3.6504e-002 microrad
P 1000000. microrad/sec
Q -500000.0596 microrad/sec
R -500000.0596 microrad/sec

Input Command

X 200 micron
Y 100 micron
z 300 micron
L 0 microrad
M 0 microrad
N 0 microrad

Measurment Value

Z1 299.83 micron
Z2 299.84 micron
Z3 299.87 micron
L1 1.231987553e-004 m
L2 -2.231488761e-004 m
L3 9.995566506e-005 m

Error Value

Ex -2.e-002 micron
Ey -5.5e-002 micron
Ez -5.e-002 micron
El -0.500000059 microrad
Em -0.500000059 microrad
En 1. microrad

Force

Fh1 0.2247 N
Fh2 -0.1415 N
Fh3 -0.217 N
Fv1 0.1289 N
Fv2 0.1366 N
Fv3 0.1357 N

Coil Current

Cv1 0.1537 A
Cv2 0.1628 A
Cv3 0.1617 A
Ch1 0.1339 A
Ch2 -8.435e-0(A
Ch3 -0.1294 A

Fig. 2-7. Graphical user interface.

The Pentek 6102 has 8-channels of ADC (ADS 7811) for the VME bus data acquisition. It offers differential inputs, 16-bit resolution, and sampling frequency up to 250 KHz. The input voltage swing is ±5.0 V with input impedance of 100 kΩ. The common mode rejection is more than 60 dB at 60 Hz for differential input. The sampled data is stored in a 1-k sample FIFO (first input first output) memory. It uses 32-bit Intel MIX mezzanine bus to transfer the data directly to the DSP without using the VME bus. We use 3 ADC channels to receive the measurement data from ADE 3800 boards. One channel of the ADC is used to generate a clock signal for interrupt at 5 kHz to trigger the ISR to run the real-time control routine. The number of output channels is 8 with16-bit resolution using AD569 DACs.

2.4 Power Amplifiers

The controller outputs indicating desired coil currents from the DSP are made available in the form of analog voltage by the data-acquisition board. However, since the actuation force is proportional to the coil current as shown in Section 5.2, the input to the maglev stage has to be in form of coil currents. Thus we use 6 transconductance amplifiers to convert this voltage output to current input to the coils. These amplifiers are connected to the coils to flow the commanded currents. The output swing of the DACs is ±5 V and the current limit in the coils is set ±2.5 A. The output current from an amplifier is linearly proportional to the input voltage. A photograph of the amplifier card that consists of two transconductance amplifier circuits is shown in Fig. 2-8.

Each amplifier consists of a differential amplifier, a feedback amplifier, and a power booster. The differential amplifier consists of an operational amplifier (one unit from a TL072) and four 10-kΩ resistors. The purpose of this circuit is to reject common-mode noise due to environmental electromagnetic waves that comes in both the ground as well as the signal cable. The feedback amplifier consists of an operational amplifier (the other unit from a TL072), a 1Ω 10W resistor and several other resisters and capacitors. The purpose of this circuit is to sense the actual current in the coils through the voltage drop across the 1 Ω resistance and stabilize the current-control loop. The power booster amplifies the current transmitting capacity of the circuit. It uses a power operational amplifier (PA12A) by Apex with a wide supply range of ±10 V to ±50 V, high output current up to 15 A, and very low thermal resistance of 1.4° C/W. On top of this power operational amplifier is a heat sink air-cooled by a set of fans.

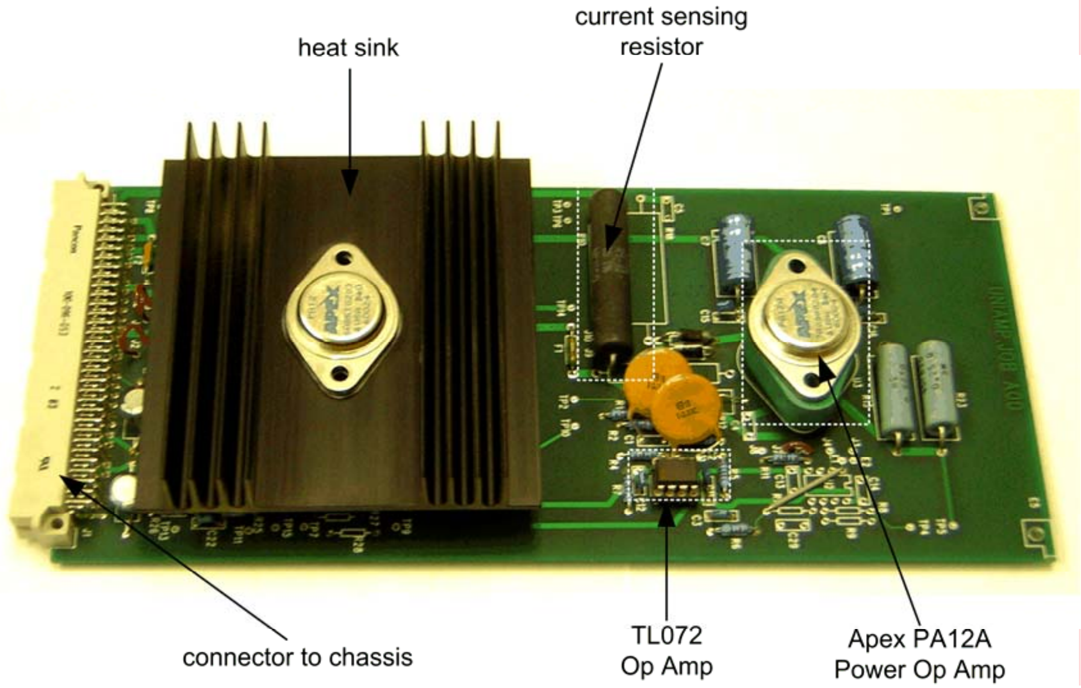

Fig. 2-8. Photograph of transconductance amplifier.

CHAPTER III

DESIGN AND ASSEMBLY OF FIRST-GENERATION MAGLEV STAGE

In this chapter we discuss the design and assembly of the first-generation maglev instrument. It can position and orient the mounted specimen in all 6 DOFs with rms position noise of 2 nm in translation and 300 nrad in rotation. It covers a travel range of 300 μm in translation and 3.5 mrad in rotation limited by the plane-mirror laser interferometry. This stage is capable of a velocity of 0.5 m/s and an acceleration of 30 m/s^2 based on actuator sizing. The nominal power consumption is only 15 mW by each horizontal actuator, and 320 mW by each vertical actuator. The actuators are sized to be able to orient and position a maximum payload of 0.4 kg. Key applications of this maglev device are manipulation at nanoscale for microassemblies and manufacturing of their parts. Other potential applications are microstereolithography, vibration-free delicate instrumentation, and microscale rapid prototyping.

3.1 Linear Actuator Units

The design of the unit actuators was performed by Maheshwari [51]. The single-axis actuators have permanent magnets and current-carrying coils. The schematic of the assemblies of horizontal and vertical actuators is shown in Fig. 3-1. The current-carrying coils generate north and south poles by the right-hand rule. With the pole arrangement shown, the axial Lorentz force is generated on the magnets with respect to the stationary coil. Reversing the direction of the current reverses the direction of the force.

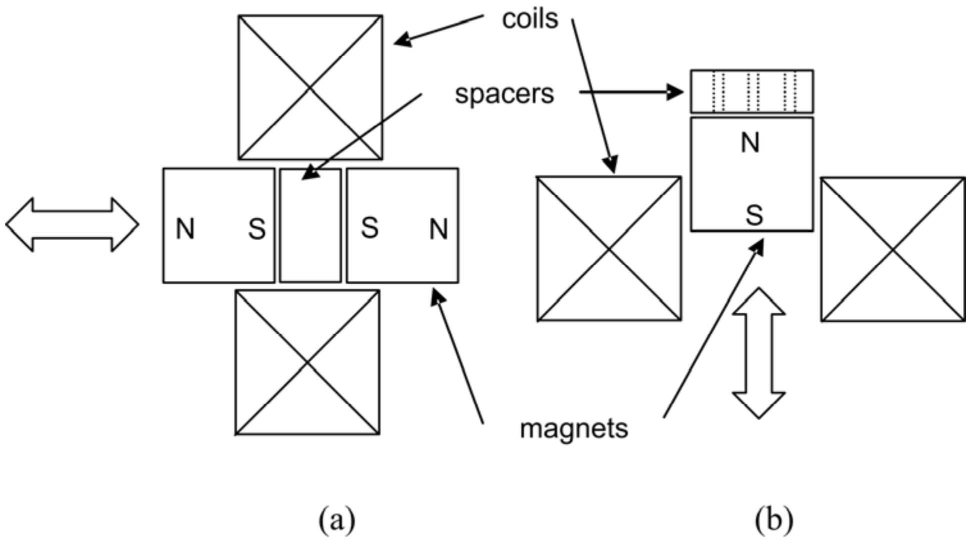

Fig. 3-1. Schematic of (a) horizontal actuator unit. (b) vertical actuator unit.

We used neodymium-iron-boron (NeFeB) magnets of 1.4-T remanence with phenolic resin coating to prevent corrosion. Each of the magnets has diameter of 11.5 mm and length of 9.5 mm. The coils are made of AWG#21 copper wire (diameter = 0.0285"), and wound and glued with heat-cured epoxy. The coils have outer diameter of 32 mm, inner diameter of 12 mm and height of 9.7 mm. The coil has a resistance of 0.552 Ω.

The horizontal actuator unit consists of two magnets glued together with one aluminum spacer between them and one current-carrying coil. The assembly of magnets and spacer is attached to the moving part. Each vertical actuator unit has one magnet glued to a mount and a current-carrying coil. All the magnets and aluminum spacers/mounts were glued using PC-7 epoxy. I designed and constructed precision tooling for the assembly of these actuator units. These toolings are shown in Fig. 3-2. A pocket of 11.5 mm square with round corners of 3.175

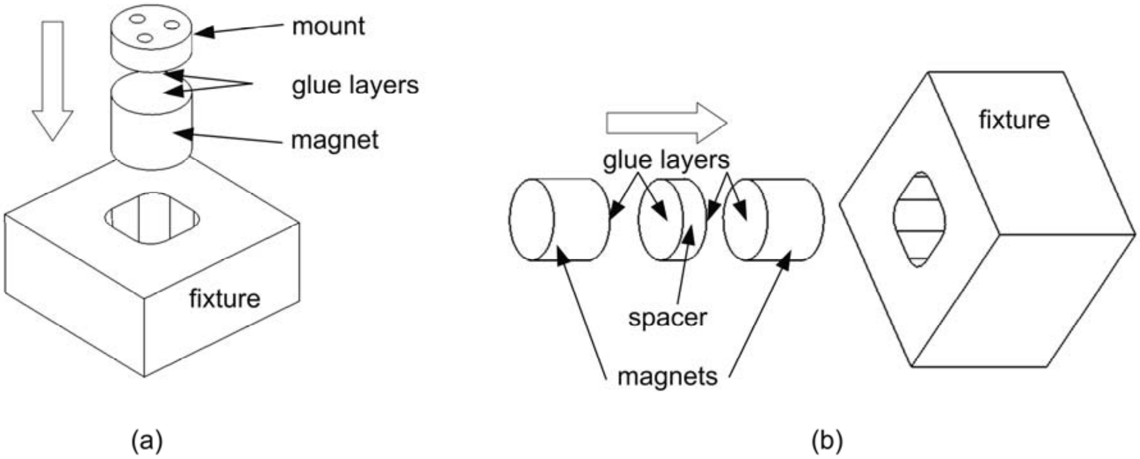

Fig. 3-2. Tooling for gluing actuator units (a) vertical actuator and (b) horizontal actuator.

mm radius was machined. The height of tooling for vertical actuators is 13.513 mm and for horizontal tooling is 22.987 mm. The surface to be glued were cleaned with MEK (Methyl Ethyl Ketone) and scratched with sand-paper which increased the bonding strength. All the surfaces to be glued were applied a thin coating of epoxy. A spray of dry film mold release was applied on the tooling so that the magnet and washers would not stick to the tooling. Then magnets and washer were placed in the tooling and were squeezed and held between two perfectly flat surfaces with G-shaped clamps. The assemblies were kept for 24 hours for curing and were taken off with slow tapping of a rubber hammer. The sides of pocket in the tooling of exact size gave us a very precise alignment of magnets and washers. The height of the tooling ensured the glue thickness and overall length of assembly.

3.2 Mechanical Design

Fig. 3-3 shows the exploded Solidworks drawing of the stage. The triangular part in the center is the platen. This assembly is the only moving part in the maglev stage. The platen carries the magnets for linear actuators. All the other parts are mounted on the base plate using screws of different sizes. The basic design on Solidworks® was performed by Jie Gu. Further modifications for efficient manufacturing, fabrication and assembly of the whole stage, and design and fabrication of all the assembly fixtures were completed by me.

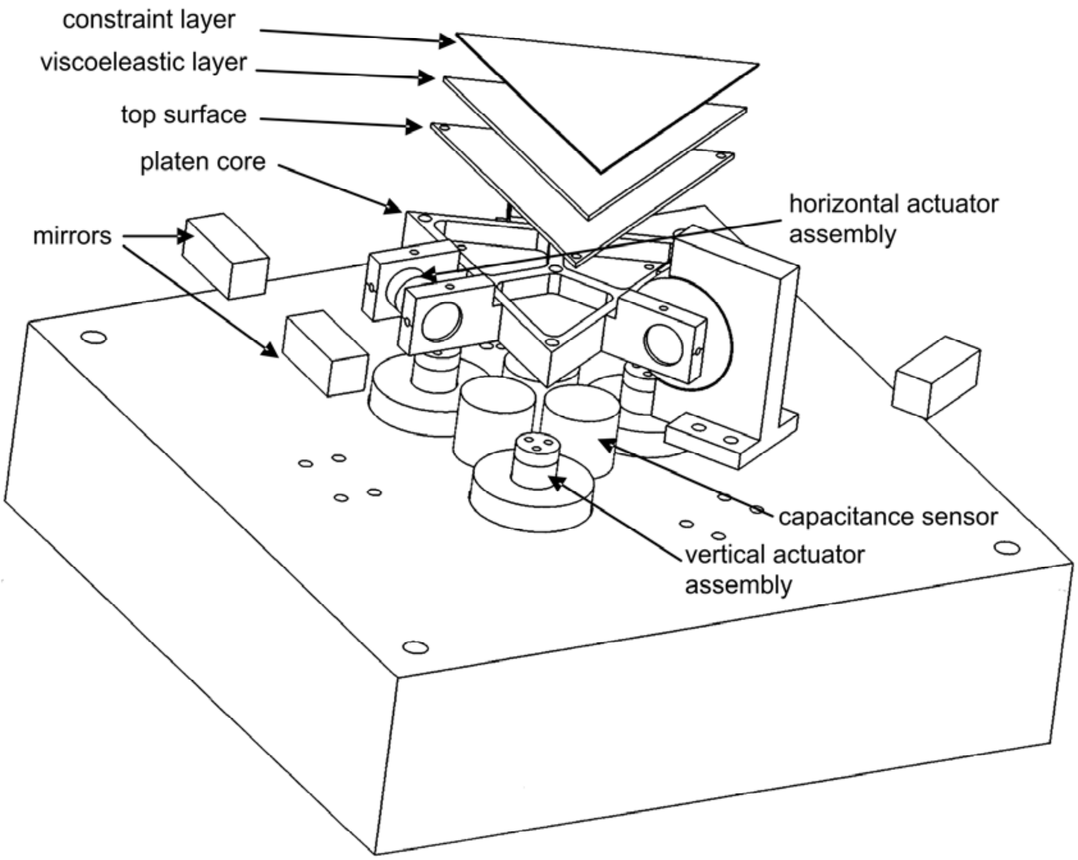

Fig. 3-3. Exploded view of the mechanical assembly [54].

3.2.1 Platen Assembly

The core of the platen is made of pocket-milled single-piece aluminum to reduce its mass and to keep its natural frequency high without sacrificing the stiffness. A finite-element analysis shows the natural frequency of the platen at as high as 4.6 kHz. There is no iron part in the assembly, which makes the system controllable at high bandwidth. The other parts attached to it are 3 horizontal actuator assemblies, 3 vertical actuators assemblies, three plane mirrors, and a set of three layers on top to minimize vibration. The total mass of the moving part is 0.2126 kg.

The horizontal and vertical actuator assemblies were described in the last section. There are 3 pairs of arms protruded on the sides of the platen to hold these assemblies for horizontal actuation. Each arm has a hole 10 μm bigger than the diameter of the cylindrical magnet. The three setscrews on the outer, top and bottom surfaces of the arm are tightened to hold the magnet. Since the magnetization directions of the magnets are kept parallel to the sides of the triangular platen, these units generate horizontal force parallel to the sides of the platen. The vertical actuator assemblies are attached to the moving part and assembled with a cylindrical magnet and an aluminum mount with three holes. These holes are tapped for thread of 2-56 screw. The magnet for a vertical actuator is glued to a spacer fastened to the bottom surface of the platen with 3 screws.

There are three layers on top of the platen, an aluminum top plate, a viscoelastic damping layer, and a stainless-steel constraint layer. The assembly of these three layers adds passive damping to the system to minimize the structural vibrations and improve the stability. The bottom most layer called the top plate covers the pockets of the platen. It is attached to the platen using four 2-56 screws three at the corners and one at the center.

There are three plane mirrors for horizontal motion sensing. These plane mirrors act as reflectors for laser interferometers. These mirrors are mounted on the platen using double sided tape. Two of the mirrors are on one side of the platen and one is on the second side at an angle of 120°. To ensure good parallelism of these mirrors a tooling was designed and fabricated. This tooling and mirror assembly are shown in Fig. 3-4. The bottom surface of the platen is machined and ground to be flat within 2.5 μm because this surface is used as the targets by capacitance probes to sense the vertical displacement of the platen.

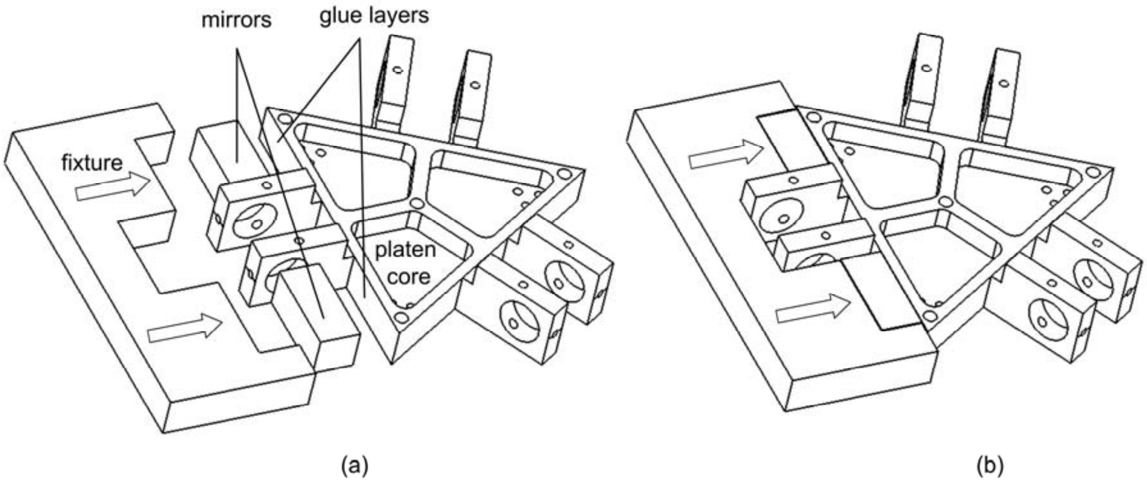

Fig. 3-4. Process for gluing mirrors with platen core (a) before clamping (b) after clamping.

3.2.2 Base Plate and Stationary Assembly

Fig. 3-5 (a) shows a picture of the base plate and some stationary parts mounted on it. The big rectangular piece in the bottom with dimension of 203.2 × 203.2 × 56.0 mm is the base plate. All the parts and assemblies are mounted on the base plate via through holes, tapped holes and pockets.

In Fig. 3-3, the three cylindrical bodies in the center of the base plate are capacitance probes. There are 3 M3 screws used to mount each probe and screwed from the bottom. Fig. 3-5 (b) shows the bottom view of the platen showing the pocket that is milled from the bottom surface of the platen to screw the screws. The 9 holes are used to mount the three capacitance probes.

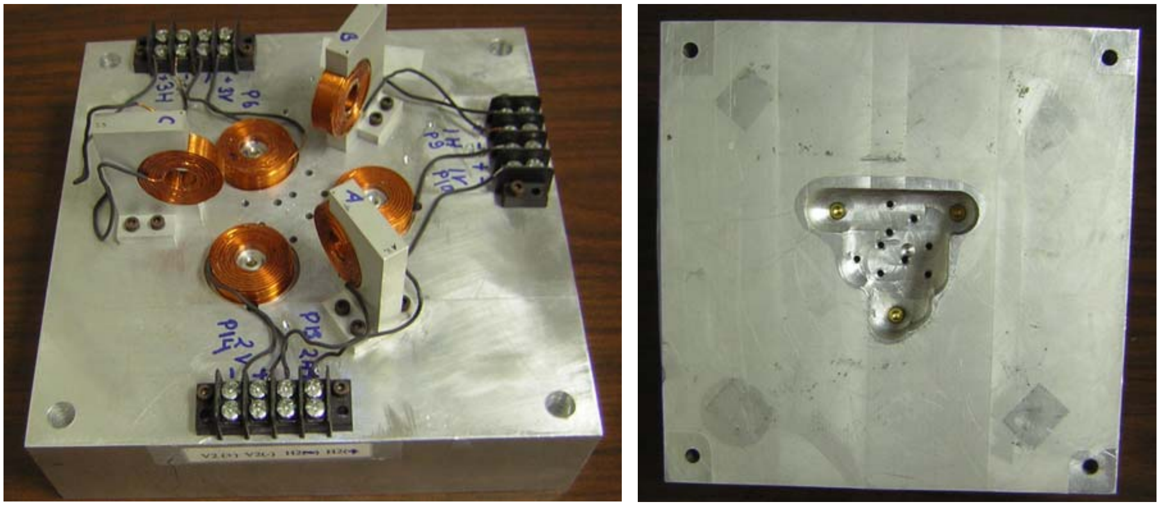

Fig. 3-5. (a) Photograph of the stationary parts (b) bottom view of platen.

There are 3 circular pockets machined on the top surface of the platen. The purpose of these pockets was to maintain the height of the coil at which the vertical magnets will get maximum force when the bottom surface of the platen is in the sensing range of the capacitance probes. In the pocket shown in Fig. 3-5 (b), there are three 10-32 brass screws screwed to hold the vertical coils. These screws are fastened to the coil holders that are glued to the inner surface of the vertical coils. Since the radial clearance between the magnets and coil is just 504 micrometers, accurate positioning of the coils is crucial. Thus a fixture was designed and fabricated to precisely position the coils at the desired location while fastening them to the base plate. This fixture is shown Fig. 3-6 has 3 cylinders mounted at a flat plate. The diameter of the cylinder is same as the inner diameter of the vertical coils so these cylinders are push fit to

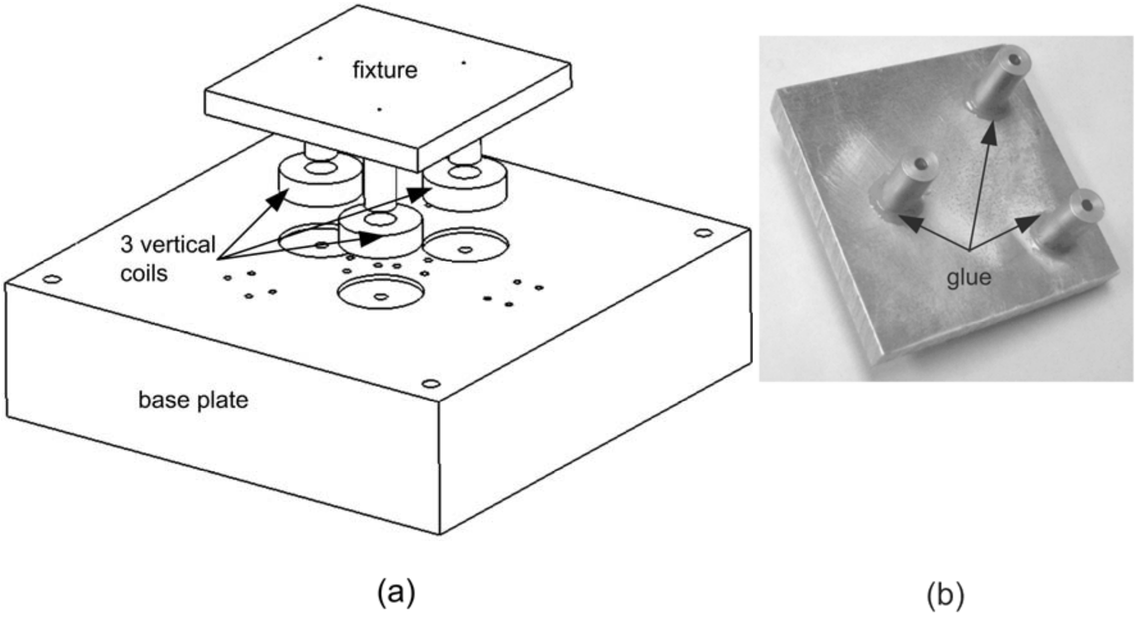

Fig. 3-6. Tooling for mounting vertical coils to the base plate.

the vertical coils. While assembling the three vertical coils were attached to the fixture and placed on the base plate. Then the screws were tightened from pocket at the bottom of the base plate. Then, this fixture was slowly taken off. This ensured the position of the coils to be as close as possible to the designed.

The coils for horizontal actuators are glued to the coil holders. These coil holders are mounted on the base plate using 4 screws. Each holder has 4 through holes, and there are tapped holes on the base plate. The position and alignment of the coil was important while gluing because of very low clearance and possible loss of travel range in case of any shift or rotation of coil. Thus a fixture was designed and fabricated for precision gluing. Fig. 3-7 shows the fixture and the coil holder. The coil holder was mounted on the fixture using the 4 screws. A cylindrical insert with the diameter the same as the coil inner diameter was used to hold the coil in position. The collar on one side and a supporting disc with a bolt on the other side keep the coil fixed at the desired position relative to the coil holder. A thin film of epoxy was applied on the surfaces of coil holder and coil. The coil was held at position for 24 hours to cure the epoxy. This process ensured a very precise alignment of the coil with respect to the platen.

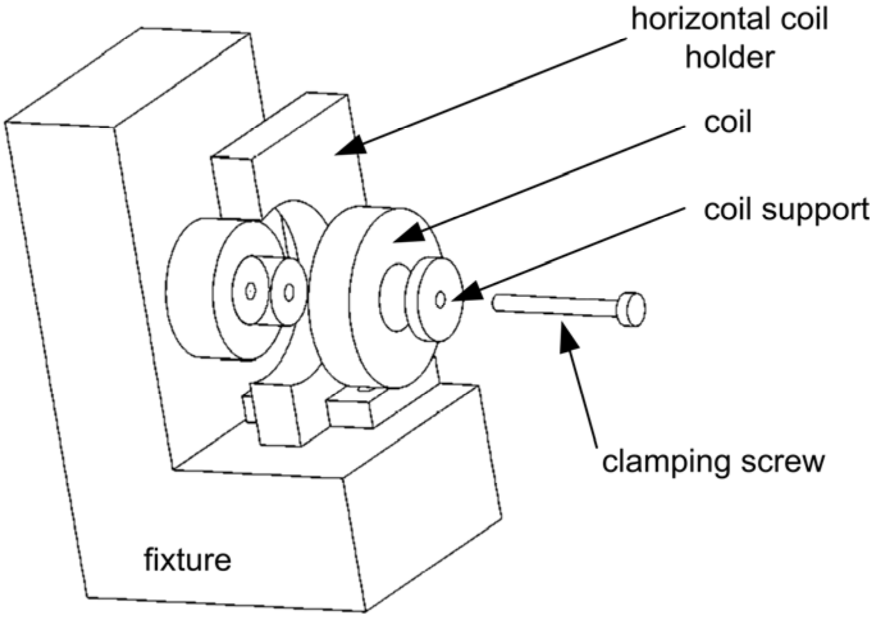

Fig. 3-7. Tooling for gluing horizontal coil to the coil holder.

3.3 Working Principle

The platen has 6 linear single-axis actuators numbered as in Fig. 3-8 (a). At its 3 corners are 3 vertical actuators (v_1, v_2 and v_3) that make it move in the 3 vertical DOFs, i.e., z-translation and rotations about the x- and y-axes (ψ and θ). In the middle of the 3 arms are 3 horizontal actuators (h_1, h_2 and h_3) that generate forces in the 3 horizontal DOFs, i.e., x- and y-translations and rotation about the z-axis (ϕ). The forces generated by the vertical actuators are shown as f_{v1}, f_{v2}, and f_{v3}, and by the horizontal actuators as f_{h1}, f_{h2}, and f_{h3}. The conceptual modal force generation of the maglev system is depicted in Fig. 3-8 Parts (b–g) of the figure show the directions of forces by individual single-axis actuators to generate the platen motion in any particular axis.

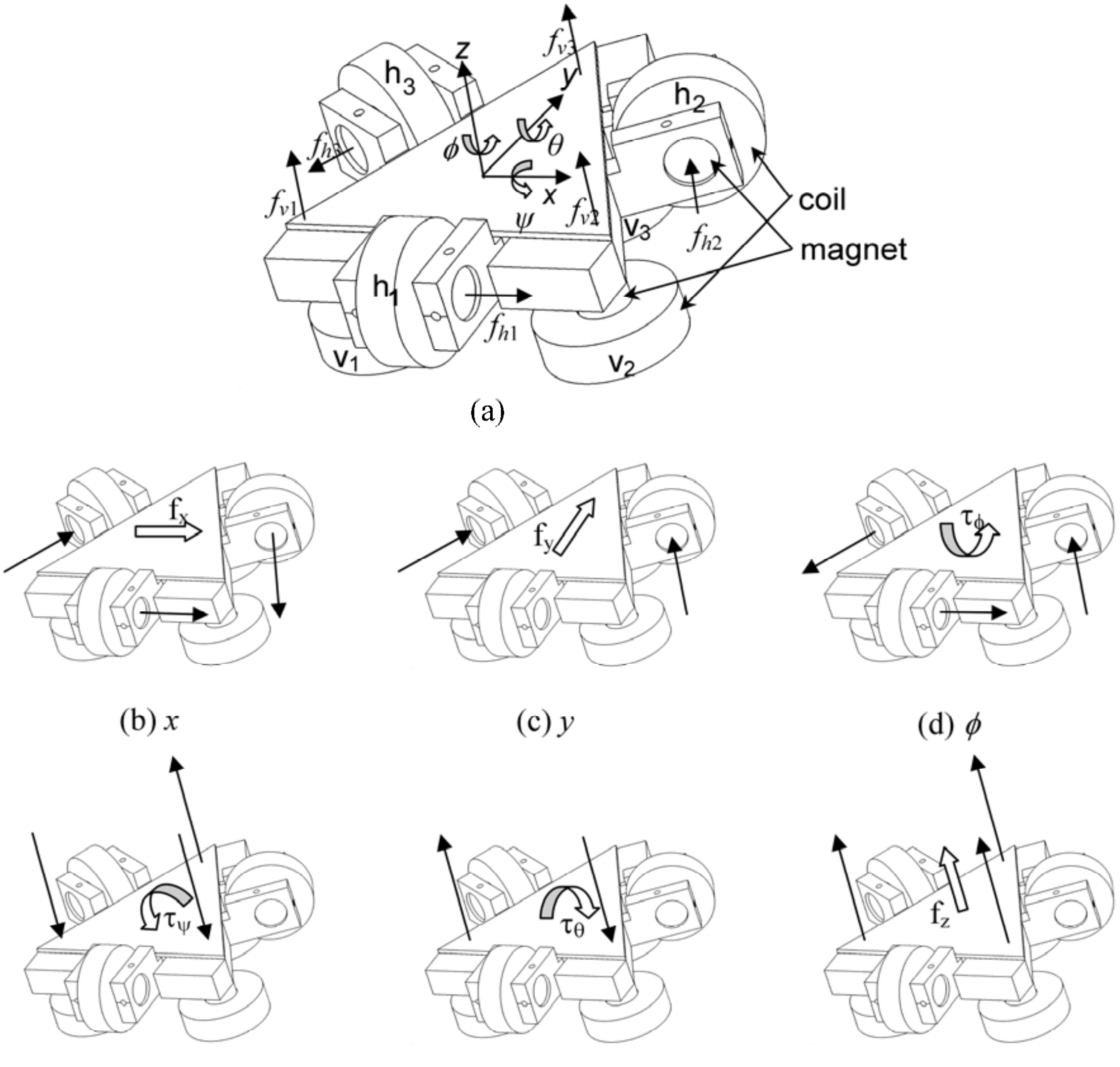

(a)

(b) x (c) y (d) ϕ

(e) ψ (f) θ (g) z

Fig. 3-8. Convention of the coordinate axes and directions of forces [54].

CHAPTER IV

DYNAMIC MODELING, CONTROL SYSTEM DESIGN AND EXPERIMENTAL RESULTS OF FIRST STAGE

In this chapter the modeling and control system design for the first-generation maglev stage is explained. Various positioning and load tests were performed that demonstrate the capabilities of the stage.

4.1 Dynamic Modeling

A 3-D model of the stage was developed using Solidworks®. All the individual parts of the maglev stage were designed and then assembled in Solidworks®. A finite-element analysis was carried out to identify various system parameters such as the mass, moment of inertia, and center of mass (CM). The mass M of the platen assembly was measured to be 0.2126 kg by a precision balance and the moment of inertia at the CM was calculated as

$$I = \begin{bmatrix} I_{xx} & -I_{xy} & -I_{xz} \\ -I_{yx} & I_{yy} & -I_{yz} \\ -I_{zx} & -I_{zy} & I_{zz} \end{bmatrix} = \begin{bmatrix} 132.88 & -3.14 & 0 \\ -3.14 & 122.28 & 0 \\ 0 & 0 & 235.87 \end{bmatrix} \tag{4.1}$$

with units in $10^{-6} \times$ kg-m^2. Since the products of inertia are less than 3% of the principal moments of inertia, they are neglected in the present dynamic model.

Since the platen is magnetically levitated, in the absence of any mechanical contact between the platen and the stationary parts, the spring and damping effects are negligible. Thus we model the platen as a pure mass, and the equation of motion for translation is

$$M\frac{d^2x}{dt^2} = f_x, \tag{4.2}$$

where f_x is the force in the x-axis. Similarly the equation of motion for rotation is

$$I_{xx}\frac{d^2\psi}{dt^2} = \tau_x, \tag{4.3}$$

where I_{xx} is the principal moment of inertia, and τ_x is moment about the x-axis. The open-loop transfer function of the platen for translation is

$$\frac{X(s)}{F(s)} = \frac{1}{0.2126\,s^2}. \tag{4.4}$$

Similarly the transfer function of the platen for rotation is

$$\frac{\Psi(s)}{T_x(s)} = \frac{1}{I_{xx}s^2} \tag{4.5}$$

where T refers to the moment about an axis, and I, the corresponding moment of inertia.

4.1.1 Modal Force Transformation

The six independent actuator forces are defined to be f_{h1}, f_{h2}, and f_{h3} as the forces generated by the horizontal actuators, and f_{v1}, f_{v2}, and f_{v3} generated by the vertical actuators, following the labeling convention in Fig. 3-8 (a). In (4.2)–(4.3), the forces/moments act at the platen CM and are called modal forces/moments. We need to allocate the modal forces/moments to the six actuator forces. Fig. 3-8 (b–g) illustrates a conceptual force allocation. By applying six equilibrium conditions around the platen CM, we derived the following modal force transformation matrix.

$$\begin{bmatrix} f_z \\ \tau_\theta \\ \tau_\psi \\ f_x \\ f_y \\ \tau_\phi \end{bmatrix} = \begin{bmatrix} 0 & 0 & 0 & 1 & 1 & 1 \\ 0 & 0 & 0 & -l_{2x} & l_{3x} & l_{1x} \\ 0 & 0 & 0 & -l_{2y} & l_{3y} & -l_{1y} \\ -\cos 60^\circ & 1 & -\cos 60^\circ & 0 & 0 & 0 \\ -\cos 30^\circ & 0 & \cos 30^\circ & 0 & 0 & 0 \\ l_{1z} & l_{2z} & l_{3z} & 0 & 0 & 0 \end{bmatrix} \begin{bmatrix} f_{h1} \\ f_{h2} \\ f_{h3} \\ f_{v1} \\ f_{v2} \\ f_{v3} \end{bmatrix} \tag{4.6}$$

The geometric parameters (l's) shown in Fig. 4-1 represent the moment arms for the modal moments and defined as following.

l_{1x}: distance in the x-axis from actuator v_1 to the y-axis;

l_{1y}: distance in the y-axis from actuator v_1 to the x-axis;

l_{2x}: distance in the x-axis from actuator v_2 to the y-axis;

l_{2y}: distance in the y-axis from actuator v_2 to the x-axis;

l_{3x}: distance in the x-axis from actuator v_3 to the y-axis;

l_{3y}: distance in the y-axis from actuator v_3 to the x-axis;

l_{1z}: distance from actuator h_1 to the z-axis;

l_{2z}: distance from actuator h_2 to the z-axis;

l_{3z}: distance from actuator h_3 to the z-axis;

The zeros in the top-left and bottom-right parts of this transformation matrix reveal the intended independence between the vertical modes and the horizontal modes.

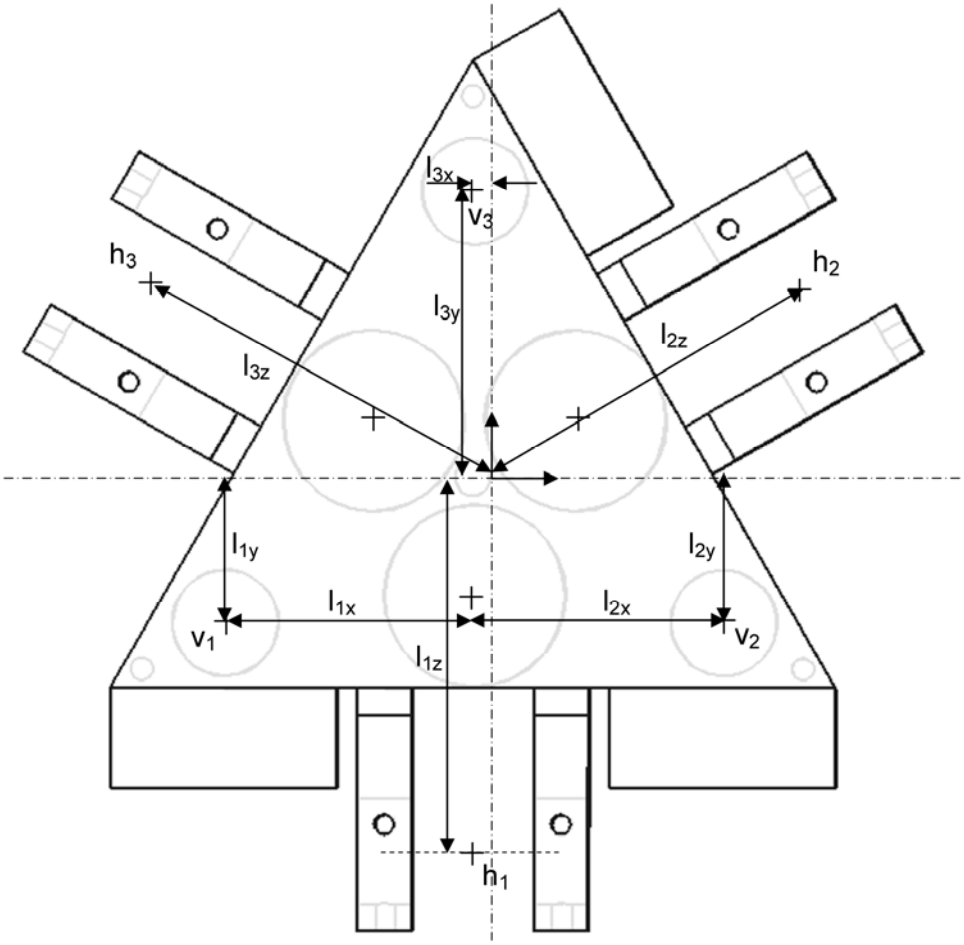

Fig. 4-1. Definitions of parameters for model force transformation.

4.1.2 Modal Displacement Transformation

Similar to the modal force transformation, a modal displacement transformation matrix was derived to relate the sensor measurements to the displacement of the platen CM. The interferometer system described in Section 2.2.1 gives a 3-DOF displacement and velocity information of the maglev stage, i.e. translations and velocity in x and y and rotation around the z axis. Three capacitance sensors fixed on the base plate measure the translation in z and rotations around the x- and y-axes.

With the definitions of the geometric parameters shown in Fig. 4-2, the displacement transformation matrix was derived to be

$$\begin{bmatrix} y_1 \\ y_2 \\ x_1 \\ u_1 \\ u_2 \\ v_1 \\ z_1 \\ z_2 \\ z_3 \end{bmatrix} = \begin{bmatrix} 1 & 0 & -Y_1 & 0 & 0 & 0 & 0 & 0 & 0 \\ 1 & 0 & Y_2 & 0 & 0 & 0 & 0 & 0 & 0 \\ \frac{-1}{2} & \frac{-\sqrt{3}}{2} & X_1 & 0 & 0 & 0 & 0 & 0 & 0 \\ 0 & 0 & 0 & 1 & 0 & -Y_1 & 0 & 0 & 0 \\ 0 & 0 & 0 & 1 & 0 & Y_2 & 0 & 0 & 0 \\ 0 & 0 & 0 & 0 & 1 & -X_1 & 0 & 0 & 0 \\ 0 & 0 & 0 & 0 & 0 & 0 & -Z_{1y} & Z_{1x} & 1 \\ 0 & 0 & 0 & 0 & 0 & 0 & Z_{2y} & -Z_{2x} & 1 \\ 0 & 0 & 0 & 0 & 0 & 0 & Z_{3y} & Z_{3x} & 1 \end{bmatrix} \begin{bmatrix} y \\ x \\ \phi \\ u \\ v \\ r \\ \psi \\ \theta \\ z \end{bmatrix}, \tag{4.7}$$

where y_1, y_2, and x_1 are the horizontal displacement measurements and u_1, u_2, and v_1 are the horizontal velocity measurements by the laser interferometers, and z_1, z_2, and z_3 are the vertical displacement measurements by the capacitance sensors. On the right-hand side of this transformation, y, x, z, ψ, θ, and ϕ are the 6-axis modal displacement variables, and u, v, and r are the horizontal velocity variables of the platen CM.

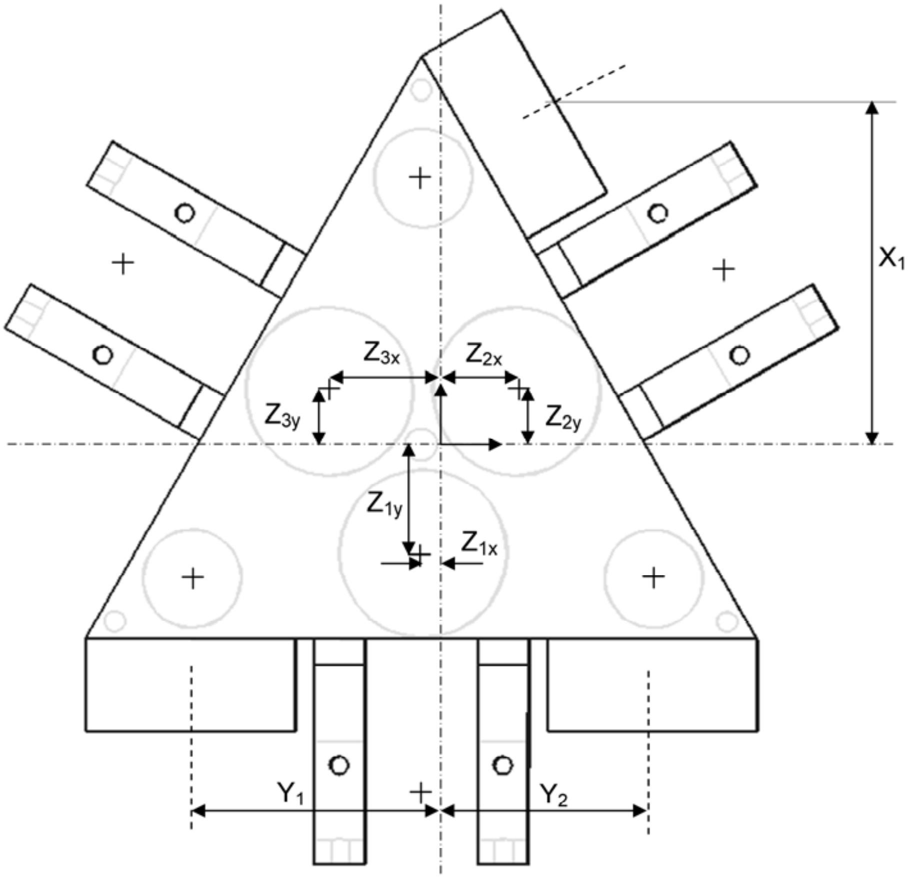

Fig. 4-2. Definitions of parameters for model displacement transformation.

4.2 Control System Design

By Earnshaw’s theorem, 6-DOF magnetostatic levitation in free space is inherently unstable because the permeability μ of any material is always greater than that of free space μ_0 [55]. Thus, six independent lead-lag controllers were designed and implemented for each of the 6 axes to stabilize the maglev system. With the modal force and displacement transformations applied, the whole maglev system can be considered a collection of 6 independent single-input-single-output (SISO) systems.

We used the Matlab® function SISOTOOL to select the control parameters. The damping ratio ζ was chosen to be 0.7 and the phase margin, 52° at a crossover frequency of 50 Hz. The lead-lag compensator designed for the z-axis motion control is given in (4.8).

$$G_z(s) = \frac{8.7315\times 10^4 (s+135)(s+11)}{s(s+1385)} \tag{4.8}$$

The free pole at the origin in the s-plane is to eliminate the steady-state error. By using the zero-order-hold (ZOH) method with a 5-kHz sampling rate, this continuous model was converted to a discrete-time model

$$G_z(z) = \frac{8.7315\times 10^4 (z-0.9767)(z-0.9978)}{(z-1)(z-0.758)} \tag{4.9}$$

We used the same controller for the x- and y-axis motion control. The controllers for the three rotational axes have the same pole-zero locations with the controller gains of 96.872 N, 54.575 N, and 50.221 N for ϕ, ψ and θ, respectively. The control law was implemented in real-time C on the DSP with the user interface running on VME PC.

The position noise in y of the maglev stage is shown in Fig. 4-3. The peak-to-peak noise in the y-axis is around 10 nm with its rms value of 2 nm. Fig. 4-4 shows a 10-nm step response in y. The positional resolution is clearly better than 2 nm. The step responses in x-, y- and z-translations, and ψ-, θ- and ϕ-rotations are shown in Fig. 4-5.

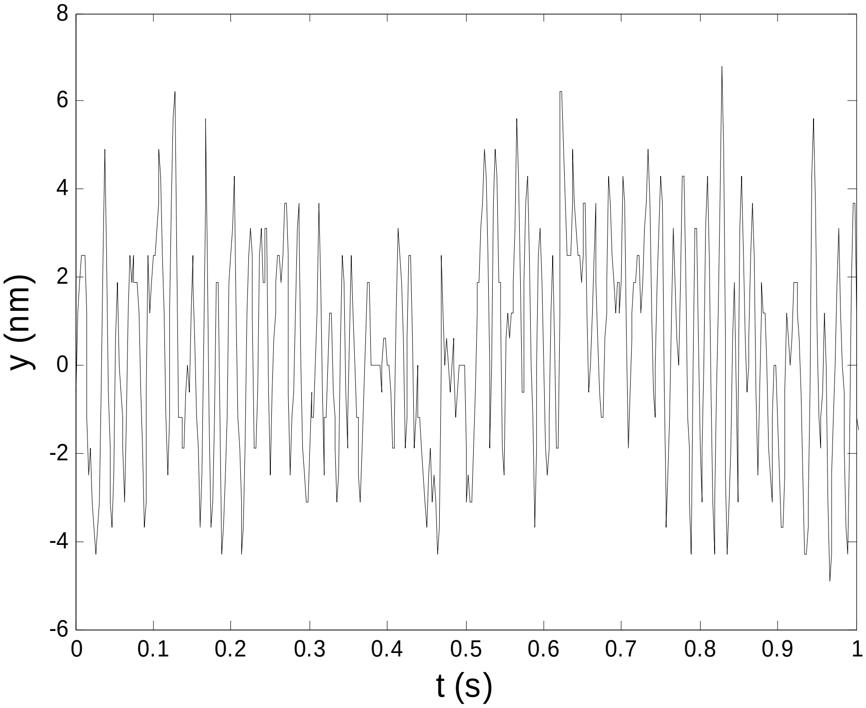

Fig. 4-3. Position noise in *y*.

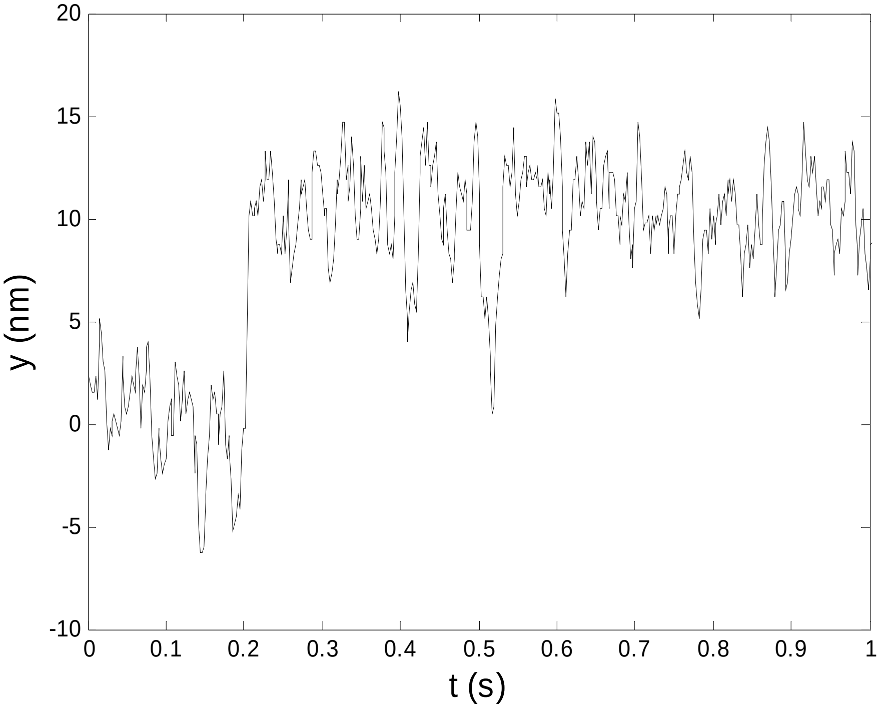

Fig. 4-4. 10-nm step response in *y* [54].

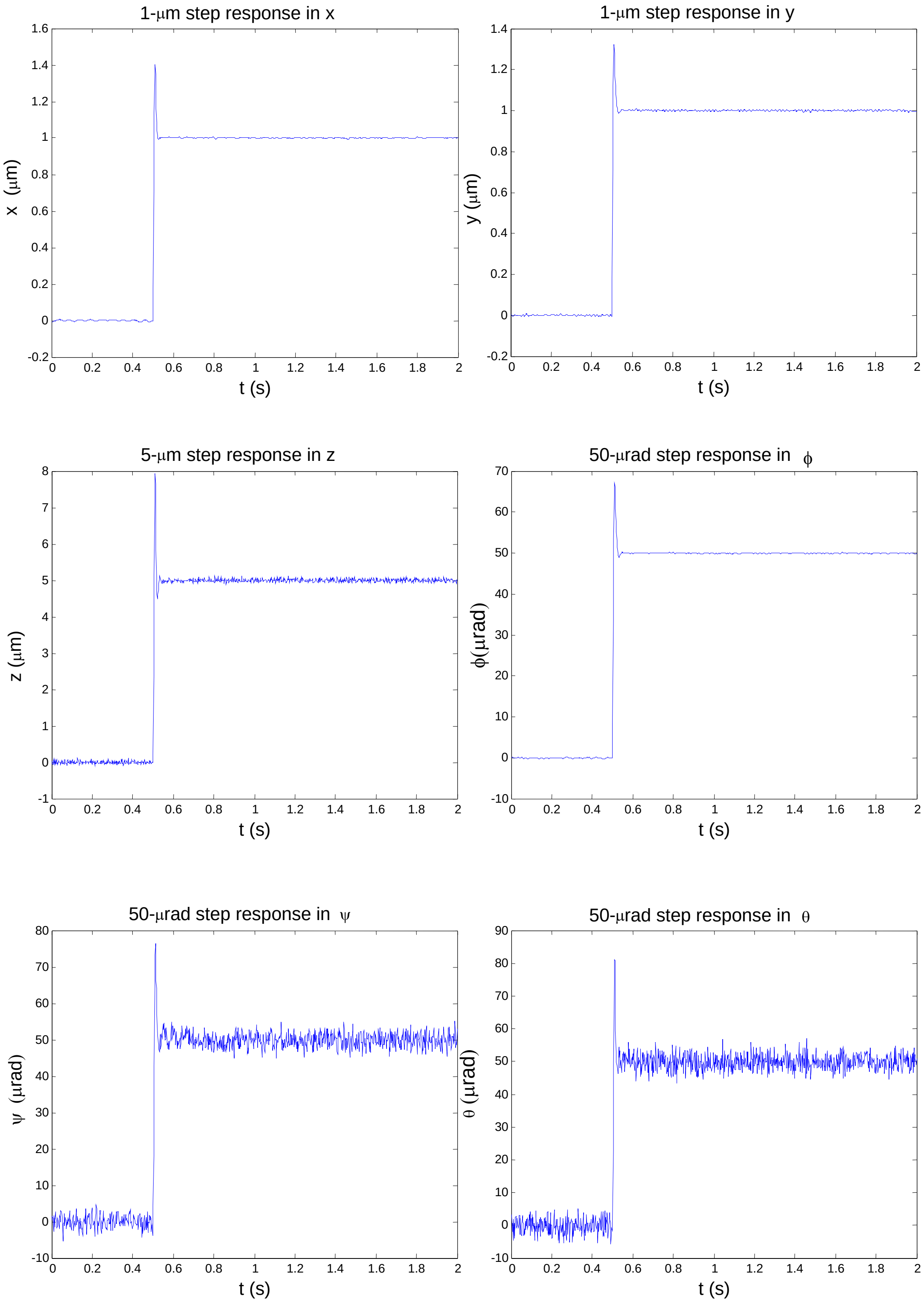

Fig. 4-5. Step responses in all the 6 axes.

4.3 Precision Motion Control

We performed various experiments with the maglev stage. This section presents the maglev stage's nanoscale multi-axis motion-control capability.

4.3.1 Nanoscale Periodic Motions

The maglev stage is capable of generating precise trajectories. In Fig. 4-6 a sinusoidal waveform of 50-nm amplitude is shown and the platen followed the commanded path very well. There were no large overshoots, and the noise level was consistently less than 3 nm rms while in motion. Fig. 4-7 shows a square-wave motion of the platen between two positions with the distance of 40 nm. The continuous line in middle of noisy path represents the commanded path, and the solid lines represent the resultant path traversed by the platen. While taking steps from one point to the other, there was an overshoot of around 15 nm. It settled down almost instantaneously and brought back the noise level to the minimum. This demonstrates that the maglev system can track commanded trajectories very precisely and fast, which is advantageous for precision positioning applications that need agile motions.

4.3.2 Nanoscale Consecutive Steps

Fig. 4-8 shows the platen responses to 15-nm consecutive step commands at every 0.5 s. Fig. 4-8 (b–c) show the errors in x and y while generating these steps. The tracking error in x has peaks at every 0.5 s due to abrupt changes in position. The regular noise level in x is close to 3 nm rms mainly due to these perturbations. The error in the y-axis is maintained below 2 nm

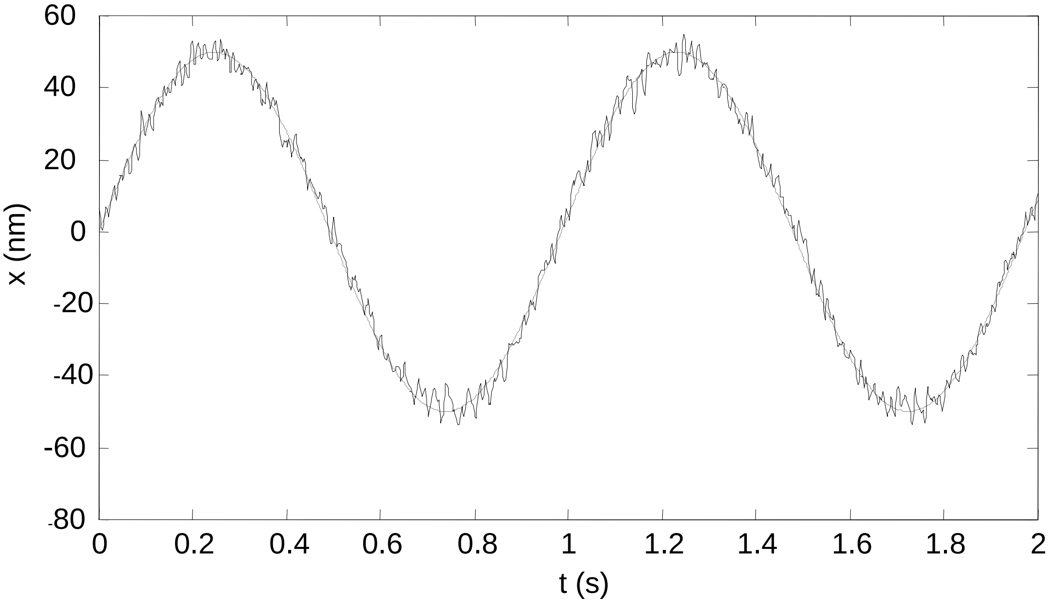

Fig. 4-6. 50-nm-amplitude sinusoidal motion in *x* [56].

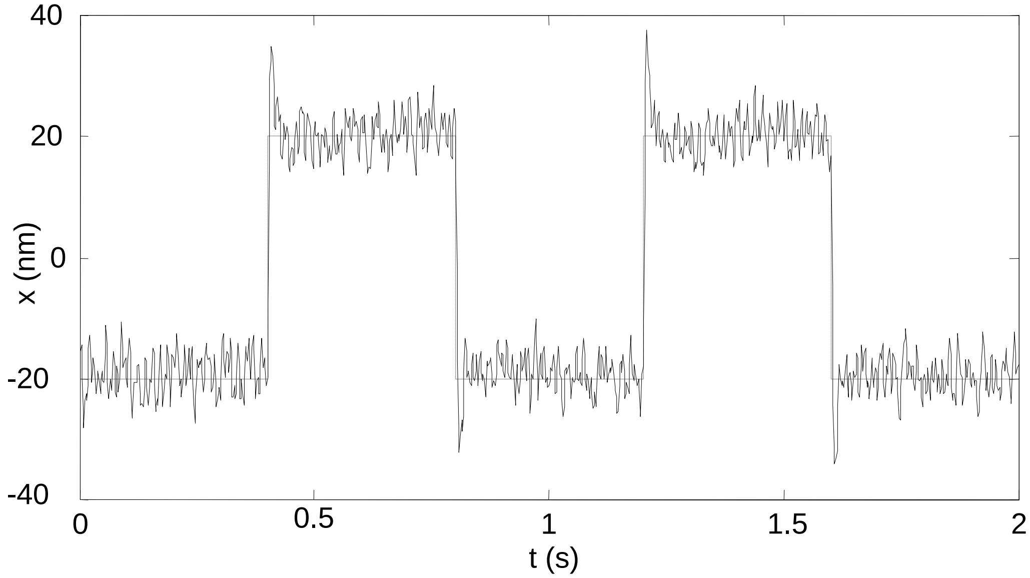

Fig. 4-7. 20-nm-amplitude square-wave motion in *x* [56].

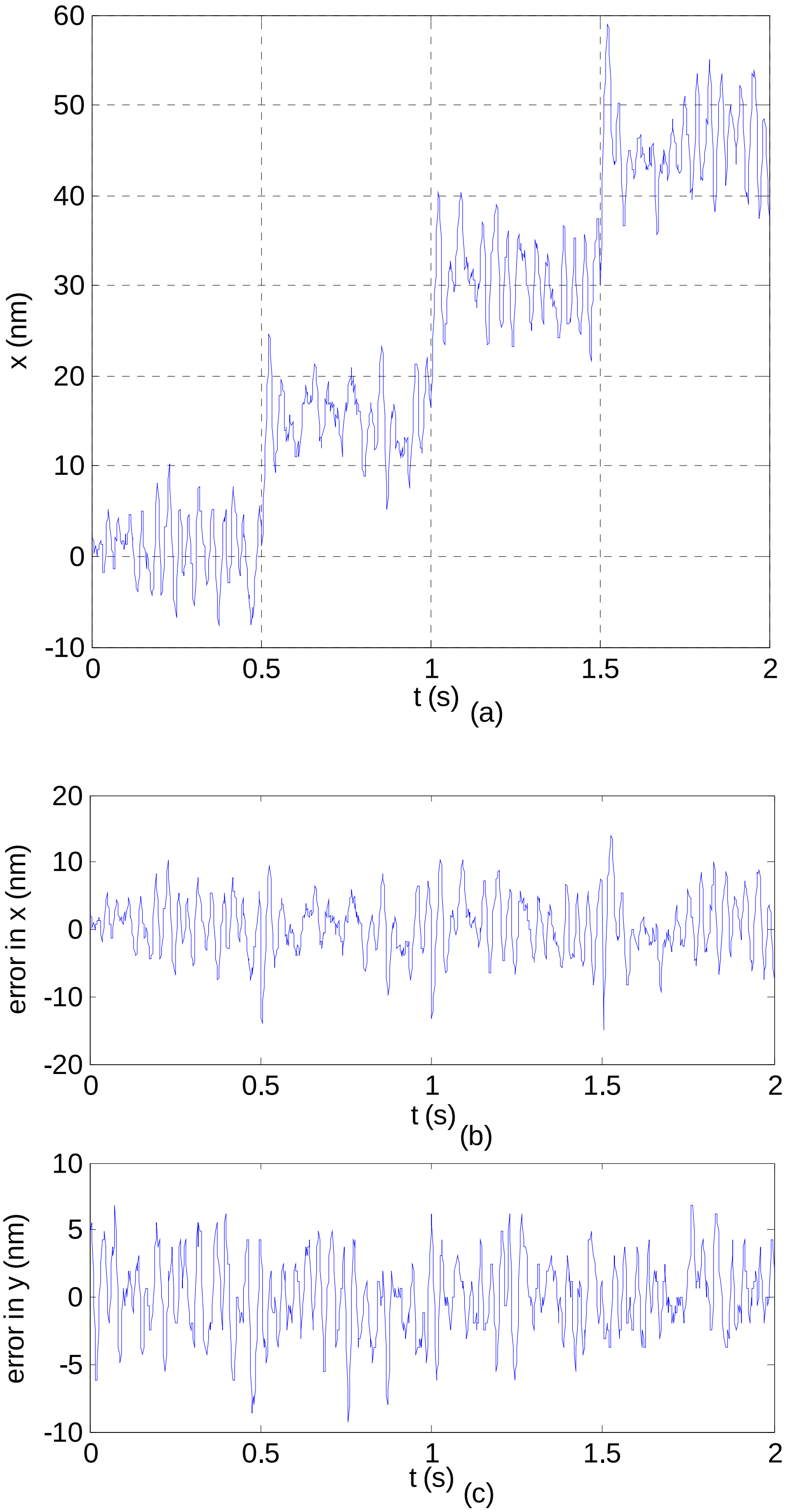

Fig. 4-8. 15-nm consecutive steps at every 0.5 s.

rms. This shows that there is very little dynamic coupling between the *x*- and *y*-axes. In other words, no sudden change in *x* affects the *y*-axis motion, and the controller is robust enough to keep the platen stable.

4.3.3 100-nm Ramp Responses

In Fig. 4-9 the commanded path for the platen is an up-and-down ramp with the peak of 100 nm. Fig. 4-9(a) shows the actual path traversed by the platen. It is visible from the figure that the starting point of the trajectory is not exactly zero. This is due to nanoscale position noise in the stage. The peaks of the trajectory appear to be at around 105 nm and –5 nm instead of 100 nm and 0 nm because of the overshoots at the ends of the ramp trajectories. The path is more distorted near the ends due to abrupt changes in the direction of motion.

4.3.4 2D Circular Motion

In the real-time control code written in the C language as an ISR, a set of data points in more than one axis can be allocated with respect to time so that the platen can follow a multi-axis trajectory. In Fig. 4-10(a), a commanded path of a 50-nm-radius circle and the response of the platen are shown. The trajectory errors in *x* and *y* in this nanoscale circular motion are shown in Fig. 4-10(b) and (c). We demonstrated that this stage could follow nanoscale 2-dimensional paths precisely.

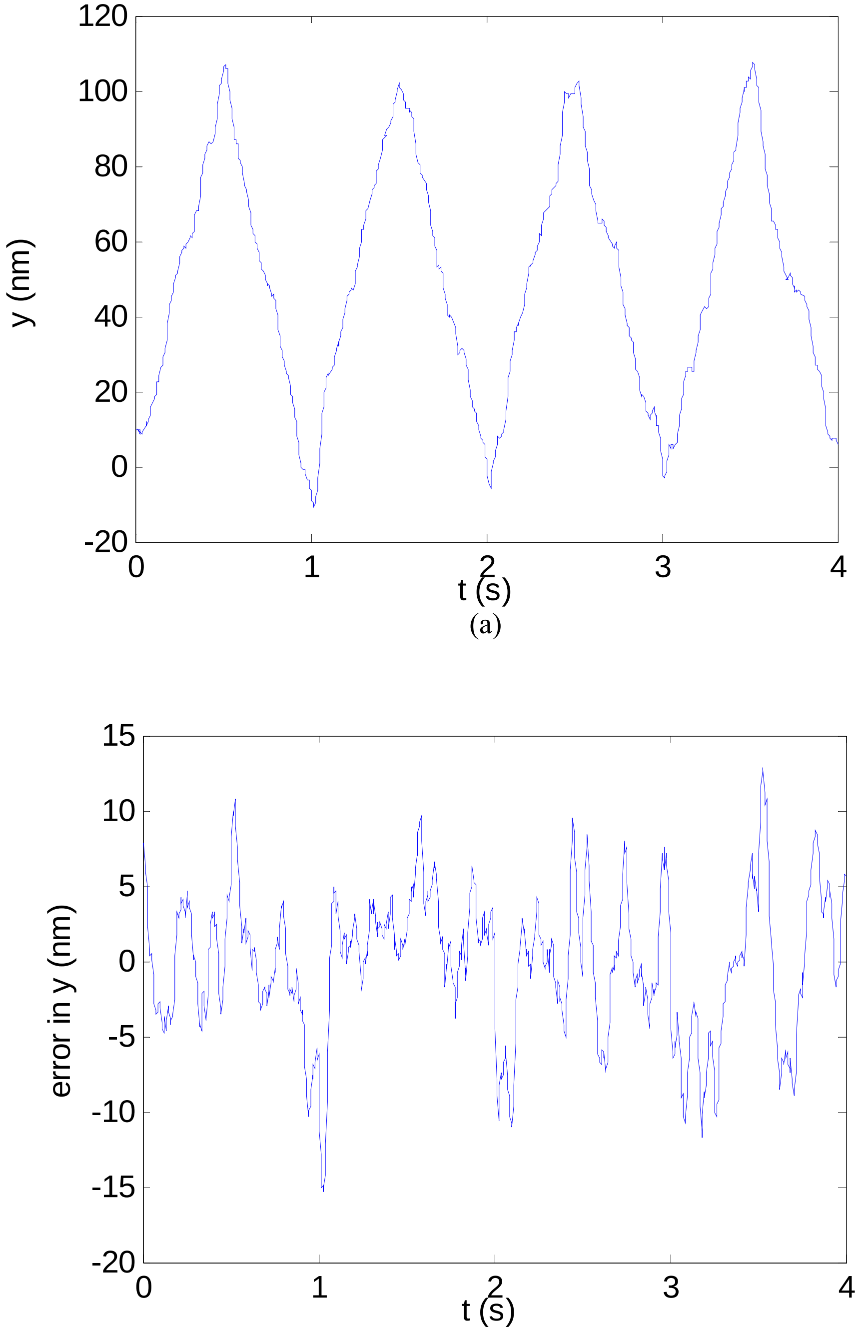

(b)

Fig. 4-9. (a) 100-nm up-and-down ramp response in *y* and (b) tracking error.

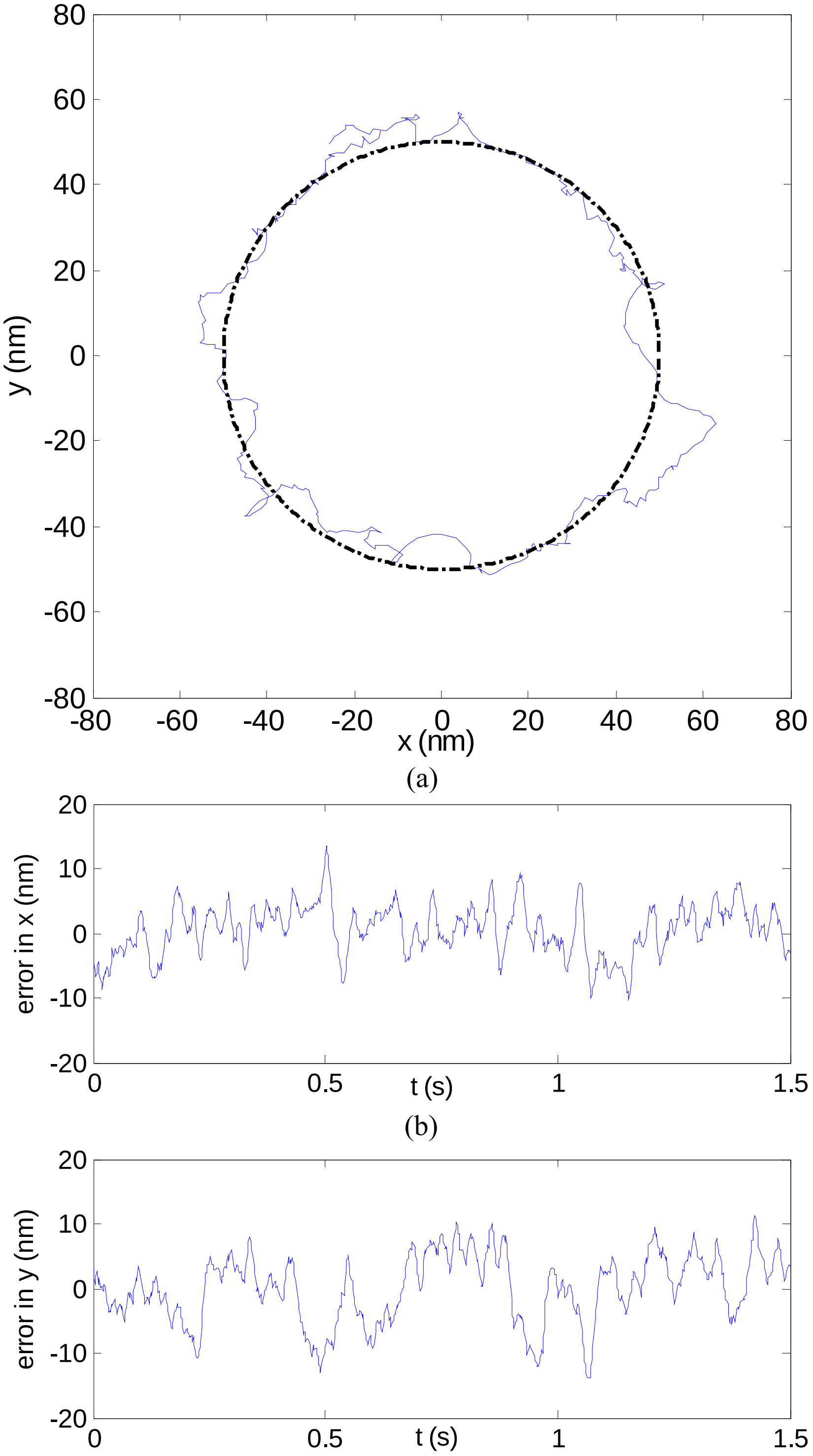

(a)

(b)

(c)

Fig. 4-10. 50-nm-radius circle traversed in the *x*-*y* plane.

4.3.5 3-D Motion Generation for Micromanufacturing

We performed several experiments to test the maglev stage with complex 3-D commanded paths. Among them a bowl-shaped trajectory with a parabolic vertical cross-section is shown in Fig. 4-11. The platen closely followed the trajectory. The commanded positions changed to make the platen move in a circular path by adding 1° rotation about the center at every sampling period of 200 μs.

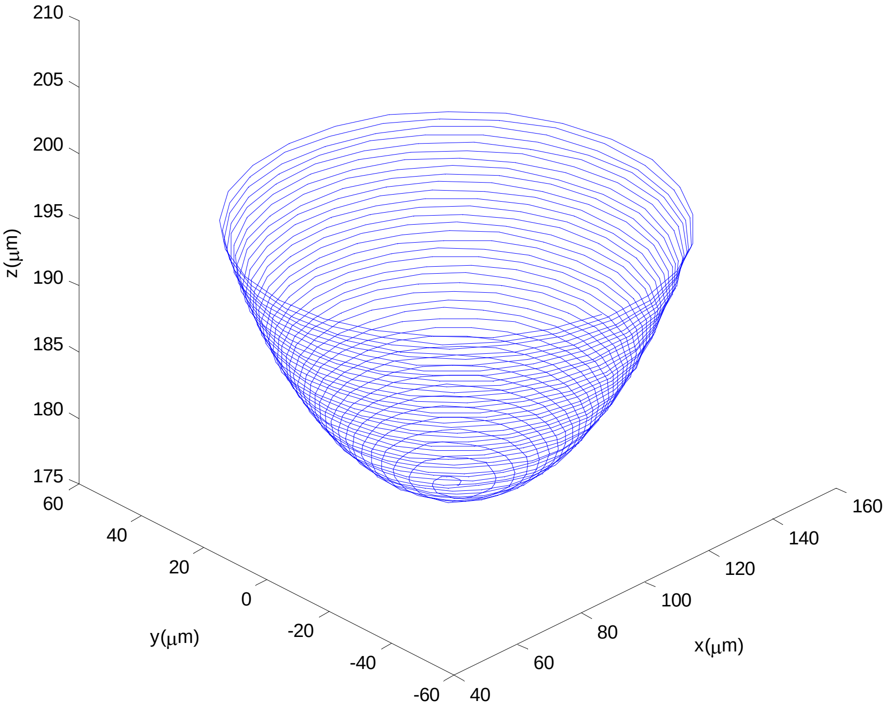

Fig. 4-11. Bowl with parabolic shape with a 20-μm height and 100-μm maximum radius.

Fig. 4-12 shows a 3-D trajectory followed by the platen layer by layer in the way as desired for μSTL to prove this maglev stage's positioning capability in micromanufacturing. The generated shape is of an impeller that has an outer radius of 25 μm and inner radius of 10 μm.

The maglev stage was made to follow this whole 3-D motion trajectory in only 18 s although the platen would need to be moved much slower in an actual μSTL process to allow sufficient time to cure photopolymer. These experimental results demonstrated the microscale 3-D motion-generation capability of the maglev stage.

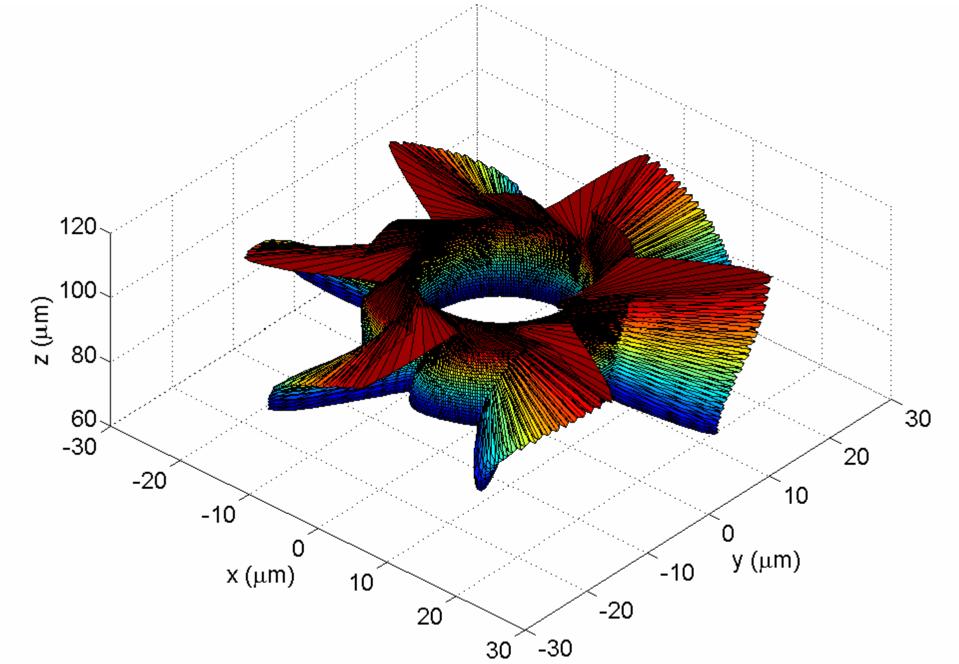

Fig. 4-12. 3-D impeller shape traversed by the platen.

4.4 Load Tests

In this section various load-test results to demonstrate the maglev stage's dynamic performance for nanomanufacturing and μSTL applications are presented. In these applications, the positioner is supposed to carry small, but time-varying loads.

4.4.1 Payload vs. Current

Experiments were carried out with various payloads applied to the platen in the form of dead-weights. The currents in the vertical actuators to maintain the platen position constant were measured. A plot of payload vs. applied current is shown in Fig. 4-13. The small circles shown in the figure are the experimental data points for various loads and the line connecting them is the least-square linear fit by Matlab®. This linear relation between the sum of the vertical coil currents and the force is as expected because the generated force is directly proportional to the coil current in our Lorentz-force unit linear actuator. From the experimental data we found the force constant to be 0.798 N/A after subtracting the force offset of 2.09 N (= 0.2126 kg × 9.81

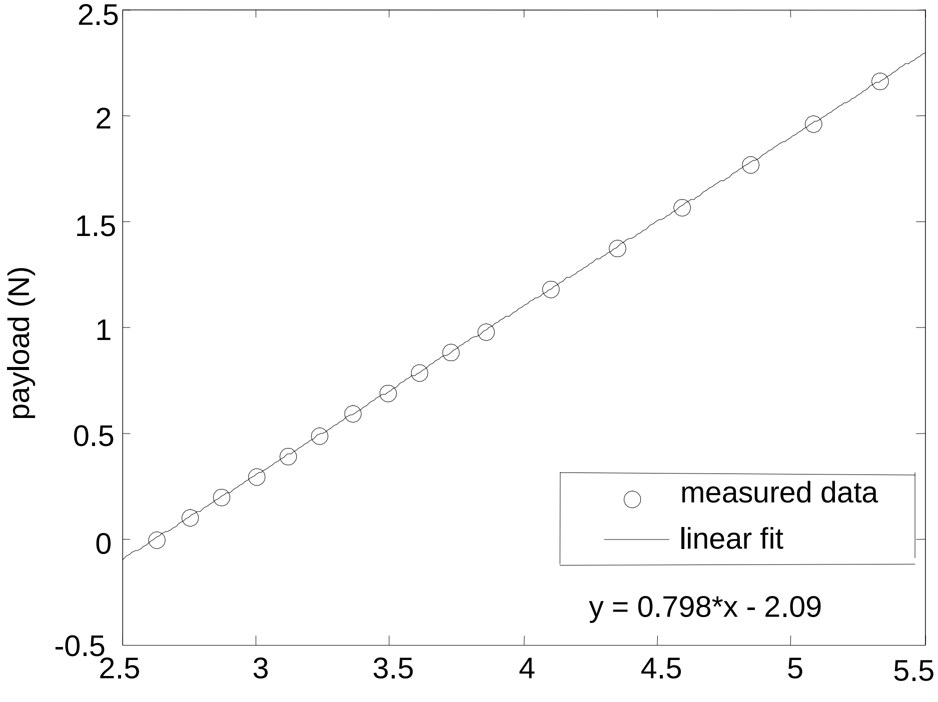

Fig. 4-13. Payload vs. current required to maintain the platen position constant.

m/s^2) to balance the weight of the platen. We also numerically calculated the theoretical Lorentz force, $\boldsymbol{f} = \int (\boldsymbol{J} \times \boldsymbol{B}) dV$ using Mathcad®, with which the force constant was found to be 0.839 N/A. Thus the error between the experimental force constant and its theoretical value is only 5%. A possible cause of the error may be inaccurate reading of data due to small continuous fluctuation in current while in closed loop, and manufacturing and assembly errors.

4.4.2 Pull-Out Force

We performed an experiment to determine the pull-out force of the maglev stage. We attached a spring at the center of the platen and applied a vertical force on it. The spring was pulled upwards manually, so the amount of the force was continuously increasing. Fig. 4-14 shows the platen position in z and the control effort f_z applied by the controller to maintain the

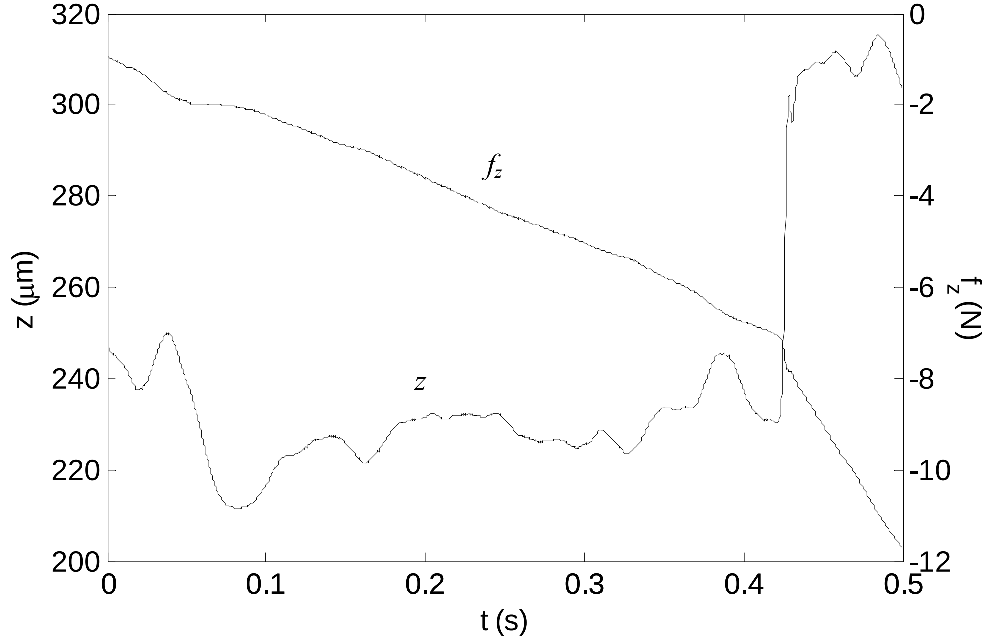

Fig. 4-14. Determination of the pull-out force with vertical position z and the control effort f_z.

platen position constant. The *z*-axis position of the platen shifted suddenly at around 0.425 s indicating the pull-out force of 7.75 N. The actuators are designed to deliver maximum current of 2.5 A with the force constant of 0.798 N/A. Thus the maximum force that the controller can apply via the three vertical actuators to maintain the platen position would be 3 × 0.798 N/A × 2.5 A = 5.99 N. Since the direction of the pull-out force is upwards, it balances the platen weight and then overcomes the vertical actuator forces. As the force to balance the weight of the platen is 2.09 N, the theoretical value of the pull-out force will be 5.99 N + 2.09 N = 8.08 N. The error in the experimental value is only about 4%.

4.4.3 Step Responses with Various Payloads

To test the dynamic performance of the maglev stage, several step responses were taken with various payloads. The experimental results are shown in Fig. 4-15. The stage was able to

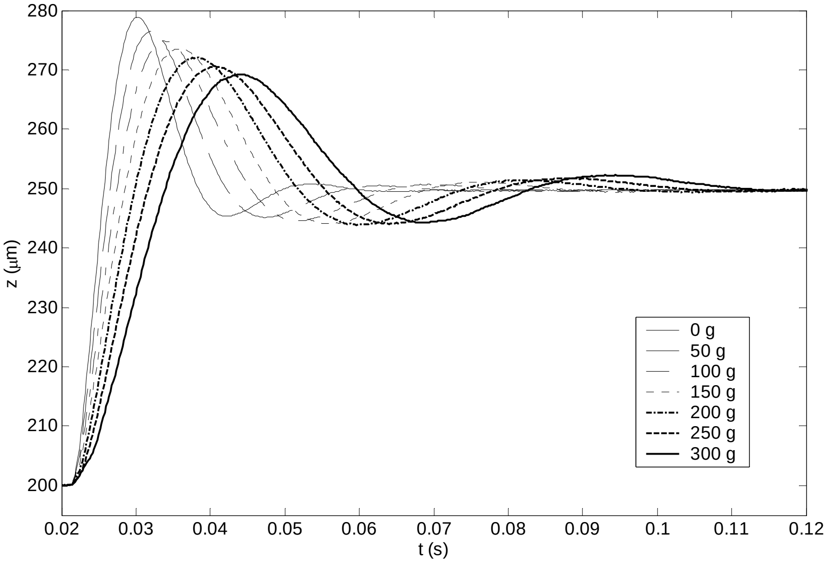

Fig. 4-15. No-load and load tests with 50-μm step responses in *z* [56].

levitate and position an additional mass of 0.3 kg on the platen. The payloads of more than 0.4 kg made the stage unstable due to actuator saturation in the overshoot. The additional payload increases the mass, keeping the system stiffness about the same, which lowers the natural frequency of the moving platen. Due to the lower natural frequency the rise time and the settling time are longer for the larger payloads as shown in the figure.

4.4.4 Recovery from Sudden Load Changes

To test the response of the platen for sudden load changes we placed small ceramic cylinders on the platen. We recorded the z-axis position and the control effort f_z by the controller to recover the position of the platen that is still under 6-axis magnetic levitation when the two ceramic cylinders were taken off one by one. Fig. 4-16(a) shows the plot of the z-axis position, and Fig. 4-16(b) shows the control effort. The load removal occurred at around 0.78 s and 2.35 s, which generated perturbations in z. In the beginning of this experiment the vertical actuators were applying the forces precisely sufficient to balance the weight of the platen and the payload. As soon as the payload was removed, the applied force became greater than that to balance the weight of the platen and the payload. This excessive force gave the platen an instantaneous push upwards that was recovered by the controller over a period of 0.6 s. The maglev system's behavior was repeatable for the second load removal. It can be observed from Fig. 4-16(b) that the control effort in z decreased as soon as a ceramic cylinder was removed. The drop in the control effort was measured to be 0.14 N for first ceramic cylinder and 0.135 N for the second cylinder. The mass of each cylinder was 14 g i.e. 0.137 N. This shows that the error between the experimental control effort and the actual force is only around 2%.

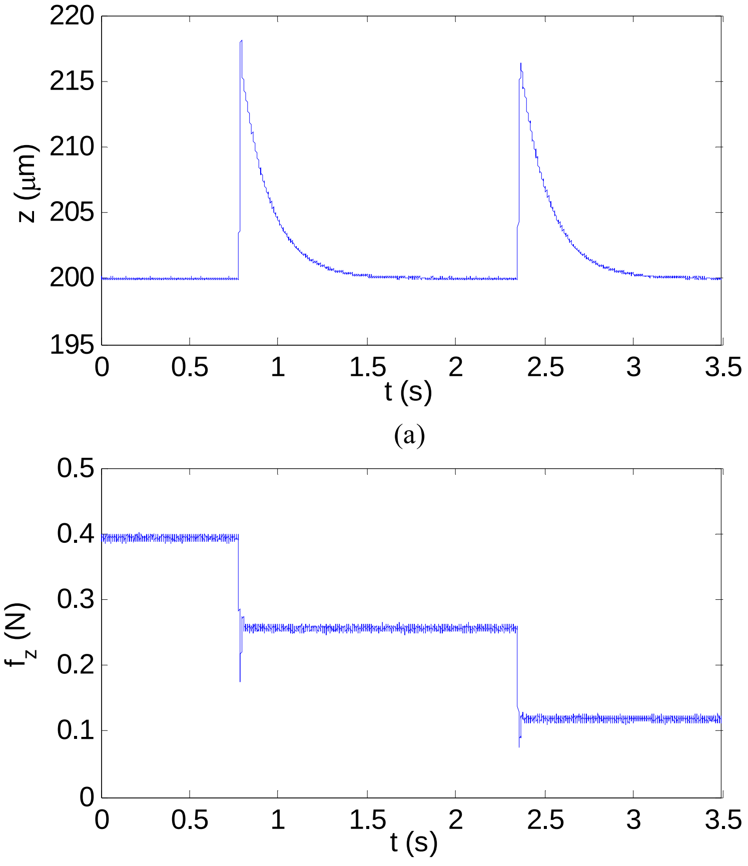

(a)

(b)

Fig. 4-16. Sudden load change, (a) position in *z* and (b) control effort f_z by the controller.

4.4.5 Recovery from Continuously Varying Load

We used a continuous flow of sand falling into a bowl placed on the platen to emulate the effect of the continuously varying load in nanomanufacturing and μSTL applications. The *z* position of the platen is shown in Fig. 4-17(a) and corresponding control effort required is shown in Fig. 4-17(b). From the initial steady-state position, the mass inflow was initiated at 3 s and was stopped at 11 s; then started again at 16 s and stopped at 22 s. Since the rate of the mass change was almost constant, the control effort linearly increased to balance the additional

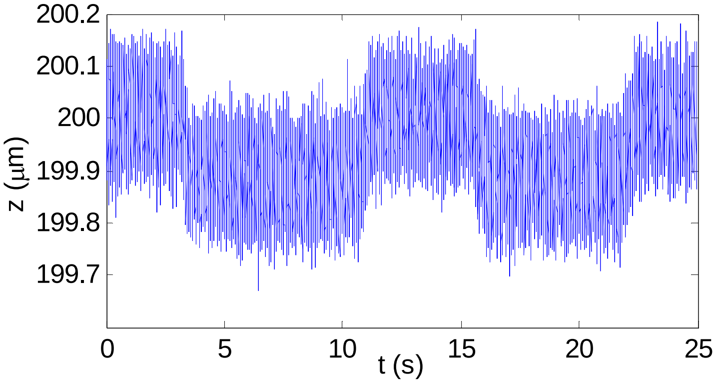

(a)

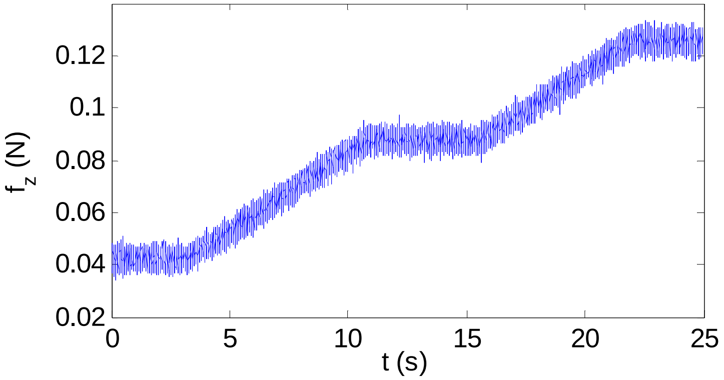

(b)

Fig. 4-17. Continuous varying load (a) Position in z and (b) control effort f_z.

mass on the platen and to regulate the vertical position of the platen at the same level. However, there was a small steady-state error in the vertical position during the mass variation, which acts like a force disturbance at the control input. This is attributed to the fact that the plant poles are not identically located at the origin in the complex plane, and the controller was originally designed to meet the zero-steady-state error requirement for the position inputs with a single pole at the origin.

This completes the description of the first-generation maglev stage. The dynamic modeling of the stage and a lead-lag controller was designed and implemented. Several positioning and load tests were performed to demonstrate capabilities of the maglev stage.

CHAPTER V

ELECTROMECHANICAL DESIGN OF SECOND-GENERATION MAGLEV STAGE

In the last two chapters we discussed the development of the first-generation six-axis maglev stage capable of 2 nm position resolution over the travel range of 300 µm in the *x*-, *y*- and *z*-axes with a payload capacity of 0.3 kg. The second-generation stage shown in Fig. 5-1 presented in this chapter onwards has the travel range around 16 times as wide as that of the first-generation maglev stage and the payload capacity of 2 kg as compared to previous 0.3 kg. The nominal power consumption per unit actuator is just 135 mW, less than half of the power consumption of the previous stage, 320 mW. Moreover the current stage has several additional unique advantages such as smaller number of parts and no mechanical restriction. There are less than two dozen parts in the whole stage with the minimum number (six) of coils. There are only three magnet pieces, and two coils share the horizontal and vertical magnetic fields of each magnet piece. Due to the absence of any mechanical restriction, the platen can be removed from the machine frame easily without disturbing any stationary parts. This facilitates easy loading and unloading of objects on the platen for various applications. Thus our new maglev stage possesses competitive advantages in terms of travel range, payload capacity, simplicity in mechanical design, and power consumption. Although the position resolution is currently a bit lower than the previous stage due to nonlinearities in the longer travel range.

In this chapter we describe the electromechanical design of second-generation stage. This includes electromechanical actuation scheme, actuator design, analysis and experimental verification of calculated forces.

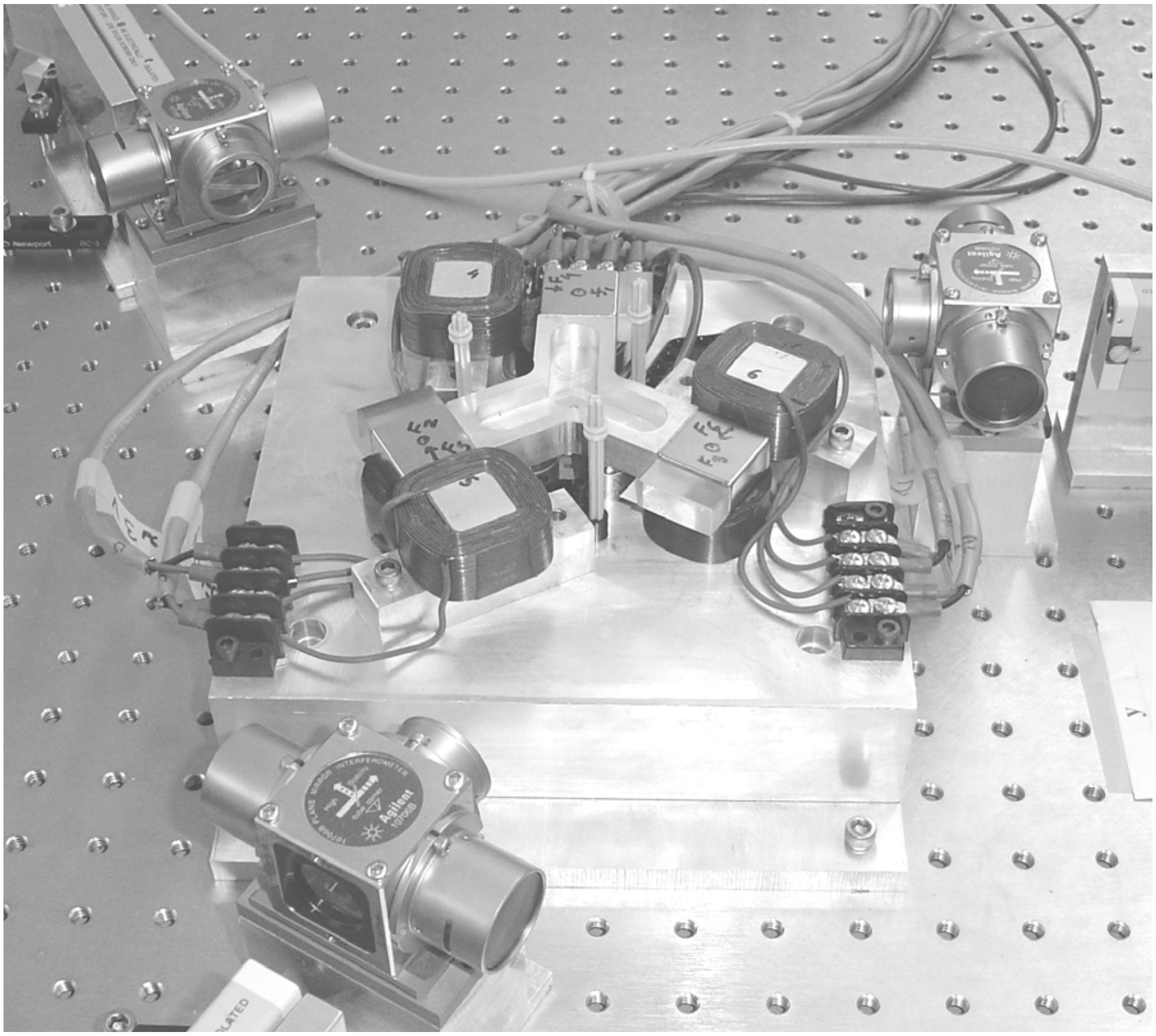

Fig. 5-1. Photograph of the large-travel-range nanopositioning stage.

5.1 Novel Electromagnetic Actuation Scheme

A novel electromagnetic force generation scheme was developed for this maglev stage. This scheme generates forces on a magnet in two perpendicular directions using two current carrying coils. This reduces mass of moving part, heat generation, and power consumption of the stage. Fig. 5-2 shows a cross-sectional side view of each actuator unit. There are three such units at the three ends of the Y-shaped platen shown in Fig. 5-1. There are two square-shaped coils below and to the right of each magnet with the vertical magnetic axis. The coils are stationary and the magnet is attached to the moving platen. The magnetic-field lines generated by the permanent magnet are shown in Fig. 5-2. The direction of the current in flow is assumed clockwise in vertical coil and counterclockwise in horizontal coil, seen from the top. The directions of the forces generated in each coil sections due to the current flow are shown in Fig. 5-3.

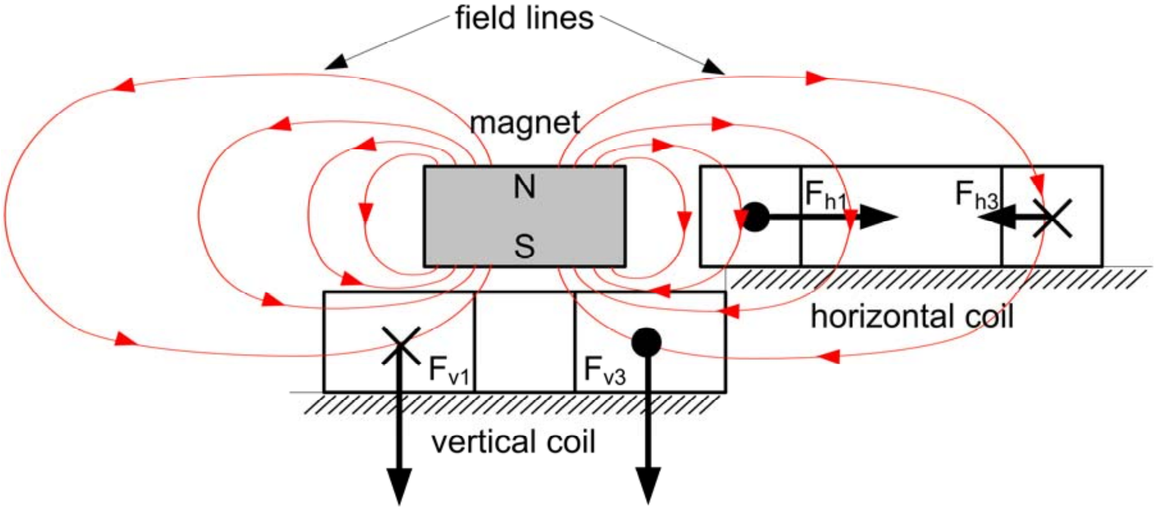

Fig. 5-2. Cross-sectional side view of the novel unit actuator.

In the vertical coil, the direction of the magnetic-field lines is from outside to inside on all the 4 sides of the coil (neglecting the corner effect). Thus the $\vec{J} \times \vec{B}$ Lorentz force on the coil is vertically downwards on all the four sides of the square. The equal electromagnetic force is applied vertically upwards on the moving magnet. In the horizontal coil the direction of the magnetic-field lines is downwards in all the 4 sides. The forces F_{h2} and F_{h4} are equal in magnitude and opposite in direction, so they cancel. The directions of F_{h1} and F_{h3} are opposite,

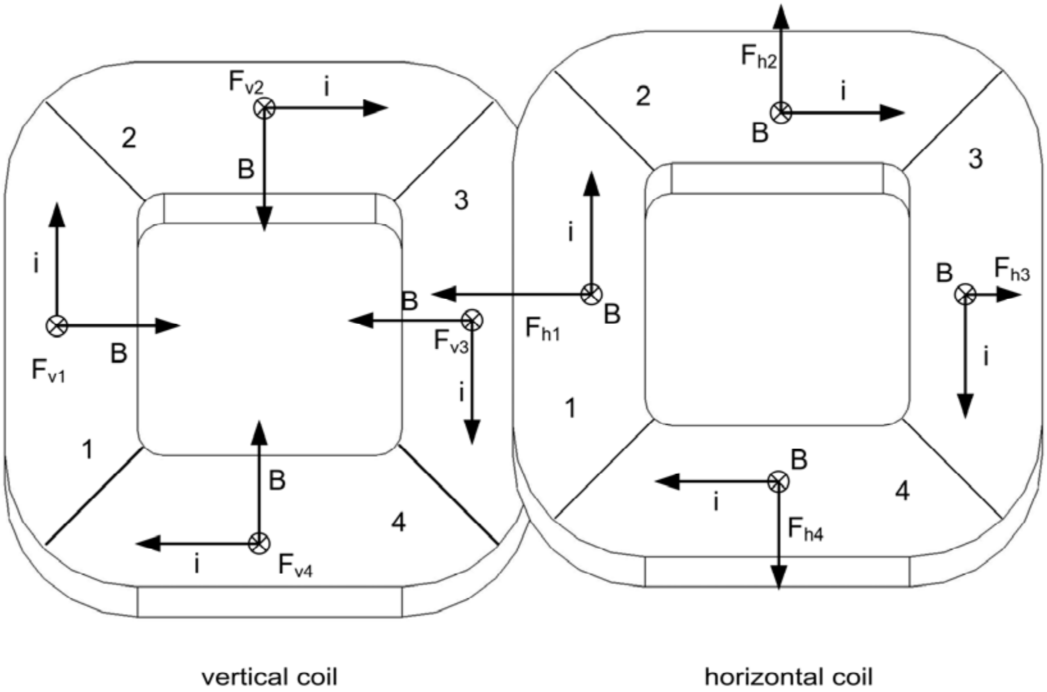

Fig. 5-3. Top view of one actuation unit.

but the magnitude of F_{h1} is greater than that of F_{h3} since Section 1 is nearer to the magnet than Section 3. Thus the effective force on the coil is to the left, and on the magnet to the right. To change the direction of the vertical and horizontal forces, we change the direction of current flow in the corresponding coils. In this manner we generate forces in the two perpendicular directions independently on a single moving magnet. For 6-axis motion generation three such magnets are mounted on the platen as shown in Fig. 7-2. The primary benefit of this scheme is reduction in the number of magnets that are the heaviest parts in the moving platen (0.185 kg out of 0.267 kg of the total platen mass). It maintains the force capability high with significant mass reduction. In magnetic levitation the moving-part mass is a very crucial design factor because a smaller mass requires smaller coil currents to levitate the moving part against gravity. This leads to less power consumption, heat generation, and thermal-expansion error that is detrimental to nanoscale positioning.

5.2 Force Calculation

The force between the current-carrying coil and the permanent magnet is calculated by the Lorentz law,

$$\vec{\boldsymbol{f}} = \int (\vec{\boldsymbol{J}} \times \vec{\boldsymbol{B}}) dV \, , \tag{5.1}$$

where $\vec{\boldsymbol{J}}$ is the current density [A/m^2] in the coil, $\vec{\boldsymbol{B}}$ is the magnetic flux density [T] generated by the permanent magnet, and dV is the small volume segment in the coil. The limits of the integral are to cover the whole volume of the coil. After substituting the parameters shown in Fig. 5-4, the expression of the force acting on the volume (V) of the coil due to the surface (S) magnetic charge on the magnet becomes the following quintuple integration.

$$f = \frac{J\sigma_m}{4\pi} \iint_S \iiint_V \frac{-(x-p)\hat{k} + (z-r_1)\hat{i}}{\{(x-p)^2 + (y-q)^2 + (z-r_1)^2\}^{1.5}} dydxdzdpdq \, , \tag{5.2}$$

where $\sigma_m = \pm\mu_0 M$ is the surface magnetic charge density on the top and bottom surfaces of the magnet with permanent magnetization M [A/m]. The permeability of free space μ_0 is $4\pi \times 10^{-7}$ H/m, and $\hat{i}$ and $\hat{k}$ are the unit vectors in the stationary frame attached to the coil.

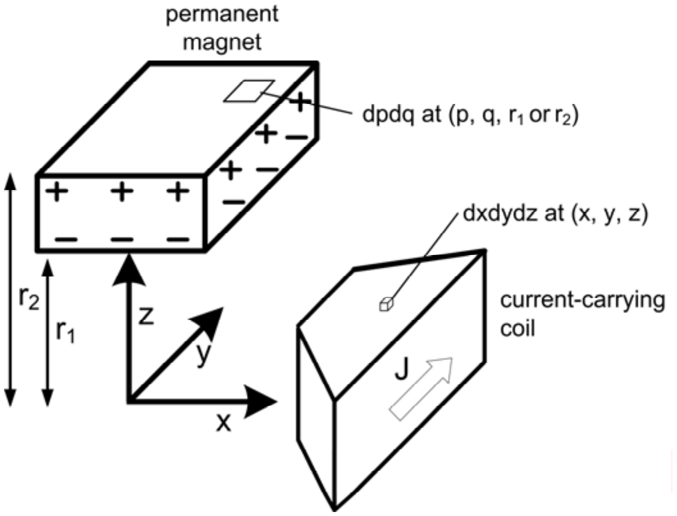

Fig. 5-4. Diagram indicating the parameters to calculate the force acting on the magnet.

5.3 Vertical Actuator

Actuation force, platen mass, and sensor, and actuator packaging were the main design issues, and several design iterations were carried out to determine the optimal sizing of coils and magnets. The calculation of the vertical force of the actuator is a crucial part for maglev stages because this is the force that works against gravity and levitates the moving part.

5.3.1 Actuator Sizing

To calculate the vertical force we divide the coil into 4 equal sections (viz.1–4) as shown in Fig. 5-3. The horizontal force components (if any) on Sections 1 and 2 cancel with the horizontal force components on Sections 2 and 4 due to equal magnitudes and opposite directions. The vertical components of these forces are added and the direction of the resultant force on the vertical coil is downward, so on the magnet, upward. We multiply a factor of 4 to (5.3) to calculate the overall vertical force

$$F_{v1}=\frac{J\sigma_m}{4\pi}\left[\int_{-d/2}^{d/2}\int_{-d/2}^{d/2}\int_{-h/2}^{h/2}\int_{a}^{b}\int_{0}^{x}\frac{(x-p)}{[(x-p)^2+(y-q)^2+(z-r_1)^2]^{1.5}}dydxdzdpdq\right]$$
$$-\frac{J\sigma_m}{4\pi}\left[\int_{-d/2}^{d/2}\int_{-d/2}^{d/2}\int_{-h/2}^{h/2}\int_{a}^{b}\int_{0}^{x}\frac{(x-p)}{[(x-p)^2+(y-q)^2+(z-r_2)^2]^{1.5}}dydxdzdpdq\right], \quad (5.3)$$

where the dimensions *d*, *h*, *a* and *b* are shown in Fig. 5-5.

The choice of sizes of strong permanent magnets for higher energy product is very limited. We compared 25.4 mm the square cross-sectional magnets of two different heights 12.7 mm and 25.4 mm from the standard options available in market. For the same size of coil and the same coil current, the forces on the two magnets were calculated for various heights of magnet. Fig. 5-6 shows the plot of the forces that shows the forces from the bigger magnet is around 10% more than that from the smaller magnet however doubling the size of magnet increases the weight of moving part by around 75%. Thus neodymium-iron-boron (NdFeB) permanent magnets with the energy product (BH_{max}) of 280 kJ/m^3 (35 MGOe) and dimensions of 25.4 × 25.4 × 12.7 mm were finally chosen for the maglev stage.

For the sizing of the coil for vertical actuators we calculated forces for different sizes of coils and compared them while considering the packaging issues for capacitance sensors. On the basis of several design iterations using (5.3) the optimal size of the coils turned out to be square of 12.5 × 12.5 mm inner dimension and 40 × 40 mm of outer dimension with 732 turns and the terminal resistance of 5.5 Ω. The coils were wound by Wirewinder Inc. with heavy-built AWG (American wire gauge) #24 copper magnet wire that had a layer of heat-bondable epoxy

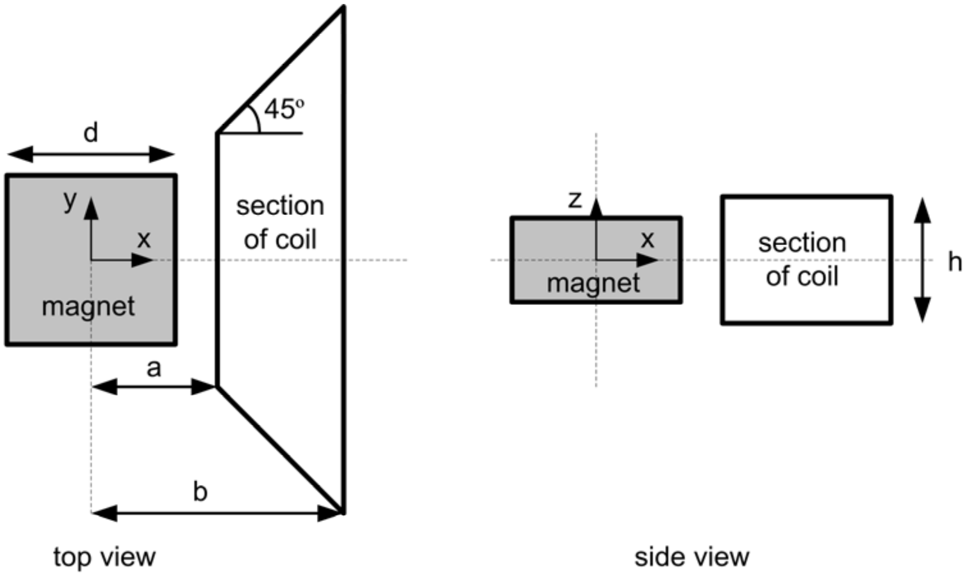

Fig. 5-5. Top view and side view of the magnet and coil arrangement showing variable.

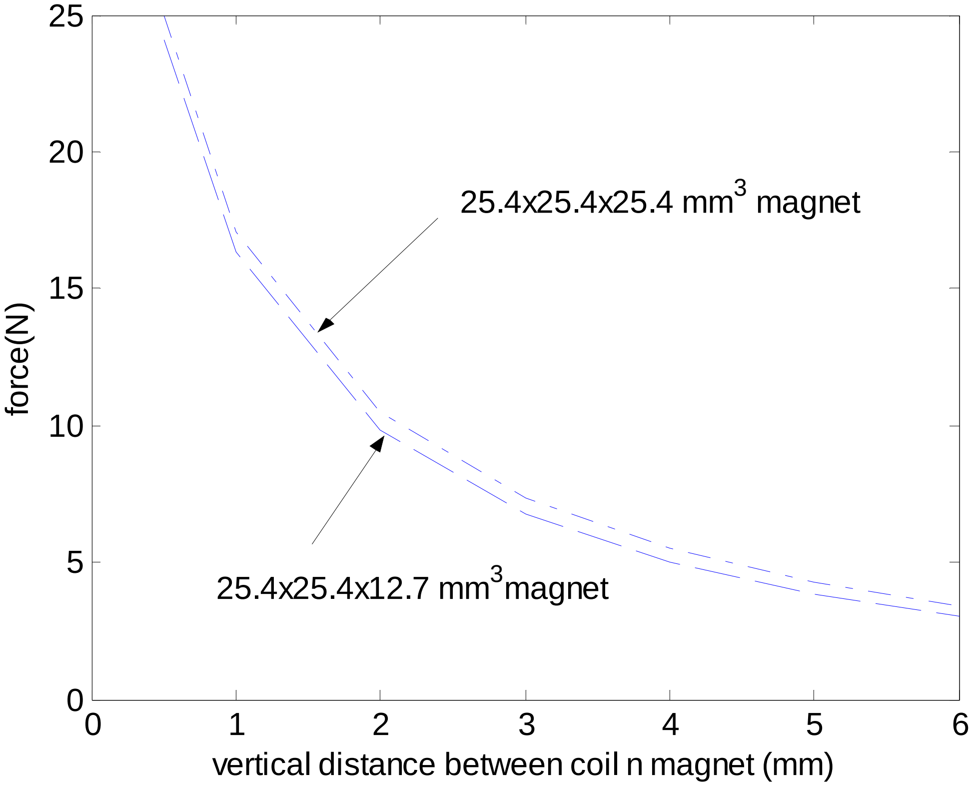

Fig. 5-6. Comparison of forces with two different sizes of magnets.

coating on it. The maximum calculated vertical force is 8.76 N by each vertical actuator at the height of 500 μm.

5.3.2 Performance Analysis at Offset Positions

The force calculated above was based on the assumption that the symmetric axis of the coil passes the center of the magnet. However the magnet is attached to the moving platen and its moves up to ±2.5 mm from the center. Thus an extensive analysis was carried out to ensure the force capability of designed vertical actuator in the whole working range. Solving the force equation for every point of travel and for whole coil using Mathcad® is a very time consuming task. Thus we divided the square coil in 8 sections and calculated for the force at offset positions due to one 1/8 section of the coil. Fig. 5-7 (a) shows the offsets *i* in the *x*-axis and *j* in the *y*-axis. The vertical force on the magnet was calculated from -3 mm to +3 mm on both *i* and *j* at every integer value of *i* and *j*. Assume that the force due to this section of coil is $F_{i,j}$ at offset position *i* and *j*. The $F_{i,j}$ is calculated using

$$\begin{aligned} F_{i,j} = {} & \frac{J\sigma_m}{4\pi}\left[\int_{[-d/2+0.001\times i]}^{[d/2+0.001\times i)]}\int_{[-d/2+0.001\times j]}^{[d/2+0.001\times j]}\int_{-h/2}^{h/2}\int_{a}^{b}\int_{0}^{x}\frac{(x-p)}{[(x-p)^2+(y-q)^2+(z-r_1)^2]^{1.5}}\,dydxdzdpdq\right] \\ & -\frac{J\sigma_m}{4\pi}\left[\int_{[-d/2+0.001\times i]}^{[d/2+0.001\times i]}\int_{[-d/2+0.001\times j]}^{[d/2+0.001\times j]}\int_{-h/2}^{h/2}\int_{a}^{b}\int_{0}^{x}\frac{(x-p)}{[(x-p)^2+(y-q)^2+(z-r_2)^2]^{1.5}}\,dydxdzdpdq\right] \end{aligned} \tag{5.4}$$

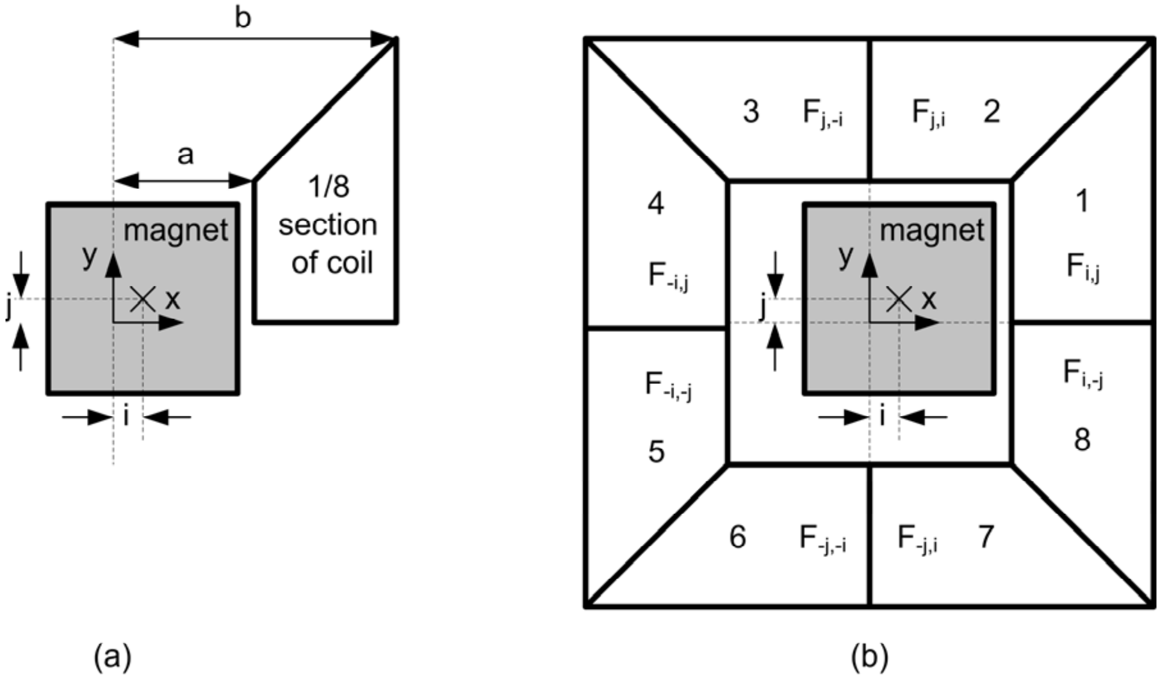

Fig. 5-7. Vertical force calculation at offset positions from center.

The equation above gives 49 values (7×7 offset positions in *x*-*y* plane) of *F* in a plane for a constant vertical gap between magnet and coil. We use these values to find the total force due to the whole coil. Consider the Sections 1 to 8 of coil as shown in Fig. 5-7 (b). For any offset of *i* and *j* we have calculated force $F_{i,j}$ due to Section 1. The force due to Section 2 will be $F_{j,i}$ for the same position of magnet. Similarly, $F_{j,-i}$ for Section 3, $F_{-i,j}$ for Section 4, $F_{-i,-j}$ for Section 5, $F_{-j,-i}$ for Section 6, $F_{-j,i}$ for Section 7 and $F_{i,-j}$ for Section 8. The summation of the forces from individual sections gives the total force on magnet at any offset position *i* and *j* for the whole horizontal plane of travel at a constant height of magnet.

The calculation mentioned above was performed for several different heights. Fig. 5-8 shows the results of the calculation for vertical force applied by the vertical coil on the permanent magnet. The figure shows 5 surfaces for the levitation heights of 1, 2, 3, 4, and 5 mm, respectively with the topmost surface corresponding to 1 mm and bottommost, 5 mm. Each surface corresponds to the force at a fixed height of magnet and offset of –3 mm to 3 mm in the *x*- and *y*-axes. As the plot shows there is a reduction in force of around 50% as the height increases from 1 mm to 5 mm. The actuation force decreases as the magnet moves away from the center of the coil.

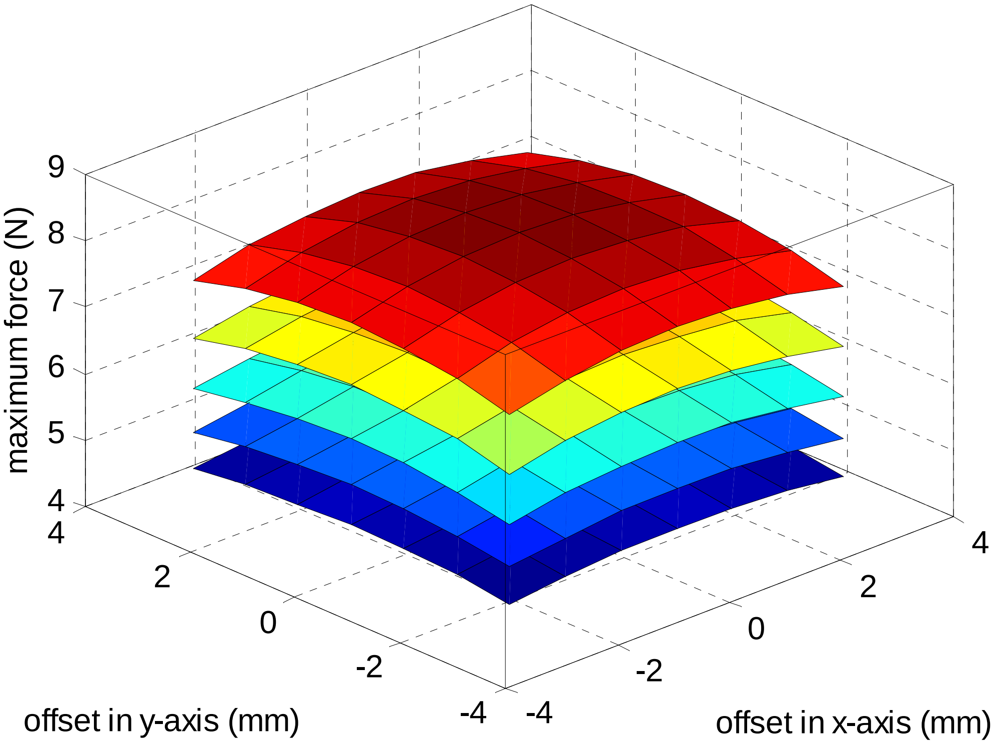

Fig. 5-8. Vertical forces at offset positions in *x*-*y* plane at the heights of 1, 2, 3, 4, and 5 mm.

5.3.3 Experimental Verification

We performed experiments to verify the analytical magnetic force derived in the previous section. An experimental setup shown in Fig. 5-9 was designed and fabricated to measure the force between the coils and the magnet. The coils were mounted on an aluminum plate with clamps. The magnet was fixed on one end of a precision load cell. The other end of the load cell was attached to a cantilever beam that was bolted on a $xyz\phi$ stage. We positioned the magnet in the 3 axes using the screw-gauges with respect to the coils at different positions and measure the load-cell voltage output. The forces due to gravity and magnetic attractions were eliminated by subtracting the load-cell reading without any current in the coils from the reading with current.

Fig. 5-10 shows the variation of vertical force as the magnet is moved up along the center axis of the coil. The comparison of the theoretical and experimental values proves that the estimation of the force is very accurate in the vertical axis as the maximum error is around 3%. Fig. 5-11 shows the values of the vertical forces that we achieved from the experiments (o) when the magnet is moved in the *x*-axis at a certain heights and its comparison with theoretical values (*) calculated in previous sections. This comparison shows that the maximum error

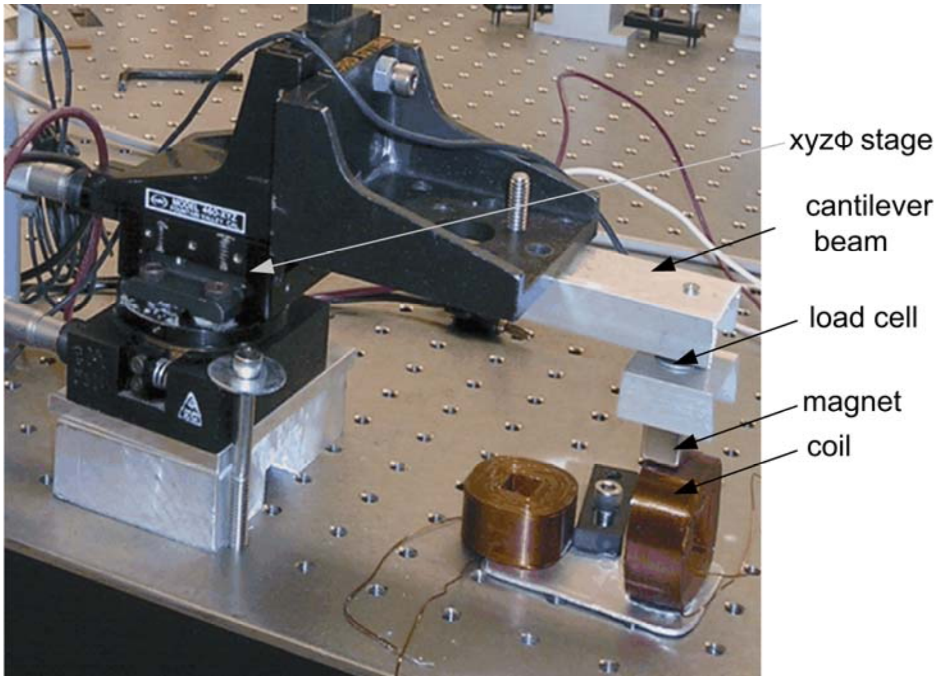

Fig. 5-9. Experimental setup to verify the analytical forces experimentally.

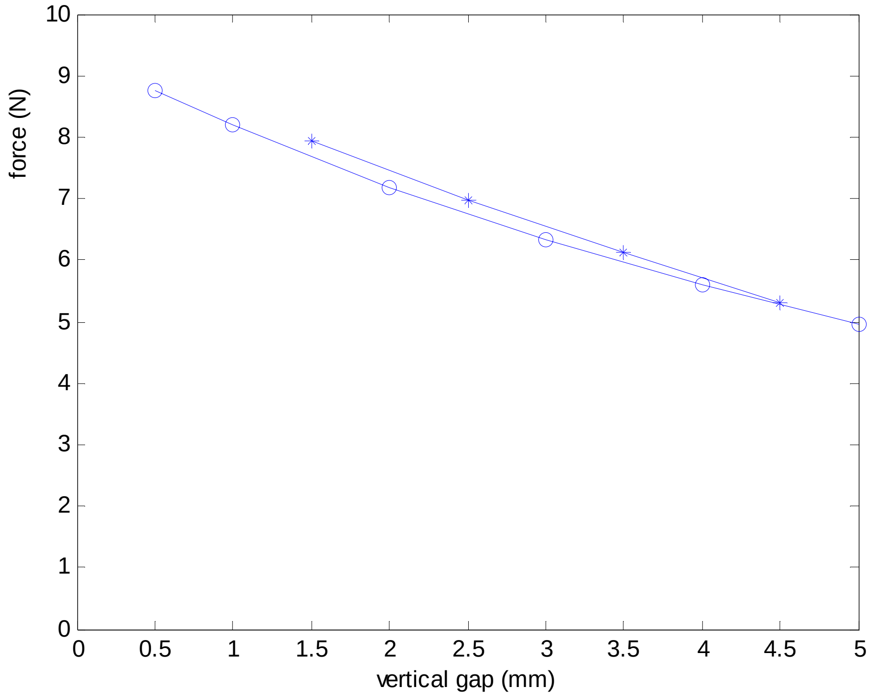

Fig. 5-10. Comparison of theoretical (*) and experimental (o) vertical forces at different heights.

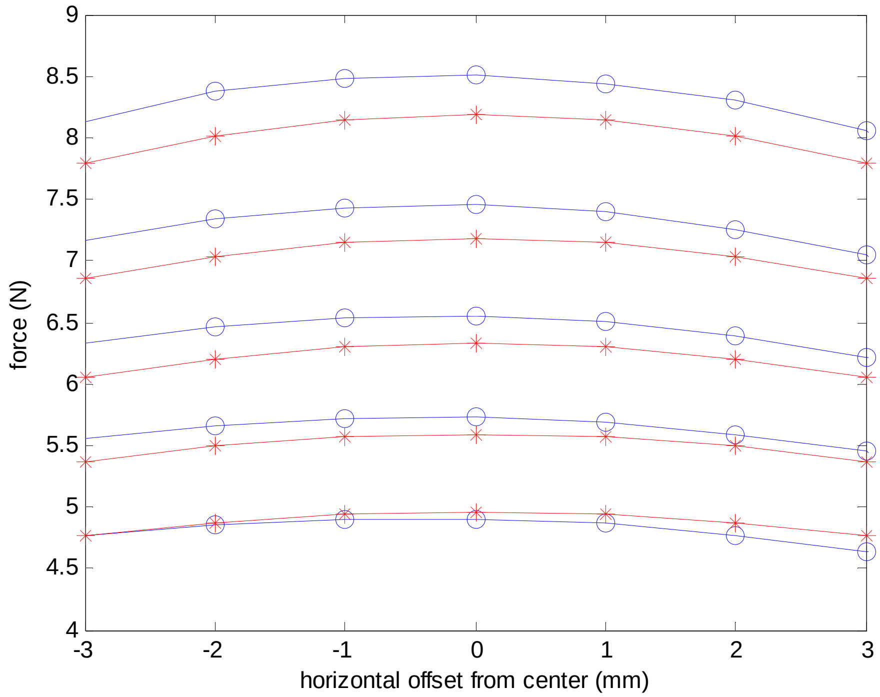

Fig. 5-11. Comparison of theoretical (*) and experimental (o) vertical forces at offset positions.

between the theoretical and experimental values is only about 4%. This error is within an acceptable limit considering the errors while reading the fluctuating voltage and other mechanical errors like backlash in the $xyz\phi$ stage, etc.

5.4 Horizontal Actuator

The horizontal force contributes towards the motion in the x-y plane. The force capacity of a horizontal actuator does not have to be as high as that of a vertical actuator. This is because there is no gravity or any other external force continuously acting on the moving part horizontally that is to be balanced. The force output in the horizontal direction is relatively low as compared to the vertical direction due to the large distance between the farther section of the coil and the magnet for the same-size coil. However, we were able to design the horizontal actuator keeping the horizontal acceleration of more than 20 m/s^2.

5.4.1 Actuator Sizing

Similar to the vertical coil we divide the horizontal coil in 4 sections as shown in Fig. 5-3. As shown in Fig. 5-2, the magnetic field lines are vertically downwards in all the sections of the horizontal coil. For the clockwise direction of current flow the directions of forces on each section come out to be perpendicular to the direction of current outwards from the center of the coil. Sections 2 and 4 are at symmetrical positions from the magnet. Thus the forces on the two sections will be equal and opposite i.e. they cancel each other. To find the horizontal force we calculate the forces F_{h1} and F_{h3} using (5.4–5.5) with parameters gap, a, b, d, r_1 and r_2 shown in Fig. 5-12.

$$
\begin{aligned}
F_{h1} = {} & \frac{J\sigma_m}{4\pi}\left[\int_{-d/2}^{d/2}\int_{-d/2}^{d/2}\int_{0}^{h}\int_{[gap+d/2]}^{[gap+b-a+d/2]}\int_{-[-x+gap+b+d/2]}^{[-x+gap+b+d/2]}\frac{(z-r_1)}{[(x-p)^2+(y-q)^2+(z-r_1)^2]^{1.5}}\,dydxdzdpdq\right] \\
& -\frac{J\sigma_m}{4\pi}\left[\int_{-d/2}^{d/2}\int_{-d/2}^{d/2}\int_{0}^{h}\int_{[gap+d/2]}^{[gap+b-a+d/2]}\int_{-[-x+gap+b+d/2]}^{[-x+gap+b+d/2]}\frac{(z-r_2)}{[(x-p)^2+(y-q)^2+(z-r_2)^2]^{1.5}}\,dydxdzdpdq\right]
\end{aligned}
\tag{5.5}
$$

$$
\begin{aligned}
F_{h3} = {} & \frac{J\sigma_m}{4\pi}\left[\int_{-d/2}^{d/2}\int_{-d/2}^{d/2}\int_{0}^{h}\int_{[gap+b+a+d/2]}^{[gap+2b+d/2]}\int_{-[x-gap-b-d/2]}^{[x-gap-b-d/2]}\frac{(z-r_1)}{[(x-p)^2+(y-q)^2+(z-r_1)^2]^{1.5}}\,dydxdzdpdq\right] \\
& -\frac{J\sigma_m}{4\pi}\left[\int_{-d/2}^{d/2}\int_{-d/2}^{d/2}\int_{0}^{h}\int_{[gap+b+a+d/2]}^{[gap+2b+d/2]}\int_{-[x-gap-b-d/2]}^{[x-gap-b-d/2]}\frac{(z-r_2)}{[(x-p)^2+(y-q)^2+(z-r_2)^2]^{1.5}}\,dydxdzdpdq\right]
\end{aligned}
\tag{5.6}
$$

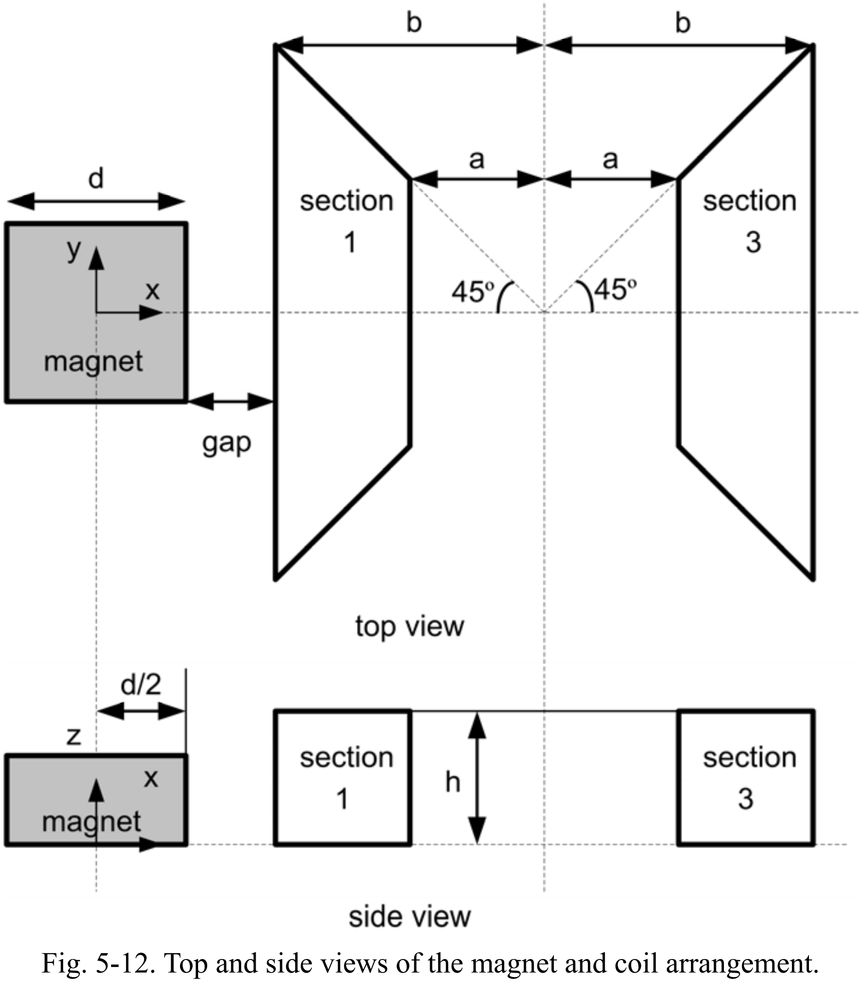

Fig. 5-12. Top and side views of the magnet and coil arrangement.

The actual force on the magnet is the difference of F_{h1} and F_{h3} (F_{h2} and F_{h4} cancel). The coil sizing was performed by several iteration using (5.5–5.6). Along with the maximum force on the magnet, keeping the magnet at the symmetric position, minimization of the corner effect and its packaging with other parts were the other issues affecting the dimensions of the coil. The optimal inner dimension of the horizontal coil was estimated as 20 × 20 mm and the optimal outer dimension as 40 × 40 mm. Each horizontal coil has 619 turns with the resistance of 5.9 Ω. To keep its similarity with vertical coils the horizontal coils were wound with heavy-built AWG #24 copper magnet wire that had a layer of heat-bondable epoxy coating on it. The maximum horizontal force varies from 4.5 N to 2 N for the gap of from 0 to 5 mm between the coil and the magnet.

5.4.2 Performance Analysis at Offset Positions

The calculation of force in the previous section had the assumption that the coil moves only along the x-axis. We estimated the force capability of the actuator when the magnet moves in the travel range at the gap of 0 to 6.3 mm and ±2.5 mm away from the x-axis. The 3-D plot in Fig. 5-13 shows the calculated force at the various offset positions in the travel volume of the stage using (5.7–5.8).

$$F_{h1} = \frac{J\sigma_m}{4\pi}\left[\int_{-d/2+0.001i}^{d/2+0.001i}\int_{-d/2}^{d/2}\int_{0}^{h}\int_{[gap+d/2]}^{[gap+b-a+d/2]}\int_{-[-x+gap+b+d/2]}^{[-x+gap+b+d/2]}\frac{(z-r_1)}{[(x-p)^2+(y-q)^2+(z-r_1)^2]^{1.5}}dydxdzdpdq\right]$$
$$-\frac{J\sigma_m}{4\pi}\left[\int_{-d/2+0.001i}^{d/2+0.001i}\int_{-d/2}^{d/2}\int_{0}^{h}\int_{[gap+d/2]}^{[gap+b-a+d/2]}\int_{-[-x+gap+b+d/2]}^{[-x+gap+b+d/2]}\frac{(z-r_2)}{[(x-p)^2+(y-q)^2+(z-r_2)^2]^{1.5}}dydxdzdpdq\right]$$

(5.7)

$$F_{h3} = \frac{J\sigma_m}{4\pi}\left[\int_{-d/2+0.001i}^{d/2+0.001i}\int_{-d/2}^{d/2}\int_{0}^{h}\int_{[gap+b+a+d/2]}^{[gap+2b+d/2]}\int_{-[x-gap-b-d/2]}^{[x-gap-b-d/2]}\frac{(z-r_1)}{[(x-p)^2+(y-q)^2+(z-r_1)^2]^{1.5}}dydxdzdpdq\right]$$
$$-\frac{J\sigma_m}{4\pi}\left[\int_{-d/2+0.001i}^{d/2+0.001i}\int_{-d/2}^{d/2}\int_{0}^{h}\int_{[gap+b+a+d/2]}^{[gap+2b+d/2]}\int_{-[x-gap-b-d/2]}^{[x-gap-b-d/2]}\frac{(z-r_2)}{[(x-p)^2+(y-q)^2+(z-r_2)^2]^{1.5}}dydxdzdpdq\right] \tag{5.8}$$

The motion of the magnet parallel to the closest face of coil does not affect the force capability much but the magnitude of force drops quickly as the magnet moves away from the coil. The force reduces to almost half when coil is moved from gap of 0.3 mm to 4 mm.

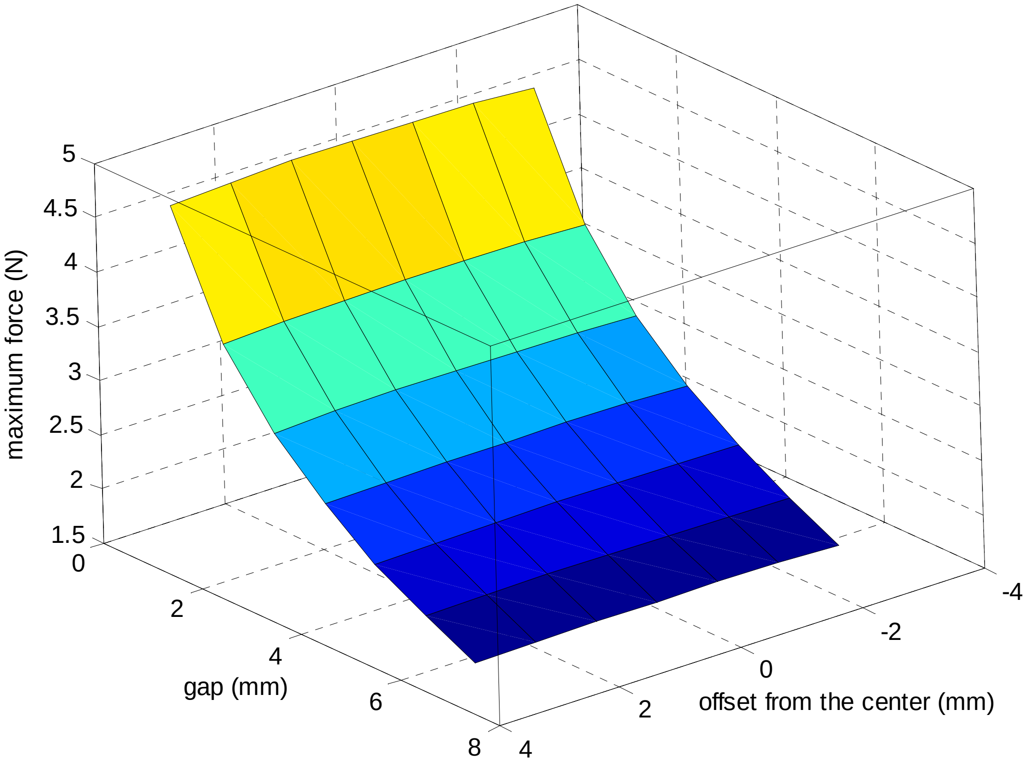

Fig. 5-13. Horizontal force at offset positions.

5.4.3 Experimental Verification

To verify the calculated force we performed experiments to measure the horizontal force between coil and magnet. The experimental setup shown Fig. 5-9 was used for these experiments. Fig. 5-14 shows the values of the horizontal forces that we achieved from the experiments (o) and its comparison with theoretical values (*) calculated in the previous sections. This comparison shows that the maximum error between the theoretical and experimental values is up to 25% where the gap between coil and magnet is small. The error at the nominal gap of 3.1 mm is 12%. It is difficult to determine the gap and parallelism between the magnet and the uneven surface of coils precisely, and the horizontal force changes very quickly as the gap

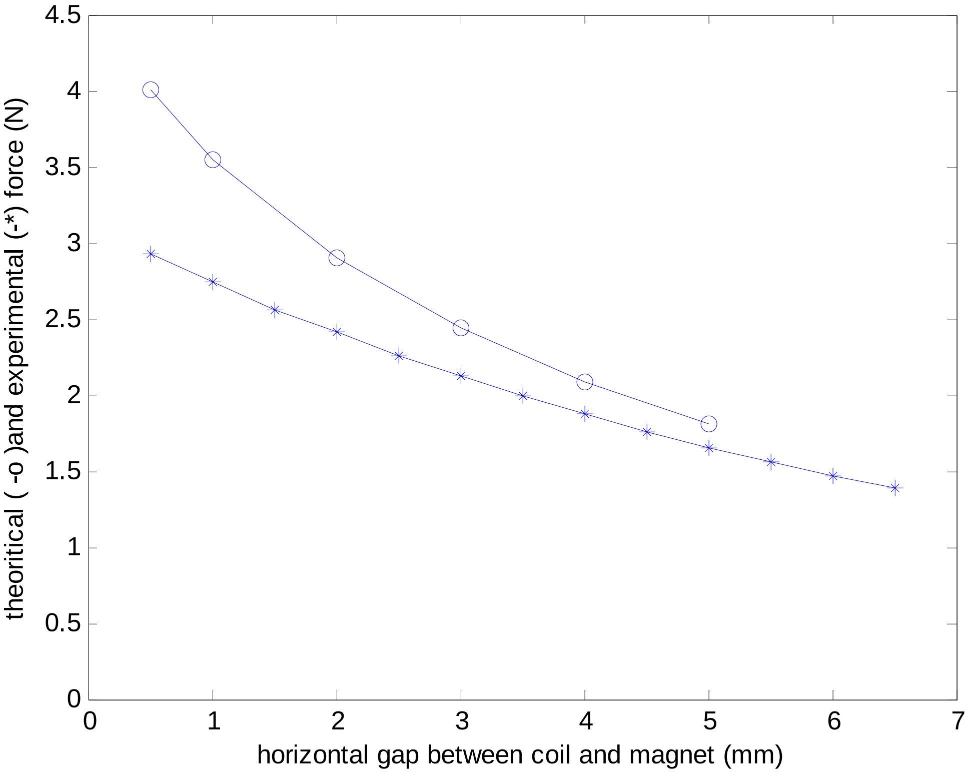

Fig. 5-14. Comparison of experimental and theoretical horizontal forces.

changes so this may give a significant error in the experimental values. Thus for modeling purpose we decided to use the theoretical values of force.

In this chapter the design of the vertical and horizontal actuators was described. An extensive analysis of the actuator performance over the whole travel range was performed and compared with the experimental forces. The comparison of the forces shows that the calculations provide a fair estimation of the forces from horizontal and vertical actuators.

CHAPTER VI

MECHANICAL DESIGN OF SECOND-GENERATION MAGLEV STAGE

In the previous chapter we discussed the design and analysis of the actuator unit that is used for the second-generation maglev stage. This chapter describes the mechanical design of various parts, their analysis and assembly. In terms of mechanical design and fabrication this stage is much simpler than the first-generation stage. The fabrication of all the parts and assembly fixtures, and precision assembly were performed by me in the mechanical engineering machine shop.

6.1 Assembly Structure

The exploded view of the second-generation maglev stage is shown in Fig. 6-1. The Y-shaped part in the center is the only moving part of the stage, namely platen. The platen consists of 3 magnets, 3 mirrors, and the core of the platen. The platen is removed from its normal operation height so that the parts below the platen are visible.

All the stationary parts are mounted on an aluminum base plate. The three cylindrical pieces placed in the center are capacitance probes. These capacitance sensors are mounted right below the platen at 120°-apart symmetrical positions and measure the height of the platen at three different positions. The vertical-axis motions of the platen are sensed by triangulation of the data from these three capacitance sensors. The coils of vertical actuators are placed right next

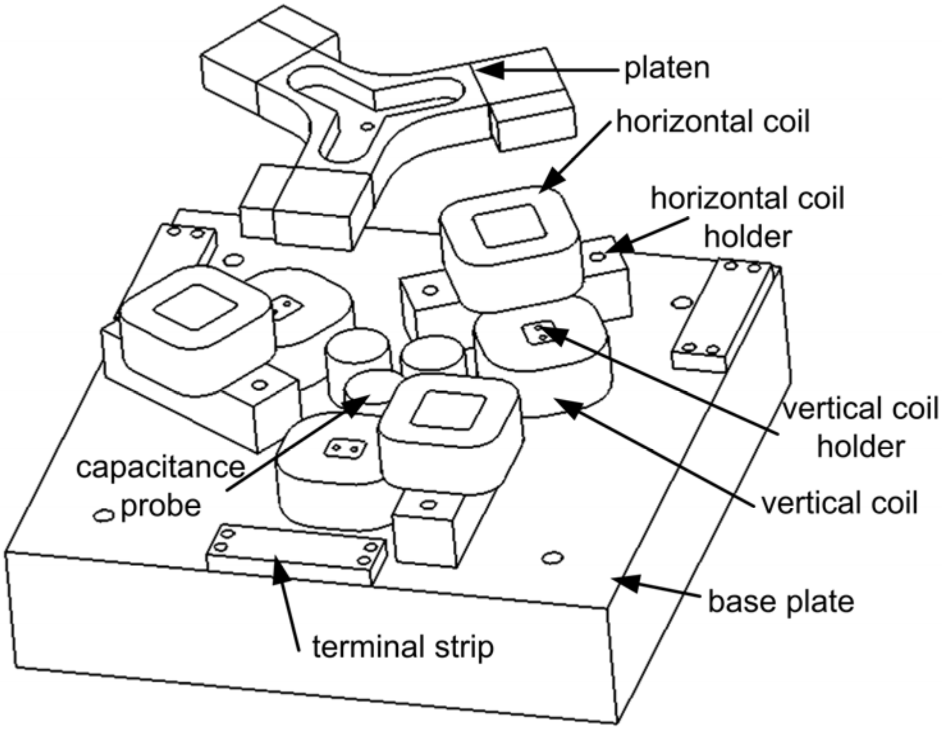

Fig. 6-1. Exploded view of second-generation maglev stage.

to the capacitance probes with vertical coil holders. Next to the vertical coils there are horizontal coils mounted using horizontal coil holders. At the edges of the base plate there are three terminal strips. Each of terminal strips has 4 contacts to make connections to one vertical and one horizontal coil.

An efficient packaging of all the parts is important for any assembly. Thus we designed all the parts and their assembly in Solidworks® in such a way that (1) the platen must be close enough to all the coils for sufficient force generation; (2) the bottom surface of the platen must be in the sensing range of all the capacitance probes; and (3) the lasers beams from the interferometers should not be blocked.

6.2 Platen Design

Since the platen is the only moving part in the whole maglev stage, the platen design is very crucial with the following considerations. The vertical actuators must continuously apply vertical force against gravity to balance the platen's weight at levitated height. To maintain the currents in the actuators low the platen should be light. The moving structure should be stiff and possess a high natural frequency. These issues were kept in in the design process of the platen.

6.2.1 Platen Core

The platen core was machined from single-piece aircraft-grade 7075 aluminum. It was pocket-milled in the center leaving the ribs on the edge for reduction of weight while keeping the high stiffness and natural frequency. The shape of the pocket was decided to make its fabrication easy. The width of the pocket is 15.875 mm that can be machined with a single pass of 5/8 inch diameter end-milling tool. Several designs of the platen core with different pocket depths were made and analyzed for the mass and natural frequency. Then, the depth of the pocket was finalized to be 7.62 mm. The three ends of the Y-shaped platen core have width of 25.4 mm and height of 12.7 mm to match the side dimension of the magnet. A small hole was drilled and tapped in the center of platen to tighten a screw to hold the grounding wire. The bottom surface of the platen was ground to achieve a surface roughness of 2.54 μm, as this surface would be used as the target by the capacitance gap sensors.

6.2.2 Assembly of Platen

The assembly process of the platen is shown in Fig. 6-2. The 3 cuboid shaped (25.4 × 25.4 × 12.7 mm) permanent magnets are attached around the platen core and then 3 mirrors attached at one of the side faces of the magnets. The 25.4 mm square faces on the top and bottom are the N and S poles of the magnets. The face of the mirror away from the magnet is the reflecting surface.

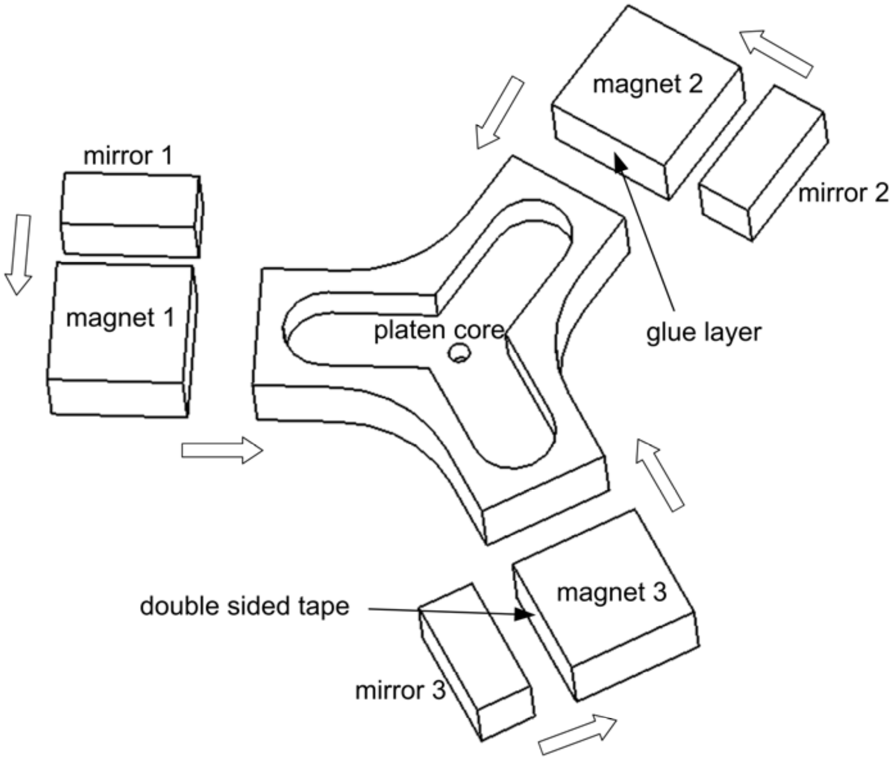

Fig. 6-2. Assembly of the platen showing the various parts.

The fixture shown in Fig. 6-3 was fabricated and used for precision in the gluing process. Several coatings of Stoner dry-film mold release were applied on the fixture so that the magnet or the platen core does not get glued to the fixture. The magnet face to be glued and the end of platen core were cleaned with MEK to remove oil and dirt and roughened using sandpaper. A thin layer of PC-7 epoxy was applied on both the surfaces and magnet is placed in the fixture. The platen core is inserted from side and squeezed. Then the fixture top is clamped with 4 screws. This assembly is kept for 24 hours to provide sufficient time to epoxy to cure. Then the clamping screws were removed and the assembly was carefully taken off the fixture. Then extra glue on the glue line was scratched and cleaned. Then the same procedure was repeated for two remaining ends.

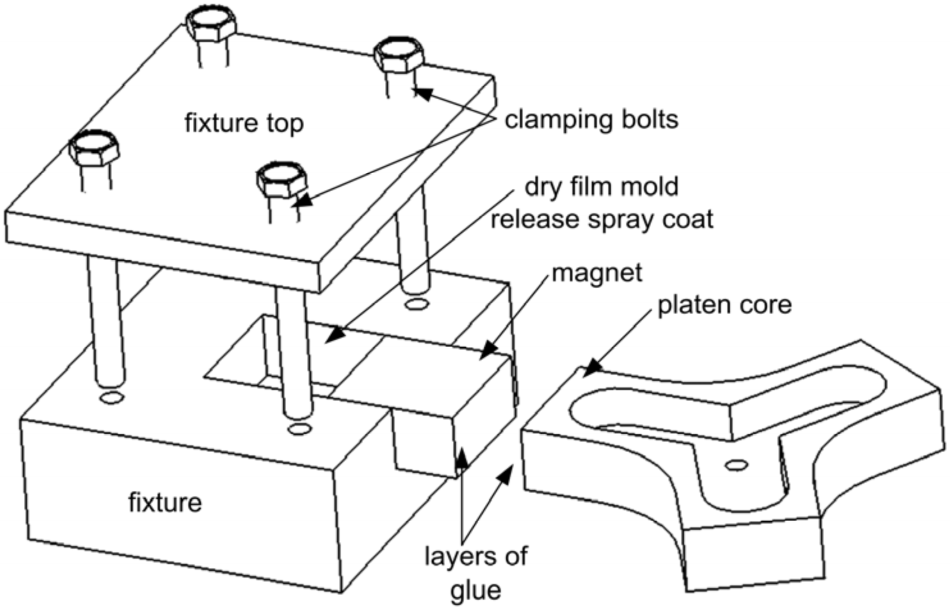

Fig. 6-3. Gluing process of the magnet with platen core.

6.2.3 Finite-Element Analysis of Platen

As mentioned in the beginning of this section that the natural frequency of the moving platen is a critical issue. The low natural frequency of the platen can cause resonance and instability when the control bandwidth is high. Therefore the natural frequency of the system should be analyzed before its fabrication and be kept as high as possible throughout the design phase.

We carried out an extensive finite-element analysis on the Solidworks® model of the system. The mechanical properties of all the parts like elastic modulus, Poisson's ratio, shear modulus, mass density, and tensile stress were assigned. We used Cosmosworks® for finite element analysis using solid mesh. Various restraints were applied on the model. Since the moving part is levitated and has no mechanical contact with the stationary parts we performed frequency analysis with soft support. In this analysis the part is assumed to be placed on a spring with a very low stiffness. The deformation pattern in first three modes is shown in Fig. 6-4. The natural frequency for first mode came out to be 6917 Hz and for second and third mode frequencies were 6923 Hz and 6946 Hz.

We also performed finite-element analysis for using fixed supports to find out any lower natural frequencies of the platen. The results of analysis with one support at the plane of magnet surface are shown in Fig. 6-5. The calculated natural frequencies turned out to be lower than the previous analysis. The first three modes of have frequencies of 619 Hz, 713 Hz, and 1331 Hz. The analysis with fixed support at the surfaces of two magnets is shown in Fig. 6-6. This analysis resulted natural frequencies of 642 Hz, 2572 Hz, and 3102 Hz as the first three modes. Then we performed analysis with fixed supports at the three magnets symmetrically and deformation pattern is shown in Fig. 6-7. The first three modes natural frequencies came out to be 6121 Hz, 10827 Hz, and 10842 Hz.

Thus from this we know that the lowest possible natural frequency of the platen is no less than 600 Hz. This natural frequency is high enough for our control applications with no requirement to introduce any higher structural modes to the dynamic model.

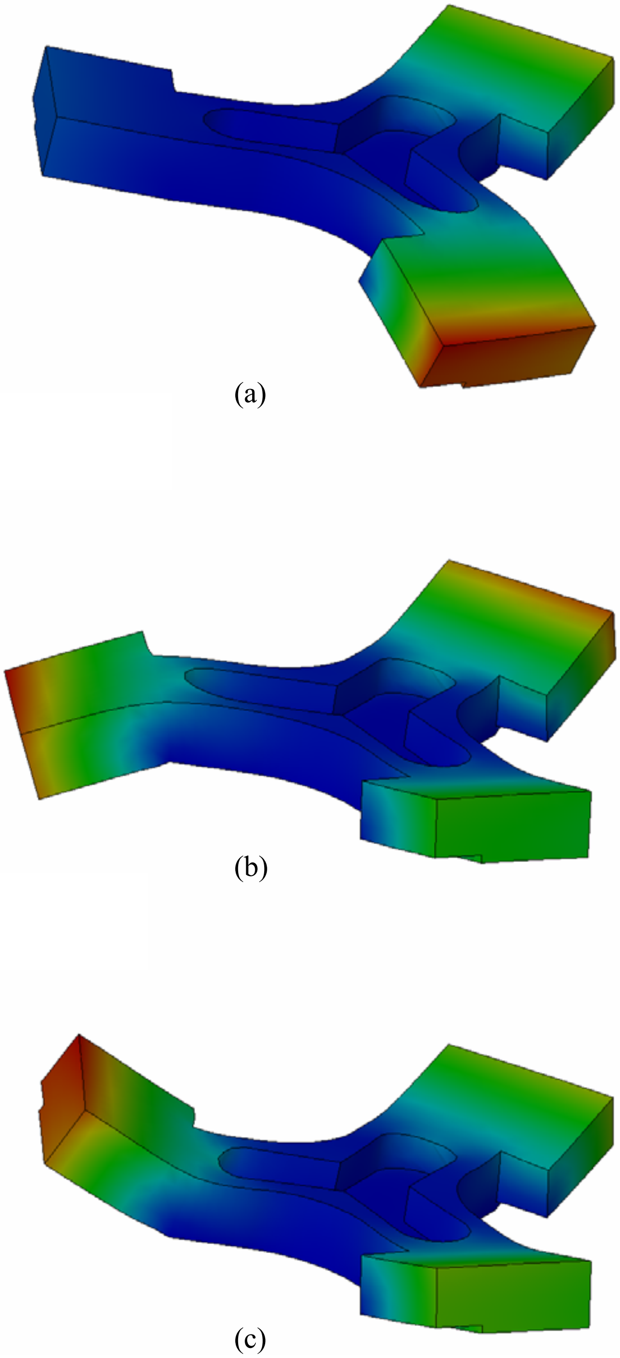
(a)

(b)

(c)

Fig. 6-4. Soft-support analysis of the platen (a) first (b) second (c) third modes of deformation.

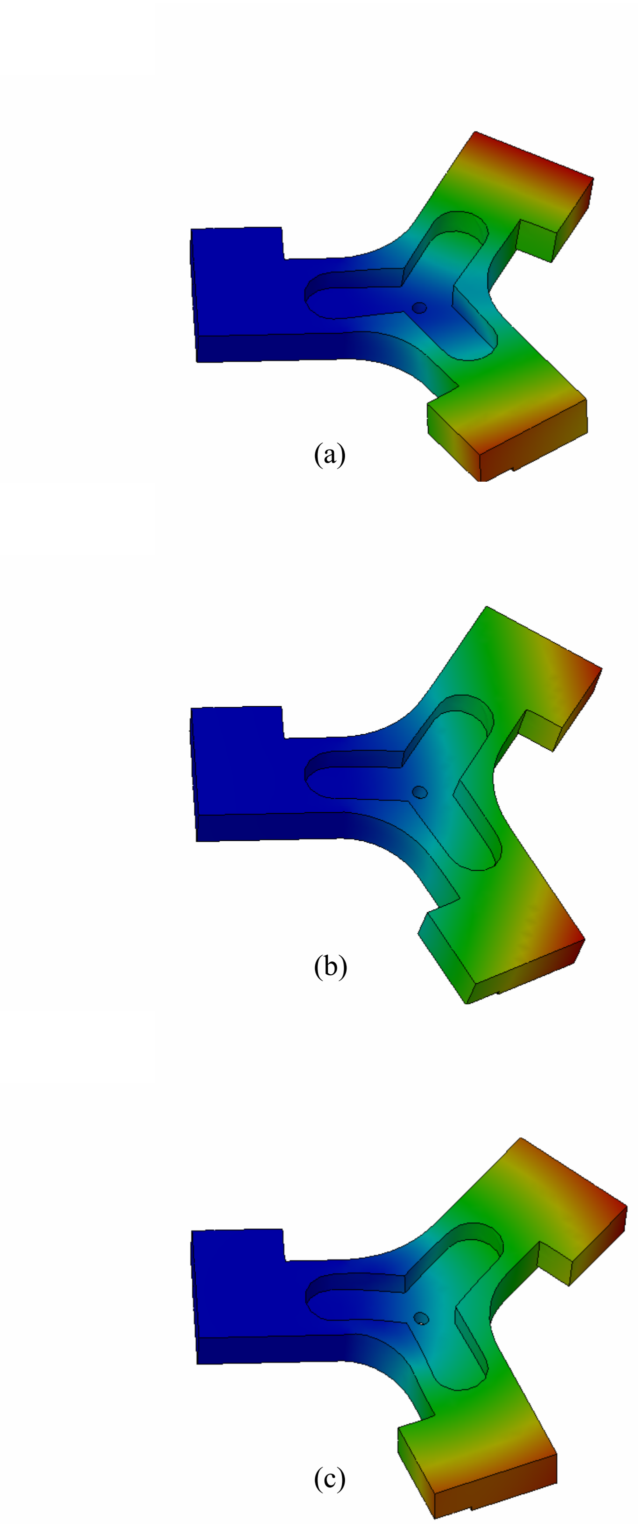
(a)
(b)
(c)

Fig. 6-5. Fixed-support analysis with one end of the platen fixed (a) first (b) second (c) third modes of deformation.

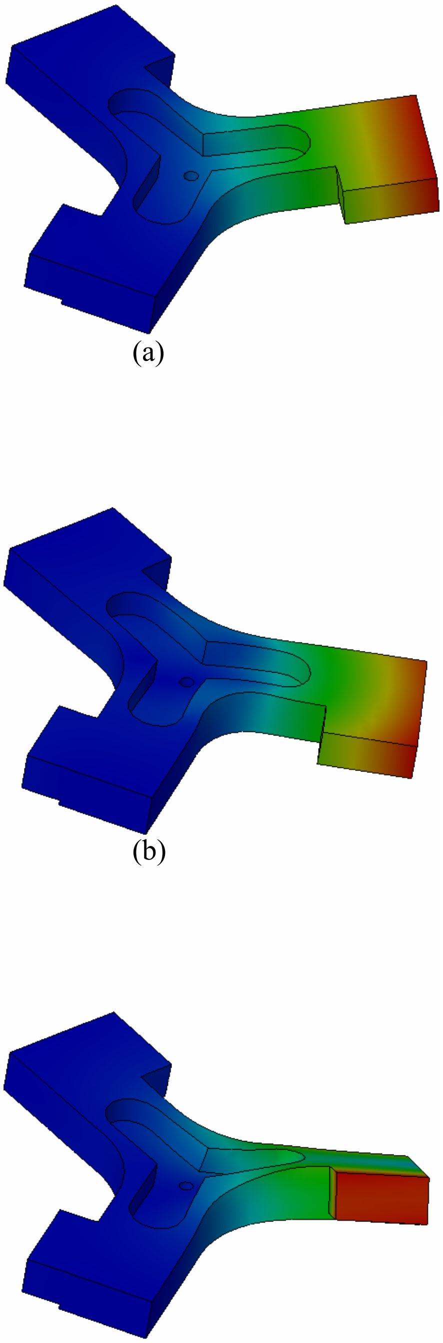

(a)

(b)

(c)

Fig. 6-6. Fixed-support analysis with two ends of the platen fixed (a) first (b) second (c) third modes of deformation.

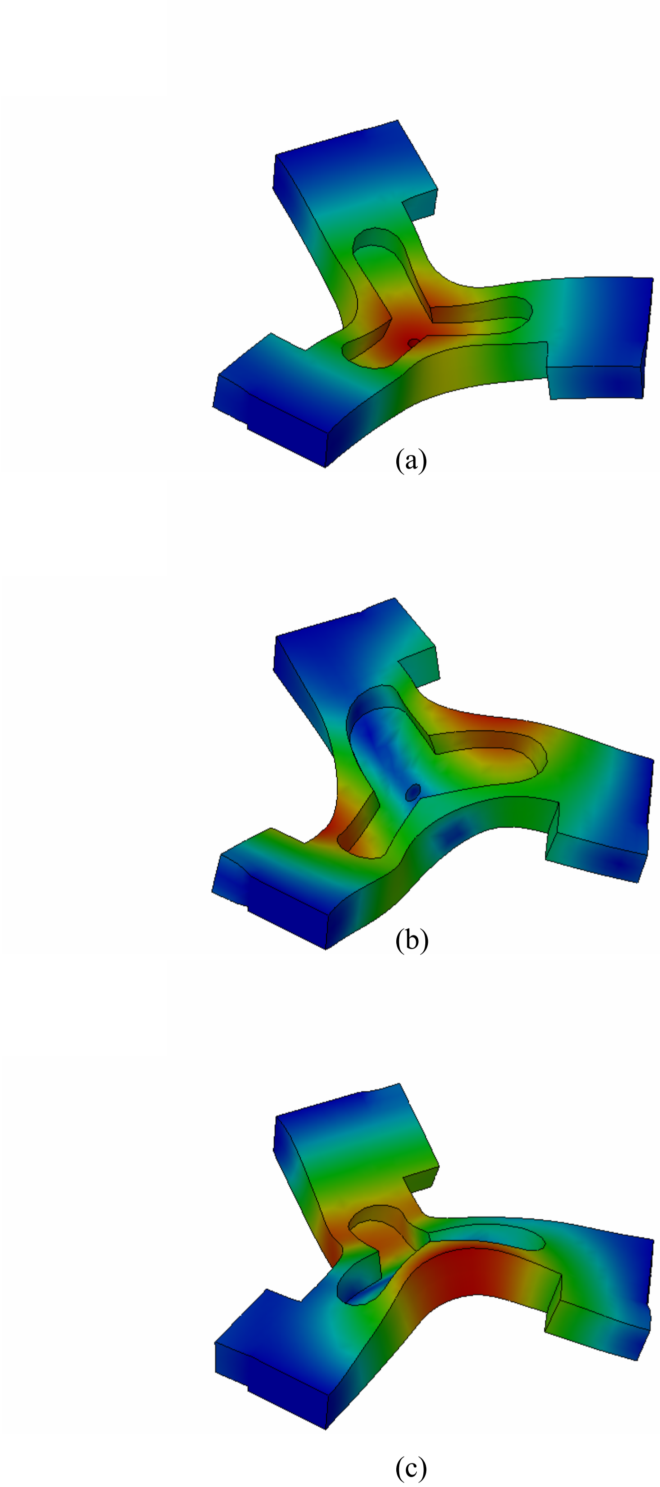

(a)

(b)

(c)

Fig. 6-7. Fixed-support analysis with all the three ends of the platen fixed (a) first (b) second (c) third modes of deformation.

6.3 Coil Mounting

The coils need to be attached to the base plate at very precise location and orientation. Also the surface of the coils should perfectly match with the plane of base plate. Therefore we designed and fabricated coil holders for both vertical and horizontal coils and glued them together using assembly fixtures.

6.3.1 Vertical Coil Assembly

Attaching the vertical coil to the base plate was somewhat difficult because this coil could not be held from outside and no part of coil holder can come out of coil because of the tight packaging. Thus we designed the coil holder as an insert in the coil and glued it inside the coil. An exploded view of vertical coil assembly is shown in Fig. 6-8 (a). The coil holder was fabricated to perfectly fit to the inner surface of coil leaving space for glue. It has 2 holes for 2-56 screws so that the coil can be placed at perfect position and orientation. To glue the coil holder precisely to the coil we designed an assembly fixture as shown in Fig. 6-9. The inner surface of coil and outer surface of coil holder were applied PC-7 epoxy. The reference plate and clamping pate were applied with dry-film mold release thoroughly. The coil holder was mounted on the reference plate using 2-56 screws and then coil was placed from the top. A clamping plate was used to press the coil from top that was held at position using 6-32 screws. This assembly was kept for 24 hours to cure the epoxy.

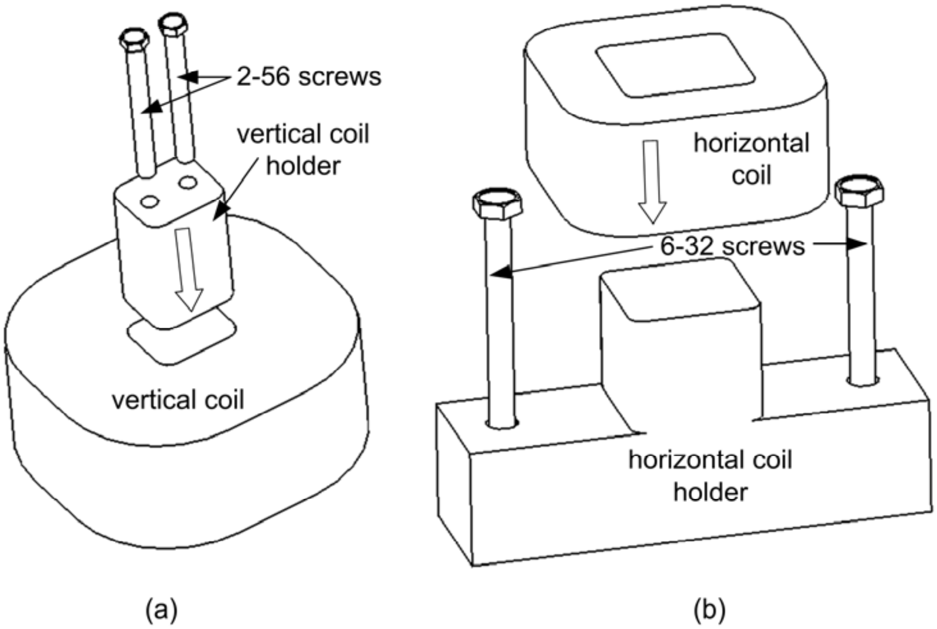

Fig. 6-8. Exploded view of (a) vertical coil and (b) horizontal coil assembly.

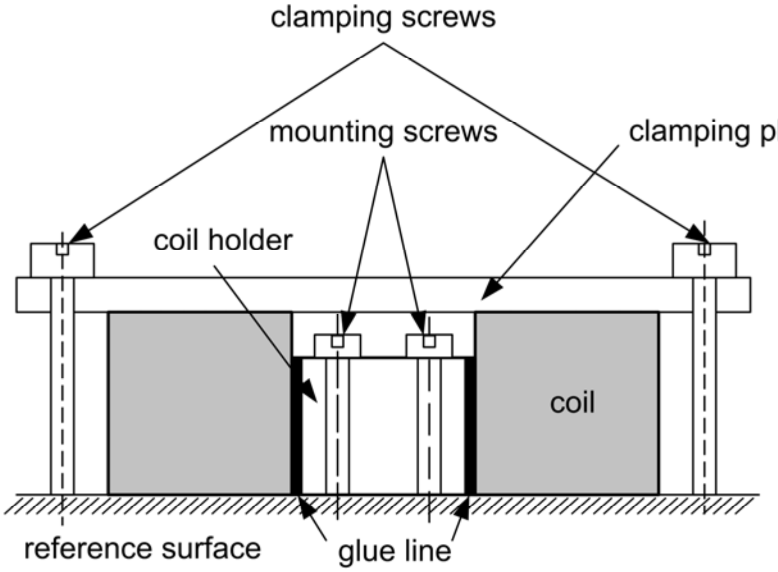

Fig. 6-9. Fixture for gluing vertical coil with coil holder.

6.3.2 Horizontal Coil Assembly

The horizontal coil needed to be placed so that it could come at the same horizontal level as the platen. A coil holder of inverted T shaped was designed and fabricated that could hold the horizontal coil from inside and support it from the bottom. An exploded view of the assembly is shown in Fig. 6-8 (b). We used two 6-32 screws to mount this assembly on the base plate. A fixture was used that was similar to the one used for the vertical coil assembly. The assembly procedure is shown in Fig. 6-10. The assembly process was also similar to the vertical coil assembly process. The coil and coil holder were applied with glue and the clamping plate with dry-film mold release. Then coil holder was mounted on reference plate and the clamping plate was fastened after placing the coil.

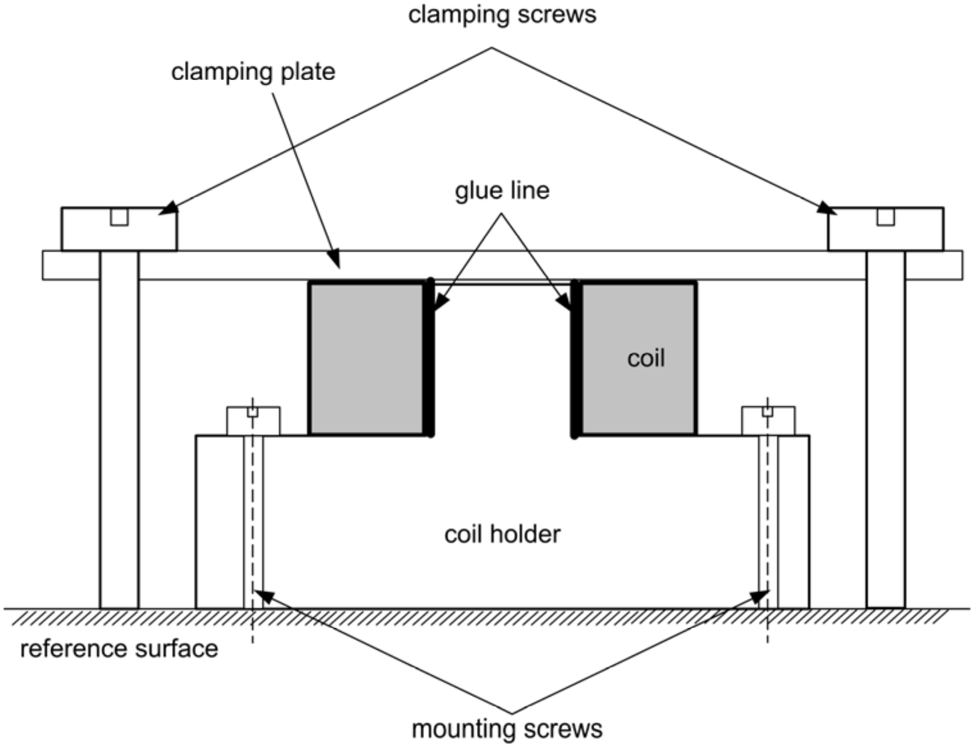

Fig. 6-10. Fixture for gluing horizontal coil with coil holder.

6.4 Base Plate

Fig. 6-11 shows the base plate that holds all the coil assemblies, capacitances probes, and terminal strips. The dimensions of the base plate are 200 × 200 × 44 mm. The dimension of 200 × 200 mm was decided to hold all the parts. The height of 44 mm was designed so that the laser beam coming from laser interferometers should fall on mirrors mounted on the platen. It was fabricated solid aluminum to keep its thermal capacity high.

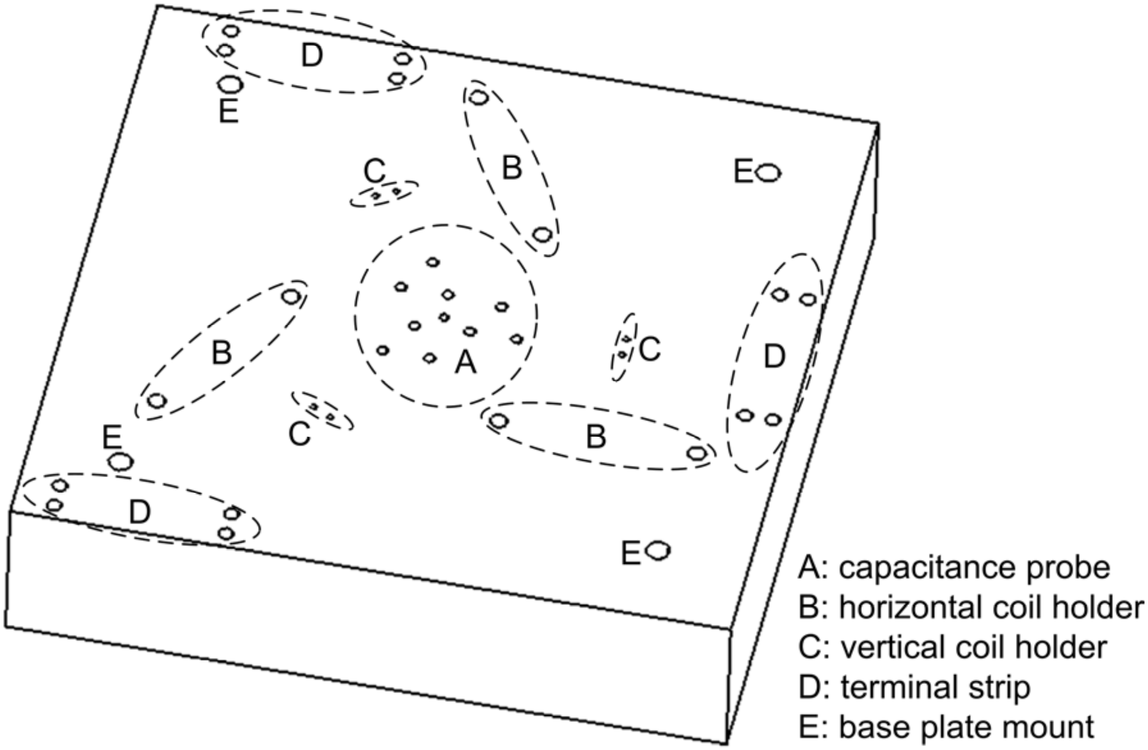

Fig. 6-11. Base plate.

As shown in Fig. 6-11, it has various holes. The set A in the center has 3 mm diameter though holes to mount capacitance probes with M3 screws. These holes are countersunk from the bottom to shorten the height of screws and take care of height of the screw heads. The set B is of 25 mm deep blind holes with 6-32 threads. These holes are used to mount horizontal coil holders. The set C is of 2-56 threaded blind holes to hold vertical coil assemblies that are 15 mm deep. The set D is used to attach electrical terminal strips and it has 10 mm deep blind holes of 6-32 thread. The set E is of 6.35 mm through holes with countersink from the top. These holes are used to mount the base plate on the optical table. Refer to Appendix C for the exact locations of these holes.

Since the reaction forces by actuators would apply on the base plate as well, we carried out finite-element analysis of it. Due to the many holes on the base plate Cosmosworks® could not mesh the actual base plate. Therefore we designed another plate of same dimensions with just 4 mounting holes for analysis purpose. The cylindrical surface of the mounting hole was fixed as constraint. Then finite element analysis was carried out using solid mesh. The first three modes of deformation are shown in Fig. 6-12. The natural frequencies of these modes came out to be 2965 Hz, 3010 Hz and 3023 Hz. These frequencies are high enough for our applications. We assume that the effect of the small holes eliminated during the analysis will not reduce the natural frequency significantly.

There is continuous current flow in the coils that generates heat. This heat is either radiated or transferred to base plate by conduction. Since we are working on nanoscale positioning the thermal expansion of the base plate may be a serious source of error. To estimate the temperature distribution and thermal expansion, we carried out a thermal analysis of the base plate. Each coil was assumed to be an area heat source of 135 mW and placed at the center of the coil. The bottom surface of the base plate was assumed to be a heat sink and at a constant temperature because this surface is in contact with a 5×6×1-foot optical table whose top surface is made of nonmagnetic steel, that is good thermal conductor. Fig. 6-13 shows the pattern of

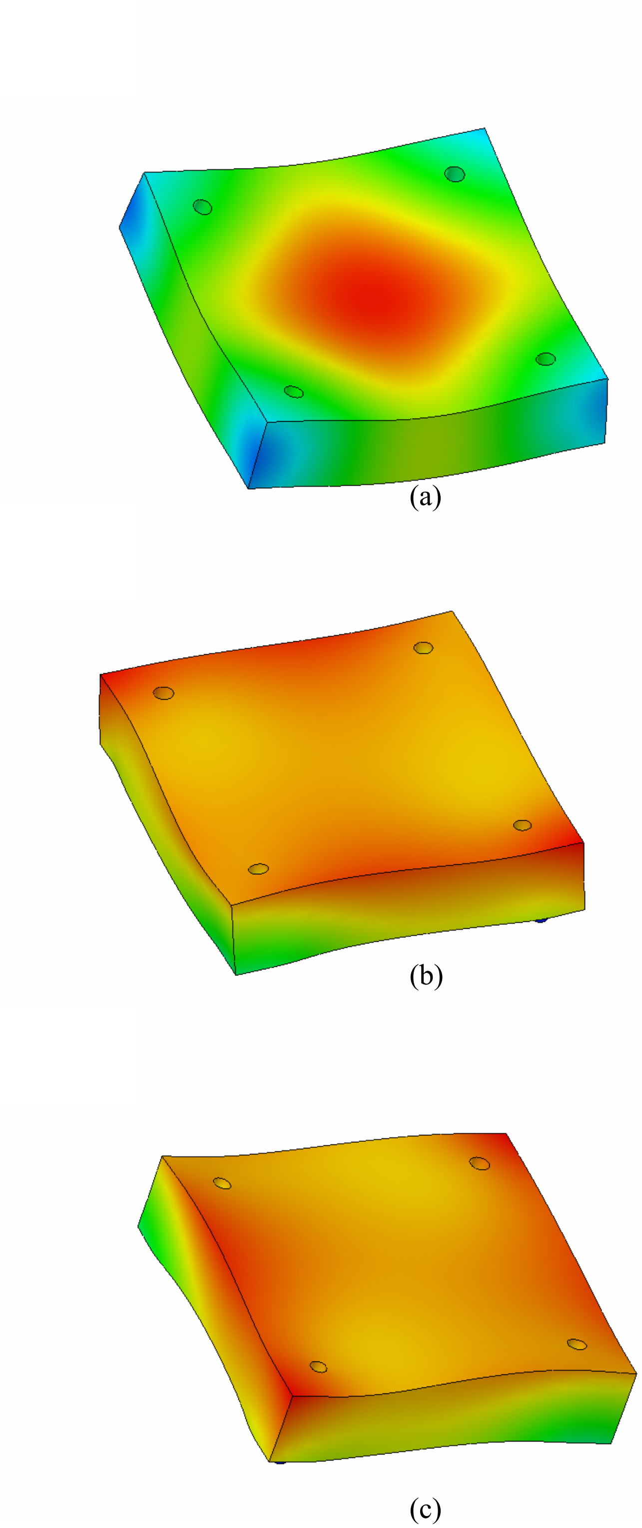

(a)

(b)

(c)

Fig. 6-12. Finite element analysis of base plate with fixed support (a) first (b) second (c) third modes of deformation.

temperature on the base plate. The scale shows that the steady state maximum temperature deviation on the platen will be 0.2 °C higher than the ambient temperature and the area of the high temperature is very small. We did not consider the heat loss due to radiation therefore this is a conservative estimate. The actual temperature will be lower than the value calculated here. Thus we assume that the thermal expansion on the base plate is negligible due to high volume and heat capacity of the base plate.

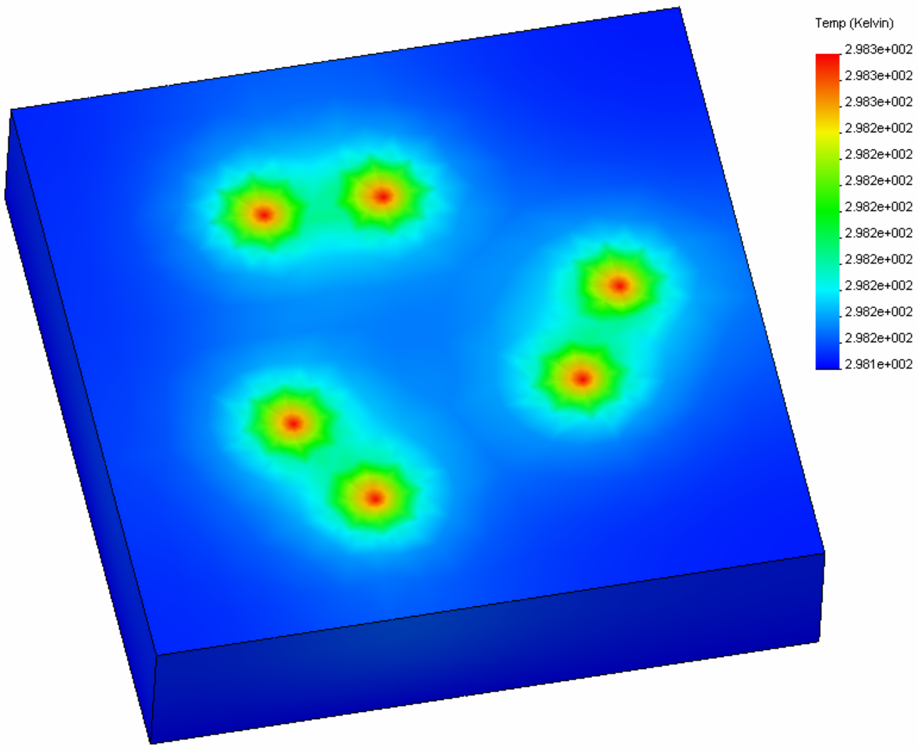

Fig. 6-13. Thermal analysis of platen.

CHAPTER VII

DYNAMIC MODELING AND CONTROL OF SECOND STAGE

Since the magnetic-levitation stage is open-loop unstable, it needs a stabilizing closed-loop control system to levitate the platen. In this chapter we discuss the dynamic modeling of the maglev stage including the modal force transformation and, modal displacement and velocity transformations. The dynamic model was used to design and implement the control system. Several experiments were carried out to test the performance of the stage and presented in this chapter.

7.1 Dynamic Modeling

7.1.1 Mass and Inertia Tensor

The platen model developed in Solidworks® was used to determine the mass, moment of inertia and location of the platen CM. The material properties of various parts of the platen were applied on the model and FE (finite element) analysis was carried out. The platen mass was found out to be 0.267 kg by Solidworks®. This value was verified with the actual platen mass measured by a precision balance. Therefore the gravitational force on the platen is 2.62 N. The force capability of the actuators calculated in Chapter 5 is around 27 N from 3 actuators i.e. a maximum acceleration of 9 g can be given to the platen.

The six forces applied on the platen are at different locations in different directions and to calculate effective acceleration in various axes we have to calculate the force and moments at center of mass of the platen. Thus we calculated the position of the platen CM using the

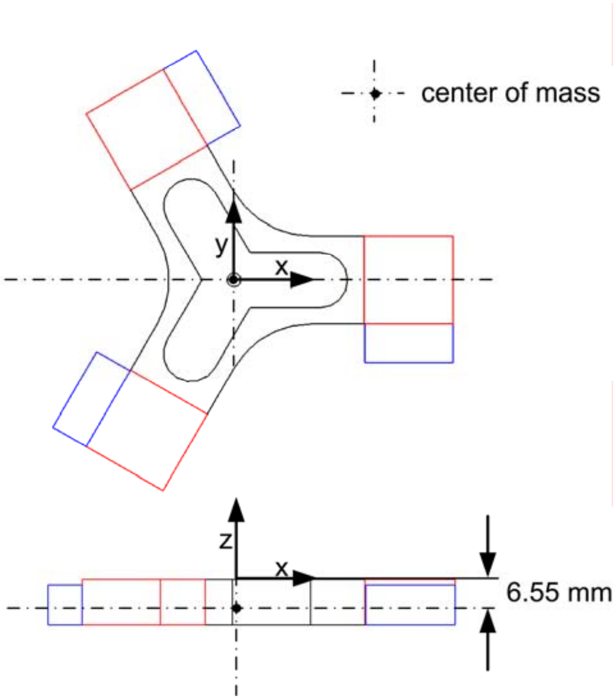

Fig. 7-1. Center of mass of the platen assembly.

Solidworks® model. Fig. 7-1 shows the location of the platen CM. Due to symmetry of the design and placement of all the parts, the CM is at platen's geometrical center in the horizontal plane. Since there is a pocket in the platen core the center of mass is slightly below the geometrical center in the vertical plane. It is at 6.55 mm below from the top surface of the platen. Thus the coordinates of the center of mass are [0, 0, –0.00655] in m.

The inertia tensor is calculated by Solidworks® as

$$\boldsymbol{I} = \begin{bmatrix} I_{xx} & -I_{xy} & -I_{xz} \\ -I_{yx} & I_{yy} & -I_{yz} \\ -I_{zx} & -I_{zy} & I_{zz} \end{bmatrix} = \begin{bmatrix} 340.37 & 0 & 0 \\ 0 & 340.37 & 0 \\ 0 & 0 & 653.61 \end{bmatrix} \times 10^{-6} \text{ kg-m}^2. \qquad (7.1)$$

All products of inertia are zero. Hence there is no dynamic coupling between the motions in all the three rotational axes. This is due to the innovative symmetrical design of the moving platen, facilitating the simplicity in modeling and control along with easy fabrication.

7.1.2 Plant Model

The maglev stage has just one moving part levitated by magnetic forces on the magnets attached to it. In the absence of any mechanical contact with the stationary parts we assume that spring and damping effects are negligible. Thus, we model this plant as a pure mass, and the equation of translational motion of the platen is

$$M\frac{d^2x}{dt^2} = f\ , \tag{7.2}$$

where M is the mass of the platen, i.e. 0.267 kg, and f is the corresponding modal force in the translational axis. Thus the transfer function of the platen for translation in x is

$$\frac{X(s)}{F_x(s)} = \frac{1}{0.267\ s^2}\ . \tag{7.3}$$

Similarly the equation of rotation about x is

$$I_{xx}\frac{d^2\psi}{dt^2} = \tau_\psi\ , \tag{7.4}$$

and the transfer function of the platen for rotation about the x-axis is

$$\frac{\Psi(s)}{\tau_{\psi}(s)} = \frac{1}{I_{xx}s^2}, \tag{7.5}$$

where I_{xx} is the principal moment of inertia about the x-axis. τ_{ψ} refers to the moment about that axis.

7.1.3 Modal Force Transformation

In Section 5.1 it was described how each actuator unit could generate force in two directions on each magnet. The direction of forces generated from each actuator unit is shown in Fig. 7-2(a). Each magnet is applied one force vertically upwards and one horizontal force towards the coil. Fig. 7-2(b) shows the direction of forces F_5 and F_6 to get an effective force in x axis. Similarly in Fig. 7-2(c) to get force in y-axis F_4 is applied in its negative direction and, F_5 and F_6 are applied in its positive direction. The x components of F_5 and F_6 cancel each other and a force in the y axis is generated. For rotation about z the three horizontal forces F_4, F_5 and F_6 are applied in their positive directions. In this way by combination of these three horizontal forces we achieve planar motion in the 3 horizontal axes. Similarly, for vertical motion, the three vertical forces F_1, F_2 and F_3 are used to get translation in z and rotation about x and y as shown in Fig. 7-2(e)–(g).

As shown in Fig. 7-2, we use a combination of 6 actuator forces to achieve forces and moments in all axes. We calculate the modal forces f_x, f_y, and f_z at the platen CM and modal moments τ_{ψ}, τ_{θ}, and τ_{ϕ} about the x-, y-, and z-axes using the following modal force transformation

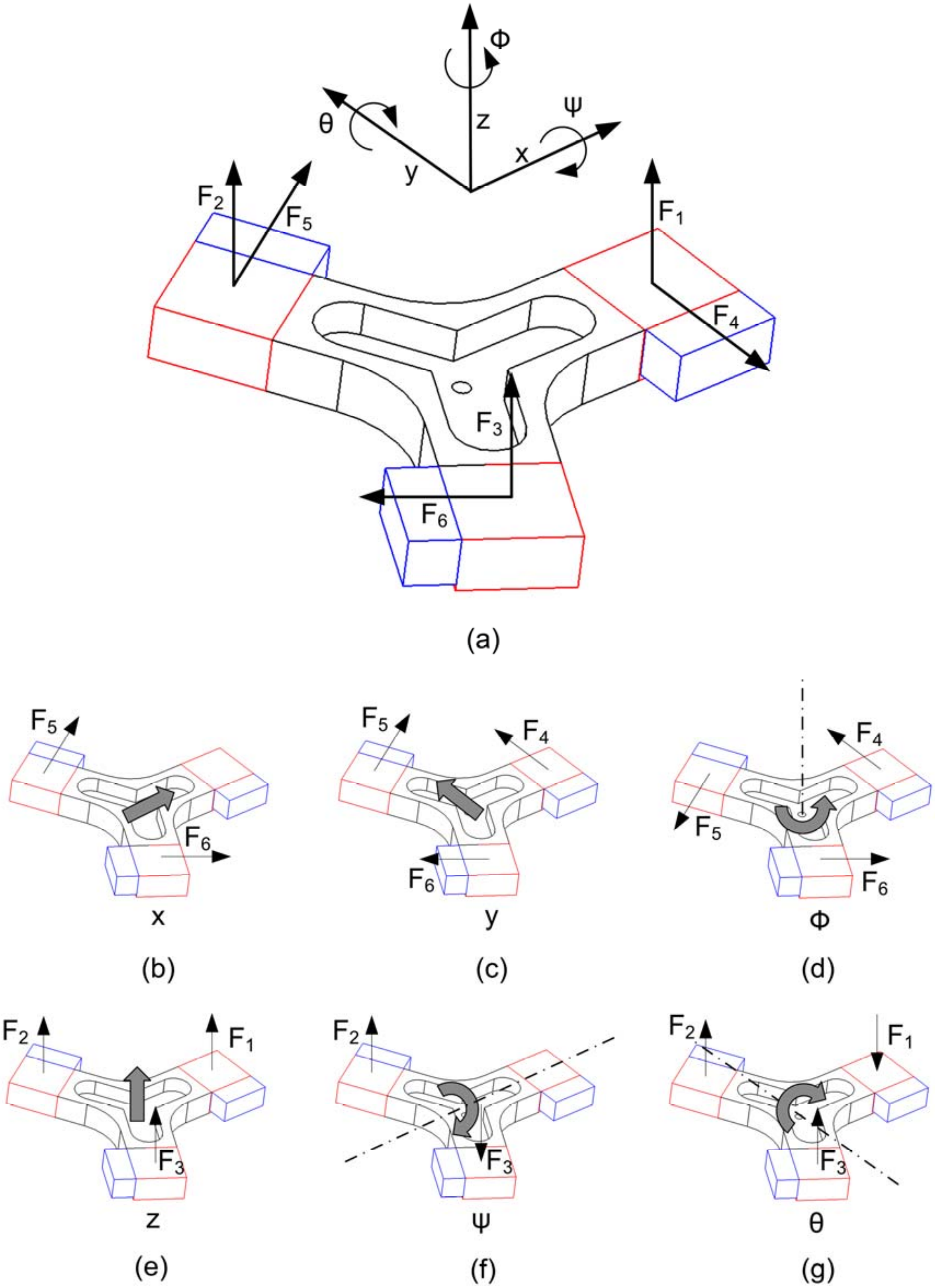

Fig. 7-2. Convention of coordinate axes and direction of forces.

$$\begin{bmatrix} f_x \\ f_y \\ \tau_\phi \\ f_z \\ \tau_\psi \\ \tau_\theta \end{bmatrix} = \begin{bmatrix} 0 & 0 & 0 & 0 & \cos 30^\circ & -\cos 30^\circ \\ 0 & 0 & 0 & -1 & \sin 30^\circ & \sin 30^\circ \\ 0 & 0 & 0 & -l_1 & -l_1 & -l_1 \\ 1 & 1 & 1 & 0 & 0 & 0 \\ 0 & l_3 & -l_3 & 0 & 0 & 0 \\ -l_1 & l_2 & l_2 & 0 & 0 & 0 \end{bmatrix} \begin{bmatrix} F_1 \\ F_2 \\ F_3 \\ F_4 \\ F_5 \\ F_6 \end{bmatrix}. \tag{7.6}$$

The definitions of various forces and distances are shown in Fig. 7-3. The lengths of physical dimensions are as follows:

l_1: distance between the center of all three magnets and the center of the platen = 0.050595 m;

l_2: distance between the center of magnet 2 or 3 and the center of the platen along the *x*-axis = 0.0253 m;

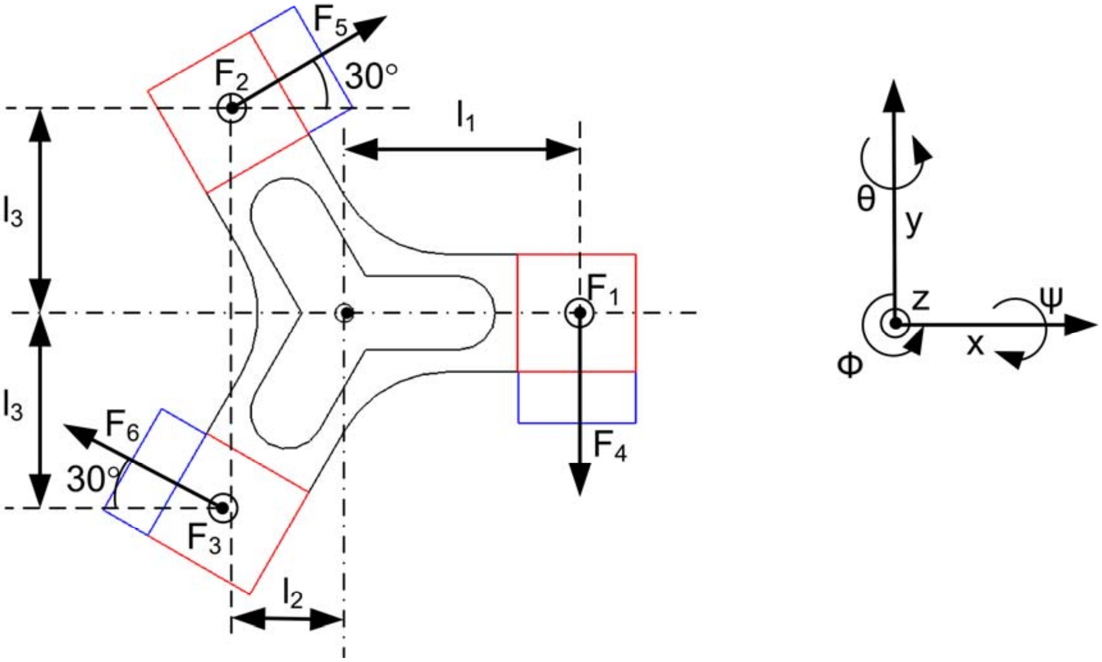

Fig. 7-3. Definitions of forces and distances of points of applications from the center.

l_3: distance between the center of magnet 2 or 3 and the center of the platen along the y-axis = 0.04382 m;

The 3 × 3 zero matrix in the first and last quarters of the matrix shows that the vertical forces F_1, F_2 and F_3 do not contribute to the horizontal motions and that the horizontal forces F_4, F_5 and F_6 do not contribute to the vertical motions. That is, there is no coupling between the horizontal and vertical modes of the dynamic model. Since the output generated by the controllers are f_x, f_y, f_z, τ_ψ, τ_θ, and τ_ϕ and the inputs to the system are forces F_1, F_2, F_3, F_4, F_5, and F_6, we use inverse of the modal force transformation to calculate the desired output forces.

$$\begin{bmatrix} F_1 \\ F_2 \\ F_3 \\ F_4 \\ F_5 \\ F_6 \end{bmatrix} = \begin{bmatrix} 0 & 0 & 0 & 0.3333 & 0 & -13.1761 \\ 0 & 0 & 0 & 0.3333 & 11.4103 & 6.5880 \\ 0 & 0 & 0 & 0.3333 & -11.4103 & 6.5880 \\ 0 & -0.6667 & -6.5883 & 0 & 0 & 0 \\ 0.5774 & 0.3333 & -6.5883 & 0 & 0 & 0 \\ -0.5774 & 0.3333 & -6.5883 & 0 & 0 & 0 \end{bmatrix} \begin{bmatrix} f_x \\ f_y \\ \tau_\phi \\ f_z \\ \tau_\psi \\ \tau_\theta \end{bmatrix} \quad (7.7)$$

7.1.4 Modal Displacement Transformation

The actual displacement and velocity measurement is essential for closed-loop control. We employed 3 laser interferometers for horizontal motion sensing and 3 capacitance probes for vertical motion sensing. The interferometry system for the second-generation maglev stage is shown in Fig. 7-4. The laser interferometers provide 3 axes displacement and velocity data along the line of laser falling on the plane mirror. Any translational motion of the plane mirror attached to the platen is sensed by the laser interferometer. Fig. 7-5 shows the motion of platen along the x, y, and ϕ axes and displacement of the plane mirrors. The modal displacement and velocity transform for horizontal motion is

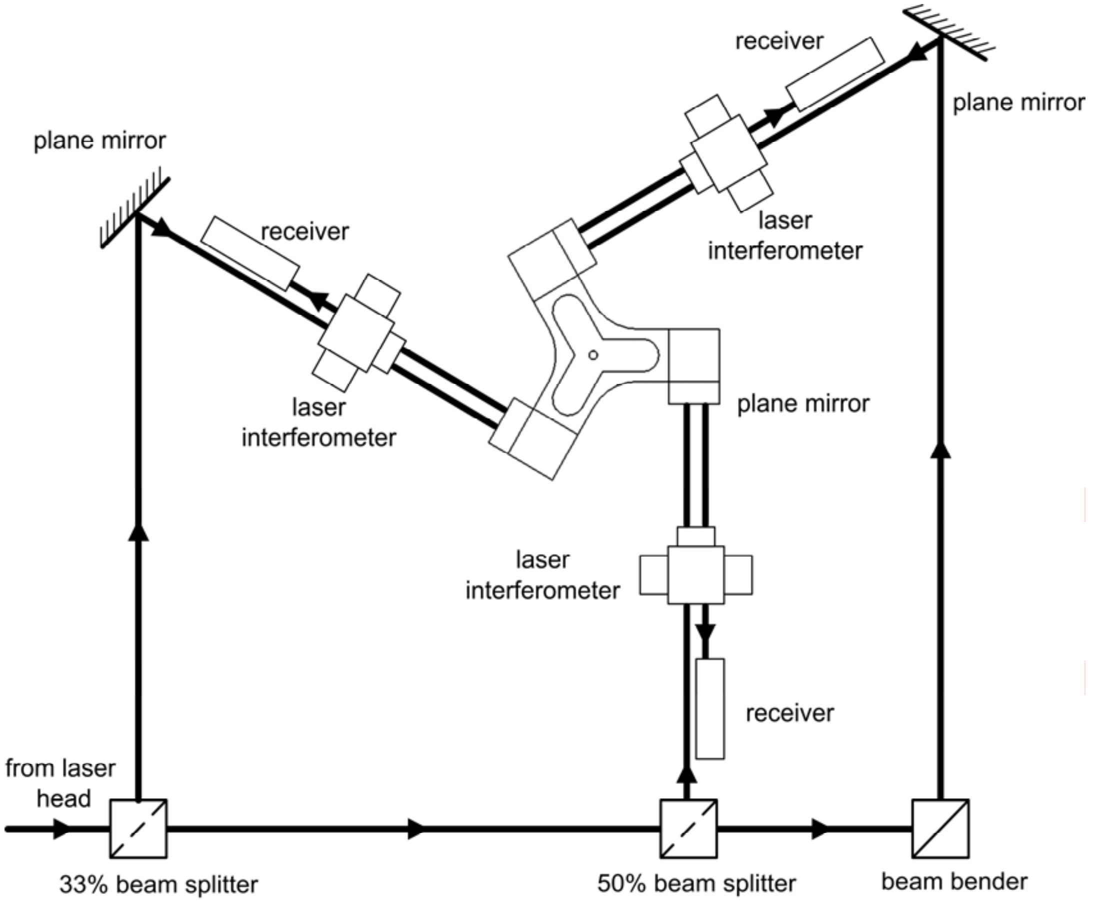

Fig. 7-4. Interferometry system for the second-generation maglev stage.

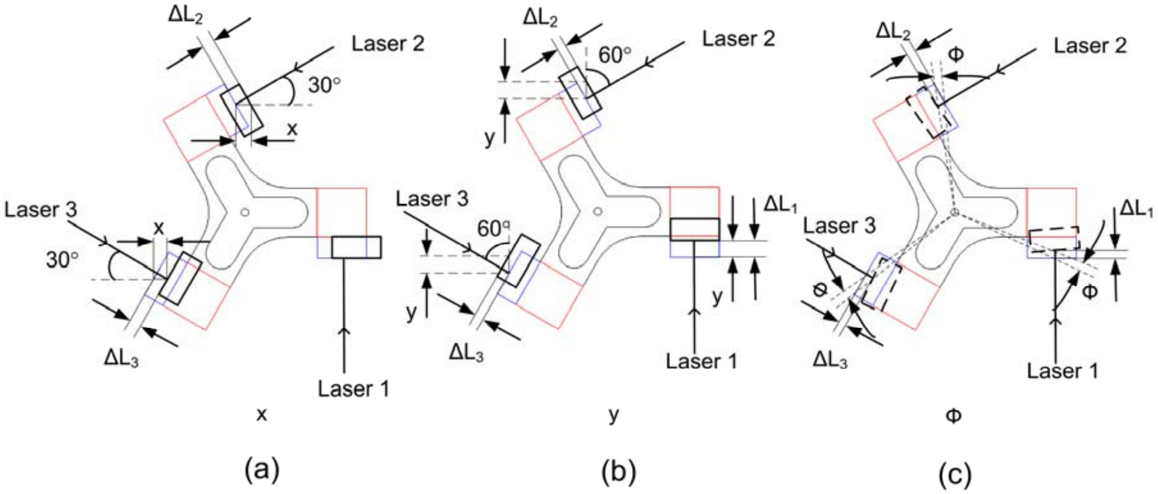

Fig. 7-5. Displacement of plane mirrors while motion in the (a) *x*, (b) *y* and, (c) ϕ.

$$\begin{bmatrix} \Delta L_1 \\ \Delta L_2 \\ \Delta L_3 \\ V_1 \\ V_2 \\ V_3 \end{bmatrix} = \begin{bmatrix} 0 & -1 & l_1 & 0 & 0 & 0 \\ \cos 30^\circ & \cos 60^\circ & l_1 & 0 & 0 & 0 \\ -\cos 30^\circ & \cos 60^\circ & l_1 & 0 & 0 & 0 \\ 0 & 0 & 0 & 0 & -1 & l_1 \\ 0 & 0 & 0 & \cos 30^\circ & \cos 60^\circ & l_1 \\ 0 & 0 & 0 & -\cos 30^\circ & \cos 60^\circ & l_1 \end{bmatrix} \begin{bmatrix} x \\ y \\ \phi \\ v_x \\ v_y \\ \omega_\phi \end{bmatrix}. \tag{7.8}$$

To get the values of translations x, y, and ϕ and, velocities v_x, v_y, and ω_ϕ we substituted the value of l_1 and calculated the inverse of the transformation matrix.

$$\begin{bmatrix} x \\ y \\ \phi \\ v_x \\ v_y \\ \omega_\phi \end{bmatrix} = \begin{bmatrix} 0 & 0.5774 & -0.5774 & 0 & 0 & 0 \\ -0.6667 & 0.3333 & 0.3333 & 0 & 0 & 0 \\ 6.5928 & 6.5928 & 6.5928 & 0 & 0 & 0 \\ 0 & 0 & 0 & 0 & 0.5774 & -0.5774 \\ 0 & 0 & 0 & -0.6667 & 0.3333 & 0.3333 \\ 0 & 0 & 0 & 6.5928 & 6.5928 & 6.5928 \end{bmatrix} \begin{bmatrix} \Delta L_1 \\ \Delta L_2 \\ \Delta L_3 \\ V_1 \\ V_2 \\ V_3 \end{bmatrix} \tag{7.9}$$

For vertical motion sensing we use 3 capacitance probes C_1, C_2 and C_3. These sensors provide the height of the platen bottom surface at 3 different positions. Fig. 7-6 shows the locations of the capacitance probes and their coordinates from the origin. The readings of the capacitance probes can be written in matrix form as

$$\begin{bmatrix} C_1 \\ C_2 \\ C_3 \end{bmatrix} = \begin{bmatrix} 1 & 0 & -d_1 \\ 1 & d_3 & d_2 \\ 1 & -d_3 & d_2 \end{bmatrix} \begin{bmatrix} z \\ \psi \\ \theta \end{bmatrix} \tag{7.10}$$

where d_1, d_2 and d_3 are shown in Fig. 7-6 and are defined as

d_1 = distance between the center and origin of the stationary coordinate system of C_1 along x-axis = 0.01443 m

d_2 = distance between the center of C_2 and C_3, and origin of the stationary coordinate system along x-axis = 0.007215 m

d_3 = distance between the center of C_2 and C_3, and origin of the stationary coordinate system along y-axis = 0.012496 m

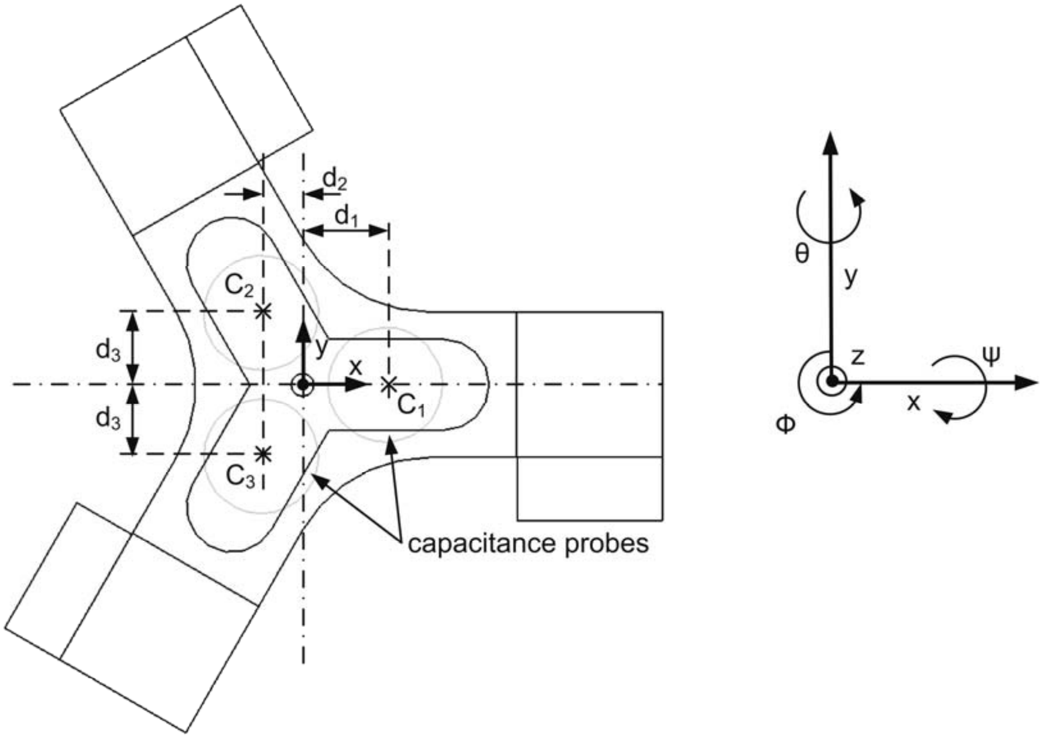

Fig. 7-6. Placement of capacitance probes C_1, C_2 and C_3.

The values of displacement along z and rotation ψ and θ are calculated using the following modal displacement transformation

$$\begin{bmatrix} z \\ \psi \\ \theta \end{bmatrix} = \begin{bmatrix} 0.3333 & 0.3333 & 0.3333 \\ 0 & 40.0128 & 40.0128 \\ -46.2000 & 23.1000 & 23.1000 \end{bmatrix} \begin{bmatrix} C_1 \\ C_2 \\ C_3 \end{bmatrix}. \tag{7.11}$$

Thus the whole modal displacement and velocity transformation turns out to be

$$\begin{bmatrix} x \\ y \\ \phi \\ v_x \\ v_y \\ \omega_\phi \\ z \\ \psi \\ \theta \end{bmatrix} = \begin{bmatrix} 0 & 0.5774 & -0.5774 & 0 & 0 & 0 & 0 & 0 & 0 \\ -0.6667 & 0.3333 & 0.3333 & 0 & 0 & 0 & 0 & 0 & 0 \\ 6.5928 & 6.5928 & 6.5928 & 0 & 0 & 0 & 0 & 0 & 0 \\ 0 & 0 & 0 & 0 & 0.5774 & -0.5774 & 0 & 0 & 0 \\ 0 & 0 & 0 & -0.6667 & 0.3333 & 0.3333 & 0 & 0 & 0 \\ 0 & 0 & 0 & 6.5928 & 6.5928 & 6.5928 & 0 & 0 & 0 \\ 0 & 0 & 0 & 0 & 0 & 0 & 0.3333 & 0.3333 & 0.3333 \\ 0 & 0 & 0 & 0 & 0 & 0 & 0 & 40.0128 & 40.0128 \\ 0 & 0 & 0 & 0 & 0 & 0 & -46.2000 & 23.1000 & 23.1000 \end{bmatrix} \begin{bmatrix} \Delta L_1 \\ \Delta L_2 \\ \Delta L_3 \\ V_1 \\ V_2 \\ V_3 \\ C_1 \\ C_2 \\ C_3 \end{bmatrix}. \tag{7.12}$$

7.2 Decoupled Lead-lag Control

In the last section we developed a dynamic model of the maglev stage that decouples all 6-axis motions. In this section we describe the design of 6 individual lead-lag controllers to control the 6-axis motions of the platen. Advanced control using the MIMO control technique and nonlinear control will be discussed in next chapter.

7.2.1 Selection of Sampling Frequency

The controller is implemented on the DSP. Each control loop consists of sampling the sensor data, transforming them to the modal values, calculating the control outputs using the reference signal and then output them to the maglev stage. This control loop repeats at the sampling frequency of the system. The selection of sampling frequency depends on several factors like sensor the sampling rate, system resonant frequency, system bandwidth, computing power, etc. There are several criteria used to select an appropriate sampling frequency [57–58]. To avoid aliasing the sampling frequency must be higher than Nyquist frequency in digital control [59]. While designing the digital control system the sampling frequency is set to be the highest to reduce the time delay in the zero-order hold (ZOH). Also at higher sampling rate the discrete-time dynamics can emulate the continuous time without much error. A typical choice of the sampling frequency could be around 20 times the closed-loop bandwidth, and higher sampling frequency is preferable [60]. The constraint for the upper value is that the DSP must be able to complete all the designated calculations within the sampling period. Based on the system clock speed and estimated processing time we decided the sampling frequency to be 5 kHz. One of the ADC channels of 6102 board is used as a clock generator for hardware interrupt that triggers the ISR on the DSP containing the digital control code. This digital control code is presented in Appendix A.

7.2.2 Horizontal-axis Control

The plant models developed before for translation and rotation can be written individually for each axis by placing mass and inertia values.

$$\frac{X(s)}{F_x(s)} = \frac{1}{0.267\, s^2} \tag{7.13}$$

$$\frac{Y(s)}{F_y(s)} = \frac{1}{0.267\, s^2} \tag{7.14}$$

$$\frac{\Phi(s)}{\tau_{\phi}(s)} = \frac{1}{653.61\times10^{-6}s^{2}} \tag{7.15}$$

Using the models shown above we designed three single-input-single-output (SISO) controllers for each axis. We used SISOTOOL function of Matlab® to design continuous-time controllers using the pole-placement technique. The closed-loop control structure for close loop is shown in Fig. 7-7.

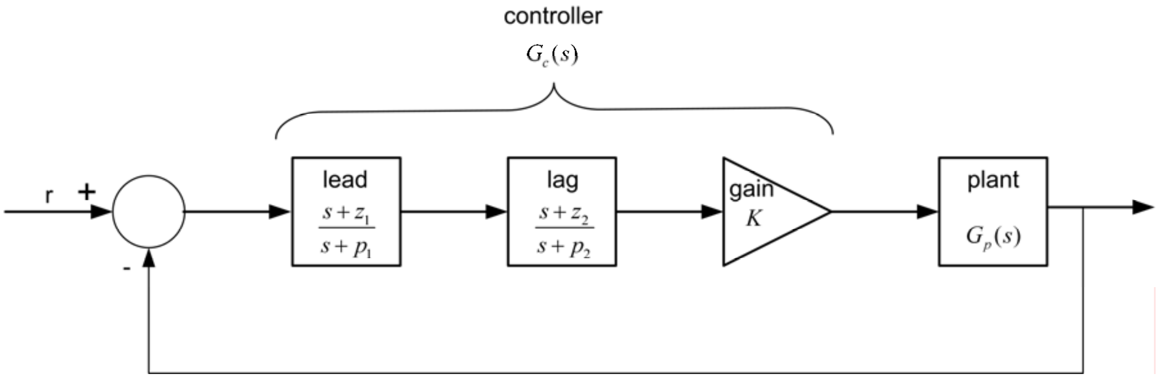

Fig. 7-7. Closed-loop control structure.

A continuous time lead-lag controller was designed with phase margin of 69.7° at the crossover frequency of 109.5 Hz. The designed compensator is

$$G_{x,y,\phi}(s) = \frac{K(s+116.6)(s+10.91)}{s(s+4014)}\,. \tag{7.16}$$

where K is gain of the controller. The value of K for x and y is 7.3726×10^{5} and 1.8041×10^{3} for ϕ. The pole placed at the origin of the s- plane ensures zero steady-state error. This continuous-time controller is converted to a discrete-time one using the ZOH method with the sampling frequency of 5 kHz decided in the previous section.

$$G_{x,y,\phi}(z) = \frac{K(z-0.985)(z-0.998)}{(z-1)(z-0.448)} \tag{7.17}$$

The loop transmission and closed-loop Bode plots of the controller are shown in Fig. 7-8 and Fig. 7-9.

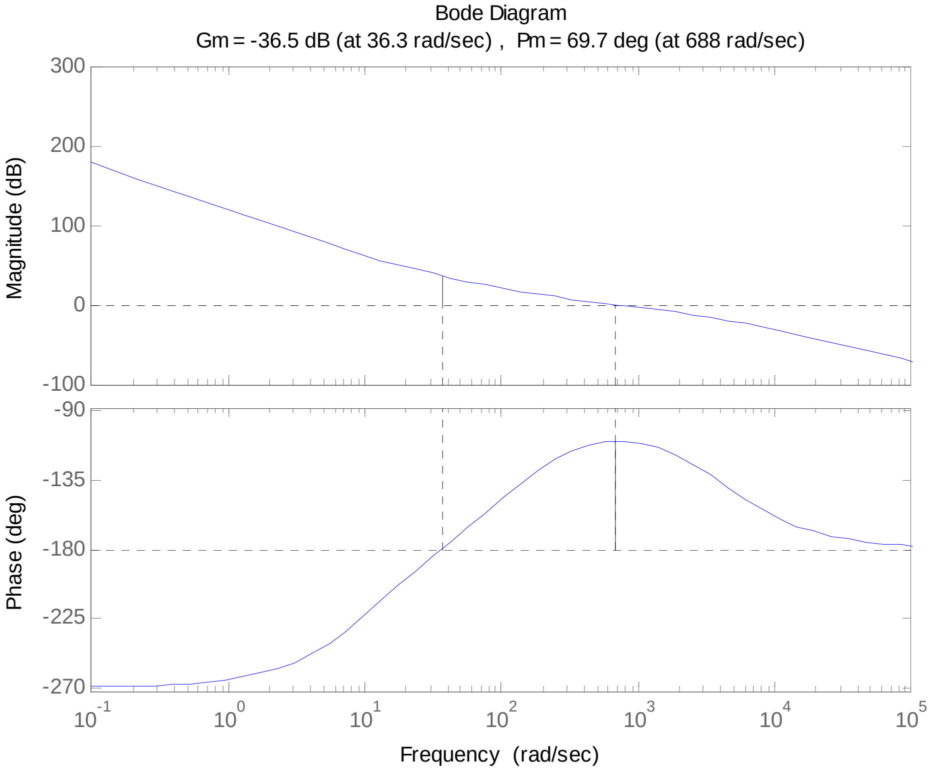

Fig. 7-8. Loop transmission for for *x*-, *y*- and *ϕ*-axes motion.

Fig. 7-10 shows a 1-µm step response in *x* and the disturbances in other 5 axes caused by it. The rise time for this motion is around 3 ms, and it settles down to the desired position in less than 35 ms. There is an overshoot of around 35% with no steady-state error. There are some perturbations in the *y*- and *ϕ*-axes due to coupled motion in the *x*-*y* plane. There is a small peak of perturbation in ψ as well. The possible reason of coupling between horizontal and vertical motions may be that the platen CM does not lie in the plane containing of horizontal forces. This unmodeled dynamics might create erroneous motions.

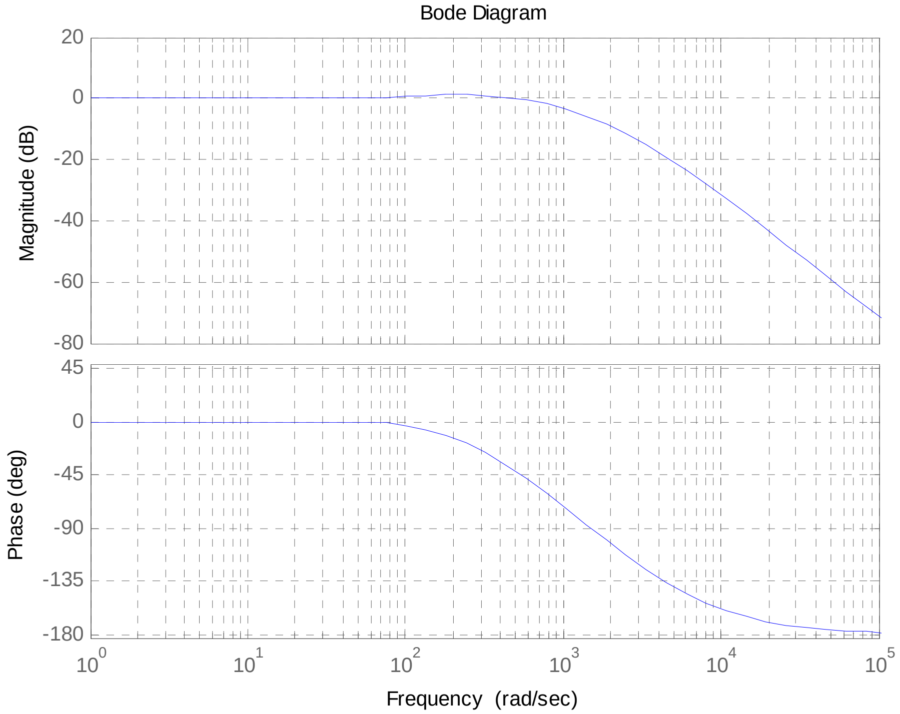

Fig. 7-9. Closed-loop Bode plot for *x*-, *y*- and ϕ-axes motion.

A similar 1-μm step in *y* is shown in Fig. 7-11 along with the perturbations in other axes. It shows overshoot of around 35% with no steady-state error. The rise time is around 15 ms and settling time is around 30 ms. A 100 μrad step was given in ϕ and its response is shown in Fig. 7-12. The overshoot is around 32%. The system settles to the desired position in around 45 ms with no steady state error.

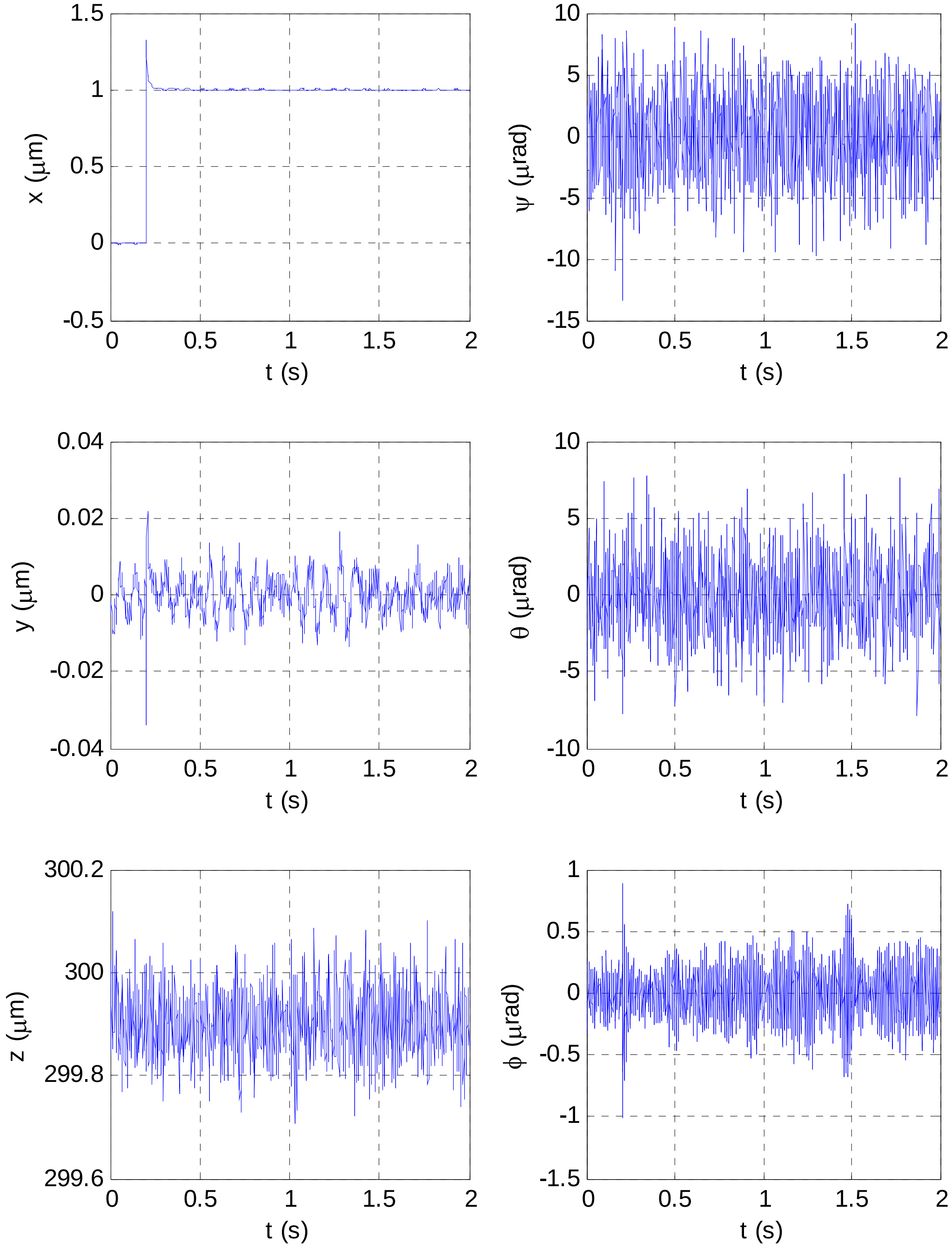

Fig. 7-10. 1-μm step response in *x* with perturbed motions in the other 5 axes.

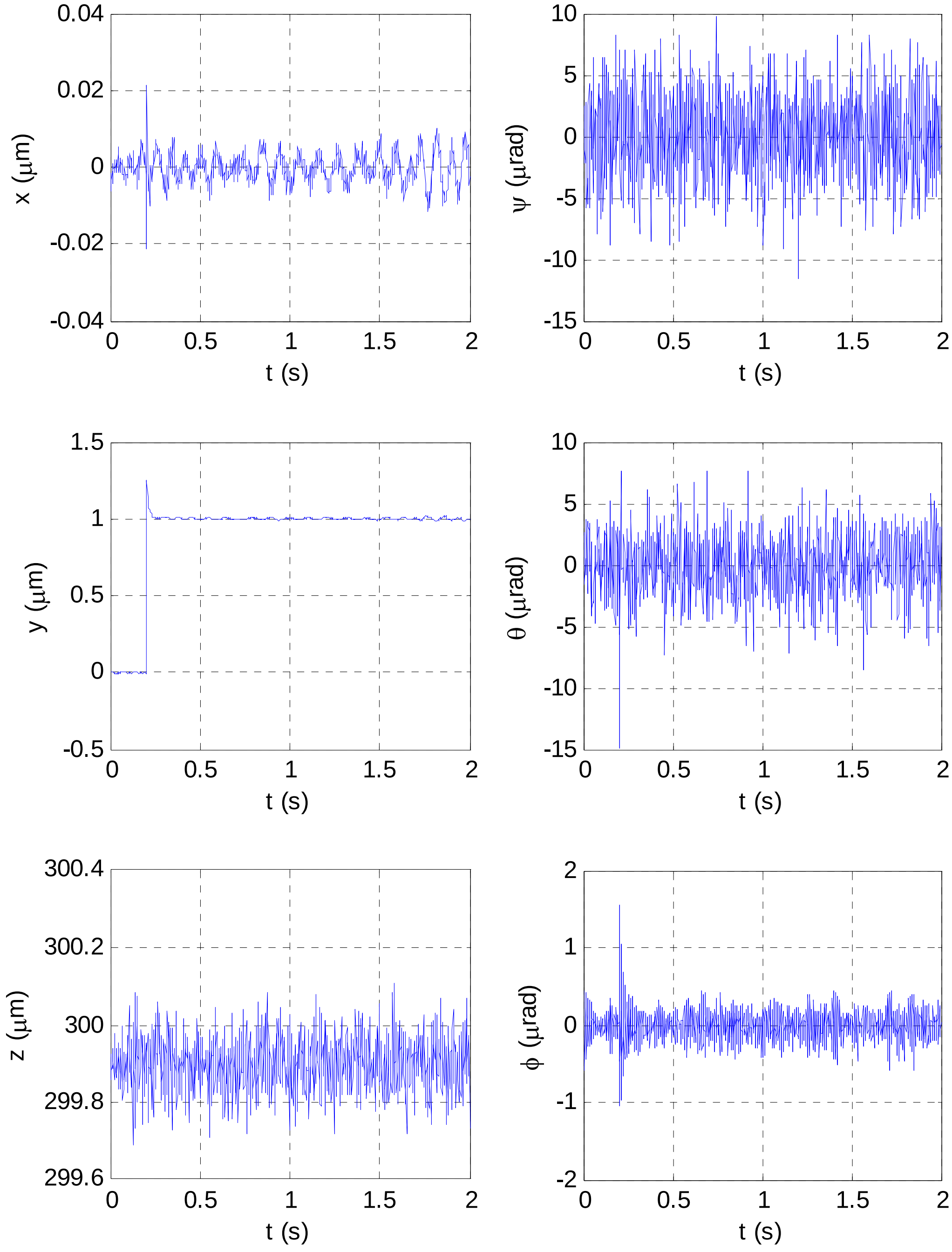

Fig. 7-11. 1-µm step response in *y* with perturbed motions in the other 5 axes.

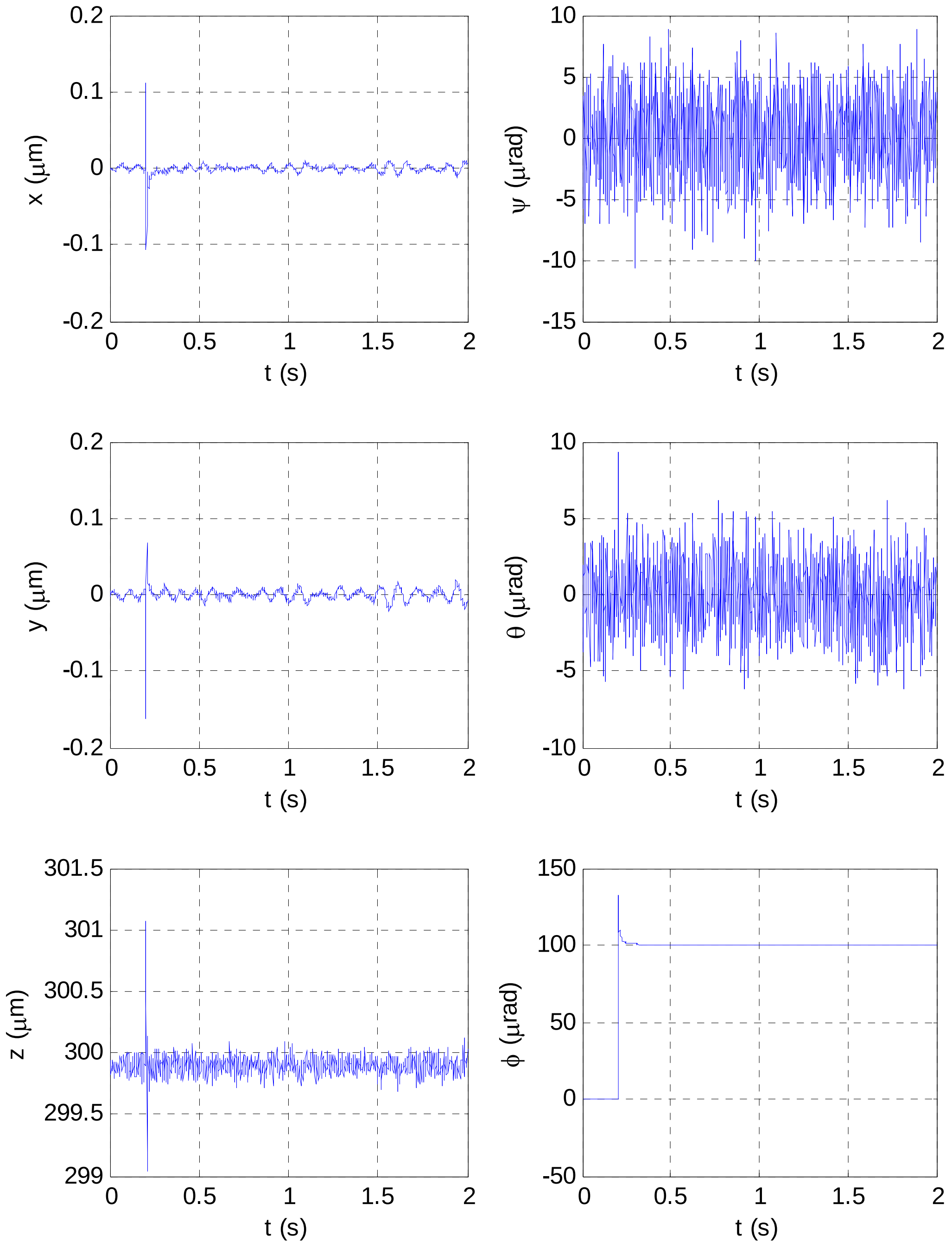

Fig. 7-12. 1000-μrad step response in ϕ with perturbed motions in the other 5 axes.

7.2.3 Vertical-axis Control

The plant model for the *z*-axis motion is exactly the same as *x* and *y*. The dynamic models for rotations about the *x*- and *y*- axes are the same because the moment of inertia I_{xx} and I_{yy} are equal. The vertical dynamic models are

$$\frac{Z(s)}{F_z(s)} = \frac{1}{0.267\, s^2} \tag{7.18}$$

$$\frac{\Psi(s)}{\tau_\psi(s)} = \frac{1}{340.37\times 10^{-6} s^2} \tag{7.19}$$

$$\frac{\Theta(s)}{\tau_\theta(s)} = \frac{1}{340.37\times 10^{-6} s^2}\ . \tag{7.20}$$

The design of three SISO controllers was performed similarly to the horizontal ones. A continuous-time lead-lag controller was designed to control the vertical motions that has phase margin of 70.1° at crossover frequency of 65 Hz. The compensator has a pole at the origin to make steady-state error zero and given as

$$G_{z,\psi,\theta}(s) = \frac{K(s+57.47)(s+6.271)}{s(s+2103)}\ , \tag{7.21}$$

where K is the gain of the controller. The value of K for z axis is 2.32003×10^5 N/m and 2.95658×10^2 N for θ and ψ. The discrete-time controller obtained by ZOH at 5 kHz is given by

$$G_{x,\psi,\theta}(z) = \frac{K(z-0.991)(z-0.999)}{(z-1)(z-0.657)} \tag{7.22}$$

The loop transmission and closed-loop Bode plots for the system above are shown in Fig. 7-13 and Fig. 7-14.

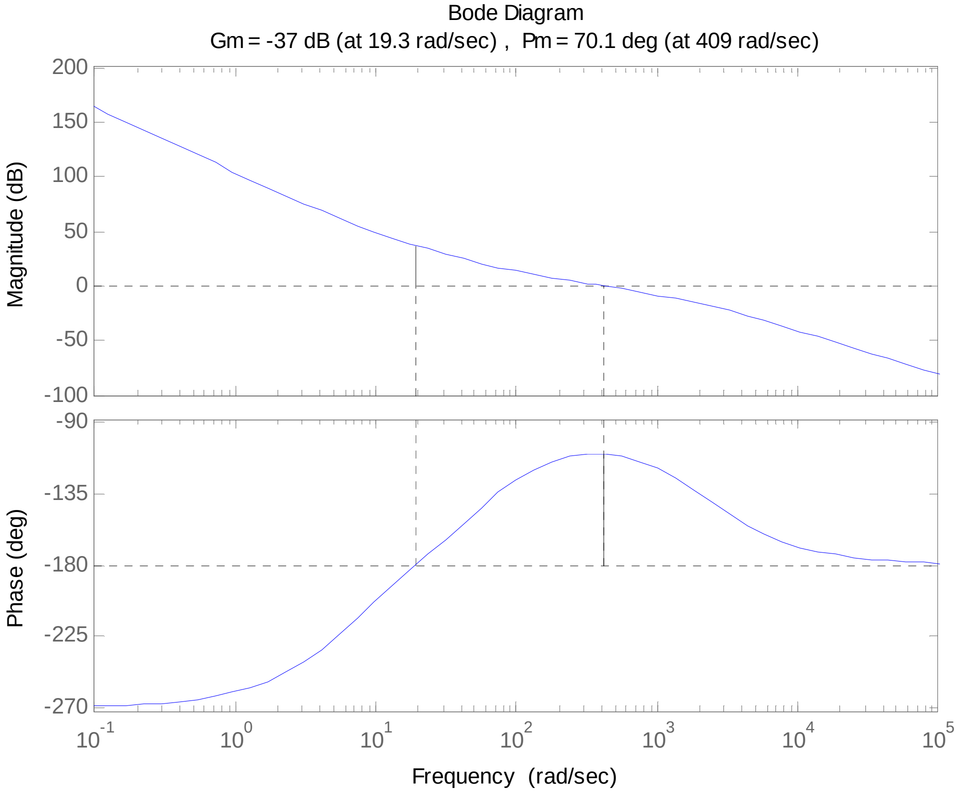

Fig. 7-13. Loop transmission for *z*-, *ψ*- and *θ*-axis motion.

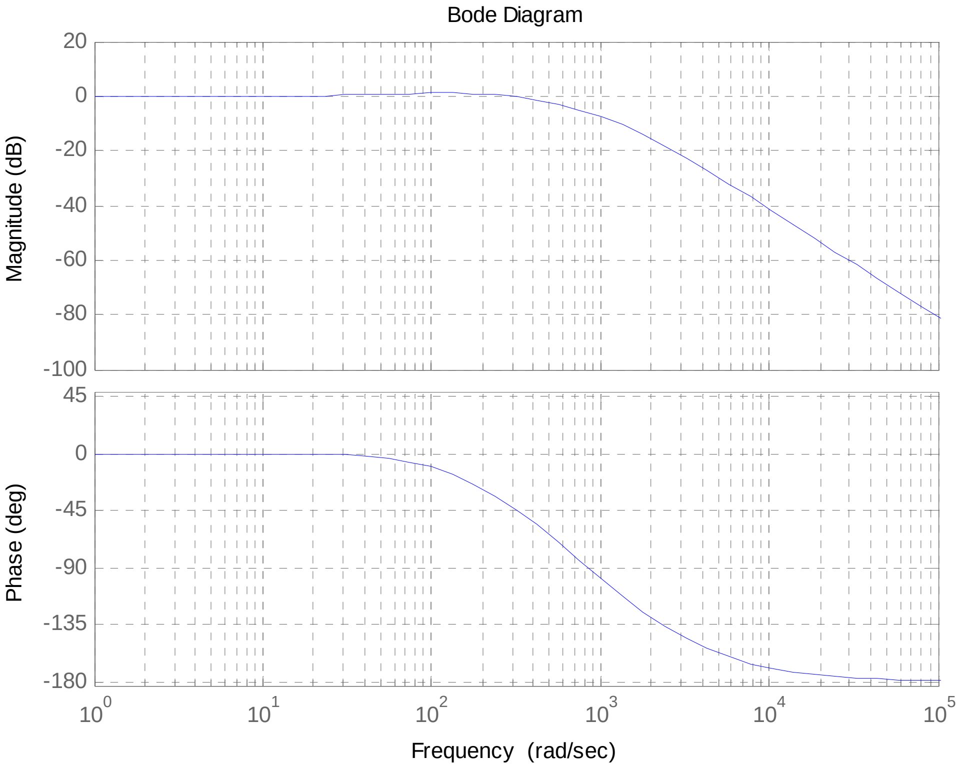

Fig. 7-14. Closed-loop Bode plot for z-, ψ- and θ-axis motion.

A 50-µm step in z is shown in Fig. 7-15. The rise time for this step is 7 ms, and it settles in around 60 ms. Fig. 7-16 and Fig. 7-17 show 1000-µrad step responses in ψ and θ along with the perturbations in other axes.

7.3 Precision Motion Control

We implemented the controller designed in the previous section and performed various experiments to test the positioning capability of the stage. Fig. 7-18(a) shows a position noise profile in the x-axis while the platen is levitated. The peak-to-peak noise is less than 18 nm, i.e. the noise level is around 3 nm rms in the horizontal directions. The noise in the vertical direction

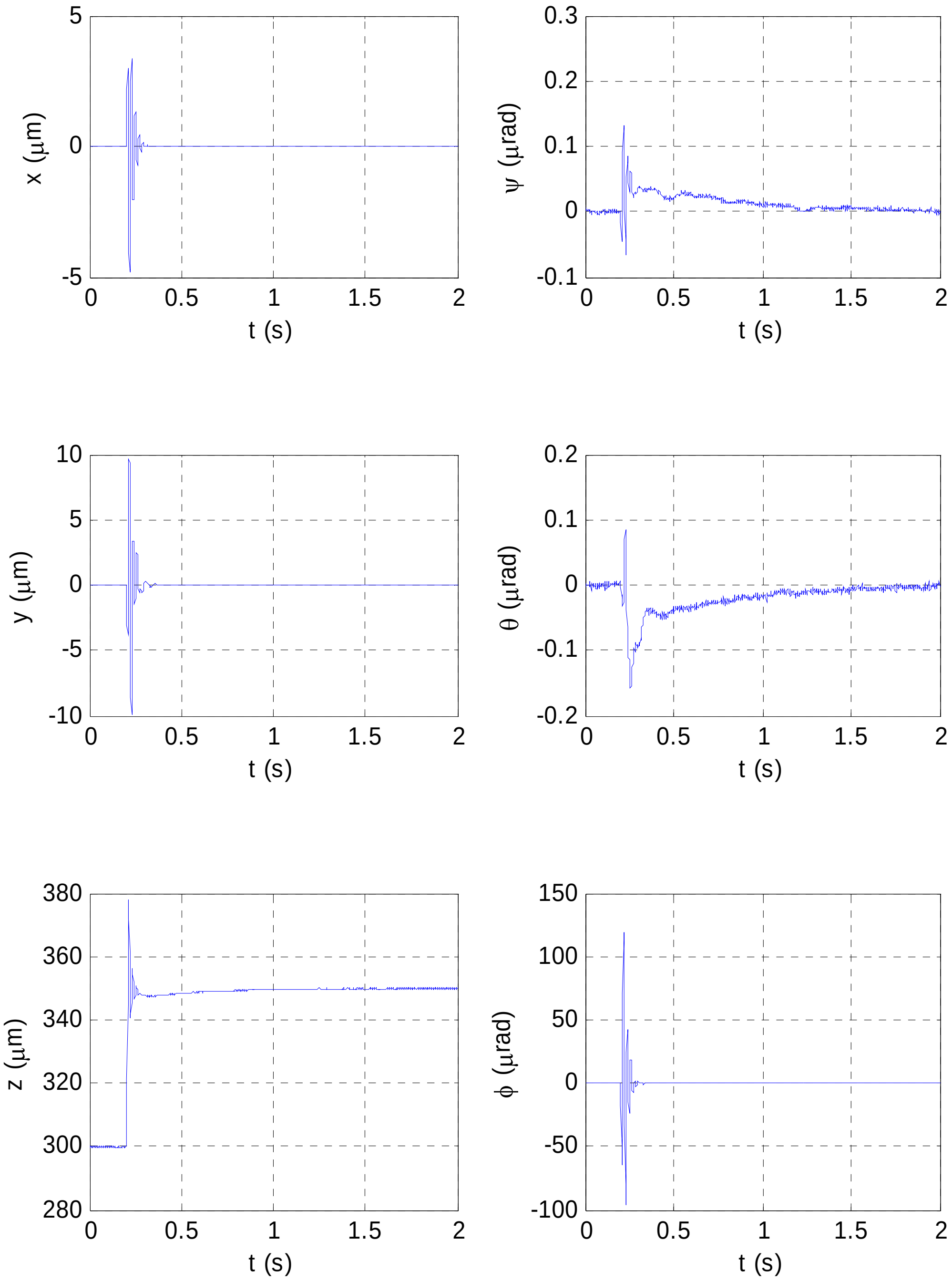

Fig. 7-15. 50-μm step response in *z* with perturbed motions in the other 5 axes.

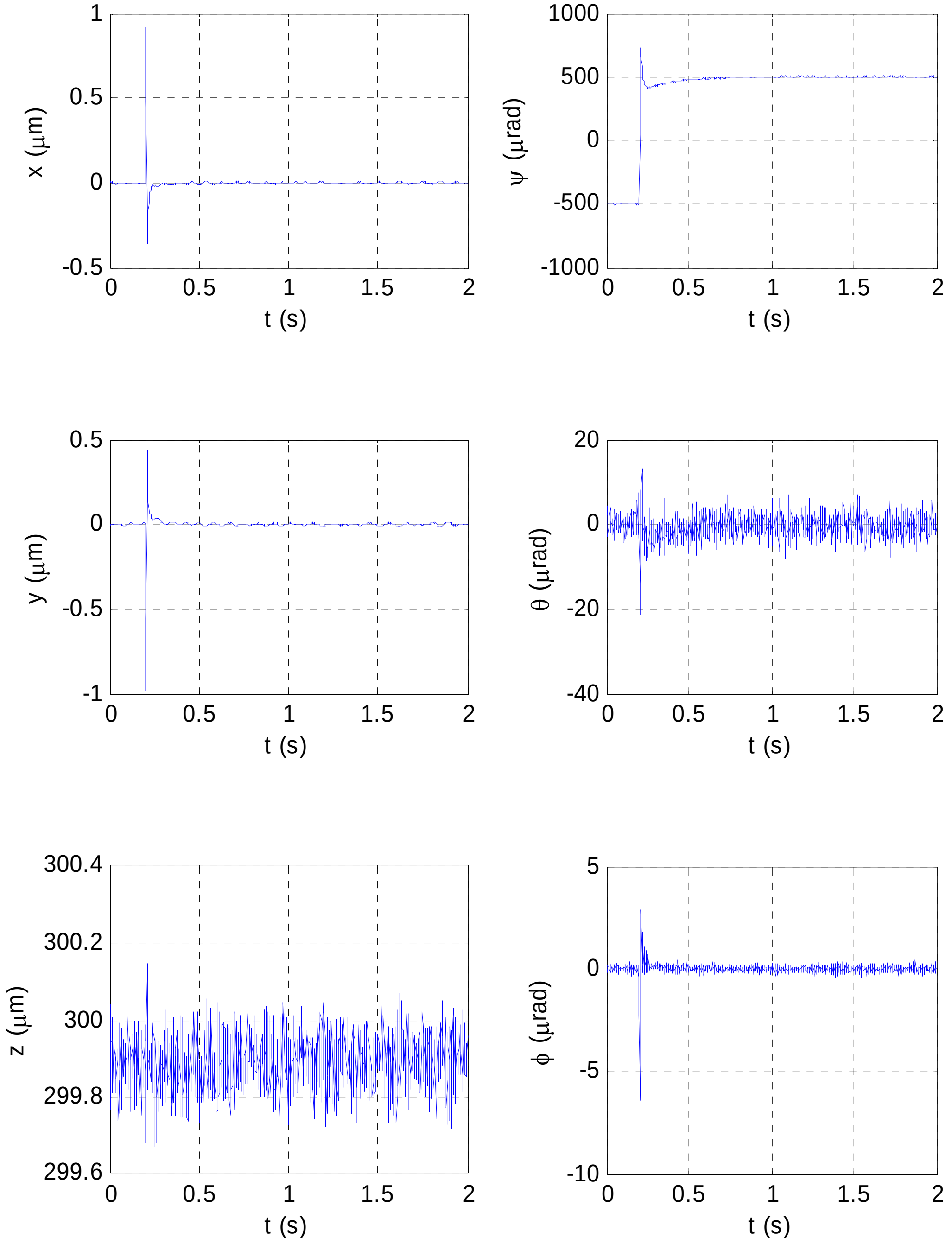

Fig. 7-16. 1000-μrad step response in ψ with perturbed motions in the other 5 axes.

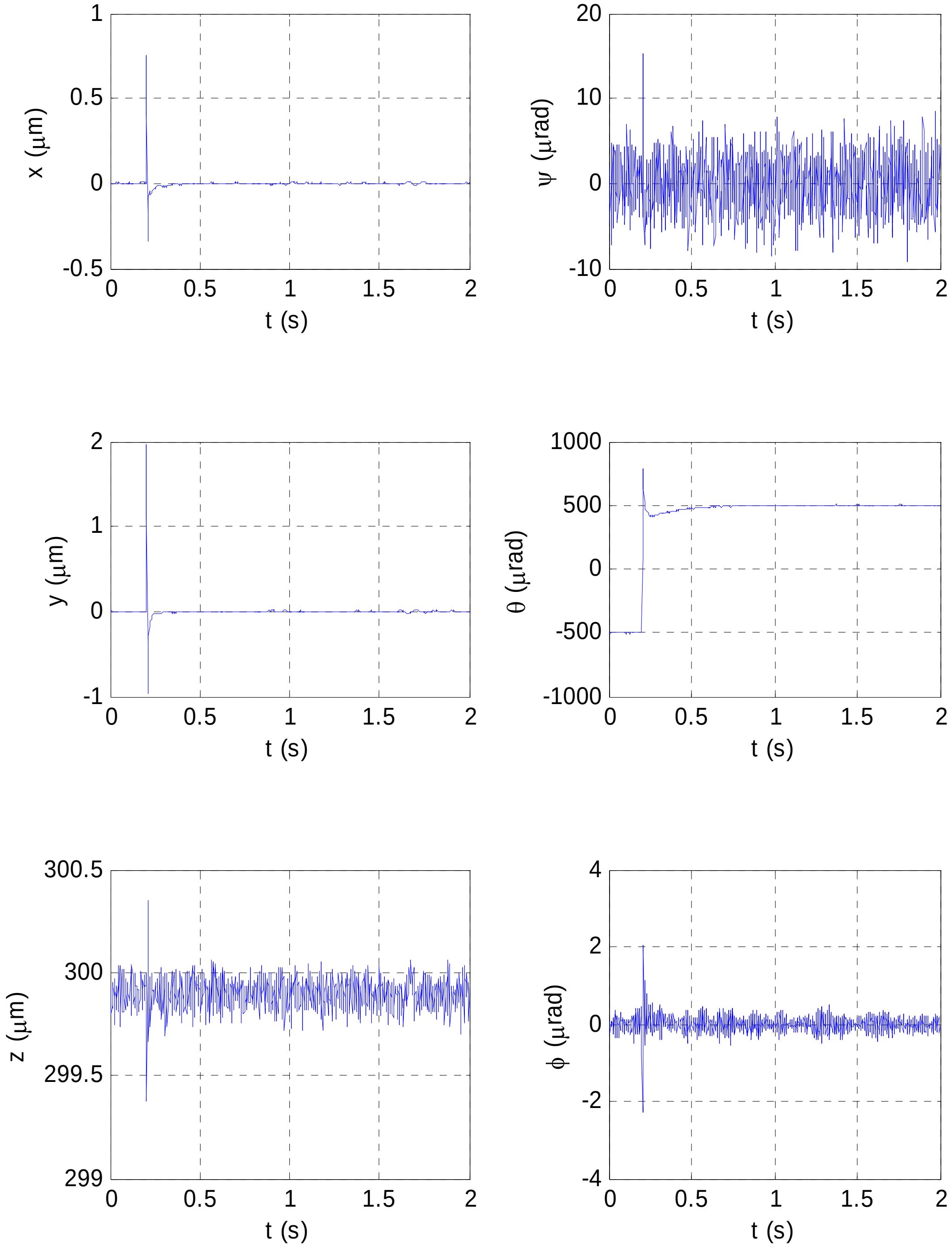

Fig 7-17. 1000-μrad step response in θ with perturbed motions in the other 5 axes.

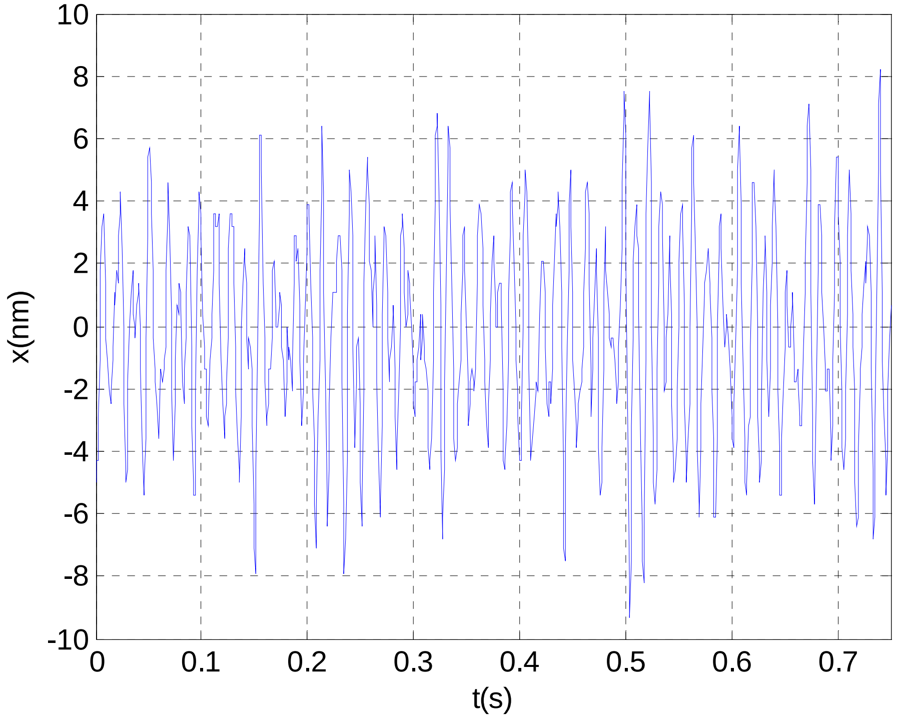

(a)

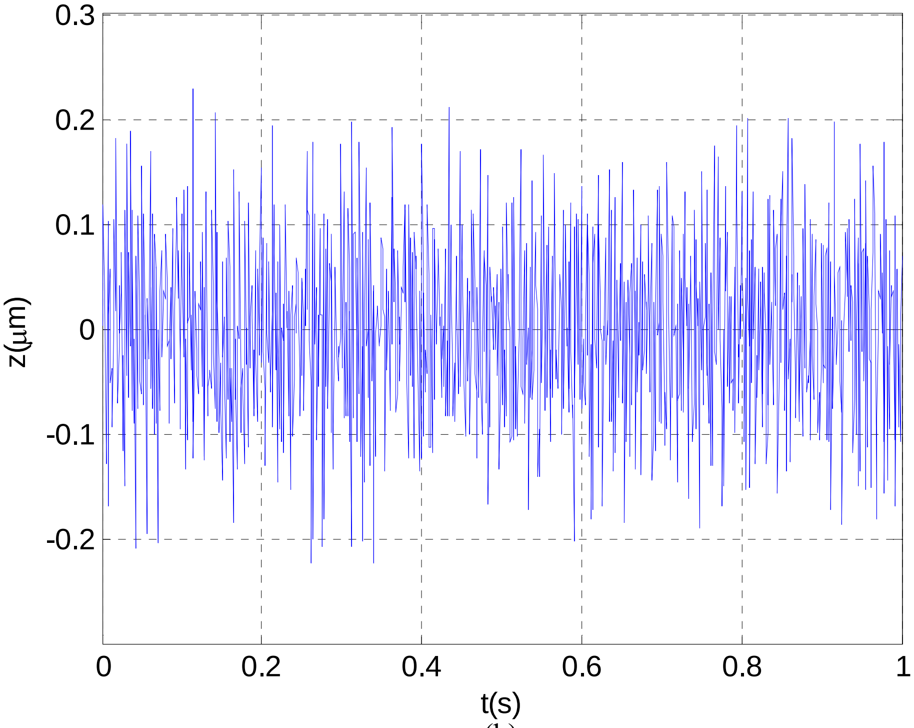

(b)

Fig 7-18. (a) Position noise in (a) *x* and (b) *z*.

is shown in Fig. 7-18 (b). The peak-to-peak noise in the *z*-axis is around 0.4 μm. The analog sensor data for vertical motion must be digitized by an ADC. The cumulative effect of sensor noise, ADC noise, and ADC quantization makes the vertical motion profile noisier. Despite the noise in the vertical axes the horizontal motion profile is very quiet. This indicates that there is little dynamic coupling between the horizontal and vertical motions of the maglev stage and that the horizontal controller is robust enough to reject any noise from the vertical motion.

Fig. 7-19 shows a 50-nm step response in the *x*-axis. The position noise level is again maintained under 3 nm rms. Fig. 7-20 shows 10-μm consecutive step responses at the interval of 0.5 s in the *x*-axis. The platen moves to the desired position without large overshoot and settles down fast and responds to the next step command. Fig. 7-21 shows a 500-μm sinusoidal motion in the *x*-axis. This indicates that the stage is able to travel smoothly in larger motions with small positioning error. Fig. 7-22 shows a 500-μm radius circular path traversed by the platen in the *x*-*y* plane. The motion of the platen is very close to a perfect circle.

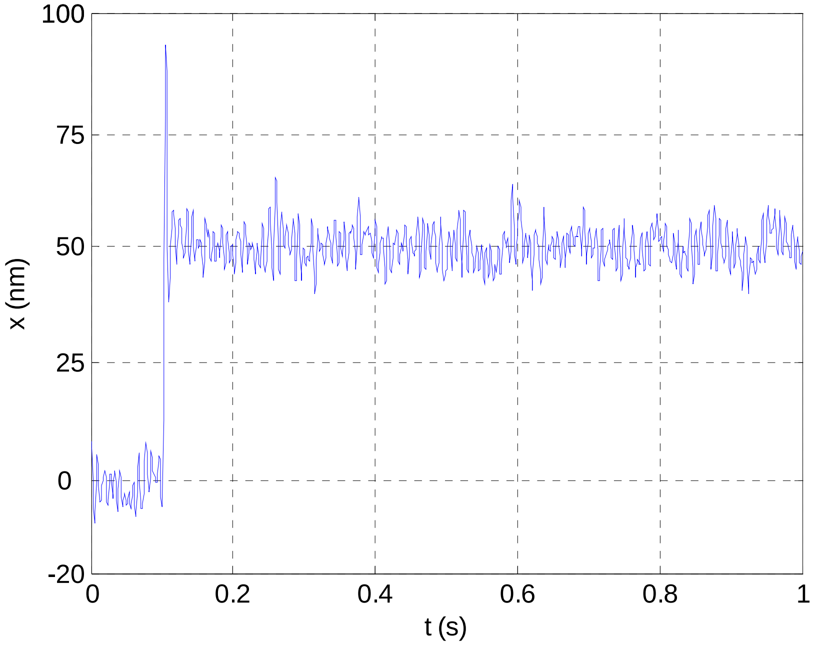

Fig. 7-19. 50-nm step response in *x*.

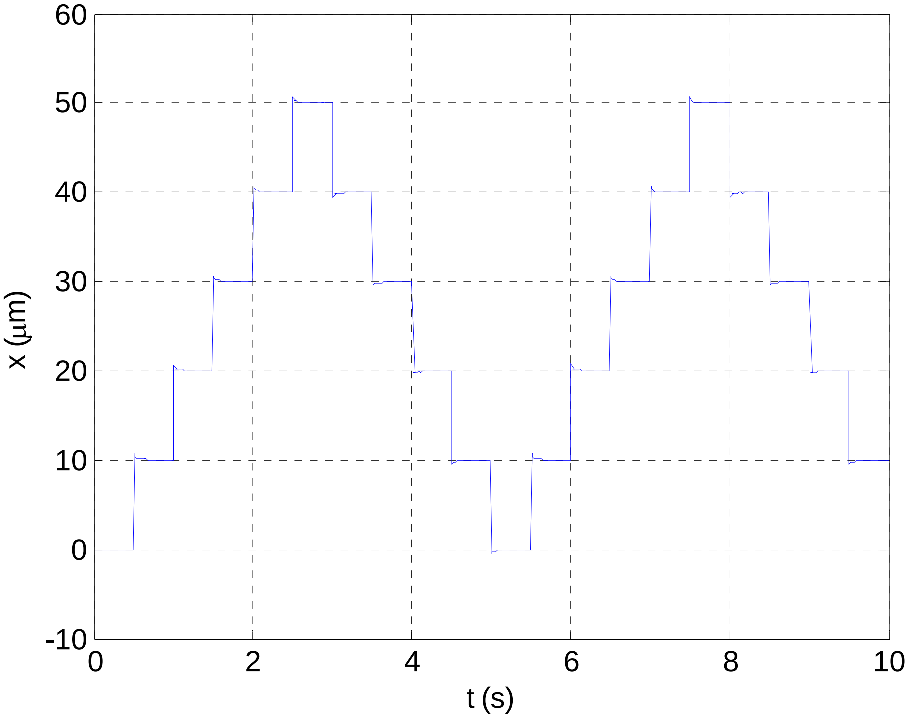

Fig. 7-20. 10-μm consecutive steps in *x*.

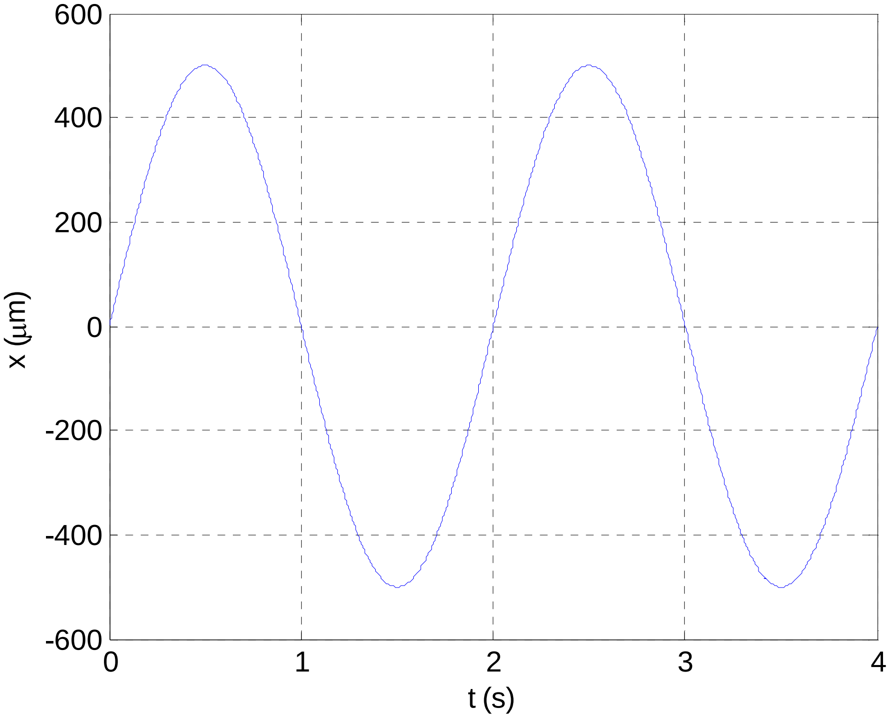

Fig. 7-21. 500-μm sinusoidal motion in *x*.

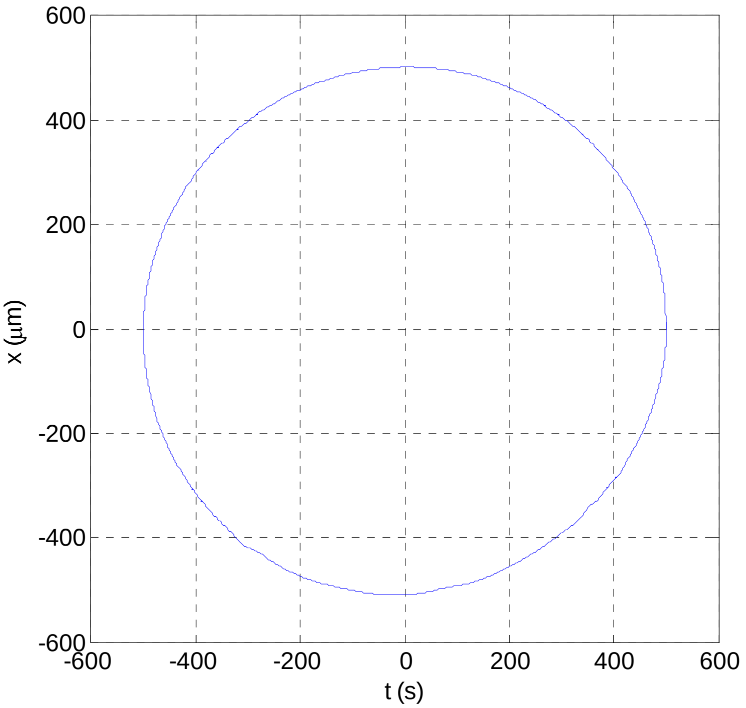

Fig. 7-22. 500-µm radius circle in the *x*-*y* plane.

Fig. 7-23 shows a path in the shape of a spur gear traversed by the platen. Its inner radius is 500 nm and outer radius is 675 nm. This proves the nanoscale positioning capability of the maglev stage. This demonstrates potential applications of this maglev stage for positioning in µSTL and nano-indentation. Fig. 7-24 shows a 3-D path traversed by the platen in the area of 80 × 60 µm. While generating the scanning path the stage took up/down steps in the z-axis from 195 µm to 200 µm. There are two different markers used here. The triangular markers show the points above 198 µm and the dots, points below 198 µm. If a stiff AFM tip is fixed to the base and a silicon substrate is attached to the moving platen, the tip will make indents/scratches and we can write small letters or draw tiny shapes on the silicon substrate. These positioning capabilities imply versatile applications of the maglev stage.

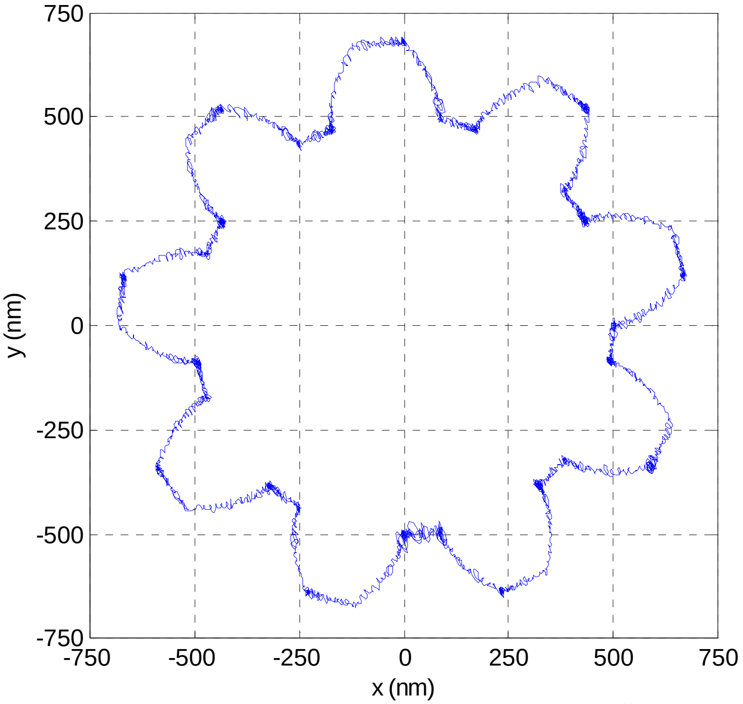

Fig. 7-23. Trajectory in a shape of a spur gear of 500-nm radius in the *x*-*y* plane.

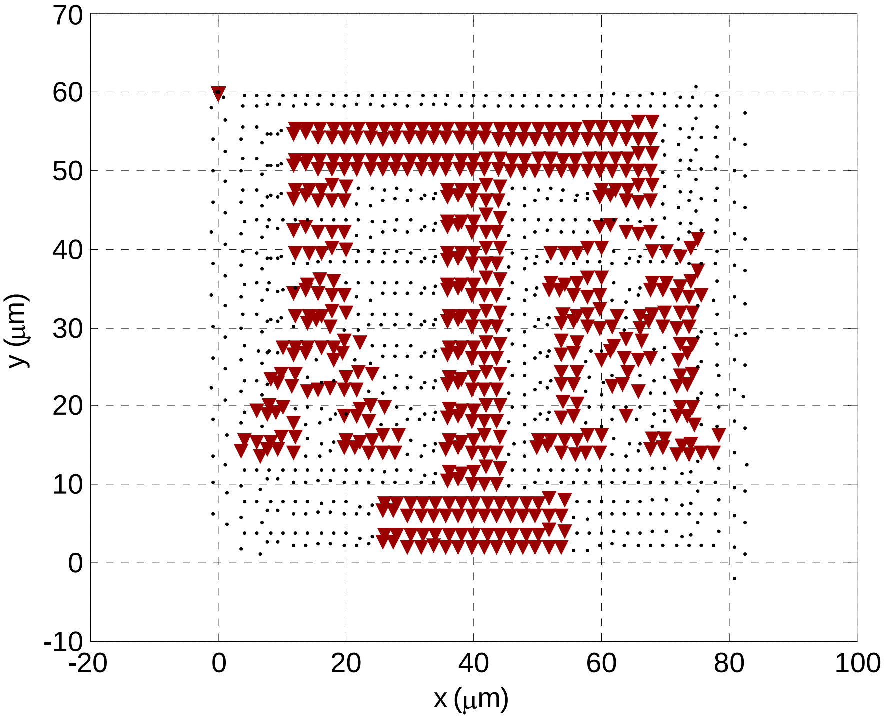

Fig. 7-24. Logo of Texas A&M University plotted over an area of 80 × 60 μm in *x*-*y*.

CHAPTER VIII

ADVANCED CONTROL

In the last chapter we designed and implemented SISO lead-lag controllers to stabilize and control the maglev stage that provided very good results. However due to simultaneous motions in the 6-axis the maglev stage is a MIMO system, and there are some existing couplings between the motions in different axes. Therefore we modeled the system in state-space that considers the coupling factor and designed a multivariable control system to control the lateral motions. There are unmodeled dynamics in the system that generated erroneous disturbances in other axes while a step input to one axis. We successfully applied feedforward decoupling compensation to reduce these disturbances. Also in the model presented in previous chapter we assumed that the force is a linear function of current that is true only within a very short travel range around the equilibrium position. The electromagnetic analysis of the actuators showed that the force is a nonlinear function of the coil current as well as the position of the magnet with respect to the coil. Thus we apply approximate feedback linearization using spline functions.

In this chapter we first present the linearized state-space model of the maglev stage used for multivariable control followed by the design and implementation of LQR (linear quadratic regulator) control. The analysis of nonlinear behavior of the actuator is explained and the implementation of feedback linearization is discussed. The experimental results demonstrating the performance of the maglev stage after the application of these advanced control strategies are shown.

8.1 State-space Modal and Linearization

The equations of motion of the maglev stage are nonlinear due to dependence of platen motion on the trigonometric functions of the angles of rotation of the platen with respect to the inertial frame. We define a transform A between the stationay frame (xyz) and the body ($x'y'z'$) frame using Euler angles such that

$$x' = Ax\,. \tag{8.1}$$

The transformation matrix A comes out to be

$$A = \begin{bmatrix} \cos\theta\cos\phi & \cos\theta\sin\phi & -\sin\theta \\ \sin\psi\sin\theta\cos\phi - \cos\psi\sin\phi & \sin\psi\sin\theta\sin\phi + \cos\psi\cos\phi & \cos\theta\sin\psi \\ \cos\psi\sin\theta\cos\phi + \sin\psi\sin\phi & \cos\psi\sin\theta\sin\phi - \sin\psi\cos\phi & \cos\theta\cos\psi \end{bmatrix} \tag{8.2}$$

The state variables that completely describe the general 3-D motion of the platen can be chosen as its displacement and velocity in 6 axes as

$$\begin{bmatrix} x & y & z & u & v & w & \psi & \theta & \phi & p & q & r \end{bmatrix}^T. \tag{8.3}$$

The x, y, and z are the displacement components in m and, u, v, and w are the velocity components in m/s of the platen CM with respect to the origin in the stationary frame. The ψ, θ, and ϕ are the Euler angles in rad and, p, q, and r are the angular velocities in rad/s about the origin of the stationary frame. These angular velocity components are approximately the same as those described in the body frame in case of small angles.

From (7.6) the transformation of force from the actuator forces is given as

$$\begin{bmatrix} f_x \\ f_y \\ \tau_\phi \\ f_z \\ \tau_\psi \\ \tau_\theta \end{bmatrix} = \begin{bmatrix} 0 & 0 & 0 & 0 & \cos 30^\circ & -\cos 30^\circ \\ 0 & 0 & 0 & -1 & \sin 30^\circ & \sin 30^\circ \\ 0 & 0 & 0 & -l_1 & -l_1 & -l_1 \\ 1 & 1 & 1 & 0 & 0 & 0 \\ 0 & l_3 & -l_3 & 0 & 0 & 0 \\ -l_1 & l_2 & l_2 & 0 & 0 & 0 \end{bmatrix} \begin{bmatrix} F_1 \\ F_2 \\ F_3 \\ F_4 \\ F_5 \\ F_6 \end{bmatrix} \tag{8.4}$$

Using the conservation of linear momentum in the inertial frame

$$\sum f_i = M\dot{v}_i \Rightarrow M\dot{v}_i = \sum A^{-1} f_i' \tag{8.5}$$

and Euler's equation

$$\sum \tau_i = \left(\frac{\partial L_i'}{\partial t}\right)_{body} + \omega_i' \times L_i' = \sum A^{-1} \tau_i' , \tag{8.6}$$

we get the following nonlinear equations of motion:

$$\dot{x} = \tilde{u}$$

$$\dot{\tilde{y}} = \tilde{v}$$

$$\dot{\tilde{z}} = \tilde{w}$$

$$\dot{\tilde{u}} = \left(\frac{1}{M}\right)\left\{(\cos\theta\cos\phi)(f_x) + (\sin\psi\sin\theta\cos\phi - \cos\psi\sin\phi)(f_y) + (\cos\psi\sin\theta\cos\phi + \sin\psi\sin\phi)(f_z)\right\}$$

$$\dot{\tilde{v}} = \left(\frac{1}{M}\right)\left\{(\cos\theta\sin\phi)(f_x) + (\sin\psi\sin\theta\sin\phi + \cos\psi\cos\phi)(f_y) + (\cos\psi\sin\theta\sin\phi - \sin\psi\cos\phi)(f_z)\right\}$$

$$\dot{\tilde{w}} = \left(\frac{1}{M}\right)\left\{-\sin\theta(f_x) + \cos\theta\sin\psi(f_y) + \cos\theta\cos\psi(f_z) - g\right\}$$

$$\dot{\tilde{\psi}} = \tilde{p} \tag{8.7}$$

$$\dot{\tilde{\theta}} = \tilde{q}$$

$$\dot{\tilde{\phi}} = \tilde{r}$$

$$\dot{\tilde{p}} = \left(\frac{1}{I_{xx}}\right)\left\{\cos\theta\cos\phi\ (\tau_\psi) + (\sin\theta\sin\psi\cos\phi - \cos\psi\sin\phi)\ (\tau_\theta) + (\cos\psi\sin\theta\cos\phi + \sin\psi\sin\phi)\ (\tau_\phi)\right\}$$

$$\dot{\tilde{q}} = \left(\frac{1}{I_{yy}}\right)\left\{\cos\theta\sin\phi\ (\tau_\psi) + (\sin\theta\sin\psi\sin\phi + \cos\psi\cos\phi)\ (\tau_\theta) + (\cos\psi\sin\theta\sin\phi - \sin\psi\cos\phi)\ (\tau_\phi)\right\}$$

$$\dot{\tilde{r}} = \left(\frac{1}{I_{zz}}\right)\left\{-\sin\theta\ (\tau_\psi) + \cos\theta\sin\psi\ (\tau_\theta) + \cos\theta\cos\psi\ (\tau_\phi)\right\}$$

The primes were not included to simplify the equations. We use (8.4) with values of l_1 = .050595 m, l_2 = 0.0253 m and l_3 = 0.04382 m and appropriate values of the mass and moment of inertia to get the full-state linearized equations of motion in state-space form for small linear and angular position variations around an operating point.

$$
\begin{bmatrix} \dot{\tilde{x}} \\ \dot{\tilde{y}} \\ \dot{\tilde{z}} \\ \dot{\tilde{u}} \\ \dot{\tilde{v}} \\ \dot{\tilde{w}} \\ \dot{\tilde{\psi}} \\ \dot{\tilde{\theta}} \\ \dot{\tilde{\phi}} \\ \dot{\tilde{p}} \\ \dot{\tilde{q}} \\ \dot{\tilde{r}} \end{bmatrix}
=
\begin{bmatrix}
0 & 0 & 0 & 1 & 0 & 0 & 0 & 0 & 0 & 0 & 0 & 0 \\
0 & 0 & 0 & 0 & 1 & 0 & 0 & 0 & 0 & 0 & 0 & 0 \\
0 & 0 & 0 & 0 & 0 & 1 & 0 & 0 & 0 & 0 & 0 & 0 \\
0 & 0 & 0 & 0 & 0 & 0 & 0 & 9.8100 & 0 & 0 & 0 & 0 \\
0 & 0 & 0 & 0 & 0 & 0 & -9.8100 & 0 & 0 & 0 & 0 & 0 \\
0 & 0 & 0 & 0 & 0 & 0 & 0 & 0 & 0 & 0 & 0 & 0 \\
0 & 0 & 0 & 0 & 0 & 0 & 0 & 0 & 0 & 1 & 0 & 0 \\
0 & 0 & 0 & 0 & 0 & 0 & 0 & 0 & 0 & 0 & 1 & 0 \\
0 & 0 & 0 & 0 & 0 & 0 & 0 & 0 & 0 & 0 & 0 & 1 \\
0 & 0 & 0 & 0 & 0 & 0 & 0 & 0 & 0 & 0 & 0 & 0 \\
0 & 0 & 0 & 0 & 0 & 0 & 0 & 0 & 0 & 0 & 0 & 0 \\
0 & 0 & 0 & 0 & 0 & 0 & 0 & 0 & 0 & 0 & 0 & 0
\end{bmatrix}
\begin{bmatrix} \tilde{x} \\ \tilde{y} \\ \tilde{z} \\ \tilde{u} \\ \tilde{v} \\ w \\ \tilde{\psi} \\ \tilde{\theta} \\ \tilde{\phi} \\ \tilde{p} \\ \tilde{q} \\ \tilde{r} \end{bmatrix}
+
\begin{bmatrix}
0 & 0 & 0 & 0 & 0 & 0 \\
0 & 0 & 0 & 0 & 0 & 0 \\
0 & 0 & 0 & 0 & 0 & 0 \\
0 & 0 & 0 & 0 & 3.24455 & -3.24455 \\
0 & 0 & 0 & -3.744 & 1.8720 & 1.8720 \\
3.744 & 3.744 & 3.744 & 0 & 0 & 0 \\
0 & 0 & 0 & 0 & 0 & 0 \\
0 & 0 & 0 & 0 & 0 & 0 \\
0 & 0 & 0 & 0 & 0 & 0 \\
0 & 125.464 & -125.464 & 0 & 0 & 0 \\
-144.942 & 72.471 & 72.471 & 0 & 0 & 0 \\
0 & 0 & 0 & -75.674 & -75.674 & -75.674
\end{bmatrix}
\begin{bmatrix} F_1 \\ F_2 \\ F_3 \\ F_4 \\ F_5 \\ F_6 \end{bmatrix}
\tag{8.8}
$$

The coupling terms between the vertical and the lateral modes exist due to the following relations:

$$
\dot{\tilde{u}} = 9.81\tilde{\theta} + f(u), \ \dot{\tilde{v}} = -9.81\tilde{\psi} + f(u) \tag{8.9}
$$

Since the maximum values of $\tilde{\theta}$ and $\tilde{\psi}$ are of the order of 1.5 mrad and their influence on the velocities $\dot{\tilde{u}}$ and $\dot{\tilde{v}}$ are less than 1.5% of their values. Thus we may neglect the effect of these coupling terms between the vertical and horizontal modes, and the linearized small-signal lateral mode dynamics can be represented as follows:

$$\begin{bmatrix} \dot{\tilde{x}} \\ \dot{\tilde{y}} \\ \dot{\tilde{\phi}} \\ \dot{\tilde{u}} \\ \dot{\tilde{v}} \\ \dot{\tilde{r}} \end{bmatrix} = \begin{bmatrix} 0 & 0 & 0 & 1 & 0 & 0 \\ 0 & 0 & 0 & 0 & 1 & 0 \\ 0 & 0 & 0 & 0 & 0 & 1 \\ 0 & 0 & 0 & 0 & 0 & 0 \\ 0 & 0 & 0 & 0 & 0 & 0 \\ 0 & 0 & 0 & 0 & 0 & 0 \end{bmatrix} \begin{bmatrix} \tilde{x} \\ \tilde{y} \\ \tilde{\phi} \\ \tilde{u} \\ \tilde{v} \\ \tilde{r} \end{bmatrix} + \begin{bmatrix} 0 & 0 & 0 \\ 0 & 0 & 0 \\ 0 & 0 & 0 \\ 0 & 3.24455 & -3.24455 \\ -3.744 & 1.8720 & 1.8720 \\ -75.674 & -75.674 & -75.674 \end{bmatrix} \begin{bmatrix} F_4 \\ F_5 \\ F_6 \end{bmatrix} \tag{8.10}$$

$$\boldsymbol{y} = \begin{bmatrix} 1 & 0 & 0 & 0 & 0 & 0 \\ 0 & 1 & 0 & 0 & 0 & 0 \\ 0 & 0 & 1 & 0 & 0 & 0 \\ 0 & 0 & 0 & 1 & 0 & 0 \\ 0 & 0 & 0 & 0 & 1 & 0 \\ 0 & 0 & 0 & 0 & 0 & 1 \end{bmatrix} \begin{bmatrix} \tilde{x} \\ \tilde{y} \\ \tilde{\phi} \\ \tilde{u} \\ \tilde{v} \\ \tilde{r} \end{bmatrix} \tag{8.11}$$

8.2 Linear Quadratic Regulation for Horizontal Control

The dynamic model of the maglev stage shown in (8.11) can represented in the standard form as

$$\dot{\boldsymbol{x}}(t) = A\boldsymbol{x}(t) + B\boldsymbol{u}(t) \tag{8.12}$$

$$\boldsymbol{y}(t) = C\boldsymbol{x}(t) \tag{8.13}$$

where $\boldsymbol{x}$ is the state vector, $\boldsymbol{u}$ is the input vector to the plant and $\boldsymbol{y}$ is the output vector of the plant. This makes a LQR problem a deterministic initial value problem with non-zero initial states where all the states known and the regulator takes the system to the zero state while minimizing the performance index [61]. The performance index is defined as

$$J(\boldsymbol{x}(\cdot),\boldsymbol{u}(\cdot),t_0)=\int_{t_0}^{\infty}\left(\boldsymbol{u}^T(t)R\boldsymbol{u}(t)+\boldsymbol{x}^T(t)Q\boldsymbol{x}(t)\right)dt \tag{8.14}$$

This time-invariant infinite-time regulator problem is a minimization problem to find an optimal control $\boldsymbol{u}^*$ to minimize J. The solution of this problem is well-known and can be found in texts on optimal control such as [61]. For any initial state the optimal solution is

$$u(t)=-K_r x(t), \tag{8.15}$$

where $K_r=R^{-1}B^TP$. The P is the unique positive-semidefinite symmetric solution to the algebraic Riccati equation [62] given by

$$A^TP+PA-PBR^{-1}B^TP+Q=0\,. \tag{8.16}$$

The Q and R are the weighting matrices that we design to penalize the states or the control effort to optimize the performance in terms of minimum overshoot, settling time and steady-state error while not saturating the actuators. The LQR controller is a regulator therefore it regulates the output of the system to be zero. However we need the system to move at different commanded positions that are not zero. So use the error value, i.e. difference between the commanded position and the actual position as the states of the system. Therefore the modified states of the system are defined as

$$\begin{aligned}
\Delta x &= x - x^{*}, \\
\Delta y &= y - y^{*}, \\
\Delta \phi &= \phi - \phi^{*}, \qquad (8.17) \\
\Delta u &= u - u^{*}, \\
\Delta v &= v - v^{*}, \\
\Delta r &= r - r^{*},
\end{aligned}$$

where x^*, y^*, ϕ^*, u^*, v^* and r^* are the commanded values and x, y, ϕ, u, v and r are the states measured by sensors. Therefore our new system becomes

$$\Delta \dot{\boldsymbol{x}}(t) = A\Delta \boldsymbol{x}(t) + B\Delta \boldsymbol{u}(t) \qquad (8.18)$$

$$\Delta \boldsymbol{y}(t) = C\Delta \boldsymbol{x}(t)\,. \qquad (8.19)$$

In the regulation problem defined above we get finite steady-state error in the step commands. The reason behind is that the LQR controllers have no integrator. Thus we need to augment the controller with integrators to eliminate the steady-state error. In our experiments our target is to get the positioner at the desired position, i.e. we are interested only in position command tracking, so we use three integrators each for positions x, y, and ϕ.

Consider the plant defined by the following equations in state-space form

$$\dot{\boldsymbol{x}}_p = A_p \boldsymbol{x}_p + B_p \boldsymbol{u}_p$$

$$\boldsymbol{y}_p = C_p \boldsymbol{x}_p \,. \tag{8.20}$$

Defining a new state vector $\boldsymbol{z}_p$ as

$$\dot{\boldsymbol{z}}_p = \boldsymbol{y}_p = C_p \boldsymbol{x}_p \,. \tag{8.21}$$

We get the augmented system dynamics as:

$$\begin{bmatrix} \dot{\boldsymbol{x}}_p \\ \dot{\boldsymbol{\xi}}_p \end{bmatrix} = \begin{bmatrix} A_p & 0 \\ C_p & 0 \end{bmatrix} \begin{bmatrix} \boldsymbol{x}_p \\ \boldsymbol{\xi}_p \end{bmatrix} + \begin{bmatrix} B_p \\ 0 \end{bmatrix} \boldsymbol{u}_p$$

$$\boldsymbol{y}_p = \begin{bmatrix} C_p & 0 \end{bmatrix} \begin{bmatrix} \boldsymbol{x}_p \\ \xi_p \end{bmatrix} \tag{8.22}$$

The augmented system with nine states can now be represented as

$$\begin{bmatrix} \dot{\tilde{x}} \\ \dot{\tilde{y}} \\ \dot{\tilde{\phi}} \\ \dot{\tilde{u}} \\ \dot{\tilde{v}} \\ \dot{\tilde{r}} \\ \dot{\xi}_1 \\ \dot{\xi}_2 \\ \dot{\xi}_3 \end{bmatrix} = \begin{bmatrix} 0 & 0 & 0 & 1 & 0 & 0 & 0 & 0 & 0 \\ 0 & 0 & 0 & 0 & 1 & 0 & 0 & 0 & 0 \\ 0 & 0 & 0 & 0 & 0 & 1 & 0 & 0 & 0 \\ 0 & 0 & 0 & 0 & 0 & 0 & 0 & 0 & 0 \\ 0 & 0 & 0 & 0 & 0 & 0 & 0 & 0 & 0 \\ 0 & 0 & 0 & 0 & 0 & 0 & 0 & 0 & 0 \\ 1 & 0 & 0 & 0 & 0 & 0 & 0 & 0 & 0 \\ 0 & 1 & 0 & 0 & 0 & 0 & 0 & 0 & 0 \\ 0 & 0 & 1 & 0 & 0 & 0 & 0 & 0 & 0 \end{bmatrix} \begin{bmatrix} \tilde{x} \\ \tilde{y} \\ \tilde{\phi} \\ \tilde{u} \\ \tilde{v} \\ \tilde{r} \\ \xi_1 \\ \xi_2 \\ \xi_3 \end{bmatrix} + \begin{bmatrix} 0 & 0 & 0 \\ 0 & 0 & 0 \\ 0 & 0 & 0 \\ 0 & 3.24455 & -3.24455 \\ -3.744 & 1.8720 & 1.8720 \\ -75.674 & -75.674 & -75.674 \\ 0 & 0 & 0 \\ 0 & 0 & 0 \\ 0 & 0 & 0 \end{bmatrix} \begin{bmatrix} F_4 \\ F_5 \\ F_6 \end{bmatrix}$$

$$\boldsymbol{y}_p = \begin{bmatrix} 1 & 0 & 0 & 0 & 0 & 0 & 0 & 0 & 0 \\ 0 & 1 & 0 & 0 & 0 & 0 & 0 & 0 & 0 \\ 0 & 0 & 1 & 0 & 0 & 0 & 0 & 0 & 0 \end{bmatrix} \begin{bmatrix} \tilde{x} \\ \tilde{y} \\ \tilde{\phi} \\ \tilde{u} \\ \tilde{v} \\ \tilde{r} \\ \xi_1 \\ \xi_2 \\ \xi_3 \end{bmatrix}. \tag{8.23}$$

We use 'lqr' function in Matlab® to calculate the gain matrix. We performed iterations on weighting matrices of Q and R, applied them to the system and recorded the response to get the optimal values. Controllers calculated using initial values of the weighting matrices resulted very the large settling time (around 6–10 sec). After several iterations the values of Q and R matrices were calculated to be

$$Q = diag\left(\begin{bmatrix} 2\times10^6 & 2\times10^6 & 2\times10^6 & 10^3 & 10^3 & 10^3 & 10^8 & 10^8 & 10^8 \end{bmatrix}\right)$$

$$R = diag\left(\begin{bmatrix} 1 & 1 & 10^3 \end{bmatrix}\right).$$

The corresponding continuous time gain matrix (K) was calculated using 'lqr' comes out to be

$$K = \begin{bmatrix} -539.361 & -1062.85 & -1147.83 & -12.00 & -27.07 & -22.62 & -3249.30 & -6288.98 & -7063.34 \\ 651.30 & 998.213 & -1147.79 & 17.452 & 23.923 & -22.621 & 3825.02 & 5956.59 & -7063.16 \\ -62.852 & 36.310 & -2.9411 & -4.4859 & 2.5916 & -0.15689 & -273.516 & 158.011 & -14.8647 \end{bmatrix}$$

The closed-loop poles of the system are placed at -7.0, 2 poles at -7.2, -44.1, -46.7, -137.1, -3385.8, $-11 \pm 11.4i$. This indicates that the closed-loop system stable. We get the discrete-time controller using ‘lqrd’ function of Matlab® since this controller is applied in discrete time at the 5-kHz sampling frequency by the DSP system. The discrete-time gain matrix is

$$K_d = \begin{bmatrix} -535.1228 & -1040.19 & -841.530 & -11.9150 & -26.6160 & -16.6509 & -3223.43 & -6150.03 & -5175.55 \\ 633.7926 & 983.221 & 841.500 & 17.1020 & 23.6198 & -16.6502 & 3717.54 & 5864.74 & -5175.37 \\ -62.7030 & 36.2243 & -2.6310 & -4.4793 & 2.5878 & -0.1445 & -272.761 & 157.576 & -12.9577 \end{bmatrix}$$

This controller designed above was implemented on the system, and step responses were taken. Fig. 8-1 and Fig. 8-2 show 100 μm step responses in x and y. The plots show that the settling time is around 0.5 s. The peak overshoot is 35% in x and 45% in y. Fig. 8-3 shows step response in ϕ that settles in around 1 s, and the peak overshoot is less than 10%.

The benefit of this controller is that the overshoots were smaller. However, the settling time was longer. To achieve faster settling time another controller was designed in which the weights on the integrator states were increased as

$$Q = diag\left(\begin{bmatrix} 2\times10^6 & 2\times10^6 & 2\times10^6 & 10^3 & 10^3 & 10^3 & 10^{10} & 10^{10} & 10^{10} \end{bmatrix}\right)$$

$$R = diag\left(\begin{bmatrix} 1 & 1 & 10^3 \end{bmatrix}\right).$$

The calculated continuous time and discrete time gain matrices were calculated to be

$$K = \begin{bmatrix} -1074.97 & -2210.68 & -2056.69 & -13.1464 & -33.3356 & -22.8322 & -32493.02 & -62889.75 & -70633.43 \\ 1378.00 & 2035.68 & -2056.63 & 22.3045 & 28.0453 & -22.831 & 38250.16 & 59565.95 & -70631.58 \\ -215.196 & 124.323 & -8.1991 & -8.1902 & 4.7317 & -0.2567 & -2735.16 & 1580.11 & -148.647 \end{bmatrix}$$

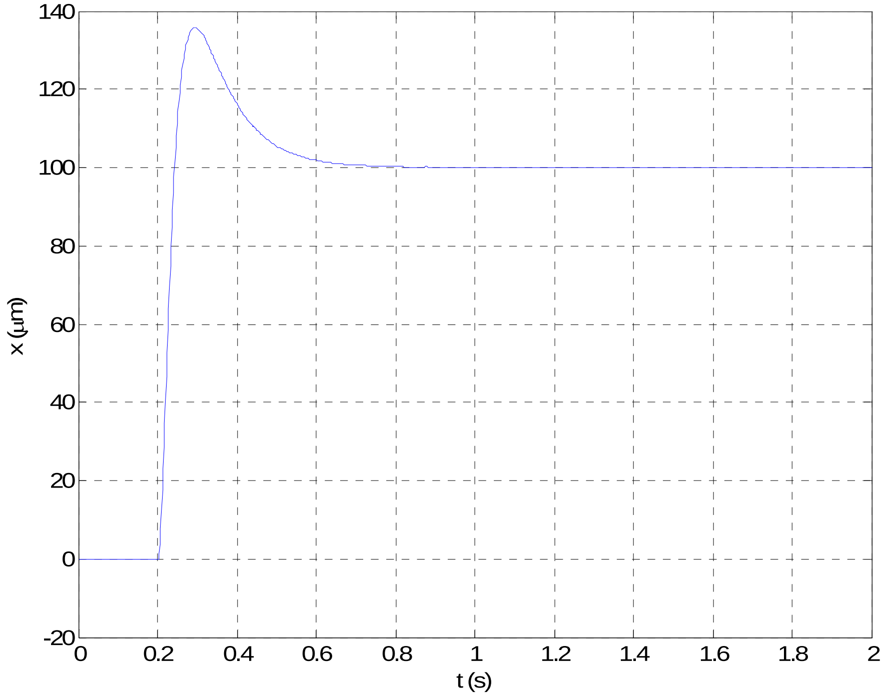

Fig. 8-1. 100-μm step in *x*.

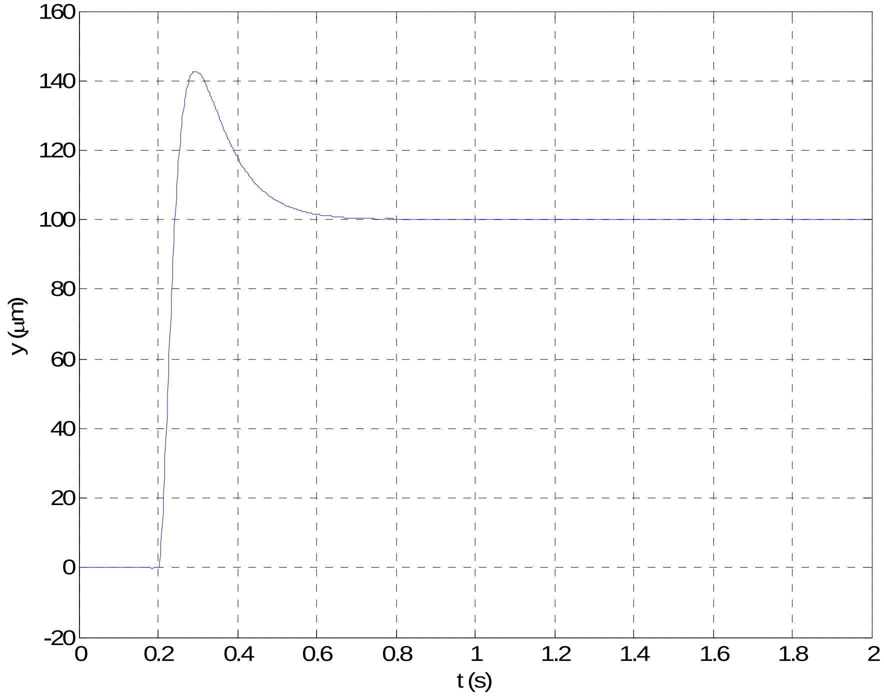

Fig. 8-2. 100-μm step in *y*.

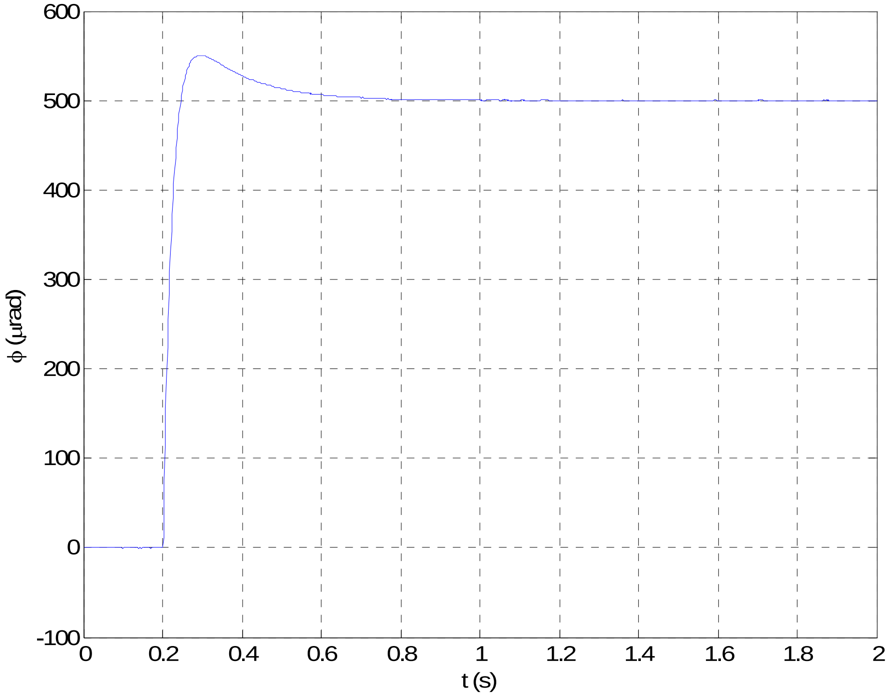

Fig. 8-3. 500-μrad step in *ϕ*.

$$K_d = \begin{bmatrix} -1062.88 & -2161.54 & -1505.95 & -13.0056 & -32.7682 & -16.7949 & -32107.34 & -61262.66 & -51549.25 \\ 1341.46 & 2000.64 & -1505.89 & 21.8833 & 27.6398 & -16.7942 & 37032.98 & 58418.63 & -51547.42 \\ -214.339 & 123.828 & -7.6245 & -8.1684 & 4.7191 & -0.2500 & -2721.06 & 1571.97 & -129.1844 \end{bmatrix}$$

The closed-loop poles of the system are placed at -25.7, -139.4, -13.7 ± 22.4*i*, -45.2 ± 35.3*i* and -45.6 ± 32.9*i* all in rad/s. Therefore the closed-loop system is close loop stable. The performance of this controller is shown in Fig. 8-4 to Fig. 8-6. For translations the settling time was reduced to 0.2 s, but the peak overshoot increased to around 50%. For rotation about *ϕ*, the overshoot is around 20% and the settling time is less than 0.2s. The comparison of the two controller responses shows that both the controllers have their own benefits and drawbacks. Thus the controller should be chosen depending on specifications from the application of the maglev stage.

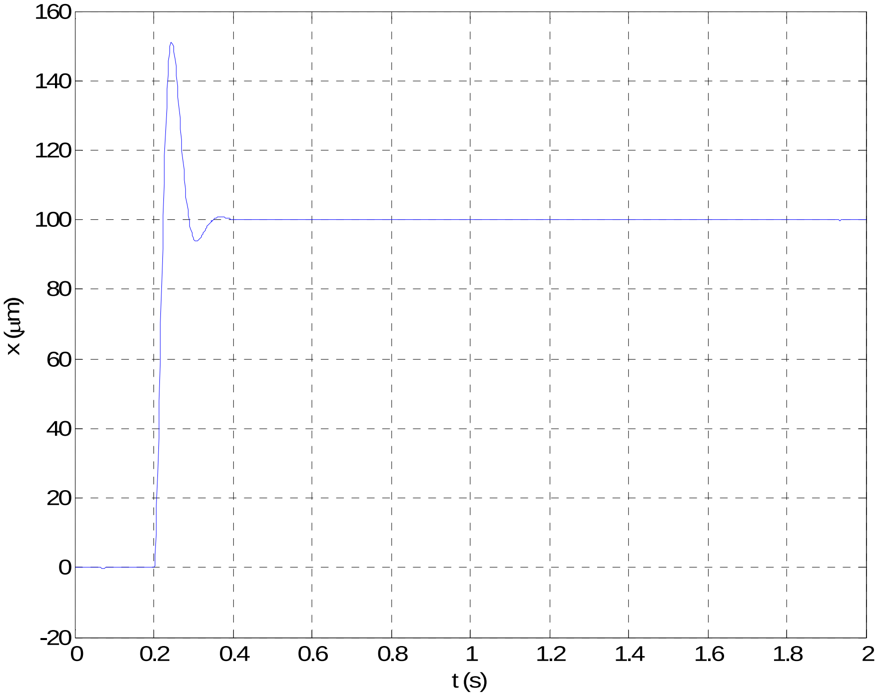

Fig. 8-4. 100-μm step in *x*.

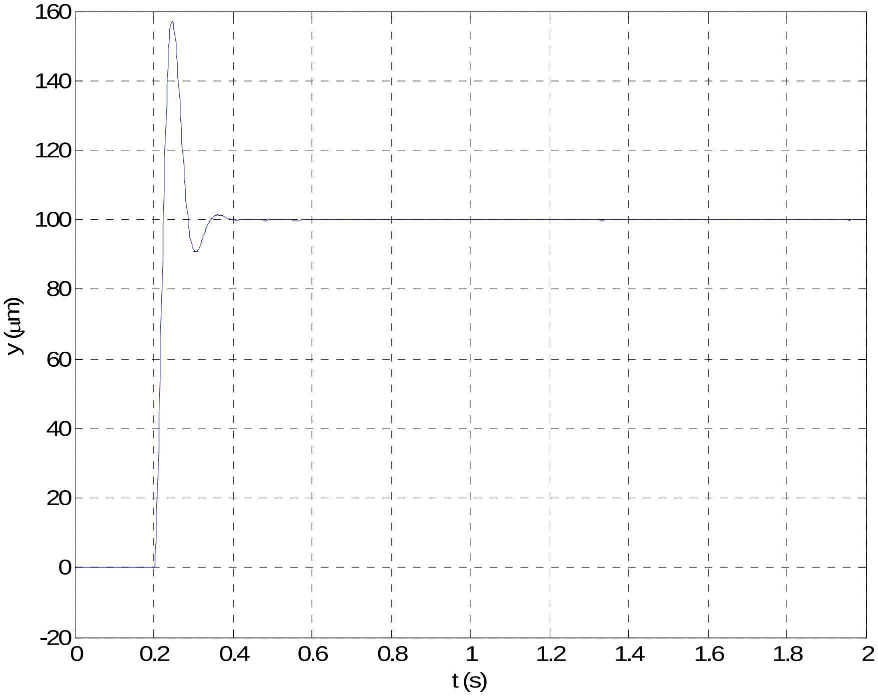

Fig. 8-5. 100-μm step in *y*.

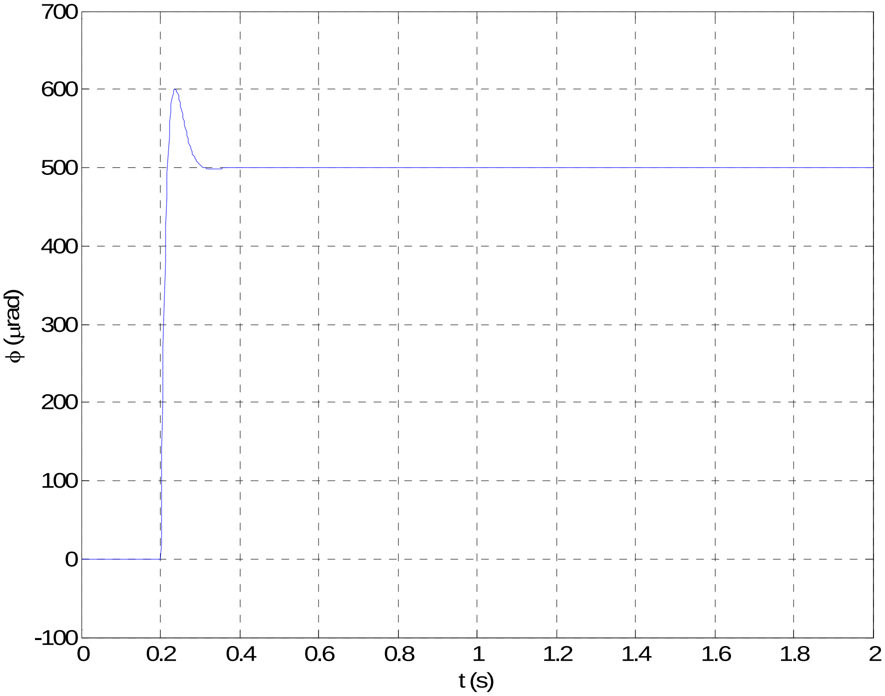

Fig. 8-6. 500-μrad step in ϕ.

8.3 Feedforward Decoupling Compensation

Any dynamic coupling between the vertical and horizontal modes of motion may create unwanted erroneous perturbation. This unmodeled dynamics may degrade the stability and transient performance of the control system [28]. Therefore while designing the stage we kept this in mind and tried to minimize this coupling by appropriate placement of actuators.

In the dynamic model developed in Chapter VII no dynamic coupling was assumed between the horizontal and vertical modes. However, there is coupling between the horizontal and vertical motions. Fig. 8-7 and Fig. 8-8 show 100-μm steps in x and y axes along with the purterbation in other 5 axes. Fig. 8-7 shows that any step in x causes a significant disturbance

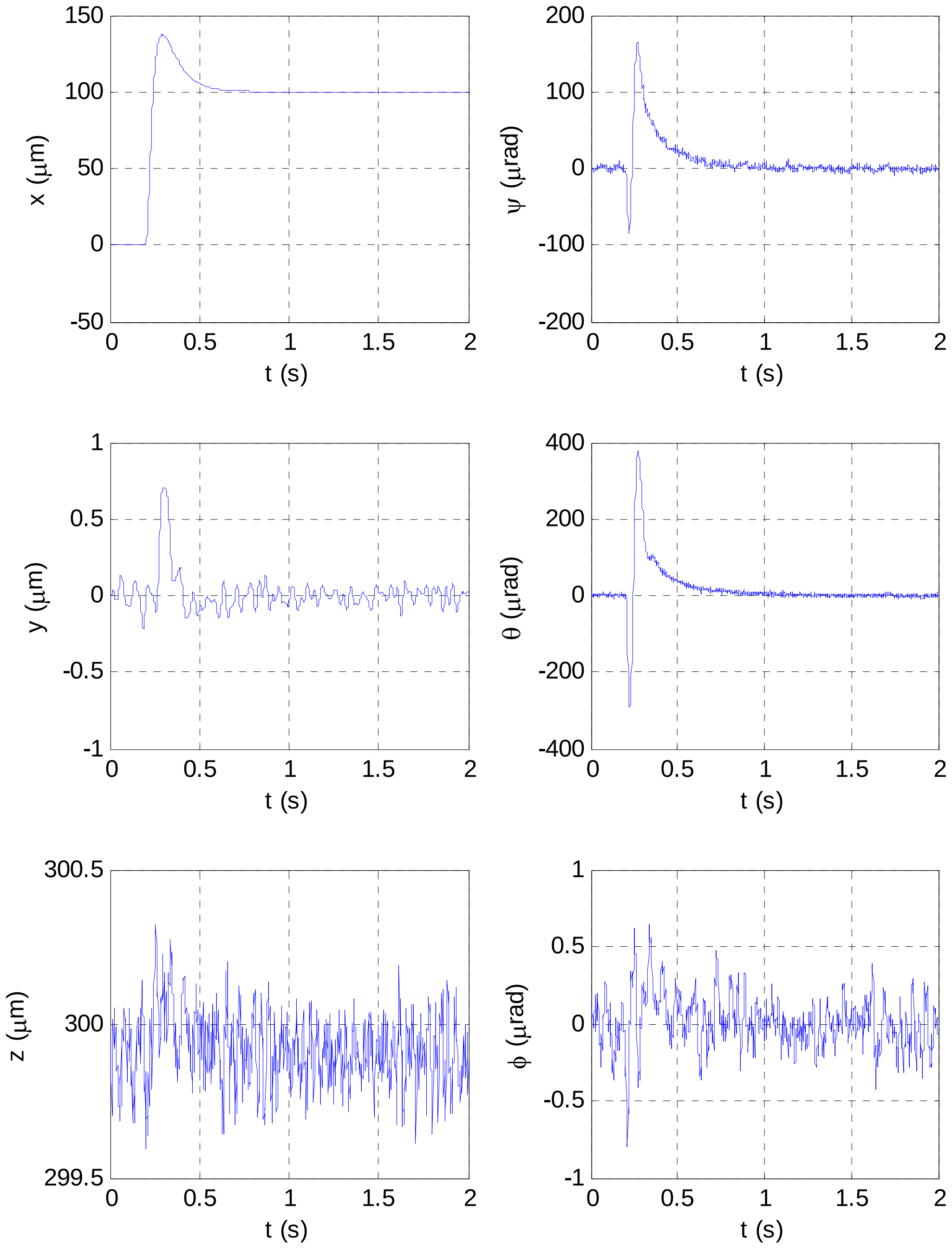

Fig. 8-7. 100-μm step in *x* and perturbations in other 5 axes.

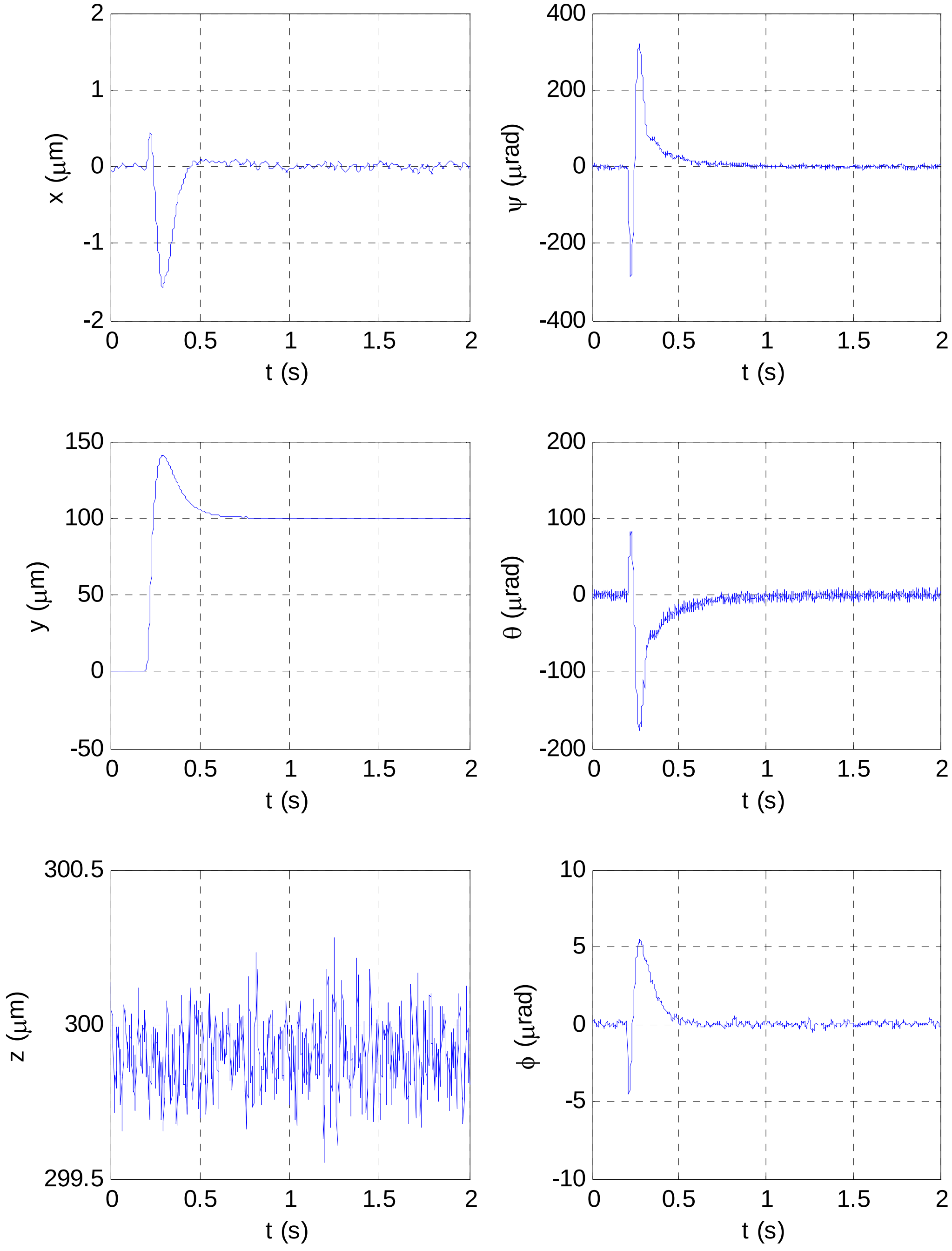

Fig. 8-8. 100-μm step in *y* and perturbations in other 5 axes.

in rotation about *y*, i.e. θ and small disturbances in other axes. Similarly Fig. 8-8 shows that any step in *y* causes a significant disturbance in rotation about *x*, i.e. *ψ* and small disturbances in other 5 axes. The possible reason for this coupling is that the platen CM does not lie in the plane of horizontal forces. Hence, horizontal actuation forces would generate erroneous coupling moments in the vertical modes, e.g. *ψ* and *θ*. To mitigate this modeling error, we applied a feedforward correction methodology as shown in Fig. 8-9. The compensation moment equal to the output actuation force f_x multiplied by the length of moment arm was subtracted to cancel the perturbation in the *θ*-axis from the *x*-axis. A similar error moment correction cancels the perturbation in the *ψ* -axis from the *y*-axis.

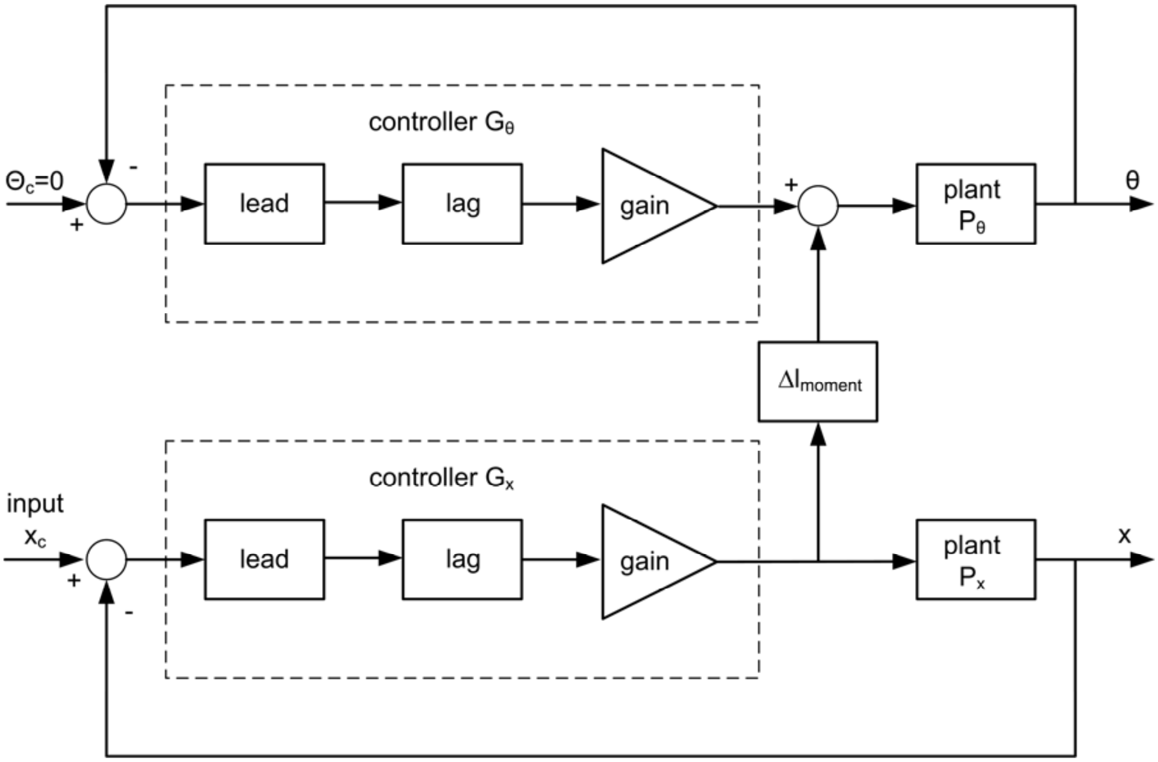

Fig. 8-9. Block diagram showing feedforward decoupling compensation technique.

The applied feedforward decoupling compensation shows satisfactory results. 100-μm step responses in the *x*-axis without and with decoupling compensation and their effects on vertical modes are shown in Fig. 8-10 and Fig. 8-11. We can see from Fig. 8-10 that the peak of the disturbance in θ has been reduced by around 90% and in ψ by around 75%. Also Fig. 8-11 shows that the disturbance in ψ has been reduced by around 90% and in θ by around 75%. Although this added some disturbances in *z* but its amplitude is insignificant as compared to the improvements is θ and ψ.

8.4 Feedback Linearization of Force

The block diagram shown in Fig. 8-12 indicates that the information flow in the feedback loop. The error in *x* is fed to controller, and the controller calculates the desired force (f_x) to be applied. Current (i_x), the plant input, is that is to be calculated depending on the value of f_x. While modeling the system in Chapter VII, we assumed that the force applied by electromagnetic actuators was proportional to current and not a function of position. However if the translation of permanent magnet is larger, this assumption is not valid because several nonlinearities come into picture. The modeling of actuators shows that the force is actually a complex function of relative position of magnet in *x*, *y* and *z* as can be seen in (8.24). All the other parameters are defined in Fig. 5-5.

$$\begin{aligned} F_{v1} = {} & \frac{i\sigma_m}{4\pi A}\left[\int_{-d/2}^{d/2}\int_{-d/2}^{d/2}\int_{-h/2}^{h/2}\int_{a}^{b}\int_{0}^{x}\frac{(x-p)}{[(x-p)^2+(y-q)^2+(z-r_1)^2]^{1.5}}\,dydxdzdpdq\right] \\ & -\frac{i\sigma_m}{4\pi A}\left[\int_{-d/2}^{d/2}\int_{-d/2}^{d/2}\int_{-h/2}^{h/2}\int_{a}^{b}\int_{0}^{x}\frac{(x-p)}{[(x-p)^2+(y-q)^2+(z-r_2)^2]^{1.5}}\,dydxdzdpdq\right] \end{aligned} \tag{8.24}$$

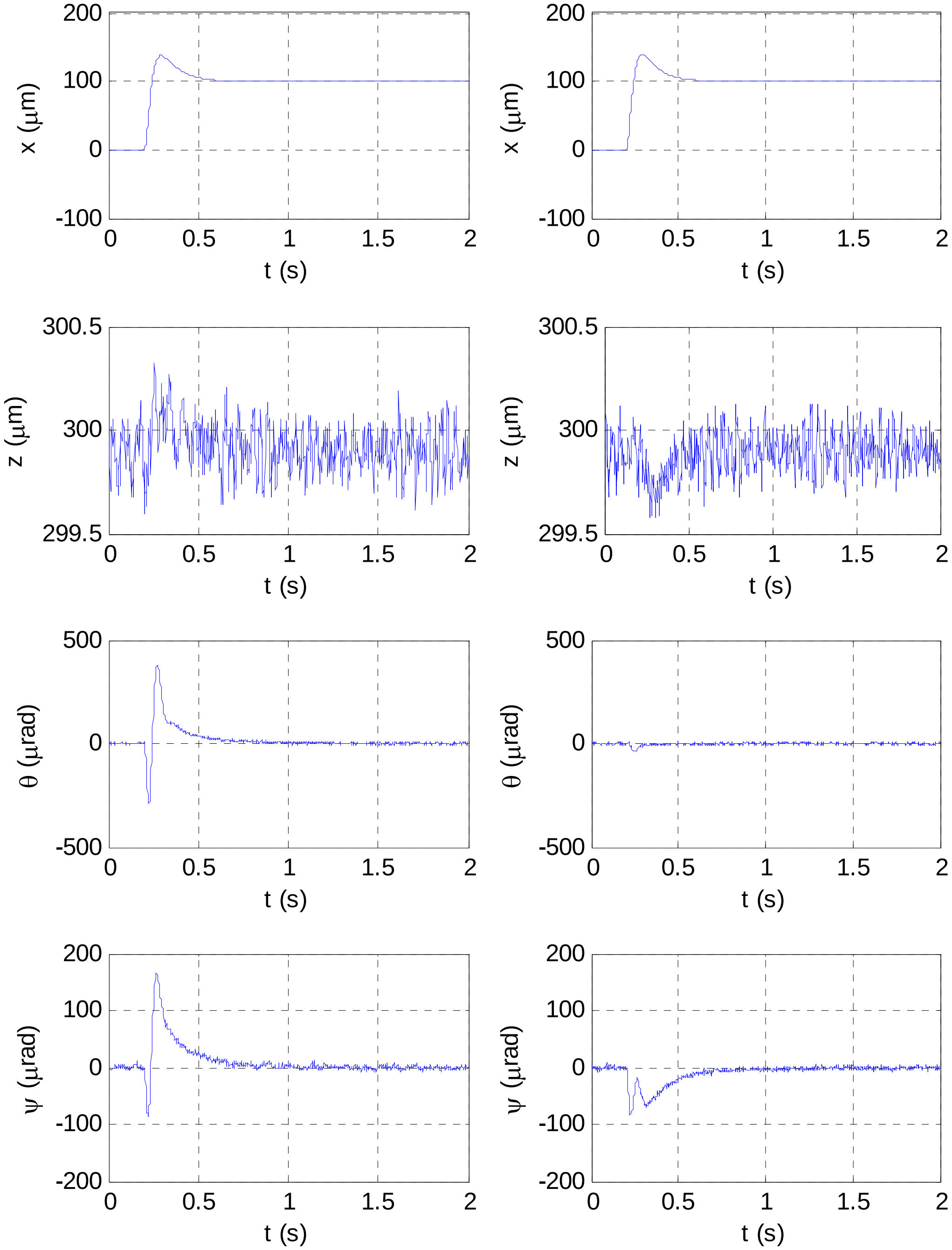

(a) (b)

Fig. 8-10. 100-µm step in *x* and disturbance in vertical modes (a) without (b) with the feedforward decoupling compensation.

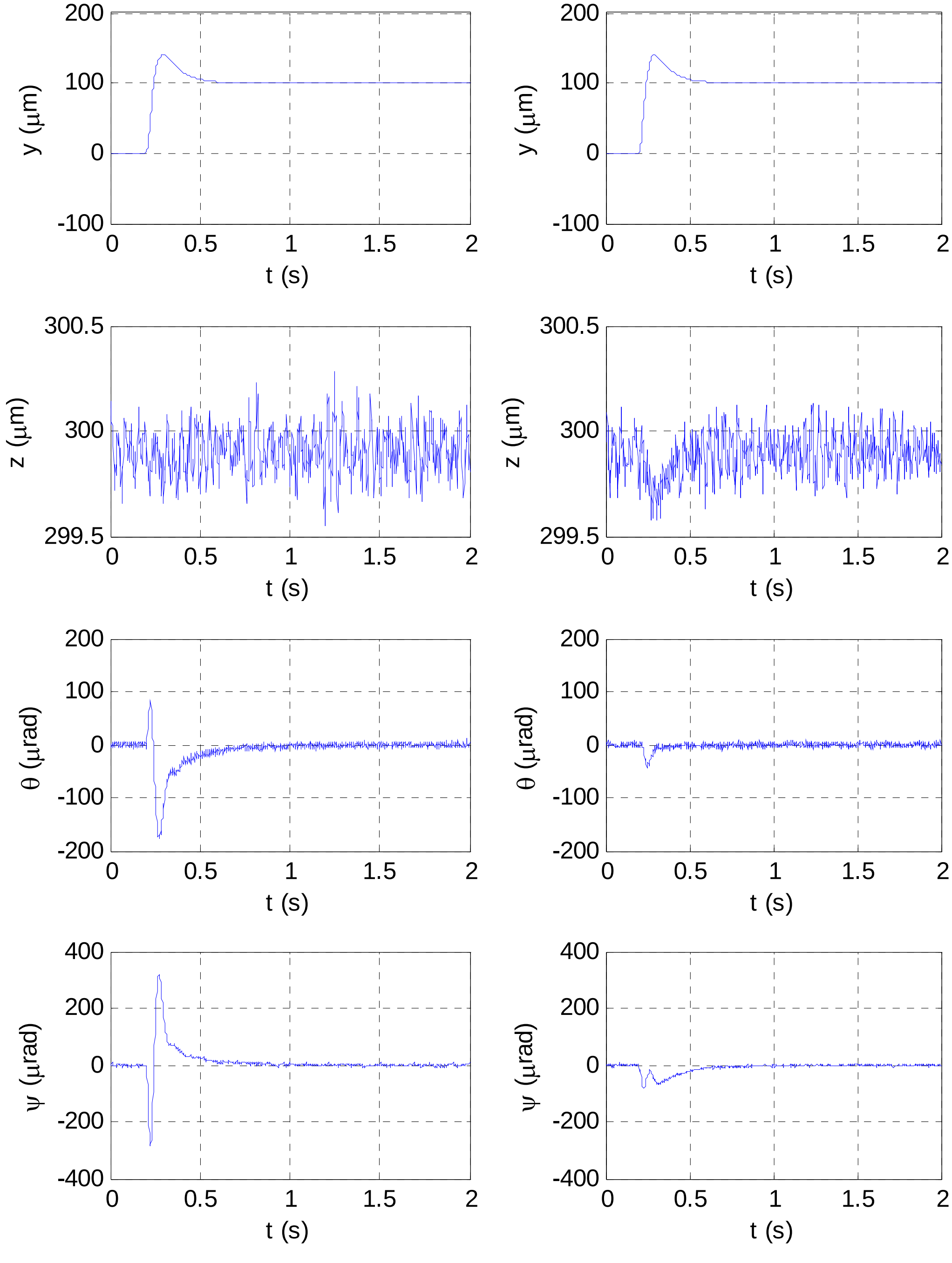

(a) (b)

Fig. 8-11. 100 μm steps in *y* and perturbations in vertical modes (a) without (b) with the feedforward decoupling compensation.

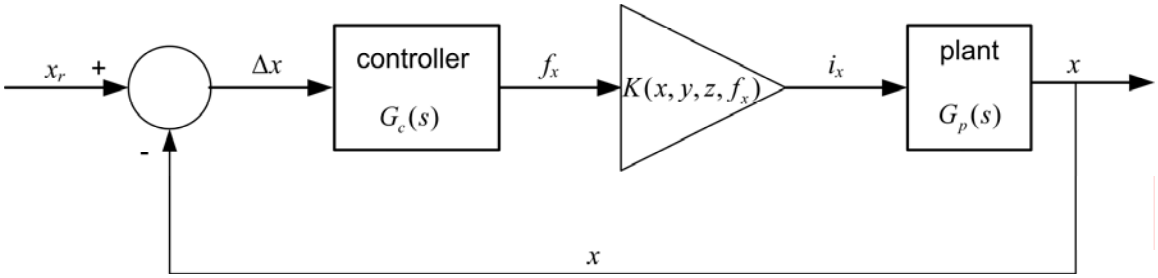

Fig. 8-12. Feedback control loop showing the information flow and conversion.

Feedback linearization has been proved to be a very successful technique for such systems [63–65]. French and Rogers used the approximate parameterizations for adaptive feedback linearization [63]. Approximate state-feedback linearization using spline functions was applied by Bortoff for single-input nonlinear systems [65]. A rotating inverted pendulum was used to demonstrate the improved performance.

We used a similar approach to overcome the nonlinearity of our system. The calculation of desired current to generate a particular force based on (8.24) can not be performed in realtime because it takes around 1 hr to calculate force at each point using Mathcad®. Therefore we calculate the force a certain points and use that value to estimate the force at other points. We use the “basic fitting” function in Matlab® and find an approximate 4th-order polynomial function that is closest to the calculated value. In Fig. 8-13 the symbol * shows the points at which we calculate the vertical force of the actuator, for 1 A of current and the continuous line is the approximate 4th-order polynomial curve that is given by

$$K_v = 1.412\times 10^8 h^4 - 4.497\times 10^6 h^3 + 7.7737\times 10^4 h^2 - 932.7h + 6.798\ \mathrm{N/A} \tag{8.25}$$

where h is the height of magnet from the top surface of coil and K_v is conversion factor. The value of current in any vertical actuator is calculated by division of the desired force with K_v after substitution of h at that instant for the actuator. Similarly for horizontal force we calculated forces from actuator at different horizontal gaps (g) between coil and magnet with 1 A of current in coil. Fig. 8-14 shows the calculated force at several gaps by * and the continuous line represents the 4th-order approximate polynomial that is given by

$$K_h = 2.502\times10^9 g^4 - 3.712\times10^7 g^3 + 2.309\times10^5 g^2 - 933.5g + 3.257\ \text{N/A} \tag{8.26}$$

The inverse of K_h is multiplied to the desired value of force to calculate the current i_h. These feedback linearization equations are implemented in the ISR on the DSP to calculate the desired current for a given value of force and position.

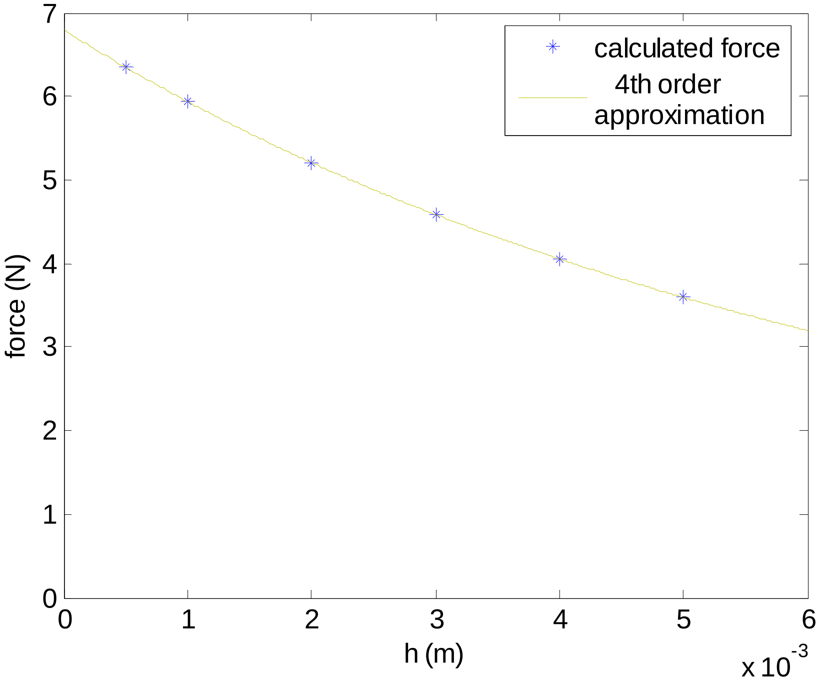

Fig. 8-13. Calculated vertical force at * points and plot of the approximate polynomial.

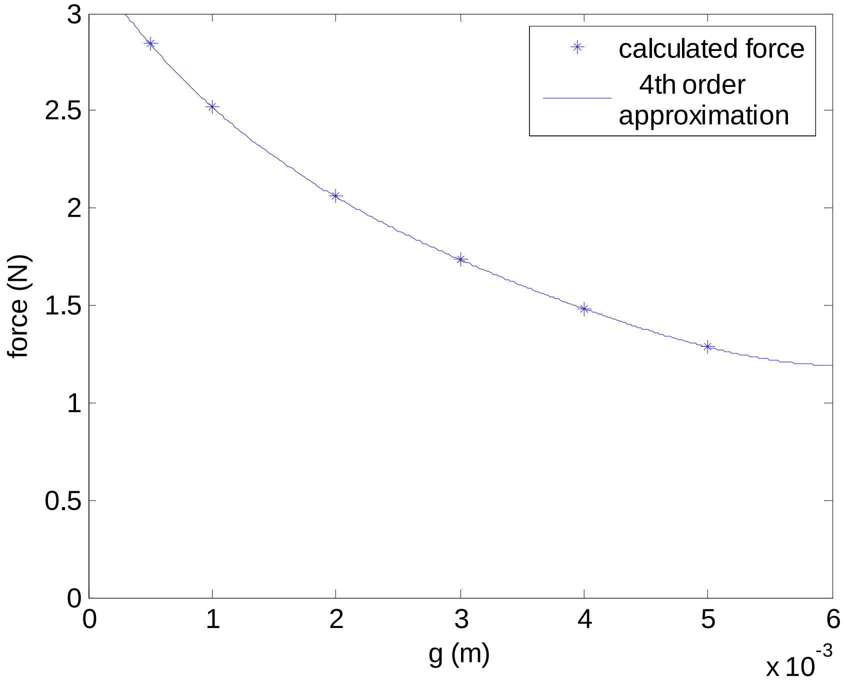

Fig. 8-14. Calculated horizontal force at * points and plot of the approximate polynomial.

8.5 Motion Control over Large Travel Range

By the successful application of feedback linearization discussed in the last section we were able to achieve larger travel range in *x* and *y*. Fig. 8-15 shows 5-mm ramp responses of the maglev stage as compared to the limited range of 1 mm without feedback linearization. This demonstrates that the maglev stage is capable of extended planar motions with the same nanometer order resolution. Fig. 8-16 shows motion of the platen in a circle of 5-mm diameter. This demonstrates the capability of large travel range planar motion capability of the maglev stage. A scanning motion in the area of 4 × 4 mm is shown in Fig. 8-17. The *y*-axis motions are slow scanning motion of velocity 0.8 mm/s and the diagonal motions are the rapid return motion with 4.12 mm/s velocity. This kind of motion is very popular for topographical imaging

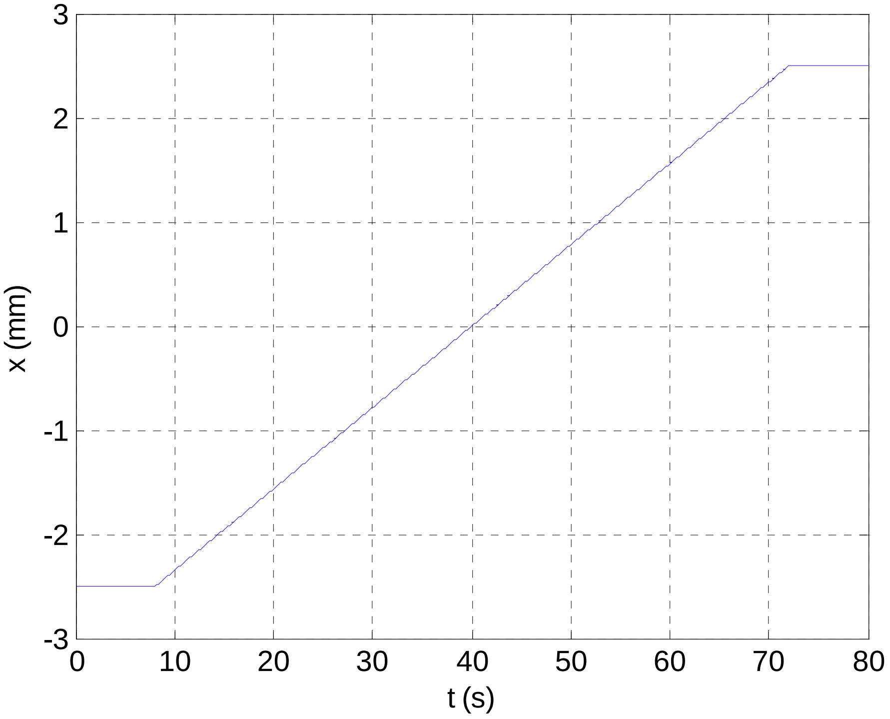

(a)

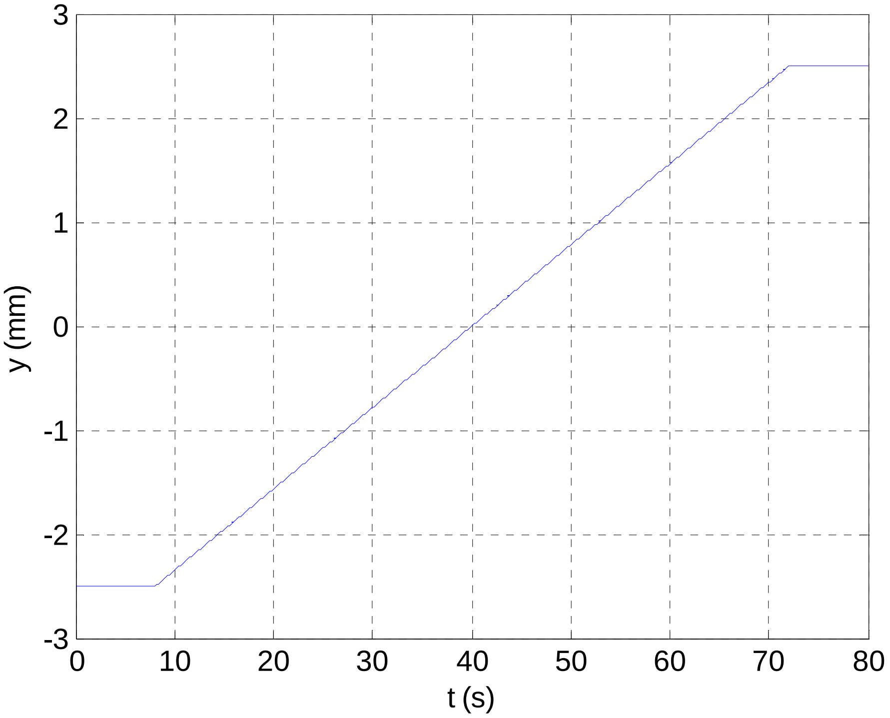

(b)

Fig. 8-15. 5-mm ramp motion followed in (a) *x* and (b) *y*.

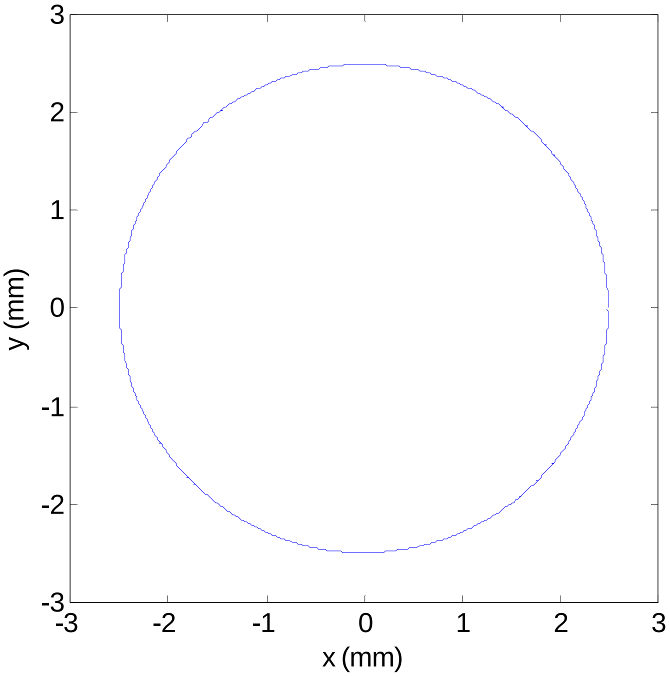

Fig. 8-16. 5-mm diameter circular motion in *x*-*y* plane.

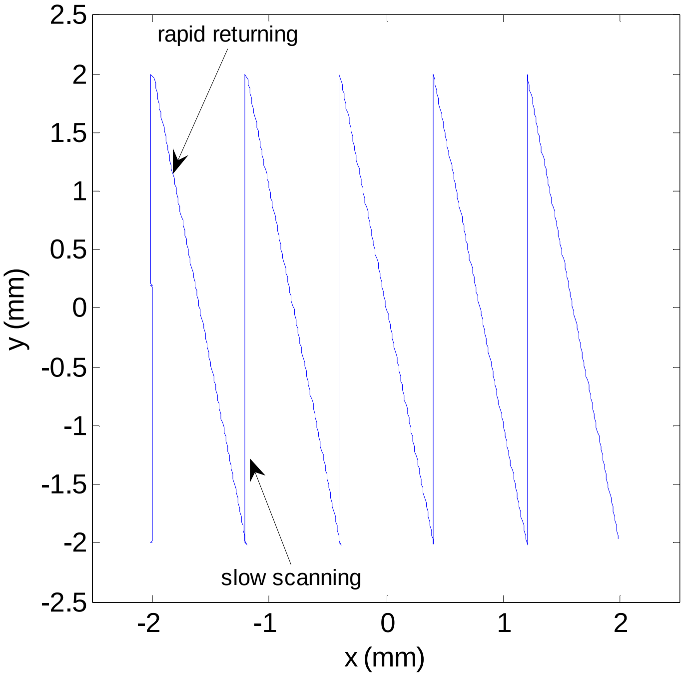

Fig. 8-17. 4 × 4-mm scanning motion in *x*-*y* plane.

of surfaces. The demonstration of large 3-D motion capability is shown in Fig. 8-18. This is a helix of 5 mm diameter and 200 μm height. Therefore this stage can be applied for precise manufacturing of objects with dimension up to 5 mm.

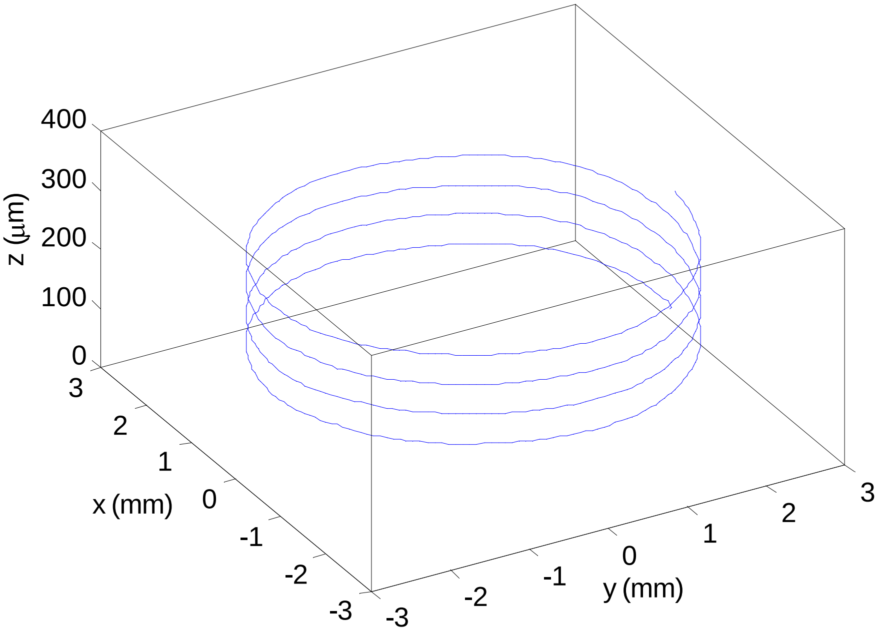

Fig. 8-18. 3-D helix motion with 5-mm diameter circle in *x*-*y* and 200 μm in *z*.

CHAPTER IX

CONCLUSIONS AND SUGGESTIONS OF FUTURE WORK

This chapter describes the achievements in this research and suggestions for future work that may help in improvement of the stage performance.

9.1 Conclusions

Precision in nanomanipulation has become the key to the development of the next-generation nanotechnology. The demand of ultra-high-resolution positioning stages is continuously increasing. Currently available stages are able to provide good resolution but over very short travel ranges on the order of several hundred micrometers. This limitation will significantly affect the nano-assembly processes when the process needs to be completed by several different tools. Moreover, prevailing stages have no or very small *z*-translation capabilities, which limits their use in micro-manufacturing processes such as μSTL or nano-indentation. The current nanotechnology requires the nanomanipulation stages that can move and position the specimen at various places and in the desired orientation with low amplitude of vibration. This motion need to be in multiple DOF, with long travel range at a nanoscale resolution.

This dissertation presented two novel maglev stages that fulfill all the requirements mentioned above. The maglev systems have no mechanical contact between the moving and stationary parts, which facilitates the maintenance of high position resolution. It also eliminates wear in the mechanical parts and increases their life spans, and does not require lubricants.

The first-generation maglev stage is compact in size and uses the minimum number of actuators required for 6-DOF motion generation. Prevailing precision positioning devices like STMs and AFMs are able to position in the travel range of 100 µm in 3 DOFs. However, this maglev device is capable of motion control in all 6 DOFs with the travel ranges of 300 µm in the *x*-, *y*-, and *z*-translations and 3.5 mrad in the θ-, ϕ-, and ψ-rotations. The position resolution is better than 5 nm with position noise less than 2 nm rms. All the experiments were performed in a usual lab environment on a vibration-isolation optical table. This implies that in a controlled atmosphere and with a better ADC board we could have improved the noise performance. However, the correction of the ambient factors requires much more resources, and was beyond the scope of this project.

We focused on the experimental demonstration of the fundamental working principles. The dynamic performance of the maglev system was demonstrated with various experimental results, such as following a saw-tooth trajectory of the whole travel range and consecutive steps of 5 nm. This system has the maximum speed capability of 0.5 m/s and the actuators are sized for 3-*g* acceleration (30 m/s^2) in horizontal directions. The light-weight, compact design led to insignificant power consumption of 15 mW by each horizontal actuator and 320 mW by each vertical actuator in steady state. The demonstration of small motions such as a 50-nm radius circle and a microscale 3-D parabolic verified the capability of this maglev device in extremely precise manipulation. Its capability to generate and control nanoscale motions in multiple axes can contribute significantly to the development of nanotechnology.

The second-generation maglev stage has travel range of 5 × 5 mm in the *x*- and *y*- axes and 500 µm in the *z*-axis. The *z*-axis travel range is limited by the capacitance-gauge specifications. However, we sized the vertical actuators that this stage could have a travel range of 5 mm in the *z*-axis as well with long-range sensors. The stage has noise level of 3 nm rms with maximum acceleration of 8 *g* in vertical and 2.5 *g* in horizontal directions, respectively. It can precisely orient and position an additional payload of 2 kg. This maglev stage has a very simple mechanical structure with a single moving part, which is easy and inexpensive to fabricate.

We discussed the novel actuation scheme and the design of the actuators. An extensive electromagnetic analysis of the actuator forces over the whole travel range was carried out. Experimental results confirmed the analysis with only a 4% maximum error. A dynamic model of the maglev system and modal force and displacement transformations were derived. The design and implementation of lead-lag controllers, linear quadratic regulator along with feedback linearization, and feedforward decoupling compensation was successfully done.

Applications of this maglev stage include nanomanipulation, fabrication, and assembly of nano-sized objects, 3-D rapid prototyping of micro-sized objects, and vibration isolation for delicate instrumentation. Several single and multi-axes experimental results demonstrated that maglev stage could be used as a positioner for μSTL [66–70] and nano-indentation applications. In summary, this maglev stage is a promising solution to nanopositioning requirements of the next-generation nanotechnology.

This concludes that the dissertation presented two 6-axes magnetic-levitation stages that are capable for precision positioning at nanoscale level. The development steps from basic design to testing were described in detail.

9.2 Suggestions for Future Work

Even though I tried to make the maglev instruments work at the best possible performance, there are certain issues that could not be addressed due to limitations in resources or time. To further improve the performance of the maglev stages there are several steps in different directions that can be taken such as

- Currently the *z*-axis motion is limited by the sensing range of the capacitance probes. Their replacement with any large-sensing-range sensors can significantly increase the *z* motion range of the second-generation stage because the actuators are capable of levitating the platen at more than 7 mm of height.
- Since the force from the electromagnetic actuators is a nonlinear function of position, we could not estimate and apply the exact force constant in the model. A further comprehensive analysis of the actuator force can improve the dynamic performance of the stage.
- Similar to the first-generation stage we can add some passive damping on the platen of the second stage. This will reduce structural vibrations.
- The analog sensors used for vertical-motion sensing performed not so well as the horizontal-motion sensors (laser interferometers). Due to coupling between the vertical and horizontal motions the noise in the vertical motions was transmitted to the horizontal motions. Therefore, if better sensors like laser interferometers are used for vertical-motion sensing too, the noise level of the maglev stage will be significantly improved.
- We used 16-bit ADCs and DACs. The ADC quantization and other noise from the data-acquisition card degraded the performance of the maglev stage. Use of a data-acquisition system with higher resolution and lower noise would definitely improve the noise performance of the stage.
- All the experiments of the maglev stages were performed in regular lab environments. Due to several mechanical-vibration sources in the building the noise in

the experiments was significantly increased. Also the atmospheric effects like change, in temperature or wind were not considered. With a less noisy environment or a better noise isolation system and correction of ambient effects may improve the stage performance.

- The last but not the least I would suggest applying this stage for creative applications like manipulation of nanoscale objects, topographical profiling of surfaces, fabrication of micro/nano parts using microstereolithography and their assembly.

REFERENCES

[1] U.S. Department of Energy website. “Nanoscale Science, Engineering and Technology Research Directions” [Online]. Available: http://www.science.doe.gov/bes/NNI.htm, (accessed on October, 2002).

[2] *Nanotechnology: Shaping the World Atom by Atom*, National Science and Technology Council, Committee in Technology, The Interagency Working Group on Nanoscience, Engineering and Technology (IWGN), September 1999.

[3] M. Sitti, “Survey of Nanomanipulation Systems,” in *Proceedings of the IEEE Conference on Nanotechnology*, Maui, HI, pp. 75–80, October 2001.

[4] M. Sitti and H. Hashimoto, “Controlled Pushing of Nanoparticles: Modeling and Experiments,” *IEEE/ASME Transactions on Mechatronics*, vol. 5, no. 2, pp. 199–211, June 2000.

[5] The Missouri Botanical Garden website. “Scanning Probe Microscopy” [Online]. Available: http://www.mobot.org/jwcross/spm/ (accessed on April 2, 2005).

[6] G. Binnig, H. Roher, C. H. Gerber, and E. Weibel, “Surface Studies by Scanning Tunneling Microscopy,” *Physical Review Letter*, vol. 49, no. 1, pp.57–61, July 5, 1982.

[7] R. M. Taylor II. *The Nanomanipulator: A Virtual-Reality Interface to a Scanning Tunneling Microscope*, Ph.D. dissertation, University of North Carolina at Chapel Hill, 1994.

[8] C. Bauer, A. Bugacov, B. E. Koel, A. Madhukar, N. Montoya, T. R. Ramachandran, A. A. G. Requicha, R. Resch, and P. Will, “Nanoparticle Manipulation by Mechanical Pushing: Underlying Phenomena and Real-Time Monitoring,” *Nanotechnology*, vol. 9, no. 4, pp. 360–364, December 1998.

[9] M. F. Yu, M. J. Dyer, H. W. Rohrs, X. K. Lu, K. D. Ausman, J. V. Her, and R. S. Ruoff, “Three-Dimensional Manipulation of Carbon Nanotubes under a Scanning Electron Microscope,” *Nanotechnology,* vol. 10, no. 3, pp. 244–252, September 1999.

[10] The Orbitz Laboratory MIT website. “Atomic Force Microscopy” [Online]. Available: http://web.mit.edu/cortiz/www/nanomechanics.html, (accessed on April 5, 2005).

[11] The Naval Research Laboratory website. “Atomic Force Microscopy” [Online]. Available: http://stm2.nrl.navy.mil/how-afm/how-afm.html, (accessed on April 5, 2005).

[12] G. Binnig, C. F. Quate, and C. H. Gerber, “Atomic Force Microscope,” *Physical Review Letter,* vol. 56, no. 9, pp. 930–933, March 1986.

[13] T. R. Albrecht, P. Grütter, D. Horne, and D. Rugar, “Frequency Modulation Detection using High-Q Cantilevers for Enhanced Force Microscope Sensitivity,” *Journal of Applied Physics*, vol. 69, no. 2, pp. 668–673, January 1991.

[14] Veeco Instruments. “Applications of AFM”[Online]. Available: http://web.mit.edu/cortiz/www/nanomechanics.html, (accessed on April 3, 2005).

[15] G. Li, N. Xi, M. Yu, and W. K. Fung, “3-D Nanomanipulation Using Atomic Force Microscopy,” in *Proceedings of 2003 IEEE International Conference on Robotics and Automation*, Taipei, Taiwan, pp. 3642–3647, September 2003.

[16] L. T. Hansen, A. Kuhle, A. H. Sorensen, J. Bohr, and P. E. Lindelof, “A Technique for Positioning Nanoparticles Using and Atomic Force Microscope,” *Nanotechnology*, vol. 9, no. 4, pp. 337–342, December 1998.

[17] G. M. Shedd and P. E. Russell, "The Scanning Tunneling Microscope as a Nanofabrication Tool for Nanofabrication," *Nanotechnology*, vol. 1, no. 1, pp. 67–80, July 1990.

[18] H. Hashimoto and M. Sitti, "Challenge to Micro/Nanomanipulation Using Atomic Force Microscope," *IEEE International Symposium on Micromechatronics and Human Science*, Nagoya, Japan, pp. 35–42, November 1999.

[19] B. Zhang and Z. Zhu, "Developing a Linear Piezomotor with Nanometer Resolution and High Stiffness," *IEEE/ASME Transactions of Mechatronics*, vol. 2, no. 1, pp. 22–29, March 1997.

[20] L. Juhas, A. Vujani, N. Adamovi, L. Nagy, and B. Borovac, " Development of Platform for Micro-positioning Actuatrd by Piezo-legs," in *Proceedings of the 2000 IEEE International Conference on Robotics and Automation*, San Francisco, CA, pp. 3647–3653, April 2000.

[21] K. K. Tan, T. H. Lee, and H. X. Zhou, "Micro-positioning of Linear-Piezoelectric Motor Based on a Learning Nonlinear PID Controller," *IEEE/ASME Transactions on Mechatronics*, vol. 6, no. 4, pp. 428–436, December 2001.

[22] L. Dong, F. Arai, and T. Fukuda, "3D Nanorobotic Manipulation of Nano-order Objects Inside SEM," in *Proceedings of 2000 International Symposium on Micromechatronics and Human Science*, Nagoya, Japan, pp. 151–156, October 2000.

[23] S. Fatikow and U. Rembold, "An Automated Microrobot-Based Desktop Station for Micro Assembly and Handling of Micro-Objects," in *Proceedings of Emerging Technologies and Factory Automation*, vol. 2, pp. 586–592, November 1996.

[24] H. Richter, E. Misawa, D. Lucca, H. Lu, “Modeling Nonlinear Behavior in a Piezoelectric Actuator,” *Precision Engineering and Nanotechnology*, vol. 25, no. 2, pp. 128–137, April 2001.

[25] A. A. G. Requicha, S. Meltzer, A. F. P. Terán, J. H. Makaliwe, H. Sikén, S. Hsieh, D. Lewis, B. E. Koel, and M. E. Thompson, “Manipulation of Nanoscale Components with the AFM: Principles and Applications,” in *Proceedings of IEEE-NANO 2001*, pp. 81–86, October 2001.

[26] S. Smith and D. Chetwynd, *Microscopic Staining Techniques*. London: Butterworths, 1963.

[27] K. S. Jung and Y. S. Baek, “Study on a Novel Contact-Free Planar System using Direct Drive DC Coils and Permanent Magnets,” *IEEE/ASME Transactions of Mechatronics*, vol. 7, no. 2, pp. 35–43, March 2002.

[28] W.-J. Kim, D. L. Trumper, “High-Precision Magnetic Levitation Stage for Photolithography,” *Precision Engineering*, vol. 22, no. 2, pp. 66–77, April 1998.

[29] W. -J. Kim, *High-Precision Planar Magnetic Levitation*, Ph.D. dissertation, Massachusetts Institute of Technology, Cambridge, MA, June 1997.

[30] R. L. Hollis, S. E. Salcudean, and A. P. Allan, “A Six Degree-of-Freedom Magnetically Levitated Variable Compliance Fine-Motion Wrist: Design, Modeling, and Control,” *IEEE Transactions on Robotics and Automation*, vol. 7, no. 3, pp. 320–332, June 1991.

[31] A. E. Hajjaji and M. Ouladsine, “Modeling and Nonlinear Control of Magnetic Levitation Systems,” *IEEE Transactions on Industrial Electronics*, vol. 48, no.4, pp. 831–838, August 2001.

[32] M. Holmes, R. Hocken, and D. L. Trumper, “The Long-Range Scanning Stage: A Novel Platform for Scanned-Probe Microscopy,” *Precision Engineering*, vol. 24, no. 3, pp. 191–209, July 2000.

[33] S. K. Kuo, X. Shan, and C. H. Menq, “Large Travel Ultra Precision x-y-θ Motion Control of a Magnetic-Suspension Stage,” *IEEE/ASME Transactions on Mechatronics*, vol. 8, no. 3, pp. 334–341, September 2003.

[34] X. Shan X, S. K. Kuo, J. Zhang and C. H. Menq, “Ultra Precision Motion Control of a Multiple Degrees of Freedom Magnetic Suspension Stage,” *IEEE/ASME Transactions on Mechatronics*, vol. 7, no. 1, pp. 67–78, March 2002.

[35] M. B. Khamesee, N. Kato, Y. Nomura, and T. Nakamura, “Design and Control of a Microrobotic System using Magnetic Levitation,” *IEEE/ASME Transactions on Mechatronics*, vol. 7, no. 1, pp. 1–13, March 2002.

[36] Y. Sun, D. Piyabongkarn, A. Sezen, B. J. Nelson, R. Rajamani, R. Schoch, and D. P. Potasek, “A Novel Dual-axis Electrostatic Microactuation System for Macromanipulation,” in *Proceedings of IEEE/RSJ International Conference on Intelligent Robots and Systems*, Lausanne, Switzerland, pp. 1796–1801, October 2002.

[37] S. Mori, T. Hoshino, G. Obinata, and K. Ouchi, “Linear Actuator with Air Bearing for Highly Precise Tracking [HDD],” *Digest of the Asia-Pacific Magnetic Recording Conference*, pp. AP4-01–AP4-02, May 2002.

[38] Y. Egashira, K. Kosaka, S. Takada, T. Iwabuchi, T. Baba, S. Moriyama, T. Harada, K. Nagamoto, A. Nakada, H. Kubota, and T. Ohmi, “0.69 nm Resolution Ultrasonic Motor for Large Stroke Precision Stage,” in *Proceedings of IEEE-NANO 2001*, Maui, Hi, pp. 397–402, October 2001.

[39] M. L. Culpepper and G. Anderson, "Design of a Low-Cost Nano-Manipulator which Utilizes a Monolithic, Spatial Compliant Mechanism," *Precision Engineering*, vol. 28, no. 4, pp. 469–482, October 2004.

[40] Zyvex Corporation website, "Molecular Nanotechnology," Richardson, TX, [Online]: www.zyvex.com, Jan. 2000. (accessed on November 21, 2000).

[41] Zyvex Corporation website. "Zyvex F100 Specifications and picture" [Online]. http://www.zyvex.com/Products/F100_Features.html#, (accessed on April 6, 2005).

[42] B. V. Jayawant, *Electromagnetic Levitation and Suspension Techniques*. London: Edward Arnold Ltd., 1981.

[43] K. Takahara, "Development of a Magnetically Suspended, Tetrahedron-Shaped Antenna Pointing System," *Proc. NASA CP–2056, 22nd Aerospace Mechanisms Symposium*, Hampton, Virginia, pp. 133–147, May 1988.

[44] A. A. Gupta, L. M. Germann, and J. D. Medbery, "Six Degree-of-Freedom Magnetically-Suspended Fast Steering Mirror (MSFSM) Tracks Atmospheric Turbulence While Providing Focusing and Collimation Travel," *Proc. 14th Annual AAS Guidance and Control Conference*, Maui, Hawaii, AAS 91–039, February 1991.

[45] O. S. Kim, H.-J. Ahn, Y. Joung, I.-B. Chang, and D.-C. Han, "Micropositioning of a Linear Motion Table with Magnetic Bearing Suspension," in *Proceedings of ASPE 1997 Annual Meeting*, Norfolk, Virginia, pp. 406–409, October 1997.

[46] O. S. Kim, S. H. Lee, and D.-C. Han, "Positioning Performance and Straightness Error Compensation of the Magnetic-Levitation Stage Supported by the Linear Magnetic Bearing," *IEEE Transactions on Industrial Electronics*, vol. 50, no. 2, pp. 374–378, April 2003.

[47] M. Y. Chen, M. J. Wang, and L. C. Fu, "A Novel Dual-Axis Repulsive Maglev Guiding System with Permanent Magnet: Modeling and Controller Design," *IEEE/ASME Transactions on Mechatronics*, vol. 8, no. 1, pp. 77–86, March 2003.

[48] D.-C. Han, I.-H. Park, H.-J. Ahn, S.-H Lee, O.-S Kim and I. -B. Chang, "The High Precision Linear Motion Table with a Novel Rare Earth Permanent Magnet Biased Magnetic Bearing Suspension," in *Proceedings of ASPE 1998 Annual Meeting*, pp. 363–366, St. Louis, Missouri, October 1998.

[49] A. Molenaar, F. Auer, and H. F. van Beek, "Application of Magnetic Bearing for Contactless Ultra High Precision Positioning," in *Proceedings of the 5th International Symposium on Magnetic Bearing,* 5ISMB, Kanazawa, Japan, pp. 441–445, August 1996.

[50] A. Molenaar, F. Auer, and H. F. van Beek, "A Novel Low Dissipation Long Stroke Planar Magnetic Suspension and Propulsion Stage," in *Proceedings of the 6th International Symposium on Magnetic Bearings*, MIT, Cambridge, 650–659, August 1998.

[51] W.-J. Kim and H. Maheshwari, "High-Precision Control of a Maglev Linear Actuator with Nanopositioning Capability," *Proc. of 2002 American Control Conference*, pp. 4279–4284, Anchorage, Alaska, May 2002.

[52] Leroy's Engineering website. "VME Specifications and details" [Online]. http://www.interfacebus.com/Design_Connector_VME.html, (accessed on February 25, 2005).

[53] Pentek Inc. website. "Details of DSP and data-acquisition boards" website. [Online]. http://www.pentek.com, (accessed on February 27, 2005).

[54] S. Verma, W.-J. Kim, and J. Gu, "6-Axis Nanopositioning Device with Precision Magnetic Levitation Technology,"*IEEE/ASME Transactions on Mechatronics*, vol. 9, no. 2, pp. 384-391, June 2004.

[55] S. Earnshaw, "On the Nature of the Molecular Forces which Regulate the Constitution of the Luminiferous Ether," *Transactions of the Cambridge Philosophical Society*, vol. 7, pp. 97–112, 1842.

[56] J. Gu, W.-J. Kim, and S. Verma, "Nanoscale Motion Control with a Compact Minimum-Actuator Magnetic Levitator," *ASME Journal of Dynamic Systems, Measurement and Control*, September 2005, in press.

[57] G. F. Franklin, J. D. Powell, and A. Emami-Naeini, *Feedback Control of Dynamic Systems 4th Ed*. Singapore: Pearson Education Pte. Ltd., 2002.

[58] B. C. Kuo and F. Golnaraghi, *Automatic Control Systems 8th Ed*. Singapore: John Wiley & Sons (ASIA) Pte Ltd, 2003.

[59] J. G. Proakis and D. G. Manolakis, *Digital Signal Processing.* Upper Saddle River, NJ: Prentice Hall, 1996.

[60] B. Lennartson, "On the Choice of Controller and Sampling Period for Linear Stochastic Control," *Automatica*, vol. 26, no. 3, pp. 573–578, May 1990.

[61] S. Skogestad and I. Postlethwaite, *Multivariable Feedback Control*. New York: John Wiley & Sons, October 1996.

[62] S. Bhattacharyya, ELEN605-linear control systems. *Lecture notes*. Dept. of Electrical Engineering, Texas A&M University, College Station, 2004.

[63] M. French and E. Rogers, "Approximate Paramaterisations for Adaptive Feedback Linearisation," in *Proceedings on the 36th Conf. on Decision & Control*, San Diego, CA, pp. 4665–4670, December 1997.

[64] A. J. Krener, *A Brief Tutorial on Linear and Nonlinear Control Theory*. [Online]: http://www.samsi.info/200304/multi/akrener.pdf (accessed on November 12, 2004)

[65] S. A. Bortoff, “Approximate State-Feedback Linearization using Spline Functions,” *Automatica*, vol. 33, no. 8, pp. 1449–1458, August 1997.

[66] V. K. Vardan, X. Jiang, and V. V. Vardan, *Microstereolithography and other Fabrication Techniques for 3D MEMS*. New York: John Wiley and Sons Ltd., 2001.

[67] L. Beluze, A. Bertsch, and P. Renaud, “Microstereolithography: A New Process to Build Complex 3D Objects,” in *Proceedings of SPIE*, vol. 3680, pp. 808–817, April 1999.

[68] X. Zhang, X. N. Jiang, and C. Sun, “Microstereolithography of Polymeric and Ceramic Microstructures,” *Sensors and Actuators A (Physical)*, vol. A77, no. 2, pp. 149–156, March 1999.

[69] X. N. Jiang, C. Sun, X. Zhang, B. Xu, and Y. H. Ye, “Microstereolithography of Lead Zirconate Titanate Thick Film on Silicon Substrate,” *Sensors and Actuators A (Physical)*, vol. A87, no. 1-2, pp. 72–77, May 2000.

[70] K. Ikuta, S. Maruo, and S. Kojima, “New Microstereolithography for Freely Movable 3D Microstructure–Super IH Process with Submicron Resolution,” in *Proceedings of IEEE MEMS*, Heidelberg, Germany, pp. 290–295, January 1998.

APPENDIX A

C CODES FOR CLOSED-LOOP CONTROL

Lead-Lag Control Interrupt Subroutine

```
void c_int01()
{
unsigned long D1reading;
long ADreading, ADreadingA, ADreadingB,ADreadingC;
int i;
float z_mea;
tr_low();
D1reading=*(unsigned long *)AD_FIFO_D1;
*(unsigned long int *)0xb0300003=0x0041;

/* READING LASER INTERFEROMETERS*/
raw_x_pos= (*(long int *)0xb0300048 << 16) & 0xffff0000;
raw_y1_pos = (*(long int *)0xb0310048 << 16) & 0xffff0000;
raw_y2_pos = (*(long int *)0xb0320048 << 16) & 0xffff0000;
tr_high();
raw_x_pos |= ((*(long int *)0xb0300048 >>16) & 0x0000ffff);
raw_y1_pos |= ((*(long int *)0xb0310048 >> 16) & 0x0000ffff);
raw_y2_pos |= ((*(long int *)0xb0320048 >> 16) & 0x0000ffff);
x_pos=raw_x_pos*6.1815119987e-10;
y1_pos=raw_y1_pos*6.1815119987e-10;
y2_pos=raw_y2_pos*6.1815119987e-10;
 tr_low();

/* READING CAPACITANCE PROBE DATA*/
ADreading=*(unsigned long int *)AD_FIFO_A1 & 0xffff;
if(ADreading & 0x8000)
```

```
ADreading = ADreading | 0xffff0000;
AD_A1=ADreading;
z_pos1=ADreading*7.629627369e-9+250e-6;
ADreading=*(unsigned long int *)AD_FIFO_B1 & 0xffff;
if(ADreading & 0x8000)
ADreading = ADreading | 0xffff0000;
z_pos2=ADreading*7.629627369e-9+250e-6;
ADreading=*(unsigned long int *)AD_FIFO_C1 & 0xffff;
if(ADreading & 0x8000)
ADreading = ADreading | 0xffff0000;
z_pos3=ADreading*7.629627369e-9+250e-6;

/*POSITION TRANSFORM*/
xr =-(       0*y2_pos + 0.5774*y1_pos - 0.5774*x_pos);
yr = -(-0.6667*y2_pos + 0.3333*y1_pos + 0.3333*x_pos);
hr = ( 6.5928*y2_pos + 6.5928*y1_pos + 6.5928*x_pos);

zr =  0.3333*z_pos1 + 0.3333*z_pos2 + 0.3333*z_pos3;
sr =  1000*(          0*z_pos1 + 0.0400*z_pos2 - 0.0400*z_pos3);
tr = 1000*(-0.0462*z_pos1 + 0.0231*z_pos2 + 0.0231*z_pos3);

/* CONTROLLER */
if (controller_flag == 1)
{
er0x=xc-xr;
er0y=yc-yr;
er0h=hc-hr;

er0z=zc-zr;
er0s=sc-sr;
er0t=tc-tr;
```

```
/*HORIZONTAL CONTROLLERS*/
/*Controller at  PM 43 and 120 Hz  */
u0x = 1.71318144*u1x -0.71318144*u2x + 350675.42123468*er0x + -682790.37405049*er1x
+ 332271.66719049*er2x;
u0y = 1.71318144*u1y  -0.71318144*u2y + 350675.42123468*er0y + -682790.37405049*er1y
+ 332271.66719049*er2y;
u0h = 1.71318144*u1h  -0.71318144*u2h +(731.59383708*er0h + -1424.46604302*er1h +
693.19915007*er2h);
/*VERTICAL CONTROLLERS*/
/*Controller with PM 70 and Freq 65 Hz */
u0z = 1.65658873*u1z - 0.65658873*u2z + 232004.55154669*er0z + -461593.23257734*er1z
+ 229591.41122804*er2z;
u0s = 1.65658873*u1s - 0.65658873*u2s + 0.5*(295.66660049*er0s + -588.25441560*er1s +
292.59129447*er2s);
u0t = 1.65658873*u1t - 0.65658873*u2t + 0.5*(295.66660049*er0t + -588.25441560*er1t +
292.59129447*er2t);

/*FORCE TRANSFORMATION*/
f1=u0z*0.3333 + u0s*0             - u0t*13.1765;
f2=u0z*0.3333 + u0s*11.4112 + u0t*6.5883;
f3=u0z*0.3333 - u0s*11.4112 + u0t*6.5883;

f4=        0*u0x - 0.6667*u0y - 6.5883*u0h;
f5= 0.5774*u0x + 0.3333*u0y - 6.5883*u0h;
f6=-0.5774*u0x + 0.3333*u0y - 6.5883*u0h;

/*FORCE TO CURRENT TRANSFORMATION*/
i1=0.18518*f1;
i2=0.18518*f2;
i3=0.18518*f3;
i4= -0.8297*f6;
i5= 0.8297*f4;
```

```
i6= 0.8297*f5;

/* CONVERSION TO DAC VOLTAGE AND LIMITING THE CURRENT VALUE */
v1=i1*i2v;
if ((v1+vn1)>=2.5) v1=2.4-vn1;
if ((v1+vn1)<=-2.5) v1=-2.4-vn1;
v2=i2*i2v;
if ((v2+vn2)>=2.5) v2=2.4-vn2;
if ((v2+vn2)<=-2.5) v2=-2.4-vn2;
v3=i3*i2v;
if ((v3+vn3)>=2.5) v3=2.4-vn3;
if ((v3+vn3)<=-2.5) v3=-2.4-vn3;

v4=i4*i2v;
if (v4>=4) v4=4;
if (v4<=-4) v4=-4;
v5=i5*i2v;
if (v5>=4) v5=4;
if (v5<=-4) v5=-4;
v6=i6*i2v;
if (v6>=4) v6=4;
if (v6<=-4) v6=-4;

}
tr_low();
if(flag_d2a==1)
{
*(unsigned int *)DA_FIFO_A1=(((unsigned int)((v1+vn1)*6553.4)) <<16) & 0xffff0000 ;
*(unsigned int *)DA_FIFO_B1=(((unsigned int)((v2+vn2)*6553.4)) <<16) & 0xffff0000;
*(unsigned int *)DA_FIFO_C1=(((unsigned int)((v3+vn3)*6553.4)) <<16) & 0xffff0000;
*(unsigned int *)DA_FIFO_A2=(((unsigned int)((prevA2+v5*hstart)*-6553.4)) <<16) &
0xffff0000;
```

```
*(unsigned int *)DA_FIFO_B2=(((unsigned int)((prevB2+v6*hstart)*-6553.4)) <<16) &
0xffff0000;
*(unsigned int *)DA_FIFO_C2=(((unsigned int)((prevC2+v4*hstart)*-6553.4*-1)) <<16) &
0xffff0000;
}

/* SET INT COUNT FOR SNAP */
if ((snap_begin==1) & (snap_enable==1))
{
int_count++;
}
/*SAVE CONTROL VARIABLES */
u2z=u1z;
u1z=u0z;
er2z=er1z;
er1z=er0z;
u2s=u1s;
u1s=u0s;
er2s=er1s;
er1s=er0s;
u2t=u1t;
u1t=u0t;
er2t=er1t;
er1t=er0t;
u2x=u1x;
u1x=u0x;
er2x=er1x;
er1x=er0x;
u2y=u1y;
u1y=u0y;
er2y=er1y;
er1y=er0y;
```

```
u2h=u1h;
u1h=u0h;
er2h=er1h;
er1h=er0h;
display=1;
MX_Int_Clr= 0x20000029;
*(unsigned int *)MX_Int_Clr=0x0;
}
```

LQR Control Interrupt Subroutine

```
void c_int01()
{
unsigned long D1reading;
long ADreading, ADreadingA, ADreadingB,ADreadingC;
int i;
float z_mea;

tr_low();
D1reading=*(unsigned long *)AD_FIFO_D1;
*(unsigned long int *)0xb0300003=0x0041;

/* READING LASER INTERFEROMETERS*/
raw_x_pos= (*(long int *)0xb0300048 << 16) & 0xffff0000;
raw_y1_pos = (*(long int *)0xb0310048 << 16) & 0xffff0000;
raw_y2_pos = (*(long int *)0xb0320048 << 16) & 0xffff0000;
raw_x_vel  = (*(long int *)0xb030004e << 16) & 0xffff0000;
raw_y1_vel = (*(long int *)0xb031004e << 16) & 0xffff0000;
raw_y2_vel = (*(long int *)0xb032004e << 16) & 0xffff0000;

tr_high();

raw_x_pos |= ((*(long int *)0xb0300048 >>16) & 0x0000ffff);
```

```
raw_y1_pos |= ((*(long int *)0xb0310048 >> 16) & 0x0000ffff);
raw_y2_pos |= ((*(long int *)0xb0320048 >> 16) & 0x0000ffff);
raw_x_vel  |= ((*(long int *)0xb030004e >> 16) & 0x0000ffff);
raw_y1_vel |= ((*(long int *)0xb031004e >> 16) & 0x0000ffff);
raw_y2_vel |= ((*(long int *)0xb032004e >> 16) & 0x0000ffff);

x_pos=raw_x_pos*6.1815119987e-10;
y1_pos=raw_y1_pos*6.1815119987e-10;
y2_pos=raw_y2_pos*6.1815119987e-10;

    x_vel = raw_x_vel * 3.77272037e-7;
    y1_vel= raw_y1_vel* 3.77272037e-7;
    y2_vel= raw_y2_vel* 3.77272037e-7;

 tr_low();

/* READING LASER INTERFEROMETERS*/
 ADreading=*(unsigned long int *)AD_FIFO_A1 & 0xffff;
if(ADreading & 0x8000)
ADreading = ADreading | 0xffff0000;
AD_A1=ADreading;
z_pos1=ADreading*7.629627369e-9+250e-6;

ADreading=*(unsigned long int *)AD_FIFO_B1 & 0xffff;
if(ADreading & 0x8000)
ADreading = ADreading | 0xffff0000;
z_pos2=ADreading*7.629627369e-9+250e-6;

ADreading=*(unsigned long int *)AD_FIFO_C1 & 0xffff;
if(ADreading & 0x8000)
ADreading = ADreading | 0xffff0000;
z_pos3=ADreading*7.629627369e-9+250e-6;
```

```
/*POSITION TRANSFORM*/
xr =-(       0*y2_pos + 0.5774*y1_pos - 0.5774*x_pos);
yr = -(-0.6667*y2_pos + 0.3333*y1_pos + 0.3333*x_pos);
hr = ( 6.5928*y2_pos + 6.5928*y1_pos + 6.5928*x_pos);

zr =  0.3333*z_pos1 + 0.3333*z_pos2 + 0.3333*z_pos3;
sr =  (       0*z_pos1 + 0.0400*z_pos2 - 0.0400*z_pos3);
tr = (-0.0462*z_pos1 + 0.0231*z_pos2 + 0.0231*z_pos3);
xr_dot =-(       0*y2_vel + 0.5774*y1_vel - 0.5774*x_vel);
yr_dot = -(-0.6667*y2_vel + 0.3333*y1_vel + 0.3333*x_vel);
hr_dot = ( 6.5928*y2_vel + 6.5928*y1_vel + 6.5928*x_vel);
/* CONTROLLER */
if (controller_flag == 1)
{
/*ERROR EQUATIONS*/
er0x=xc-xr;
er0y=yc-yr;
er0h=hc-hr;

er0z=zc-zr;
er0s=sc-sr;
er0t=tc-tr;

/*INTEGRATOR ERROR EQUATIONS */

ier0x=ier1x+0.0002*er0x;
ier0y=ier1y+0.0002*er0y;
ier0h=ier1h+0.0002*er0h;

/* LQR HORIZONTAL CONTROLLERS*/
```

```
/* LQR 1: very first one stable but settles in 6 sec, gave 700 micron step*
u0x = 1443.66572167*er0x + 1000.00000000*ier0x + 42.08535797*(-xr_dot) ;
u0y = 1443.66572167*er0y + 1000.00000000*ier0y + 42.08535797*(-yr_dot) ;
u0h = 45.44036924*er0h + 31.62277660*ier0h + 1.02500734*(-hr_dot) ;
*/

/* LQR 3: simulation settles in 2 s , 10% overshoot
Q=diag([2000000 100000000 1000])
R=1*/

u0x = 1695.00024352*er0x + 10000.00000000*ier0x + 43.65129128*(-xr_dot) ;
u0y = 1695.00024352*er0y + 10000.00000000*ier0y + 43.65129128*(-yr_dot) ;
u0h = 51.51118628*er0h + 316.22776602*ier0h + 1.03311977*(-hr_dot) ;


/* LQR 4      BEST SO FAR
simulation settles in .18 s , 25% overshoot
Q=diag([2000000 1e10 1000]);
R=1*/
u0x = 3576.24816767*er0x + 100000.00000000*ier0x + 53.94775478*(-xr_dot) ;
u0y = 3576.24816767*er0y + 100000.00000000*ier0y + 53.94775478*(-yr_dot) ;
u0h = 93.26854967*er0h + 3162.27766017*ier0h + 1.05920844*(-hr_dot) ;

/*VERTICAL CONTROLLERS*/

/*Controller with PM 70 and Freq 65 Hz  BEST */
u0z = 1.65658873*u1z - 0.65658873*u2z + 232004.55154669*er0z + -461593.23257734*er1z
+ 229591.41122804*er2z;
u0s = 1.65658873*u1s - 0.65658873*u2s + 100*(295.66660049*er0s + -588.25441560*er1s +
292.59129447*er2s);
u0t = 1.65658873*u1t - 0.65658873*u2t + 100*(295.66660049*er0t + -588.25441560*er1t +
292.59129447*er2t);
```

```
/*FORCE TRANSFORMATION*/
f1=u0z*0.3333 + u0s*0               - u0t*13.1765;
f2=u0z*0.3333 + u0s*11.4112 + u0t*6.5883;
f3=u0z*0.3333 - u0s*11.4112 + u0t*6.5883;

f4=                  0*u0x - 0.6667*u0y - 6.5883*u0h;
f5= 0.5774*u0x + 0.3333*u0y - 6.5883*u0h;
f6=-0.5774*u0x + 0.3333*u0y - 6.5883*u0h;

/*FORCE TO CURRENT TRANSFORMATION*/
i1=0.18518*f1;
i2=0.18518*f2;
i3=0.18518*f3;
i4= -0.8297*f6;
i5= 0.8297*f4;
i6= 0.8297*f5;

/* CONVERSION TO DAC VOLTAGE AND LIMITING THE CURRENT VALUE */
v1=i1*i2v;
if ((v1+vn1)>=2.5) v1=2.4-vn1;
if ((v1+vn1)<=-2.5) v1=-2.4-vn1;
v2=i2*i2v;
if ((v2+vn2)>=2.5) v2=2.4-vn2;
if ((v2+vn2)<=-2.5) v2=-2.4-vn2;
v3=i3*i2v;
if ((v3+vn3)>=2.5) v3=2.4-vn3;
if ((v3+vn3)<=-2.5) v3=-2.4-vn3;

v4=i4*i2v;
if (v4>=4) v4=4;
if (v4<=-4) v4=-4;
```

```
v5=i5*i2v;
if (v5>=4) v5=4;
if (v5<=-4) v5=-4;
v6=i6*i2v;
if (v6>=4) v6=4;
if (v6<=-4) v6=-4;
}

tr_low();
if(flag_d2a==1)
{
*(unsigned int *)DA_FIFO_A1=(((unsigned int)((v1+vn1)*6553.4)) <<16) & 0xffff0000 ;
*(unsigned int *)DA_FIFO_B1=(((unsigned int)((v2+vn2)*6553.4)) <<16) & 0xffff0000;
*(unsigned int *)DA_FIFO_C1=(((unsigned int)((v3+vn3)*6553.4)) <<16) & 0xffff0000;
*(unsigned int *)DA_FIFO_A2=(((unsigned int)((prevA2+v5*hstart)*-6553.4)) <<16) &
0xffff0000;
*(unsigned int *)DA_FIFO_B2=(((unsigned int)((prevB2+v6*hstart)*-6553.4)) <<16) &
0xffff0000;
*(unsigned int *)DA_FIFO_C2=(((unsigned int)((prevC2+v4*hstart)*-6553.4*-1)) <<16) &
0xffff0000;
}

/* SET INT COUNT FOR SNAP */
if ((snap_begin==1) & (snap_enable==1))
{
int_count++;
}

/*SAVE CONTROL VARIABLES */
ier1x=ier0x;
ier1y=ier0y;
ier1h=ier0h;
```

```
u2z=u1z;
u1z=u0z;
er2z=er1z;
er1z=er0z;

u2s=u1s;
u1s=u0s;
er2s=er1s;
er1s=er0s;

u2t=u1t;
u1t=u0t;
er2t=er1t;
er1t=er0t;

u2x=u1x;
u1x=u0x;
er2x=er1x;
er1x=er0x;

u2y=u1y;
u1y=u0y;
er2y=er1y;
er1y=er0y;

u2h=u1h;
u1h=u0h;
er2h=er1h;
er1h=er0h;

display=1;
```

```
MX_Int_Clr= 0x20000029;
*(unsigned int *)MX_Int_Clr=0x0;
}
```

Feedforward Decoupling Compensation Interrupt Subroutine

```
void c_int01()
{
unsigned long D1reading;
long ADreading, ADreadingA, ADreadingB,ADreadingC;
int i;
float z_mea;
tr_low();
D1reading=*(unsigned long *)AD_FIFO_D1;
*(unsigned long int *)0xb0300003=0x0041;

/* READING LASER INTERFEROMETERS*/
raw_x_pos= (*(long int *)0xb0300048 << 16) & 0xffff0000;
raw_y1_pos = (*(long int *)0xb0310048 << 16) & 0xffff0000;
raw_y2_pos = (*(long int *)0xb0320048 << 16) & 0xffff0000;
tr_high();
raw_x_pos |= ((*(long int *)0xb0300048 >>16) & 0x0000ffff);
raw_y1_pos |= ((*(long int *)0xb0310048 >> 16) & 0x0000ffff);
raw_y2_pos |= ((*(long int *)0xb0320048 >> 16) & 0x0000ffff);
x_pos=raw_x_pos*6.1815119987e-10;
y1_pos=raw_y1_pos*6.1815119987e-10;
y2_pos=raw_y2_pos*6.1815119987e-10;
 tr_low();

/* READING CAPACITANCE PROBE DATA*/
ADreading=*(unsigned long int *)AD_FIFO_A1 & 0xffff;
if(ADreading & 0x8000)
ADreading = ADreading | 0xffff0000;
```

```
AD_A1=ADreading;
z_pos1=ADreading*7.629627369e-9+250e-6;
ADreading=*(unsigned long int *)AD_FIFO_B1 & 0xffff;
if(ADreading & 0x8000)
ADreading = ADreading | 0xffff0000;
z_pos2=ADreading*7.629627369e-9+250e-6;
ADreading=*(unsigned long int *)AD_FIFO_C1 & 0xffff;
if(ADreading & 0x8000)
ADreading = ADreading | 0xffff0000;
z_pos3=ADreading*7.629627369e-9+250e-6;

/*POSITION TRANSFORM*/
xr =-(      0*y2_pos + 0.5774*y1_pos - 0.5774*x_pos);
yr = -(-0.6667*y2_pos + 0.3333*y1_pos + 0.3333*x_pos);
hr = ( 6.5928*y2_pos + 6.5928*y1_pos + 6.5928*x_pos);

zr =  0.3333*z_pos1 + 0.3333*z_pos2 + 0.3333*z_pos3;
sr =  1000*(       0*z_pos1 + 0.0400*z_pos2 - 0.0400*z_pos3);
tr = 1000*(-0.0462*z_pos1 + 0.0231*z_pos2 + 0.0231*z_pos3);

/* CONTROLLER */
if (controller_flag == 1)
{
er0x=xc-xr;
er0y=yc-yr;
er0h=hc-hr;

er0z=zc-zr;
er0s=sc-sr;
er0t=tc-tr;

/*HORIZONTAL CONTROLLERS*/
```

```
/*LQR 3*/
u0x = 1695.00024352*er0x + 10000.00000000*ier0x + 43.65129128*(-xr_dot) ;
u0y = 1695.00024352*er0y + 10000.00000000*ier0y + 43.65129128*(-yr_dot) ;
u0h = 51.51118628*er0h + 316.22776602*ier0h + 1.03311977*(-hr_dot) ;

/*VERTICAL CONTROLLERS*/
/*Controller with PM 70 and Freq 65 Hz */
u0z = 1.65658873*u1z - 0.65658873*u2z + 232004.55154669*er0z + -461593.23257734*er1z
+ 229591.41122804*er2z;
u0s = 1.65658873*u1s - 0.65658873*u2s + 0.5*(295.66660049*er0s + -588.25441560*er1s +
292.59129447*er2s);
u0t = 1.65658873*u1t - 0.65658873*u2t + 0.5*(295.66660049*er0t + -588.25441560*er1t +
292.59129447*er2t);

/*FORCE TRANSFORMATION*/
/*single axis decoupling factors*/
dcpX = 0.0065;
dcpY = 0.0053;

/*Force Transformation */
f1=u0z*0.3333 + (u0s + dcpX*u0x - 0.0025*u0y)*0 - (u0t + dcpY*u0y +
0.0025*u0x)*13.1765;
f2=u0z*0.3333 + (u0s + dcpX*u0x - 0.0025*u0y)*11.4112 + (u0t + dcpY*u0y +
0.0025*u0x)*6.5883;
f3=u0z*0.3333 - (u0s + dcpX*u0x - 0.0025*u0y)*11.4112 + (u0t + dcpY*u0y +
0.0025*u0x)*6.5883;

f4=        0*u0x - 0.6667*u0y - 6.5883*u0h;
f5= 0.5774*u0x + 0.3333*u0y - 6.5883*u0h;
f6=-0.5774*u0x + 0.3333*u0y - 6.5883*u0h;

/*FORCE TO CURRENT TRANSFORMATION*/
```

```
i1=0.18518*f1;
i2=0.18518*f2;
i3=0.18518*f3;
i4= -0.8297*f6;
i5= 0.8297*f4;
i6= 0.8297*f5;

/* CONVERSION TO DAC VOLTAGE AND LIMITING THE CURRENT VALUE */
v1=i1*i2v;
if ((v1+vn1)>=2.5) v1=2.4-vn1;
if ((v1+vn1)<=-2.5) v1=-2.4-vn1;
v2=i2*i2v;
if ((v2+vn2)>=2.5) v2=2.4-vn2;
if ((v2+vn2)<=-2.5) v2=-2.4-vn2;
v3=i3*i2v;
if ((v3+vn3)>=2.5) v3=2.4-vn3;
if ((v3+vn3)<=-2.5) v3=-2.4-vn3;

v4=i4*i2v;
if (v4>=4) v4=4;
if (v4<=-4) v4=-4;
v5=i5*i2v;
if (v5>=4) v5=4;
if (v5<=-4) v5=-4;
v6=i6*i2v;
if (v6>=4) v6=4;
if (v6<=-4) v6=-4;

}
tr_low();
if(flag_d2a==1)
{
```

```
*(unsigned int *)DA_FIFO_A1=(((unsigned int)((v1+vn1)*6553.4)) <<16) & 0xffff0000 ;
*(unsigned int *)DA_FIFO_B1=(((unsigned int)((v2+vn2)*6553.4)) <<16) & 0xffff0000;
*(unsigned int *)DA_FIFO_C1=(((unsigned int)((v3+vn3)*6553.4)) <<16) & 0xffff0000;
*(unsigned int *)DA_FIFO_A2=(((unsigned int)((prevA2+v5*hstart)*-6553.4)) <<16) &
0xffff0000;
*(unsigned int *)DA_FIFO_B2=(((unsigned int)((prevB2+v6*hstart)*-6553.4)) <<16) &
0xffff0000;
*(unsigned int *)DA_FIFO_C2=(((unsigned int)((prevC2+v4*hstart)*-6553.4*-1)) <<16) &
0xffff0000;
}

/* SET INT COUNT FOR SNAP */
if ((snap_begin==1) & (snap_enable==1))
{
int_count++;
}
/*SAVE CONTROL VARIABLES */
u2z=u1z;
u1z=u0z;
er2z=er1z;
er1z=er0z;
u2s=u1s;
u1s=u0s;
er2s=er1s;
er1s=er0s;
u2t=u1t;
u1t=u0t;
er2t=er1t;
er1t=er0t;
u2x=u1x;
u1x=u0x;
er2x=er1x;
```

```
er1x=er0x;
u2y=u1y;
u1y=u0y;
er2y=er1y;
er1y=er0y;
u2h=u1h;
u1h=u0h;
er2h=er1h;
er1h=er0h;
display=1;
MX_Int_Clr= 0x20000029;
*(unsigned int *)MX_Int_Clr=0x0;
}
```

Feedback Linearization Interrupt Subroutine

```
void c_int01()
{
unsigned long D1reading;
long ADreading, ADreadingA, ADreadingB,ADreadingC;
int i;
float z_mea;
tr_low();
D1reading=*(unsigned long *)AD_FIFO_D1;
*(unsigned long int *)0xb0300003=0x0041;

/* READING LASER INTERFEROMETERS*/
raw_x_pos= (*(long int *)0xb0300048 << 16) & 0xffff0000;
raw_y1_pos = (*(long int *)0xb0310048 << 16) & 0xffff0000;
raw_y2_pos = (*(long int *)0xb0320048 << 16) & 0xffff0000;
tr_high();
raw_x_pos |= ((*(long int *)0xb0300048 >>16) & 0x0000ffff);
raw_y1_pos |= ((*(long int *)0xb0310048 >> 16) & 0x0000ffff);
```

```
raw_y2_pos |= ((*(long int *)0xb0320048 >> 16) & 0x0000ffff);
x_pos=raw_x_pos*6.1815119987e-10;
y1_pos=raw_y1_pos*6.1815119987e-10;
y2_pos=raw_y2_pos*6.1815119987e-10;
 tr_low();

/* READING CAPACITANCE PROBE DATA*/
ADreading=*(unsigned long int *)AD_FIFO_A1 & 0xffff;
if(ADreading & 0x8000)
ADreading = ADreading | 0xffff0000;
AD_A1=ADreading;
z_pos1=ADreading*7.629627369e-9+250e-6;
ADreading=*(unsigned long int *)AD_FIFO_B1 & 0xffff;
if(ADreading & 0x8000)
ADreading = ADreading | 0xffff0000;
z_pos2=ADreading*7.629627369e-9+250e-6;
ADreading=*(unsigned long int *)AD_FIFO_C1 & 0xffff;
if(ADreading & 0x8000)
ADreading = ADreading | 0xffff0000;
z_pos3=ADreading*7.629627369e-9+250e-6;

/*POSITION TRANSFORM*/
xr =-(       0*y2_pos + 0.5774*y1_pos - 0.5774*x_pos);
yr = -(-0.6667*y2_pos + 0.3333*y1_pos + 0.3333*x_pos);
hr = ( 6.5928*y2_pos + 6.5928*y1_pos + 6.5928*x_pos);

zr =  0.3333*z_pos1 + 0.3333*z_pos2 + 0.3333*z_pos3;
sr =  1000*(        0*z_pos1 + 0.0400*z_pos2 - 0.0400*z_pos3);
tr = 1000*(-0.0462*z_pos1 + 0.0231*z_pos2 + 0.0231*z_pos3);

/* CONTROLLER */
if (controller_flag == 1)
```

```
{
er0x=xc-xr;
er0y=yc-yr;
er0h=hc-hr;

er0z=zc-zr;
er0s=sc-sr;
er0t=tc-tr;

/*HORIZONTAL CONTROLLERS*/
/*Controller at  PM 43 and 120 Hz  */
u0x = 1.71318144*u1x -0.71318144*u2x + 350675.42123468*er0x + -682790.37405049*er1x
+ 332271.66719049*er2x;
u0y = 1.71318144*u1y  -0.71318144*u2y + 350675.42123468*er0y + -682790.37405049*er1y
+ 332271.66719049*er2y;
u0h = 1.71318144*u1h   -0.71318144*u2h +(731.59383708*er0h + -1424.46604302*er1h +
693.19915007*er2h);
/*VERTICAL CONTROLLERS*/
/*Controller with PM 70 and Freq 65 Hz */
u0z = 1.65658873*u1z - 0.65658873*u2z + 232004.55154669*er0z + -461593.23257734*er1z
+ 229591.41122804*er2z;
u0s = 1.65658873*u1s - 0.65658873*u2s + 0.5*(295.66660049*er0s + -588.25441560*er1s +
292.59129447*er2s);
u0t = 1.65658873*u1t - 0.65658873*u2t + 0.5*(295.66660049*er0t + -588.25441560*er1t +
292.59129447*er2t);

/*FORCE TRANSFORMATION*/
f1=u0z*0.3333 + u0s*0              - u0t*13.1765;
f2=u0z*0.3333 + u0s*11.4112 + u0t*6.5883;
f3=u0z*0.3333 - u0s*11.4112 + u0t*6.5883;
f4=        0*u0x - 0.6667*u0y - 6.5883*u0h;
f5= 0.5774*u0x + 0.3333*u0y - 6.5883*u0h;
```

```
f6=-0.5774*u0x + 0.3333*u0y - 6.5883*u0h;

/*FORCE TO CURRENT TRANSFORMATION*/
i1=0.18518*f1;
i2=0.18518*f2;
i3=0.18518*f3;

/* APPLICATION OF FEEDBACK LINEARIZATION FOR LARGE TRAVEL RANGE*/
gap1 = 31e-4 - y2_pos;
gap2 = 31e-4 - y1_pos;
gap3 = 31e-4 - x_pos;

f2i1 = 1.41/(0.01469*gap1*gap1 - 0.3062*gap1 + 2.487);
f2i2 = 1.41/(0.01469*gap2*gap2 - 0.3062*gap2 + 2.487);
f2i3 = 1.41/(0.01469*gap3*gap3 - 0.3062*gap3 + 2.487);

i4 = -f2i3*f6;
i5 =  f2i1*f4;
i6 =  f2i2*f5;
 /* CONVERSION TO DAC VOLTAGE AND LIMITING THE CURRENT VALUE */
v1=i1*i2v;
if ((v1+vn1)>=2.5) v1=2.4-vn1;
if ((v1+vn1)<=-2.5) v1=-2.4-vn1;
v2=i2*i2v;
if ((v2+vn2)>=2.5) v2=2.4-vn2;
if ((v2+vn2)<=-2.5) v2=-2.4-vn2;
v3=i3*i2v;
if ((v3+vn3)>=2.5) v3=2.4-vn3;
if ((v3+vn3)<=-2.5) v3=-2.4-vn3;

v4=i4*i2v;
if (v4>=4) v4=4;
```

```
if (v4<=-4) v4=-4;
v5=i5*i2v;
if (v5>=4) v5=4;
if (v5<=-4) v5=-4;
v6=i6*i2v;
if (v6>=4) v6=4;
if (v6<=-4) v6=-4;
}
tr_low();
if(flag_d2a==1)
{
*(unsigned int *)DA_FIFO_A1=(((unsigned int)((v1+vn1)*6553.4)) <<16) & 0xffff0000 ;
*(unsigned int *)DA_FIFO_B1=(((unsigned int)((v2+vn2)*6553.4)) <<16) & 0xffff0000;
*(unsigned int *)DA_FIFO_C1=(((unsigned int)((v3+vn3)*6553.4)) <<16) & 0xffff0000;
*(unsigned int *)DA_FIFO_A2=(((unsigned int)((prevA2+v5*hstart)*-6553.4)) <<16) &
0xffff0000;
*(unsigned int *)DA_FIFO_B2=(((unsigned int)((prevB2+v6*hstart)*-6553.4)) <<16) &
0xffff0000;
*(unsigned int *)DA_FIFO_C2=(((unsigned int)((prevC2+v4*hstart)*-6553.4*-1)) <<16) &
0xffff0000;
}
 /* SET INT COUNT FOR SNAP */
if ((snap_begin==1) & (snap_enable==1))
{
int_count++;
}
/*SAVE CONTROL VARIABLES */
u2z=u1z;
u1z=u0z;
er2z=er1z;
er1z=er0z;
u2s=u1s;
```

```
u1s=u0s;
er2s=er1s;
er1s=er0s;
u2t=u1t;
u1t=u0t;
er2t=er1t;
er1t=er0t;
u2x=u1x;
u1x=u0x;
er2x=er1x;
er1x=er0x;
u2y=u1y;
u1y=u0y;
er2y=er1y;
er1y=er0y;
u2h=u1h;
u1h=u0h;
er2h=er1h;
er1h=er0h;
display=1;
MX_Int_Clr= 0x20000029;
*(unsigned int *)MX_Int_Clr=0x0;
}
```

APPENDIX B

MATLAB® CODES

To Get and Print Controller from SISOTOOL

```
plant = tf([1],[0.26709 0 0]);
sisotool(plant);

[num,den] = tfdata(C)
n = num{1}
d = den{1}

rh = 0.00055721441/0.26709;
rs = 0.00029092009/0.26709;
rt = rs;

sprintf('u0x = %10.8f*u1x %10.8f*u2x + %10.8f*er0x + %10.8f*er1x + %10.8f*er2x;',-d(2),-
d(3),n(1),n(2),n(3))
sprintf('u0y = %10.8f*u1y %10.8f*u2y + %10.8f*er0y + %10.8f*er1y + %10.8f*er2y;',-d(2),-
d(3),n(1),n(2),n(3))
sprintf('u0h = %10.8f*u1h %10.8f*u2h + 1*(%10.8f*er0h + %10.8f*er1h + %10.8f*er2h);',-
d(2),-d(3),rh*n(1),rh*n(2),rh*n(3))

sprintf('u0z = %10.8f*u1z %10.8f*u2z + %10.8f*er0z + %10.8f*er1z + %10.8f*er2z;',-d(2),-
d(3),n(1),n(2),n(3))
sprintf('u0s = %10.8f*u1s %10.8f*u2s + 1*(%10.8f*er0s + %10.8f*er1s + %10.8f*er2s);',-d(2),-
d(3),rs*n(1),rs*n(2),rs*n(3))
sprintf('u0t = %10.8f*u1t %10.8f*u2t + 1*(%10.8f*er0t + %10.8f*er1t + %10.8f*er2t);',-d(2),-
d(3),rt*n(1),rt*n(2),rt*n(3))
```

To Plot Data

```
clear all;
close all;
i=1:1000;
data = load('data.txt');
figure;
subplot(3,2,1),
plot(i/500, data(i*9-8)*1e6);
xlabel('t (s)');
ylabel('x (\mum)');
grid on;

subplot(3,2,3),
plot(i/500, data(i*9-7)*1e6);
xlabel('t (s)');
ylabel('y (\mum)');
grid on;

subplot(3,2,5),
plot(i/500, data(i*9-6)*1e6);
xlabel('t (s)');
ylabel('z (\mum)');
grid on;

subplot(3,2,4),
plot(i/500, data(i*9-5)*1e9);
xlabel('t (s)');
ylabel('\theta (\murad)');
grid on;

subplot(3,2,2),
```

```
plot(i/500, data(i*9-4)*1e9);
xlabel('t (s)');
ylabel('\psi (\murad)');
grid on;

subplot(3,2,6),
plot(i/500, data(i*9-3)*1e6);
xlabel('t (s)');
ylabel('\phi (\murad)');
grid on;
```

To Design Linear Quadratic Controller

```
clear all;  close all;
A=[ 0 0 0 1 0 0 0 0 0;
    0 0 0 0 1 0 0 0 0;
    0 0 0 0 0 1 0 0 0;
    0 0 0 0 0 0 0 0 0;
    0 0 0 0 0 0 0 0 0;
    0 0 0 0 0 0 0 0 0;
    1 0 0 0 0 0 0 0 0;
    0 1 0 0 0 0 0 0 0;
    0 0 1 0 0 0 0 0 0]
B=[ 0 0 0;
    0 0 0;
    0 0 0;
    0 3.24455 -3.24455;
   -3.744 1.8720  1.8720;
    -75.674 -75.674 -75.674;
    0 0 0;
    0 0 0;
    0 0 0]
```

```
% Define Weights
Q=diag([2e6 2e6 2e6 1e3 1e3 1e3 1e8 1e8 1e8]);
R=diag([1 1 1e3]);
N=zeros(9,3);

%Continuous time
[K,S,E] = lqr(A,B,Q,R,N);
K
%Find Closed-loop Poles
eig(A-B*K)

%Discrete time
[K,S,E] = lqrd(A,B,Q,R,N,1/5000);

%Print the Controller for DSP Program
sprintf('u0x = %0.8f*er0x + %0.8f*(-xr_dot) + %0.8f*ier0x ;',K(1,1),K(1,4),K(1,7))
sprintf('u0y = %0.8f*er0y + %0.8f*(-yr_dot) + %0.8f*ier0y ;',K(2,2),K(2,5),K(2,8))
sprintf('u0h = %0.8f*er0h + %0.8f*(-hr_dot) + %0.8f*ier0h ;',K(3,3),K(3,6),K(3,9))
```

APPENDIX C

ENGINEERING DRAWINGS

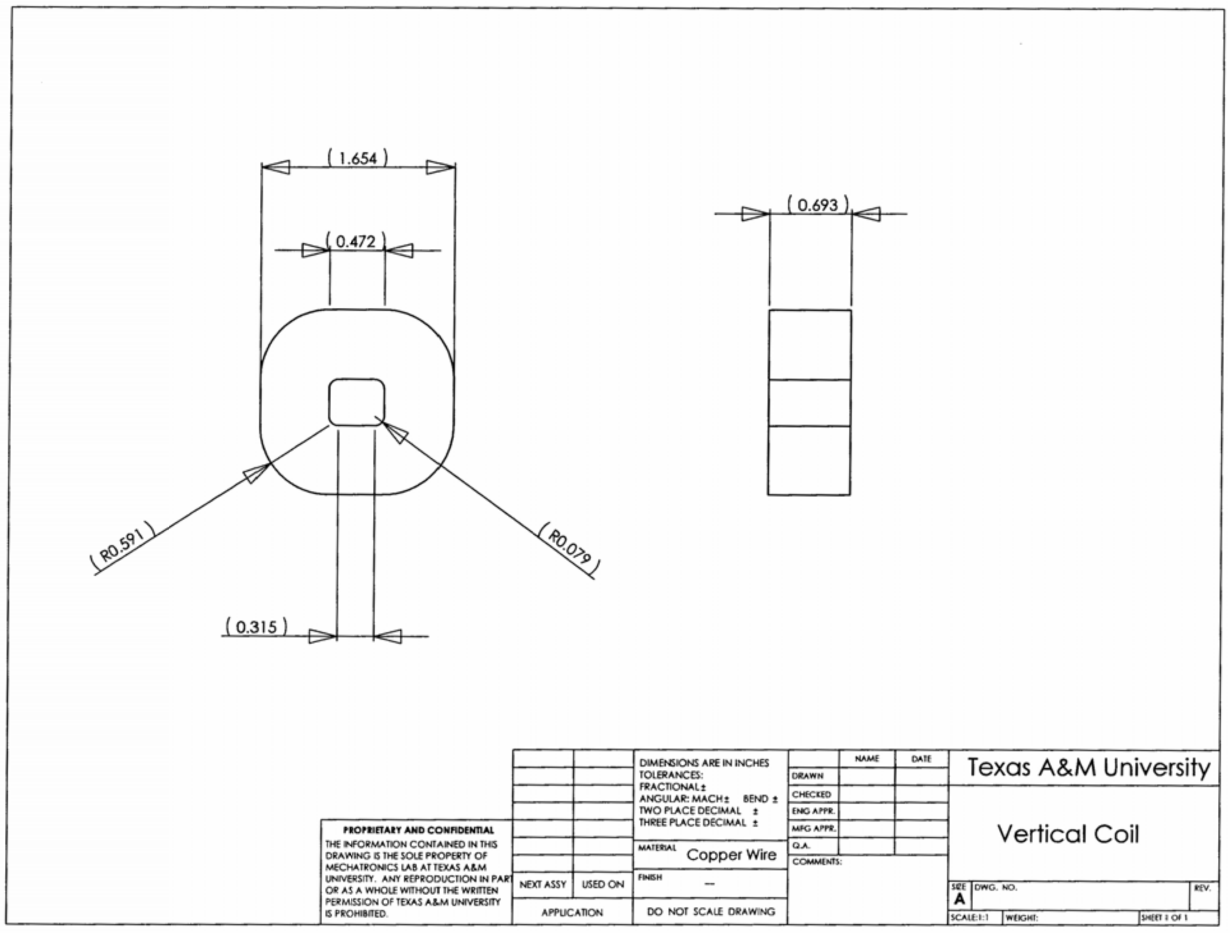

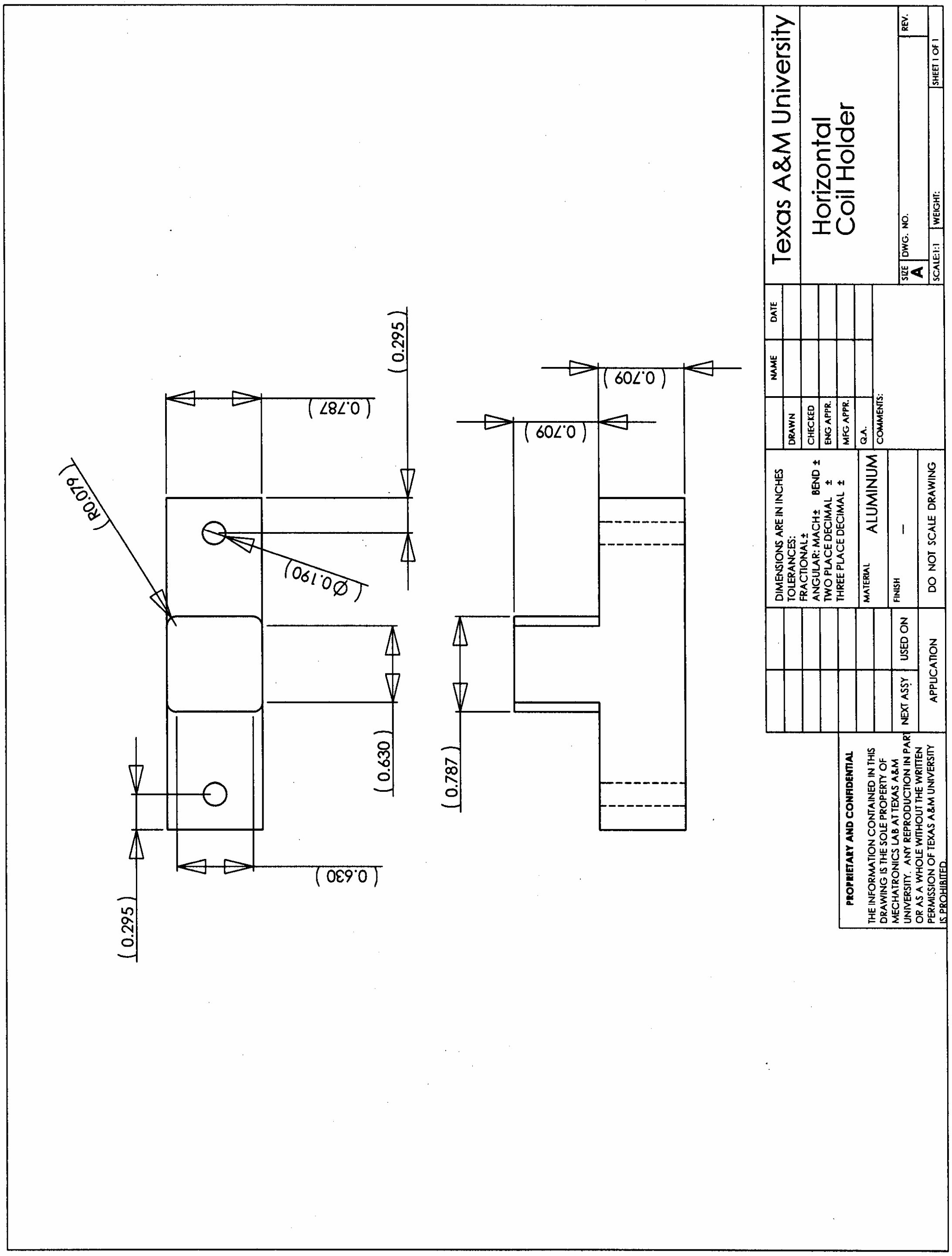
Texas A&M University
Horizontal
Coil Holder
(0.295)
(0.787)
R0.079
(Ø0.190)
(0.630)
(0.787)
(0.709)
(0.709)
(0.630)
(0.295)
DIMENSIONS ARE IN INCHES
TOLERANCES:
FRACTIONAL±
ANGULAR: MACH± BEND ±
TWO PLACE DECIMAL ±
THREE PLACE DECIMAL ±
MATERIAL
ALUMINUM
FINISH
—
DO NOT SCALE DRAWING
NEXT ASSY
USED ON
APPLICATION
NAME
DATE
DRAWN
CHECKED
ENG APPR.
MFG APPR.
Q.A.
COMMENTS:
SIZE
A
DWG. NO.
REV.
SCALE:1:1
WEIGHT:
SHEET 1 OF 1
PROPRIETARY AND CONFIDENTIAL
THE INFORMATION CONTAINED IN THIS DRAWING IS THE SOLE PROPERTY OF MECHATRONICS LAB AT TEXAS A&M UNIVERSITY. ANY REPRODUCTION IN PART OR AS A WHOLE WITHOUT THE WRITTEN PERMISSION OF TEXAS A&M UNIVERSITY IS PROHIBITED

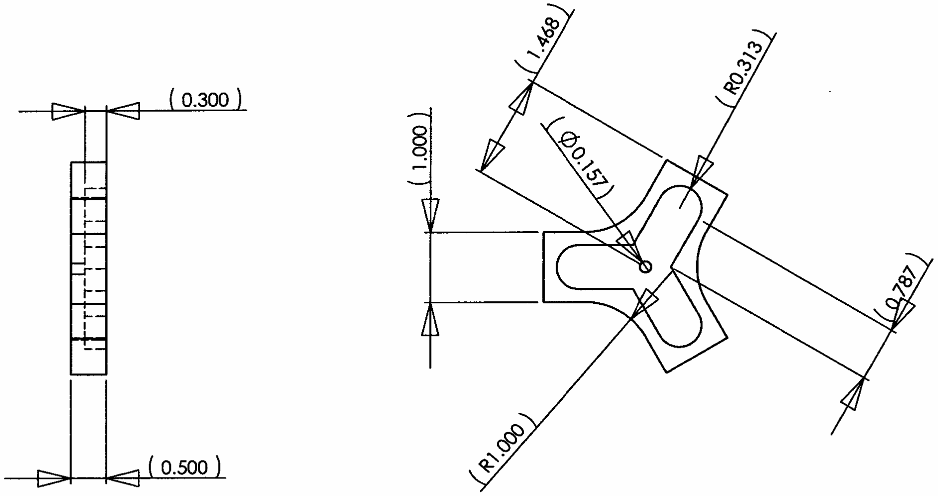

PROPRIETARY AND CONFIDENTIAL

THE INFORMATION CONTAINED IN THIS DRAWING IS THE SOLE PROPERTY OF MECHATRONICS LAB AT TEXAS A&M UNIVERSITY. ANY REPRODUCTION IN PART OR AS A WHOLE WITHOUT THE WRITTEN PERMISSION OF TEXAS A&M UNIVERSITY IS PROHIBITED.

NEXT ASSY | USED ON

APPLICATION

DIMENSIONS ARE IN INCHES
TOLERANCES:
FRACTIONAL±
ANGULAR: MACH± BEND ±
TWO PLACE DECIMAL ±
THREE PLACE DECIMAL ±

MATERIAL ALUMINUM

FINISH —

DO NOT SCALE DRAWING

	NAME	DATE
DRAWN		
CHECKED		
ENG APPR.		
MFG APPR.		
Q.A.		

COMMENTS:

Texas A&M University

Platen Core

SIZE A | DWG. NO. | REV.

SCALE:1:2 | WEIGHT: | SHEET 1 OF 1

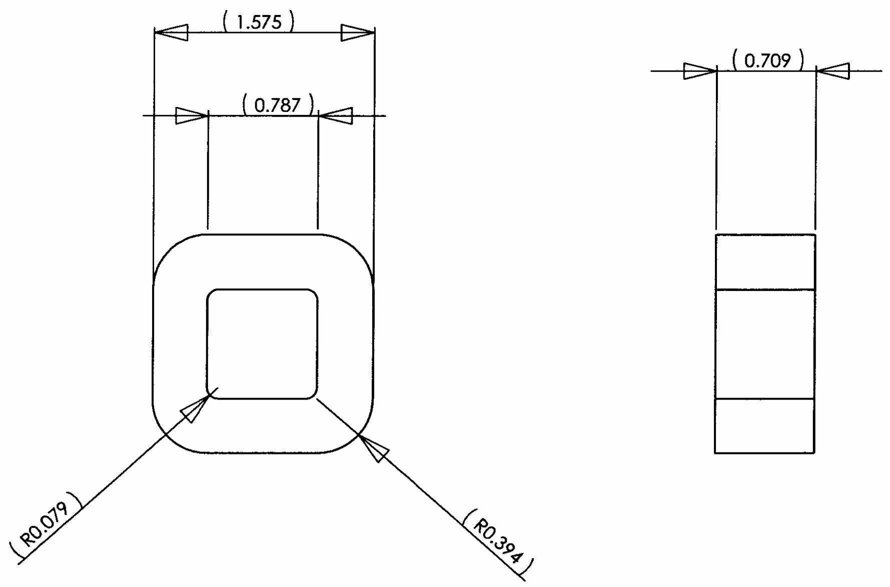

PROPRIETARY AND CONFIDENTIAL
THE INFORMATION CONTAINED IN THIS DRAWING IS THE SOLE PROPERTY OF MECHATRONICS LAB AT TEXAS A&M UNIVERSITY. ANY REPRODUCTION IN PART OR AS A WHOLE WITHOUT THE WRITTEN PERMISSION OF TEXAS A&M UNIVERSITY IS PROHIBITED.

NEXT ASSY
USED ON
APPLICATION

DIMENSIONS ARE IN INCHES
TOLERANCES:
FRACTIONAL ±
ANGULAR: MACH ± BEND ±
TWO PLACE DECIMAL ±
THREE PLACE DECIMAL ±

MATERIAL Copper Wire
FINISH --
DO NOT SCALE DRAWING

	NAME	DATE
DRAWN		
CHECKED		
ENG APPR.		
MFG APPR.		
Q.A.		

COMMENTS:

Texas A&M University

Horizontal Coil

SIZE A
DWG. NO.
REV.
SCALE:1:1
WEIGHT:
SHEET 1 OF 1

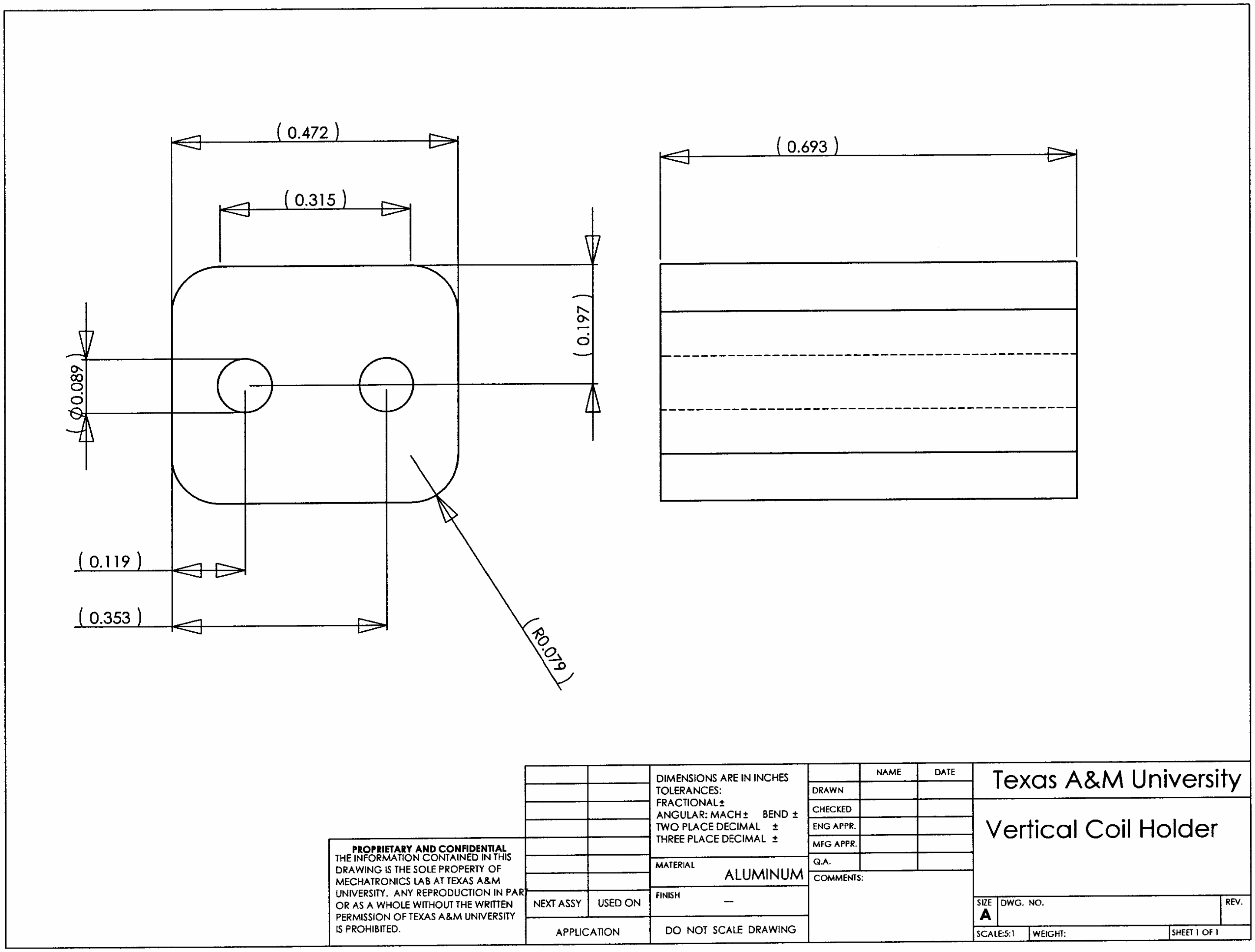
(0.472)
(0.315)
(0.693)
(0.197)
(∅0.089)
(0.119)
(0.353)
(R0.079)
PROPRIETARY AND CONFIDENTIAL
THE INFORMATION CONTAINED IN THIS DRAWING IS THE SOLE PROPERTY OF MECHATRONICS LAB AT TEXAS A&M UNIVERSITY. ANY REPRODUCTION IN PART OR AS A WHOLE WITHOUT THE WRITTEN PERMISSION OF TEXAS A&M UNIVERSITY IS PROHIBITED.
NEXT ASSY
USED ON
APPLICATION
DIMENSIONS ARE IN INCHES
TOLERANCES:
FRACTIONAL±
ANGULAR: MACH± BEND ±
TWO PLACE DECIMAL ±
THREE PLACE DECIMAL ±
MATERIAL
ALUMINUM
FINISH
—
DO NOT SCALE DRAWING
NAME
DATE
DRAWN
CHECKED
ENG APPR.
MFG APPR.
Q.A.
COMMENTS:
Texas A&M University
Vertical Coil Holder
SIZE
A
DWG. NO.
REV.
SCALE:5:1
WEIGHT:
SHEET 1 OF 1

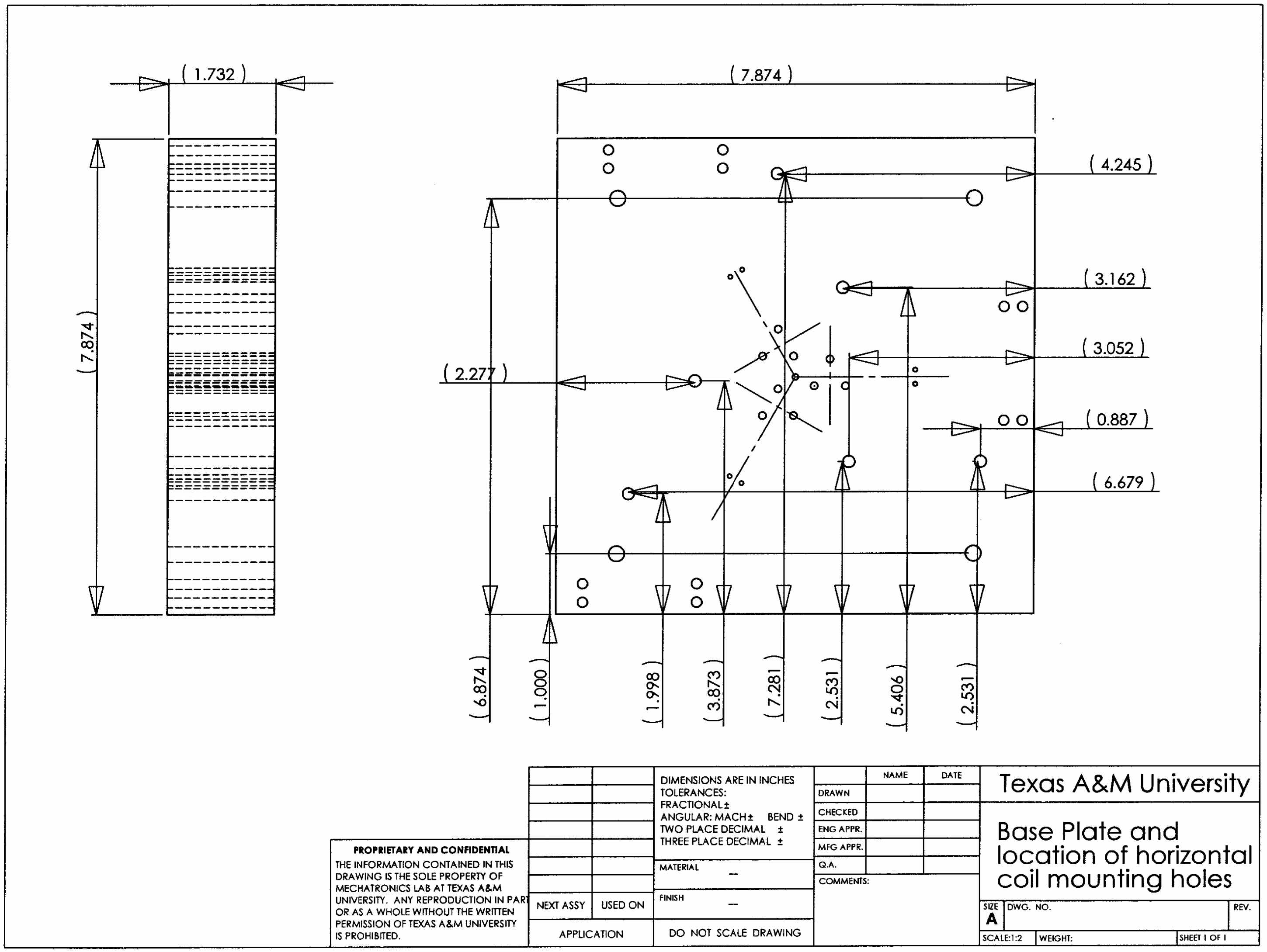

PROPRIETARY AND CONFIDENTIAL

THE INFORMATION CONTAINED IN THIS DRAWING IS THE SOLE PROPERTY OF MECHATRONICS LAB AT TEXAS A&M UNIVERSITY. ANY REPRODUCTION IN PART OR AS A WHOLE WITHOUT THE WRITTEN PERMISSION OF TEXAS A&M UNIVERSITY IS PROHIBITED.

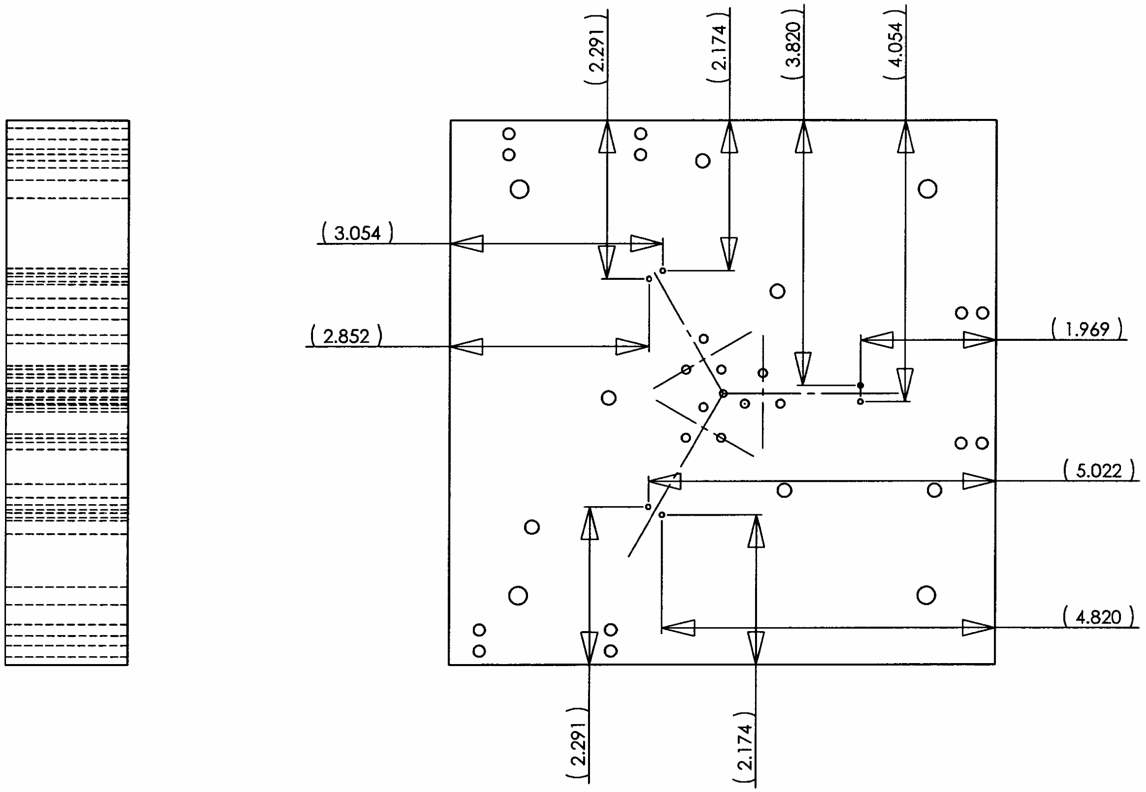

PROPRIETARY AND CONFIDENTIAL

THE INFORMATION CONTAINED IN THIS DRAWING IS THE SOLE PROPERTY OF MECHATRONICS LAB AT TEXAS A&M UNIVERSITY. ANY REPRODUCTION IN PART OR AS A WHOLE WITHOUT THE WRITTEN PERMISSION OF TEXAS A&M UNIVERSITY IS PROHIBITED.

NEXT ASSY

USED ON

APPLICATION

DIMENSIONS ARE IN INCHES
TOLERANCES:
FRACTIONAL±
ANGULAR: MACH± BEND ±
TWO PLACE DECIMAL ±
THREE PLACE DECIMAL ±

MATERIAL —

FINISH —

DO NOT SCALE DRAWING

	NAME	DATE
DRAWN		
CHECKED		
ENG APPR.		
MFG APPR.		
Q.A.		

COMMENTS:

Texas A&M University

Base Plate and location of vertical coil mounting holes

SIZE A DWG. NO. REV.

SCALE:1:2 WEIGHT: SHEET 1 OF 1

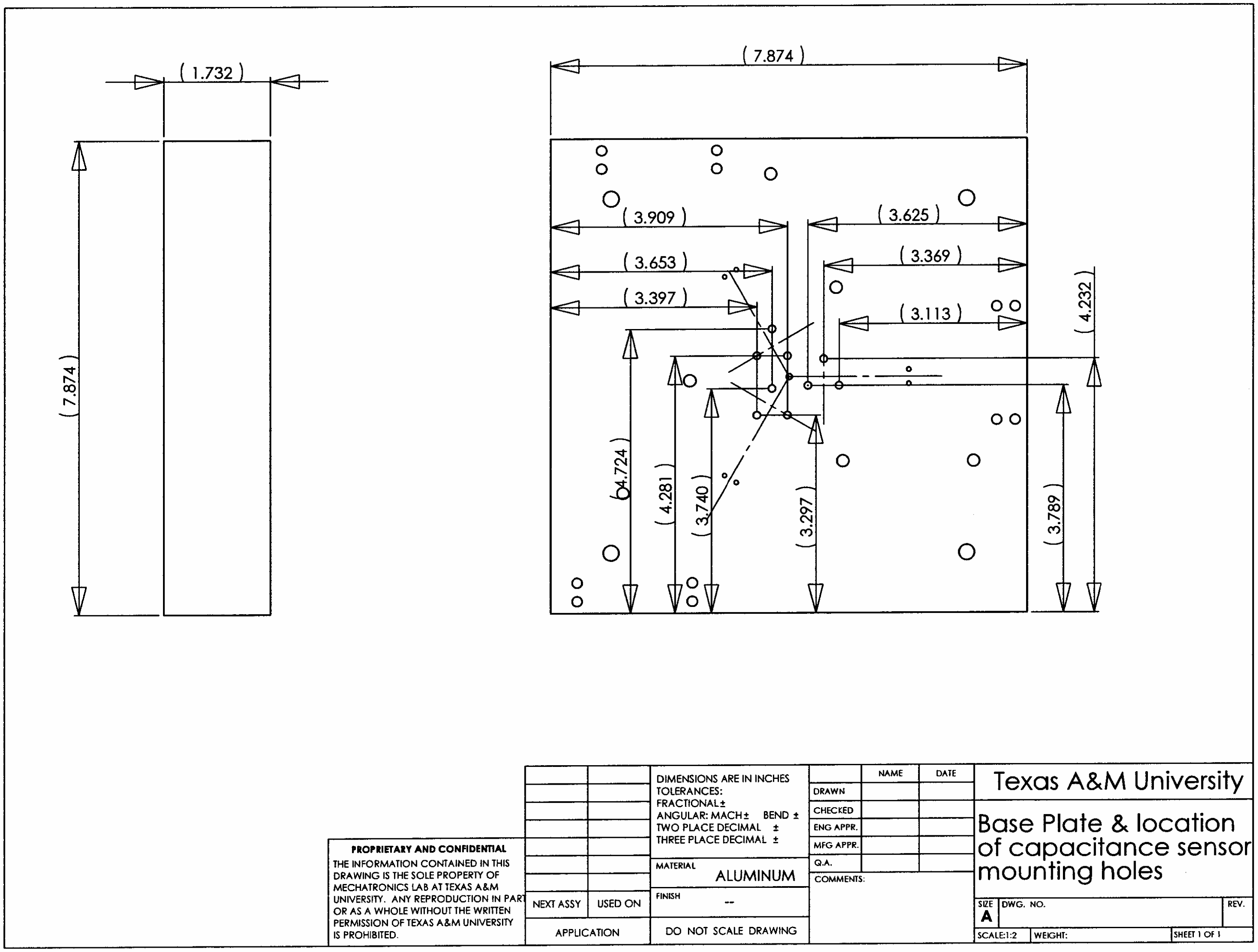
(1.732)
(7.874)
(7.874)
(3.909)
(3.653)
(3.397)
(3.625)
(3.369)
(3.113)
(4.232)
(4.724)
(4.281)
(3.740)
(3.297)
(3.789)
PROPRIETARY AND CONFIDENTIAL
THE INFORMATION CONTAINED IN THIS DRAWING IS THE SOLE PROPERTY OF MECHATRONICS LAB AT TEXAS A&M UNIVERSITY. ANY REPRODUCTION IN PART OR AS A WHOLE WITHOUT THE WRITTEN PERMISSION OF TEXAS A&M UNIVERSITY IS PROHIBITED.
NEXT ASSY
USED ON
APPLICATION
DIMENSIONS ARE IN INCHES
TOLERANCES:
FRACTIONAL±
ANGULAR: MACH± BEND ±
TWO PLACE DECIMAL ±
THREE PLACE DECIMAL ±
MATERIAL
ALUMINUM
FINISH
--
DO NOT SCALE DRAWING
NAME
DATE
DRAWN
CHECKED
ENG APPR.
MFG APPR.
Q.A.
COMMENTS:
Texas A&M University
Base Plate & location of capacitance sensor mounting holes
SIZE
A
DWG. NO.
REV.
SCALE:1:2
WEIGHT:
SHEET 1 OF 1

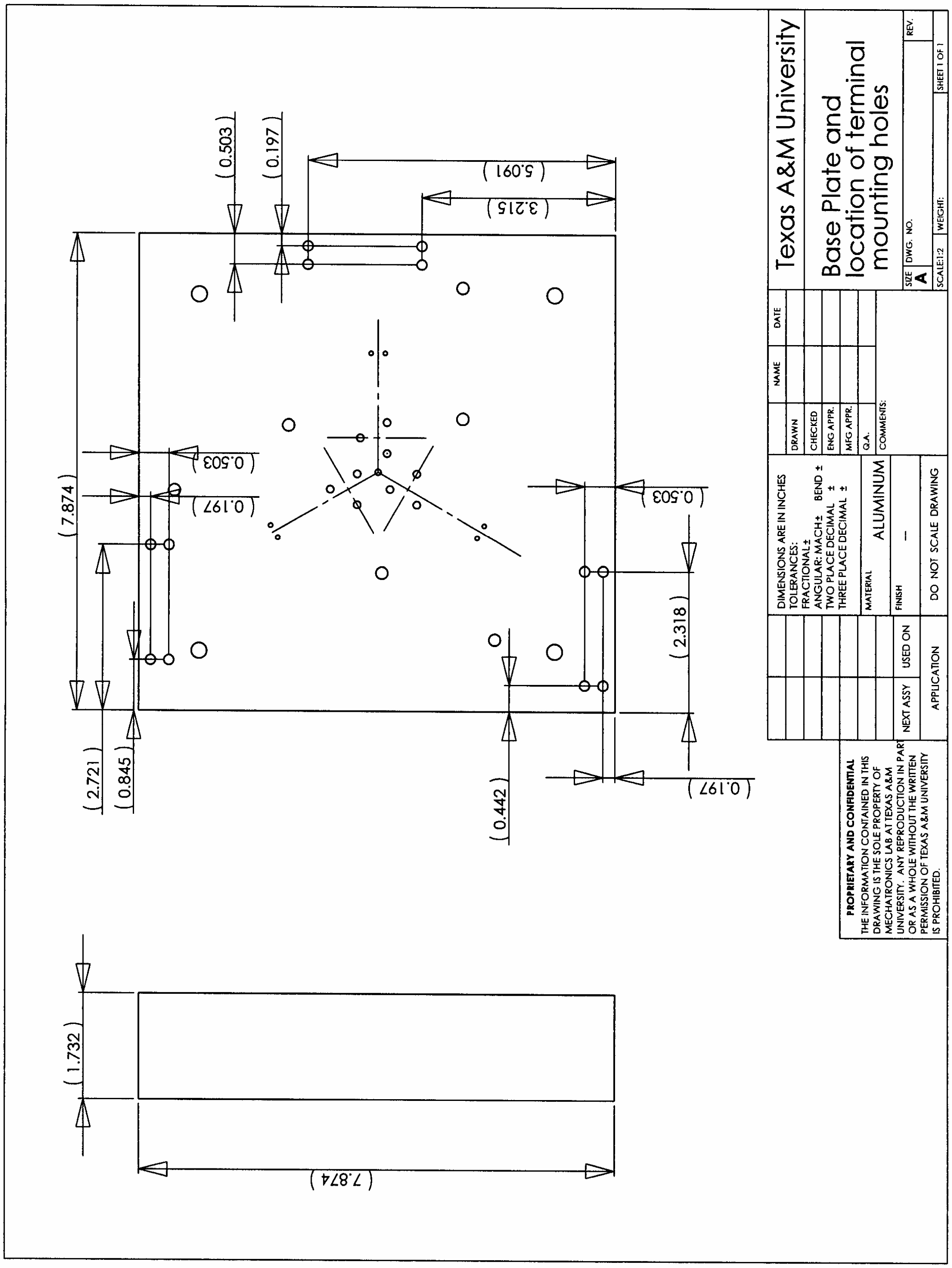
Texas A&M University
Base Plate and location of terminal mounting holes
DIMENSIONS ARE IN INCHES
TOLERANCES:
FRACTIONAL±
ANGULAR: MACH± BEND ±
TWO PLACE DECIMAL ±
THREE PLACE DECIMAL ±
MATERIAL
ALUMINUM
FINISH
—
DO NOT SCALE DRAWING
NEXT ASSY
USED ON
APPLICATION
DRAWN
CHECKED
ENG APPR.
MFG APPR.
Q.A.
COMMENTS:
NAME
DATE
SIZE
A
DWG. NO.
REV.
SCALE:1:2
WEIGHT:
SHEET 1 OF 1
PROPRIETARY AND CONFIDENTIAL
THE INFORMATION CONTAINED IN THIS DRAWING IS THE SOLE PROPERTY OF MECHATRONICS LAB AT TEXAS A&M UNIVERSITY. ANY REPRODUCTION IN PART OR AS A WHOLE WITHOUT THE WRITTEN PERMISSION OF TEXAS A&M UNIVERSITY IS PROHIBITED.
(0.503)
(0.197)
(5.091)
(3.215)
(7.874)
(0.503)
(0.197)
(0.503)
(2.318)
(2.721)
(0.845)
(0.442)
(0.197)
(1.732)
(7.874)

VITA

SHOBHIT VERMA

Education

Texas A&M University, College Station, Texas. August 2005,
Doctor of Philosophy in Mechanical Engineering.

Indian Institute of Technology, Bombay, India. August 2002,
Master of Technology in Computer Integrated Manufacturing.

Indian Institute of Technology, Bombay, India. August 2002,
Bachelor of Technology in Mechanical Engineering.

Publications

[1] **S. Verma**, W.-J. Kim, and J. Gu, "6-Axis Nanopositioning Device with Precision Magnetic Levitation Technology," *IEEE/ASME Transactions on Mechatronics*, vol. 9, no.2, June 2004.

[2] J. Gu, W.-J. Kim, and **S. Verma**, "Nanoscale Motion Control With a Compact Minimum-Actuator Magnetic Levitator," *ASME Journal of Dynamic Systems, Measurement and Control*, in press.

[3] **S. Verma**, and W.-J. Kim, "Maglev 6-Axis Nanopositioner with Permanent-Magnet Cylindrical Actuators," submitted to *IEEE Transactions on Industry Applications*.

[4] W.-J. Kim, and **S. Verma**, "Multi-Axis Maglev Positioner with High Resolution over Large Travel Range," submitted to *Mechatronics*.

Awards

ASME Worldwide Student Design Contest 2001, Manhattan, NY. Won Region XIII World championship (includes all countries except those in North America) and achieved 5th rank in the finals.

ASME Worldwide Student Design Contest 2000, Orlando, FL. Won Region XIII World championship and achieved 9th rank in the finals.

Permanent Address
667, C-Block
Panki, Kanpur
India-208020